



Cyprus
University of
Technology

Faculty of Engineering
and Technology

Doctoral Dissertation

**GRID-CONNECTED PHOTOVOLTAIC SYSTEM IN
BUILDINGS WITH HYBRID ENERGY STORAGE**

Maria Argyrou

Limassol, June 2021

CYPRUS UNIVERSITY OF TECHNOLOGY
FACULTY OF ENGINEERING AND TECHNOLOGY
DEPARTMENT OF ELECTRICAL ENGINEERING, COMPUTER
ENGINEERING AND INFORMATICS

Doctoral Dissertation

**GRID-CONNECTED PHOTOVOLTAIC SYSTEM IN
BUILDINGS WITH HYBRID ENERGY STORAGE**

Maria Argyrou

Limassol, June 2021

Approval Form

Doctoral Dissertation

GRID-CONNECTED PHOTOVOLTAIC SYSTEM IN BUILDINGS WITH HYBRID ENERGY STORAGE

Presented by

Maria Argyrou


Supervisor*: Dr. Paul Christodoulides, Assistant Professor

Faculty of Engineering and Technology, Cyprus University of Technology

Signature  _____

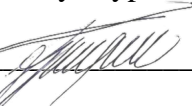
Chair of the committee: Dr. Christakis Damianou, Professor

Faculty of Engineering and Technology, Cyprus University of Technology

Signature  _____

Member of the committee: Dr. Alexis Polycarpou, Assistant Professor

Department of Electrical Engineering, Computer Engineering and Informatics,
Frederick University, Cyprus

Signature  _____

*Co-supervisor: Dr. Soteris Kalogirou, Professor

Faculty of Engineering and Technology, Cyprus University of Technology

Cyprus University of Technology

Limassol, June 2021

Copyrights

Copyright © 2021 Maria Argyrou

All rights reserved.

The approval of the dissertation by the Department of Electrical Engineering, Computer Engineering and Informatics does not imply necessarily the approval by the Department of the views of the writer.

ACKNOWLEDGEMENTS

Firstly, I would like to express my deep gratitude to my supervisor, Dr. Paul Christodoulides, for his valuable support and guidance throughout my journey. I also acknowledge my co-supervisor, Prof. Soteris Kalogirou, for his feedback and support during this study. Moreover, I would like to thank Dr. Christos Marouchos for his encouragement and his helpful suggestions and guidelines.

I am also grateful to my friends and colleagues at the Department of Electrical Engineering for supporting me all these years. Specifically, I want to thank Panayiotis, Harris and Chrysovalantis for the valuable discussions we had, their recommendations and their support. Furthermore, I would like to acknowledge all the academic and administrative staff I collaborated with, especially the academics who believed in me and trusted me as their teaching assistant, Dr. H. Michael, Dr. K. Kalli and my supervisor Dr. P. Christodoulides.

Furthermore, I would like to express my sincere gratitude to my family, who believed in me and raised me to be the person I am today. Finally, I want to thank my life partner, Yiannis, for his unconditional love and patience all these years. Without their endless support and encouragement, none of my goals would have been achieved.

PUBLICATIONS

List of publications (peer-reviewed journals and conferences):

- **M. C. Argyrou**, C. C. Marouchos, S. A. Kalogirou, and P. Christodoulides, “A novel power management algorithm for a residential grid-connected PV system with battery-supercapacitor storage for increased self-consumption and self-sufficiency,” *Energy Conversion and Management* (submitted).
- **M. C. Argyrou**, C. C. Marouchos, S. A. Kalogirou, and P. Christodoulides, “Modeling a residential grid-connected PV system with battery-supercapacitor storage: Control design and stability analysis,” *Energy Reports* (submitted).
- S. Ioannou, **M. C. Argyrou**, P. Christodoulides, and C. C. Marouchos, “Small signal transfer functions and mathematical model of the boost power converter,” in *MEDPOWER 2020*, 2020, pp. 1–6.
- S. Ioannou, **M. C. Argyrou**, M. Darwish, and C. C. Marouchos, “Modulation Processes in Power Electronic Converters,” in *2020 55th International Universities Power Engineering Conference (UPEC)*. IEEE, 2020, pp. 1–6.
- R. Agathokleous, G. Bianchi, G. P. Panayiotou, L. Aresti, **M. C. Argyrou**, G. Georgiou, S. Tassou, H. Jouhara, S. A. Kalogirou, G. Florides, and P. Christodoulides, “Waste heat recovery in the EU industry and proposed new technologies,” *Energy Procedia*, vol. 161, pp. 489–496, 2019.
- S. Ioannou, **M. C. Argyrou**, C. Marouchos, and M. Darwish, “Efficiency Investigation of a Grid Connected PV System with Power Smoothing,” in *2019 54th International Universities Power Engineering Conference (UPEC)*. IEEE, 2019, pp. 1–6.
- **M. C. Argyrou**, C. Spanias, C. C. Marouchos, S. A. Kalogirou, and P. Christodoulides, “Energy management and modeling of a grid-connected BIPV system with battery energy storage,” in *2019 54th International Universities Power Engineering Conference (UPEC)*. IEEE, 2019, pp. 1–6.
- **M. C. Argyrou**, P. Christodoulides, and S. A. Kalogirou, “Modeling of a photovoltaic system with different MPPT techniques using MATLAB / Simulink,” in *2018 IEEE International Energy Conference (ENERGYCON)*, 2018.

- **M. C. Argyrou**, P. Christodoulides, C. C. Marouchos, and S. A. Kalogirou, “Hybrid battery-supercapacitor mathematical modeling modeling for PV application using Matlab/Simulink,” in 2018 53rd International Universities Power Engineering Conference (UPEC). IEEE, 2018, pp. 1–6.
- **M. C. Argyrou**, F. Paterakis, C. Panagi, C. Makarounas, M. Darwish, and C. Marouchos, “Supercapacitor application for PV power smoothing,” in 2018 53rd International Universities Power Engineering Conference (UPEC), 2018, pp. 1–5. (*Best Oral Presentation Award by a Young Engineer*)
- **M. C. Argyrou**, P. Christodoulides, and S. A. Kalogirou, “Energy storage for electricity generation and related processes: Technologies appraisal and grid scale applications,” *Renew. Sustain. Energy Rev.*, vol. 94, pp. 804–821, 2018.
- **M. C. Argyrou**, C. C. Marouchos, M. Darwish, E. Iosif, and F. Paterakis, “Investigation of the switched inductor circuit for harmonics compensation,” in 2017 52nd International Universities Power Engineering Conference (UPEC). IEEE, 2017, pp. 1–5.
- G. P. Panayiotou, G. Bianchi, G. Georgiou, L. Aresti, **M. Argyrou**, R. Agathokleous, K. M. Tsamos, S. A. Tassou, G. Florides, S. Kalogirou, and P. Christodoulides, “Preliminary assessment of waste heat potential in major European industries,” *Energy Procedia*, vol. 123, pp. 335–345, 2017.
- **M. C. Argyrou**, P. Christodoulides, C. C. Marouchos, and S. A. Kalogirou, “A grid-connected photovoltaic system: mathematical modeling using MATLAB/Simulink,” in 2017 52nd International Universities Power Engineering Conference (UPEC). IEEE, 2017, pp.1–6.
- **M. C. Argyrou**, P. Christodoulides, C. C. Marouchos, and G. A. Florides, “Energy storage technologies, nearly Zero Energy Buildings and a short-term storage application,” in 5th International Conference on Renewable Energy Sources & Energy Efficiency - New Challenges, 2016.
- **M. C. Argyrou**, P. Christodoulides, C. C. Marouchos, S. A. Kalogirou, G. A. Florides, and L. Lazari, “Overview of energy storage technologies and a short-term storage application for wind turbines,” in Proceedings of the International Offshore and Polar Engineering Conference, 2016.

ABSTRACT

The increasing penetration of renewable energy technologies causes major problems in the power network, as their generation cannot be totally predicted. Along with fluctuations in Renewable Energy Sources (RES) production due to weather uncertainties, storage is very important for mitigating several problems that may arise, affecting the stability and reliability of the grid. Thus, storage technologies have gained an increased attention in recent years. In particular, there has been an emphasis on residential storage applications (behind-the-meter storage), with the aim of increasing the energy self-consumption and therefore reducing electricity bills.

A model containing a 3 kW_p rooftop solar photovoltaic (PV) system connected to the grid through converters and a battery-supercapacitor hybrid energy storage system is proposed. The storage devices are connected to the common 400 V DC-bus in a fully active parallel configuration through two bidirectional DC-DC converters. This configuration allows the battery and supercapacitor to have different voltages and their power flow to be controlled separately. A small-signal stability analysis is considered for the design of the current controllers for both the bidirectional converters of the battery and supercapacitor. Moreover, the small-signal stability analysis of the voltage source inverter (VSI) is considered in order to design the DC-bus voltage controller, from which a reference output current is extracted using a phase-locked loop (PLL) for grid synchronization. A new filtration-based power management algorithm (PMA) is proposed, which prioritizes the utilization of the PVs and battery-supercapacitor instead of the grid, thus increasing the self-consumption and self-sufficiency of the building. A comparison between a battery-only and a battery-supercapacitor storage application is performed in long-term operation (24 hours), verifying the effectiveness of the integration of the supercapacitor. In addition, the dynamic performance of the proposed model is verified through several simulations for different scenarios over short time periods (10–30 seconds). The results show that the model works properly and responds extremely fast during different mode transitions, exhibiting a fast DC-bus voltage regulation with a very low ripple voltage (a maximum of $\pm 0.625\%$). Also, the supercapacitor handles rapid changes that occur within 0.2 seconds, which can relieve the battery stress and, hence, extend the battery lifetime. Finally, an effective power sharing is achieved between the PV, the battery-supercapacitor storage, the building load and the grid. The proposed model is developed and simulated in the MATLAB/Simulink software environment, based on mathematical analysis and average modeling.

Keywords: grid-connected photovoltaics, battery, supercapacitor, hybrid energy storage, modeling, control, filtration-based power management

TABLE OF CONTENTS

PUBLICATIONS.....	vi
ABSTRACT.....	viii
TABLE OF CONTENTS.....	ix
LIST OF TABLES.....	xii
LIST OF FIGURES.....	xiii
LIST OF ABBREVIATIONS.....	xix
NOMENCLATURE.....	xxi
1 Introduction.....	1
1.1 General Overview/Problem statement.....	1
1.2 Literature review on PV systems with energy storage.....	3
1.3 Objectives and contributions of the Thesis.....	13
1.4 Outline of the Thesis.....	14
2 Theoretical Background.....	16
2.1 Renewable energy.....	16
2.1.1 Solar Energy.....	16
2.1.2 Photovoltaic Module.....	19
2.2 Energy Storage.....	20
2.2.1 Pumped Hydro Storage (PHS).....	23
2.2.2 Compressed Air Energy Storage (CAES).....	25
2.2.3 Batteries.....	27
2.2.4 Hydrogen Energy Storage - Fuel Cells.....	38
2.2.5 Thermal Energy Storage (TES).....	40
2.2.6 Superconducting Magnetic Energy Storage (SMES).....	42
2.2.7 Flywheel Energy Storage (FES).....	43
2.2.8 Supercapacitors/Ultracapacitors.....	44
2.2.9 Comparison of all storage methods.....	46
2.3 Energy Storage Applications.....	49
2.4 Hybrid Energy Storage (HES).....	55
2.5 Configurations of a grid-connected PV system with hybrid energy storage (HES).....	58

3	Grid-connected PV system in buildings: mathematical analysis and simulation modeling	64
3.1	PV array	67
3.1.1	Theory and mathematical analysis	67
3.1.2	Modeling and simulation	69
3.2	Maximum Power Point Tracking (MPPT)	72
3.2.1	Theory and mathematical analysis	72
3.2.2	Modeling and simulation	78
3.3	DC-DC Boost Converter	84
3.3.1	Theory and mathematical analysis	84
3.3.2	Modeling and simulation	86
3.4	Battery storage	86
3.4.1	Theory and mathematical analysis	86
3.4.2	Modeling and simulation	90
3.4.3	Battery pack sizing	94
3.5	Supercapacitor Storage	95
3.5.1	Theory and mathematical analysis	95
3.5.2	Modeling and simulation	97
3.5.3	Supercapacitor pack sizing	99
3.6	Bidirectional DC-DC Converter	99
3.6.1	Theory and mathematical analysis	99
3.6.2	Modeling and simulation	110
3.6.3	Transfer functions and parameters of the bidirectional converter	110
3.7	DC-AC Inverter	112
3.7.1	Theory and mathematical analysis	112
3.7.2	Modeling and simulation	113
3.8	System control and stability analysis	114
3.8.1	Battery-supercapacitor hybrid storage system: Design of current controllers and stability analysis	115
3.8.2	DC-link: Capacitance calculation and dynamics	120
3.8.3	Inverter control: Design of DC-bus voltage controller and calculation of inverter reference current	123

3.9	Power management algorithm (PMA).....	125
3.9.1	Battery-only algorithm	126
3.9.2	Battery-supercapacitor hybrid energy storage algorithm	129
4	Complete Model Results	141
4.1	Results for the PV system with battery-only storage in long-term operation.....	144
4.2	Comparison between the battery-only and the battery-supercapacitor hybrid storage system	146
4.3	Results for the PV system with battery-supercapacitor hybrid storage in short-term operation	148
4.3.1	Excess Power Mode (EPM)	148
4.3.2	Deficit Power Mode (DPM).....	161
5	Conclusions	174
5.1	Summary.....	174
5.2	Future directions	175
	REFERENCES.....	177

LIST OF TABLES

Table 1.1: Summary of related work in the literature	9
Table 2.1: Comparison of the various storage methods (except batteries)	47
Table 2.2: Comparison of various battery storage technologies	48
Table 3.1: Electrical characteristics of photovoltaic module	69
Table 3.2: Fuzzy logic rules base table	77
Table 3.3: Comparison table of studied MPPT methods	82
Table 3.4: System parameters for the simulation of the battery and supercapacitor converters	111
Table 3.5: Transfer functions of the battery and supercapacitor converters	111
Table 3.6: Table of all possible cases with their corresponding modes' and reference currents' setting	133
Table 4.1: Simulation results of proposed PV system with battery-only storage in long-term operation (24 hours)	145
Table 4.2: Simulation results of proposed PV system with hybrid storage in EPM (Scenario 1)	150
Table 4.3: Simulation results of proposed PV system with hybrid storage in EPM (Scenario 2)	156
Table 4.4: Simulation results of proposed PV system with hybrid storage in DPM (Scenario 3)	162
Table 4.5: Simulation results of proposed PV system with hybrid storage in DPM (Scenario 4)	169

LIST OF FIGURES

Figure 1.1: Typical example of a nZEB building.....	3
Figure 2.1: Solar PV Global installed capacity, by country [47]	17
Figure 2.2: CSP Global installed capacity, by country [47].....	18
Figure 2.3: Solar water heating collectors Global installed Capacity [47]	19
Figure 2.4: Structure of a silicon PV cell [54]	20
Figure 2.5: Global energy storage power capacity by technology group until 2017	21
Figure 2.6: Global energy storage power capacity shares in MW of several storage technologies until 2017	22
Figure 2.7: Classification of energy storage technologies by the form of stored energy	23
Figure 2.8: A typical diagram of PHS system.....	24
Figure 2.9: A typical diagram of a CAES system	26
Figure 2.10: Lead–acid battery storage with chemical reactions during discharge	28
Figure 2.11: Schematic of the advanced lead-acid battery (ultra-battery)	28
Figure 2.12: NiMH battery storage reaction diagram during discharge.....	29
Figure 2.13: Schematic of a NaS battery	30
Figure 2.14: Schematic of a lithium-ion battery	32
Figure 2.15: Metal-air (Zn-air) battery storage during discharge	34
Figure 2.16: Schematic of a flow battery	35
Figure 2.17: Topology of fuel cell and hydrogen storage	38
Figure 2.18: CSP plant with thermal energy storage	42
Figure 2.19: SMES system.....	43
Figure 2.20: The flywheel storage system	44
Figure 2.21: Supercapacitor cell	45
Figure 2.22: Energy Storage Applications by the needs in energy, power and discharge time duration	49
Figure 2.23: Energy Storage Technologies by power capacity and discharge time.....	50
Figure 2.24: Energy storage load profile in peak shaving.....	52
Figure 2.25: Energy storage load profile in load leveling.....	52
Figure 2.26: Classification of PV systems	59
Figure 2.27: Block diagram of a basic grid-connected rooftop PV system	60

Figure 2.28: Passive topology of the rooftop PV system with HES	61
Figure 2.29: Battery semi-active topology of the rooftop PV system with HES	62
Figure 2.30: Supercapacitor semi-active topology of the rooftop PV system with HES	62
Figure 2.31: Fully active topology of the rooftop PV system with HES	63
Figure 3.1: Block diagram of the proposed grid-connected PV system with battery- supercapacitor hybrid storage	65
Figure 3.2: Architecture of the proposed grid-connected PV system with battery-supercapacitor hybrid storage.....	65
Figure 3.3: Equivalent circuit of the one-diode PV cell.....	67
Figure 3.4: Output characteristics of a PV module [226]	68
Figure 3.5: Inside the PV array subsystem.....	69
Figure 3.6: Calculation of output current of PV module I_{pv}	70
Figure 3.7: I-V curve with varying irradiance at 25°C.....	71
Figure 3.8: P-V curve with varying irradiance at 25°C.....	71
Figure 3.9: I-V curve with varying temperature at 1000 W/m ²	72
Figure 3.10: P-V curve with varying temperature at 1000 W/m ²	72
Figure 3.11: Characteristic <i>P-V</i> curve of a photovoltaic array.....	73
Figure 3.12: Flowchart of the P&O algorithm	74
Figure 3.13: Characteristic <i>P-V</i> curve of a photovoltaic array.....	74
Figure 3.14: Flowchart of the Incremental Conductance algorithm	75
Figure 3.15: Fuzzy Logic controller diagram.....	76
Figure 3.16: Membership function for inputs and output of fuzzy logic controller.....	76
Figure 3.17: Characteristic <i>P-V</i> curve of a photovoltaic array, showing the nine regions according to voltage and power variation	77
Figure 3.18: PV system with P&O control in Simulink.....	78
Figure 3.19: PV system with Fuzzy logic control in Simulink.....	78
Figure 3.20: Fuzzy logic designer and membership function editor	79
Figure 3.21: Fuzzy logic rule editor.....	79
Figure 3.22: Surface viewer for the fuzzy logic controller	79
Figure 3.23: PV array voltage for P&O (blue), incremental conductance (red) and fuzzy logic (black) control	80

Figure 3.24: PV array current for P&O (blue), incremental conductance (red) and fuzzy logic (black) control	81
Figure 3.25: PV array power for P&O (blue), incremental conductance (red) and fuzzy logic (black) control	81
Figure 3.26: P-V curve (dashed line) and MPPT P-V curve (solid line) for different values of irradiance.....	83
Figure 3.27: P-I curve (dashed line) and MPPT P-I curve (solid line) for different values of irradiance.....	83
Figure 3.28: I-V curve (dashed line) and MPPT I-V curve (solid line) for different values of irradiance.....	84
Figure 3.29: Circuit of a DC-DC boost converter	85
Figure 3.30: Averaged model of DC-DC boost converter	86
Figure 3.31: Dual polarization battery cell circuit	87
Figure 3.32: Battery characteristic curves of usable capacity with respect to: (a) cycle number, (b) temperature, (c) battery current, (d) storage time, as well as (e) open-circuit voltage V_{oc} versus SOC, and (f) transient response to a step load current event [257].....	88
Figure 3.33: Battery cell 2 nd -order RC model	91
Figure 3.34: Subsystem calculation of series voltage and RC parallel networks voltages	91
Figure 3.35: Varying curve of V_{oc} with SOC	92
Figure 3.36: Battery pulse discharging/charging current with time	93
Figure 3.37: Battery SOC with time	93
Figure 3.38: Battery voltage during discharging/charging with time	93
Figure 3.39: Usable Capacity vs. cycle number.....	94
Figure 3.40: Battery pack subsystem in Simulink.....	95
Figure 3.41: Two branches equivalent circuit of a supercapacitor cell.....	95
Figure 3.42: Simulink model of supercapacitor pack	97
Figure 3.43: Supercapacitor charging/discharging current with time	98
Figure 3.44: Supercapacitor charging/discharging voltage with time.....	98
Figure 3.45: Supercapacitor SOC with time	98
Figure 3.46: Bidirectional DC-DC converter circuit.....	100
Figure 3.47: Steps of power stage modeling	101
Figure 3.48: Circuit of the boost-mode converter	102

Figure 3.49: Circuit of the buck-mode converter	106
Figure 3.50: Battery bidirectional converter in Simulink	110
Figure 3.51: Full-bridge grid-side voltage-source inverter circuit	112
Figure 3.52: Averaged model of single-phase DC-AC inverter.....	114
Figure 3.53: Block diagram of the (a) supercapacitor current controller, (b) battery current controller	115
Figure 3.54: Small-signal Simulink model for boost-mode operation for the (a) supercapacitor current controller, (b) battery current controller	116
Figure 3.55: Open-loop Bode plot of the supercapacitor current control loop (boost-mode)...	117
Figure 3.56: Open-loop Bode plot of the battery current control loop (boost-mode)	118
Figure 3.57: Small-signal Simulink model for buck-mode operation for the (a) supercapacitor current controller, (b) battery current controller	118
Figure 3.58: Open-loop Bode plot of the supercapacitor current control loop (buck-mode)....	119
Figure 3.59: Open-loop Bode plot of the battery current control loop (buck-mode)	119
Figure 3.60: Currents balance at DC-link and AC-link	120
Figure 3.61: DC-link subsystem in Simulink.....	121
Figure 3.62: Schematic of the inverter control which consists of the DC-bus voltage control and the PLL for the calculation of the inverter reference output current.....	123
Figure 3.63: Block diagram of the DC-bus voltage control loop.....	124
Figure 3.64: Simulink model for the DC-bus voltage control and the reference inverter current calculation	124
Figure 3.65: Small-signal Simulink model of the DC-bus voltage control loop.....	124
Figure 3.66: Open-loop Bode plot of the DC-bus voltage control loop.....	125
Figure 3.67: Block diagram of the grid-connected PV system with battery-only storage	126
Figure 3.68: Power management flowchart of the battery-only operation.....	127
Figure 3.69: PMA for the battery-only operation in Simulink.....	129
Figure 3.70: Block diagram of the grid-connected PV system with battery-supercapacitor energy storage	130
Figure 3.71: Control block diagram of the battery and supercapacitor current calculation through the PMA	131
Figure 3.72: PMA system for the charging and discharging process of the hybrid battery-supercapacitor storage system in Simulink	139

Figure 3.73: PMA for the charging and discharging process of the hybrid battery-supercapacitor storage system	140
Figure 4.1: Complete model of the grid-connected PV system with battery-only storage in Simulink	142
Figure 4.2: Complete model of the grid-connected PV system with battery-supercapacitor hybrid storage in Simuli	143
Figure 4.3: PV power (blue), Load power (red), Battery power (green) and Grid power (purple) in long-term operation (24 hours)	146
Figure 4.4: Battery SOC and battery current in long-term operation (24 hours)	146
Figure 4.5: Battery SOC for the battery-only (blue) and the hybrid (red) storage application .	147
Figure 4.6: Battery current for the battery-only (blue) and the hybrid (red) storage application	147
Figure 4.7: PV power (blue), Load power (red), Battery power (green), Supercapacitor power (yellow) and Grid power (purple) (Scenario 1).....	151
Figure 4.8: Mode of the battery converter, and availability modes of the battery and the supercapacitor (charging and discharging), respectively (Scenario 1).....	151
Figure 4.9: Battery current and supercapacitor current (Scenario 1)	152
Figure 4.10: PV current, battery current and supercapacitor current on DC-link side (Scenario 1)	152
Figure 4.11: Battery SOC and battery voltage (Scenario 1)	153
Figure 4.12: Supercapacitor SOC and supercapacitor voltage (Scenario 1)	153
Figure 4.13: DC-bus voltage and duty cycle for the battery and the supercapacitor bidirectional converters, respectively (Scenario 1)	154
Figure 4.14: Inverter output current, load current and grid current (Scenario 1).....	155
Figure 4.15: PV power (blue), Load power (red), Battery power (green), Supercapacitor power (yellow) and Grid power (purple) (Scenario 2).....	157
Figure 4.16: Mode of the battery converter, and availability modes of the battery and the supercapacitor (charging and discharging), respectively (Scenario 2).....	157
Figure 4.17: Battery current and supercapacitor current (Scenario 2)	158
Figure 4.18: PV current, battery current and supercapacitor current on DC-link side (Scenario 2)	158
Figure 4.19: Battery SOC and battery voltage (Scenario 2)	159
Figure 4.20: Supercapacitor SOC and supercapacitor voltage (Scenario 2)	159

Figure 4.21: DC-bus voltage and duty cycle for the battery and the supercapacitor bidirectional converters, respectively (Scenario 2)	160
Figure 4.22: Inverter output current, load current and grid current (Scenario 2).....	160
Figure 4.23: PV power (blue), Load power (red), Battery power (green), Supercapacitor power (yellow) and Grid power (purple) (Scenario 3).....	163
Figure 4.24: Mode of the battery converter, and availability modes of the battery and the supercapacitor (charging and discharging), respectively (Scenario 3).....	164
Figure 4.25: Battery current and supercapacitor current (Scenario 3)	164
Figure 4.26: PV current, battery current and supercapacitor current on DC-link side (Scenario 3)	165
Figure 4.27: Battery SOC and battery voltage (Scenario 3)	165
Figure 4.28: Supercapacitor SOC and supercapacitor voltage (Scenario 3)	166
Figure 4.29: DC-bus voltage and duty cycle for the battery and the supercapacitor bidirectional converters, respectively (Scenario 3)	167
Figure 4.30: Inverter current, load current and grid current (Scenario 3)	167
Figure 4.31: PV power (blue), Load power (red), Battery power (green), Supercapacitor power (yellow) and Grid power (purple) (Scenario 4).....	169
Figure 4.32: Mode of the battery converter, and availability modes of the battery and the supercapacitor (charging and discharging), respectively (Scenario 4).....	170
Figure 4.33: Battery current and supercapacitor current (Scenario 4)	170
Figure 4.34: PV current, battery current and supercapacitor current on DC-link side (Scenario 4)	171
Figure 4.35: Battery SOC and battery voltage (Scenario 4)	171
Figure 4.36: Supercapacitor SOC and supercapacitor voltage (Scenario 4)	172
Figure 4.37: DC-bus voltage and duty cycle for the battery and the supercapacitor bidirectional converters, respectively (Scenario 4)	173
Figure 4.38: Inverter current, load current and grid current (Scenario 4)	173

LIST OF ABBREVIATIONS

BW	Bandwidth
CAES	Compressed Air Energy Storage
CCM	Continuous Conduction Mode
CCVSI	Current Controlled Voltage Source Inverter
CES	Cryogenic Energy Storage
CSP	Concentrated Solar Power
DoD	Depth-of-Discharge
DPM	Deficit Power Mode
EES	Electrical Energy Storage
EPM	Excess Power Mode
FES	Flywheel Energy Storage
GM	Gain Margin
HES	Hybrid Energy Storage
LPF	Low Pass Filter
LTI	Linear time-invariant
MPP	Maximum Power Point
MPPT	Maximum Power Point Tracking
nZEB	Nearly Zero Energy Building
P&O	Perturbation and Observation
PCM	Phase Change Materials
PHS	Pumped Hydroelectric Storage
PI	Proportional Integral
PLL	Phase-Locked Loop
PM	Phase Margin
PMA	Power Management Algorithm
PSB	Polysulfide bromide battery
PV	Photovoltaic
PWM	Pulse Width Modulation
RES	Renewable Energy Sources
RHP	Right Half Plane
SISO	Single-input single-output

SMC	Sliding Mode Control
SMES	Superconducting Magnetic Energy Storage
SOC	State of Charge
TES	Thermal Energy Storage
UPS	Uninterruptable Power Supply
VRB	Vanadium Redox flow Battery
VSI	Voltage Source Inverter
V2H	Vehicle-to-Home
ZBR	Zinc-bromine Battery

NOMENCLATURE

Section 3.1

A	Diode ideality factor
G	Solar irradiation on PV module [W/m^2]
G_{ref}	Reference irradiation on PV module ($G_{ref} = 1000 \text{ W}/\text{m}^2$)
I_o	Reverse saturation current of PV module [A]
I_{ph}	Photocurrent of PV module [A]
I_{pv}	Output current of PV module [A]
I_{sc}	Short-circuit current of PV module [A]
k	Boltzmann's constant ($k = 1.381 \times 10^{-23} \text{ J}/\text{K}$)
K_i	Temperature coefficient of the short-circuit current of PV module [A/K]
K_v	Temperature coefficient of the open-circuit voltage of PV module [V/K]
N_s	Number of cells in series connection in a PV module
q	Electron charge ($q = 1.602 \times 10^{-19} \text{ C}$)
R_p	Shunt resistance of PV module [Ω]
R_s	Series resistance of PV module [Ω]
T_c	Temperature on PV module [K]
T_{ref}	Reference temperature on PV module ($T_{ref} = 298 \text{ K}$)
V_{oc}	Open-circuit voltage of PV module [V]
V_{pv}	Output voltage of PV module [V]

Section 3.2

I_{MPP}	Current at maximum power point [A]
P_{MPP}	Maximum power point [W]
V_{MPP}	Voltage at maximum power point [V]

Section 3.3

C	Capacitance of the DC-DC boost converter [F]
D	Duty cycle of the DC-DC boost converter
I_L	Inductor current of the DC-DC boost converter [A]
I_o	Output current of the DC-DC boost converter [A]

I_{sw}	Switching loss current parameter [A]
L	Inductance of the DC-DC boost converter [H]
R	Output (Load) resistance [Ω]
R_L	Inductor winding resistance [Ω]
V_{in}	Input voltage of the DC-DC boost converter [V]
V_o	Output voltage of the DC-DC boost converter [V]

Section 3.4

a_0, a_1, a_2, a_3	Constant parameters of the third-order polynomial relationship between V_{oc} and SOC
C_{init}	Nominal capacity of the battery [Ah]
C_{p1}	Capacitance on the first RC network of the battery cell [F]
C_{p2}	Capacitance on the second RC network of the battery cell [F]
C_{usable}	Usable capacity of the battery [C]
$f_1(N)$	Battery cycle number-dependent correction factor
$f_2(T)$	Battery temperature-dependent correction factor
I_b	Battery current [A]
k_1	Capacity loss correction coefficient due to aging effect
N	Battery cycle number
R_s	Series resistance of the battery cell [Ω]
$R_{self-discharge}$	Self-discharge resistance of the battery cell [Ω]
R_{p1}	Resistance on the first RC network of the battery cell [Ω]
R_{p2}	Resistance on the second RC network of the battery cell [Ω]
SOC_b	State-of-charge of the battery
$SOC_{b,0}$	Initial state-of-charge of the battery
V_b	Battery voltage [V]
V_{oc}	Open-circuit battery voltage [V]
V_{p1}	Voltage of the first RC network [V]
V_{p2}	Voltage of the second RC network [V]

Section 3.5

η_{sc}	Efficiency of the supercapacitor
-------------	----------------------------------

C_0	Constant capacitance of the supercapacitor cell [F]
C_1	Capacitance on the supercapacitor main cell [F]
C_2	Capacitance on the supercapacitor slow cell [F]
C_{eq}	Equivalent capacitance of the supercapacitor pack [F]
C_{sc}	Rated capacitance of the supercapacitor cell [F]
$C_{sc,Ah}$	Capacity of the supercapacitor [Ah]
C_v	Constant parameter of the supercapacitor [F/V]
E_{sc}	Energy stored in the supercapacitor [J]
i_2	Current on the supercapacitor slow cell [A]
I_{sc}	Current of the supercapacitor pack [A]
N_p	Number of supercapacitor strings in parallel connection
N_s	Number of supercapacitor cells in series connection
Q_1	Instantaneous charge of C_1 [F.V]
R_1	Series resistance on the supercapacitor main cell [Ω]
R_2	Series resistance on the supercapacitor slow cell [Ω]
R_f	Parallel resistance describing the self-discharge losses on the supercapacitor [Ω]
SOC_{sc}	State-of-charge of the supercapacitor
$SOC_{sc,0}$	Initial state-of-charge of the supercapacitor
U_{sc}	Voltage of the supercapacitor cell [V]
V_1	Voltage across the capacitor C_1 on the supercapacitor main cell [V]
V_2	Voltage across the capacitor C_2 on the supercapacitor slow cell [V]
V_{max}	Maximum voltage of the supercapacitor (i.e., the rated voltage) [V]
V_{min}	Minimum voltage of the supercapacitor [V]
V_{sc}	Voltage of the supercapacitor pack [V]

Section 3.6

A, B, C, D	State equation matrices
C_1	Capacitance on the boost-mode operation [F]
C_2	Capacitance on the buck-mode operation [F]
C	Capacitance of the DC-DC bidirectional converter [F]
D_1	Duty cycle of the DC-DC bidirectional converter for boost-mode operation (steady-state)

d_1	Duty cycle of the DC-DC bidirectional converter for boost-mode operation (large signal)
$\hat{d}_1(t)$	Duty cycle of the DC-DC bidirectional converter for boost-mode operation (small-signal)
D_2	Duty cycle of the DC-DC bidirectional converter for buck-mode operation (steady-state)
d_2	Duty cycle of the DC-DC bidirectional converter for buck-mode operation (large signal)
$\hat{d}_2(t)$	Duty cycle of the DC-DC bidirectional converter for buck-mode operation (small-signal)
$G_{id}^{bo}(s)$	Control-to-input current transfer function for boost-mode operation (small-signal)
$G_{vd}^{bo}(s)$	Control-to-output voltage transfer function for boost-mode operation (small-signal)
$G_{vi}^{bo}(s)$	Input current-to-output voltage transfer function for boost-mode operation (small-signal)
$G_{id}^{bu}(s)$	Control-to-input current transfer function for buck-mode operation (small-signal)
$G_{vd}^{bu}(s)$	Control-to-output voltage transfer function for buck-mode operation (small-signal)
$G_{vi}^{bu}(s)$	Input current-to-output voltage transfer function for buck-mode operation (small-signal)
I_b	Battery current (steady-state) [A]
I_{dc}	Output current for boost-mode operation (steady-state) [A]
i_{dc}	Output current for boost-mode operation (averaged large signal) [A]
$\hat{i}_{dc}(t)$	Output current for boost-mode operation (small-signal) [A]
I_L	Inductor current (steady-state) [A]
i_L	Inductor current (averaged large signal) [A]
$\hat{i}_L(t)$	Inductor current, in time-domain (small-signal) [A]
L	Inductance of the DC-DC bidirectional converter [H]
mode	Mode of the battery converter (i.e., boost-mode: mode=1, buck-mode: mode=0)
R	Output (Load) resistance [Ω]
sign_sc	Sign of the supercapacitor current that defines the mode of the supercapacitor converter (i.e., boost-mode: sign_sc>0, buck-mode: sign_sc <0)
$\hat{\mathbf{u}}(t)$	Input vector, in time-domain (small-signal)
$\hat{\mathbf{U}}(s)$	Input vector, in frequency-domain (small-signal)
V_b	Battery voltage (steady-state) [V]

v_b	Battery voltage (averaged large signal) [V]
$\hat{v}_b(t)$	Battery voltage (small-signal) [V]
V_{dc}	DC-bus voltage (steady-state) [V]
v_{dc}	DC-bus voltage (averaged large signal) [V]
$\hat{v}_{dc}(t)$	DC-bus voltage (small-signal) [V]
$\hat{\mathbf{x}}(t)$	State vector, in time-domain (small-signal)
$\hat{\mathbf{X}}(s)$	State vector, in frequency-domain (small-signal)
$\hat{\mathbf{y}}(t)$	Output vector, in time-domain (small-signal)
$\hat{\mathbf{Y}}(s)$	Output vector, in frequency-domain (small-signal)

Section 3.7

ω	Grid line frequency [rad/s]
D	Duty cycle of the inverter
I_{ac}	Amplitude (peak value) of the output current of the inverter [A]
$i_{ac}(t)$	Instantaneous output current of the inverter [A]
$i_{dc,inv}$	Input current of the inverter [A]
I_{rms}	RMS value of the output current of the inverter [A]
P_{ac}	Average output power of the inverter [W]
$p_{inv}(t)$	Instantaneous output power of the inverter [W]
T_s	Switching period [s]
V_{ac}	Amplitude (peak value) of the output voltage of the inverter [V]
$v_{ac}(t)$	Instantaneous output voltage of the inverter [V]
V_{dc}	Input voltage of the inverter (i.e., DC-bus voltage) [V]
V_{rms}	RMS value of the output voltage of the inverter [V]

Section 3.8

ΔV_{dc}	Peak-to-peak ripple voltage of the DC-bus voltage [V]
ω	Grid line frequency [rad/s]
ω_c	Crossover frequency [rad/s]
C_{dc}	Capacitance on the DC-link [F]
\hat{d}_b	Duty cycle of the battery converter (small-signal)
\hat{d}_{sc}	Duty cycle of the supercapacitor converter (small-signal)

f_c	Crossover frequency [Hz]
f_{sw}	Switching frequency [Hz]
$G_c(s)$	Transfer function of a PI compensator, in the s-domain
$G_{vi}(s)$	Transfer function of the input voltage by the grid current (small-signal)
$H_{i,b}$	Feedback sensor gain of the battery current controller
$H_{i,sc}$	Feedback sensor gain supercapacitor current controller
$i_{b,dc}$	Battery current on the DC-bus [A]
$i_{dc,inv}$	Input current of the inverter [A]
I_g	Amplitude of grid current (steady-state) [A]
i_g	Amplitude of grid current (averaged large signal) [A]
$\hat{i}_g(t)$	Amplitude of grid current (small-signal) [A]
i_{load}	Load AC current [A]
$\hat{i}_{L,b}$	Inductor current of the battery converter (small-signal) [A]
$\hat{i}_{L,b}^*$	Reference inductor current for the battery converter (small-signal) [A]
$\hat{i}_{L,sc}$	Inductor current of the supercapacitor converter (small-signal) [A]
$\hat{i}_{L,sc}^*$	Reference inductor current for the supercapacitor converter (small-signal) [A]
$i_{pv,dc}$	Photovoltaic current on the DC-bus [A]
$i_{sc,dc}$	Supercapacitor current on the DC-bus [A]
K_i	Integral gain
K_p	Proportional gain
mode	Mode of the battery converter (i.e., boost-mode: mode=1, buck-mode: mode=0)
P_{ac}	Average output power of the inverter [W]
P_{dc}	Input power of the inverter [W]
P_g	Average active power injected into the grid [W]
p_{inv}	Instantaneous output power of the inverter [W]
P_{load}	Load power (average) [W]
sign_sc	Sign of the supercapacitor current that defines the mode of the supercapacitor converter (i.e., boost-mode: sign_sc>0, buck-mode: sign_sc <0)
V_{dc}	DC-bus voltage (steady-state) [V]
v_{dc}	DC-bus voltage (averaged large signal) [V]
$\hat{v}_{dc}(t)$	DC-bus voltage (small-signal) [V]
V_g	Amplitude of grid voltage (steady-state) [V]

v_g Amplitude of grid voltage (averaged large signal) [V]

Section 3.9

d_b	Duty cycle of the battery converter
d_{sc}	Duty cycle of the supercapacitor converter
i_{ac}, i_{inv}	Output current of the inverter [A]
i_{avg}	Average current of the reference hybrid current [A]
i_b	Battery current [A]
$i_{b,dc}$	Battery current on the DC-bus [A]
$i_{b,osc}$	Compensated high-frequency current for the battery side [A]
i_{comp}	Compensated error battery current [A]
$i_{dc,inv}$	Input current of the inverter [A]
i_g	Grid current [A]
i_{hes}^*	Reference total hybrid current [A]
$i_{L,b,err}$	Error battery inductor current [A]
$i_{L,b}$	Inductor current of the battery converter [A]
$i_{L,b}^* = i_b^*$	Reference inductor current for the battery converter [A]
i_{load}	Load current [A]
$i_{L,PF}^*$	Low-frequency current of the reference hybrid current [A]
$i_{L,sc}$	Inductor current of the supercapacitor converter [A]
$i_{L,sc}^* = i_{sc}^*$	Reference inductor current for the supercapacitor converter [A]
i_{osc}	High-frequency current of the reference hybrid current [A]
I_{pv}	Photovoltaic array current [A]
$i_{pv,dc}$	Photovoltaic current on the DC-bus [A]
i_{sc}	Supercapacitor current [A]
$i_{sc,osc}$	Compensated high-frequency current for the supercapacitor side [A]
mode	Mode of the battery converter (i.e., boost-mode: mode=1, buck-mode: mode=0)
mode _{bat}	Availability mode of the battery (i.e., battery available for charging/ discharging: mode _{bat} = 1, battery idle: mode _{bat} = 0)
mode _{sc,ch}	Charging availability mode of the supercapacitor (i.e., supercapacitor available for charging: mode _{sc,ch} = 1, supercapacitor fully charged: mode _{sc,ch} = 0)

$\text{mode}_{sc,disch}$	Discharging availability mode of the supercapacitor (i.e., supercapacitor available for discharging: $\text{mode}_{sc,disch} = 1$, supercapacitor fully discharged: $\text{mode}_{sc,disch} = 0$)
P_{bat}	Battery power [W]
P_{grid}	Grid power (average) [W]
P_{load}	Load power (average) [W]
P_{pv}	Photovoltaic power [W]
P_{sc}	Supercapacitor power [W]
sign_{sc}	Sign of the supercapacitor current that defines the mode of the supercapacitor converter (boost-mode: $\text{sign}_{sc} > 0$, buck-mode: $\text{sign}_{sc} < 0$)
SOC_b	State-of-charge of the battery
$SOC_{b,max}$	Maximum limit of the state-of-charge of the battery
$SOC_{b,min}$	Minimum limit of the state-of-charge of the battery
SOC_{sc}	State-of-charge of the supercapacitor
$SOC_{sc,max}$	Maximum limit of the state-of-charge of the supercapacitor
$SOC_{sc,min}$	Minimum limit of the state-of-charge of the supercapacitor
V_b	Battery voltage [V]
V_{dc}	DC-bus voltage [V]
V_{dc}^*	Reference DC-bus voltage ($V_{dc}^* = 400$ V)
V_{mpp}^*	Reference value of photovoltaic array voltage at the maximum power point [V]
V_{pv}	Photovoltaic array voltage [V]
V_{sc}	Supercapacitor voltage [V]

1 Introduction

1.1 General Overview/Problem statement

In March 2007, the European Council set a list of goals for 2020 in order to face the problems of the environment; the 20% improvement in energy efficiency, the 20% contribution of Renewable Energies to total energy production and the 20% reduction of greenhouse gases below 1990 emissions (20-20-20 targets) [1]. Cyprus has been considering renewable energy policy during the past few years. Specifically, the Cyprus action plan included a 16% contribution of renewable energies to total energy production by 2020, which was successfully achieved [2]. In October 2014, the European Council set new targets at European Union (EU) level for 2030 for the energy and climate policy framework, namely a 32.5% improvement in energy efficiency, a 32% contribution of Renewable Energies to total energy production and a 40% reduction of greenhouse gas emissions compared to 1990 levels [3]. Specifically, Cyprus set local targets towards 2030 in order to achieve a share of at least 23% of RES in final energy consumption, while the transport target was set at 14% in final energy consumption by 2030 [4]. Finally, the vision for an EU long-term strategy includes net-zero emissions of greenhouse gases by 2050 [5], [6].

Renewable Energy Sources (RES) have been growing rapidly over the last few years. The spreading of renewables has become stronger due to the increased air pollution, which is largely believed to be irreversible for the environment [7]. Moreover, the depletion of fossil fuel resources, the increased oil prices and the growth in electricity demand are important factors for the growing attention in RES. In addition to that, buildings in Europe are responsible for the 40% of the total EU energy consumption, and as a result they contribute to greenhouse gas emissions and, possibly, to climate change. Therefore, the reduction of the energy consumption and the use of RES in buildings are believed to have a positive impact on climate and gradual independency on conventional fuels [8], [9].

In addition, through the integration of renewable technologies, all EU member States shall ensure that all new buildings in EU have to be nearly zero energy building (nZEB)¹ by the end of 2020, according to EU directive 2010/31/EU, Article 9 [1]. The aim of a nZEB is not only to minimize the energy performance of the building with the above methods, but to integrate renewable technologies to balance the energy requirements of the building.

On the other hand, the increasing penetration of renewable energy technologies causes major problems in the power network, as their generation cannot be totally predicted. Along with fluctuations in the generation of renewables due to weather uncertainties, storage is very important for mitigating several problems that may arise, affecting the stability and reliability of the grid. Specifically, over the last years there has been an emphasis on residential storage applications and behind-the-meter storage. Behind-the-meter storage for residential customers allows prosumers² to decrease their electricity bills, reducing peak demand charges and increasing local self-consumption [10]. Statistically, in Germany the 40% of recent rooftop solar PV systems have been installed with behind-the-meter batteries. In addition, 21000 behind-the-meter batteries were installed in Australia by 2017, with the government aiming to reach 1 million by 2025. Finally, the installation of 500 kW behind-the-meter batteries for Morgan Stanley in the US resulted in a 20% reduction of peak demand [11].

Figure 1.1 shows an example of a nZEB building that includes behind-the-meter battery energy storage [12]. Rooftop solar PVs are used for supplementary generation. Also, solar energy is utilized for water heating (solar water collectors) or HVAC (heating, ventilation and air conditioning). All devices and lighting are energy efficient. In addition, an electric vehicle can be charged by the household charging station. A substantial device is the home energy manager device, in which the owner of the building can control and optimize

¹ 'Nearly zero-energy building' means a building that has a very high energy performance. The nearly zero or very low amount of energy required should be covered to a very significant extent by energy from renewable sources, including energy from renewable sources produced on-site or nearby; (from EU directive 2010/31/EU, Article 2 [1])

² Prosumer, in the energy field, denotes consumers who both produce and consume electricity. They 'self-consume' some of the electricity they produce and sell the excess to the grid. But when their production falls short, they also buy power from the grid, which makes them both producers and consumers [313].

energy consumption. Real-time communication between the smart grid and the building can be achieved using a smart meter. Finally, energy storage is the key factor in increasing RES self-consumption and self-sufficiency, providing backup power and meeting electricity demands [13]–[15].

It should be noted here that RES self-consumption can be defined as the share of the produced electricity that is directly consumed or used for energy storage charging, while self-sufficiency is defined as the share of total load demand supplied directly from generated RES or energy storage discharging [16], [17].



Figure 1.1: Typical example of a nZEB building

1.2 Literature review on PV systems with energy storage

In recent years, there has been increasing attention to power management and control between a PV system, a load and a storage method, either on DC or AC microgrids. Some publications refer to the different methods that can be applied to the control and management of PV systems connected to microgrids using energy storage. Other studies focus on storage sizing, technical or economic aspects, scheduling, and optimization of certain system parameters. This Thesis focuses on the technical aspect and the filtration-based power management and control of a grid-connected system. Next, a literature review of different systems is presented, focusing on their advantages and limitations.

Zhou et al. [18] implemented a composite battery-supercapacitor hybrid storage with dynamic energy management. The research focused on the DC side and voltage and current control of the modular battery and supercapacitor, where the corresponding reference currents were calculated using a low pass filter (LPF). The low-frequency current corresponds to the battery current and the high-frequency current fluctuations in the supercapacitor. It should be noted that in that study the DC-bus voltage control was implemented by the supercapacitor converter. The proposed modular topology for the battery-supercapacitor hybrid storage requires a large number of converters, and therefore there is a considerable increase in cost and power loss.

Kollimalla, Mishra and Narasamma [19] improved the above research in order to avoid the problems of the high charging/discharging rates that may arise. Hence, they added a rate limiter after the LPF of the total current, to control the charging/discharging rates of the battery current and reduce the battery stresses by increasing the battery lifetime. In addition, a compensator was added to the supercapacitor current calculation to compensate for the slow dynamics (regarding battery, controller and converter operation) that the battery may not track instantly. The study focused on the design of voltage and current controllers for the battery and the supercapacitor converters. The design was made for a standalone PV system with DC load, where the DC-bus voltage control was implemented by the supercapacitor converter. Manandhar et al. [20] used the same configuration in performing a stability analysis and the controllers design. A comprehensive stability analysis was performed where all the required transfer functions were given. However, the authors did not consider the state-of-charge (SOC) of the battery and the supercapacitor, but assumed that the battery and supercapacitor operated within their acceptable limits. This can cause deep charging/discharging cycles and affect the battery lifetime.

Kotra and Mishra [21] proposed a new configuration for a residential grid-connected and islanded PV system with hybrid energy storage, containing both DC and AC loads. The control algorithm maintained the DC-bus at 200 V for high power DC loads and 48 V for low power DC loads. Moreover, the real power between the DC grid and the utility grid, as well as the required local AC load power, were transferred through a single-phase voltage source converter. The study considered the SOC limits of the battery and the supercapacitor for the charging/discharging power management algorithm (PMA),

including detailed diagrams for calculating the reference currents for the battery, supercapacitor, PV and grid. However, the stability analysis and the control design of the controllers for battery, supercapacitor and PV converters are missing. The same authors later proposed an advanced power management algorithm in which a peak pricing mode was considered [22].

Hajiaghahi, Salemnia and Hamzeh [23] proposed a standalone PV system with hybrid storage and DC and AC loads. The authors investigated a design for the voltage and current controllers of the converters. For the current control of the battery and supercapacitor converters, PI controllers were used. Also, regarding the DC-link voltage control, a fuzzy controller was chosen. The results showed that the PI-fuzzy control strategy improved the dynamic stress and the peaks and ripples in the current of the battery.

Singh and Lather [24] proposed a combined PI and SMC (Sliding mode control) method for a DC microgrid application that included PVs and battery-supercapacitor hybrid storage. A power management algorithm (PMA) was presented, where the SOC of the battery and the SOC of the supercapacitor were considered, so that the storage technologies were utilized within their minimum and maximum limits. DC-bus voltage control and battery current control were performed by PI controllers, while supercapacitor current control was performed by a SMC. Also, for the design of the controllers, a stability analysis was conducted using the appropriate small-signal transfer functions. The same authors extended their aforementioned work by proposing a modified control structure that included a rate limiter (for reducing the high charging/discharging rates), a PI controller for the DC-bus voltage control and two SMCs for controlling the currents of the battery and the supercapacitor, respectively [25]. The same power management as in [24] was used to calculate the required reference currents. The results showed lower DC-bus voltage overshoot and faster voltage regulation of the proposed strategy.

Vieira, Moura and Almeida [26] proposed a battery energy storage system for self-consumption of PV generation in residential zero energy buildings. In their work, they presented a 2.4 kW_p PV system with a 10.2 kWh lithium-ion battery storage, for increased matching between local generation and demand and reduced electricity bill. The correct battery sizing was calculated on the basis of average consumption, battery efficiency and SOC limits of the battery. Also, the incremental conductance algorithm was chosen for

MPPT (Maximum Power Point Tracking), while the dual polarization battery model was employed for the battery modeling. A hysteresis controller was used for the regulation of the output current of the grid inverter. A management strategy, considering the SOC limits of the battery, was proposed for the battery charging/discharging process, where a reference battery current was extracted. A current control was then performed by the bidirectional battery converter using a PI controller. However, the stability analysis and the design of the controllers were not analyzed in detail. Finally, an economic assessment was carried out and showed that there was a decrease of 87.2% in the annual electricity bill.

Cabrane, Ouassaid and Maaroufi have done several studies on modeling and control of standalone PV systems with hybrid energy storage. In [27], a detailed mathematical analysis was performed on the PV system, the battery (CIEMAT model) and the supercapacitor (two branches model) storage, where the SOC limits of the supercapacitor and battery were considered. The DC-bus voltage and the battery and supercapacitor currents were controlled by PI controllers. In a similar study [28], a comparative simulation was presented for both a battery-only storage system and a battery-supercapacitor storage system. The results showed that supercapacitors can reduce the battery stress by reducing battery current peaks, and hence can increase battery lifetime. Finally, in [29] the same authors suggested the integration of a fuzzy logic supervisor for the energy management of the system. The fuzzy logic strategy was used for managing the power flow, while maintaining at the same time the SOC limits of the battery and supercapacitor. The simulation results demonstrated the effectiveness of the suggested method by requiring the DC-bus voltage to be stable at 400 V and keeping the SOC of the battery and supercapacitor within their acceptable limits.

Saxena, Singh and Vyas [30] proposed a grid-connected PV system with battery energy storage. The authors presented a mathematical model for the PV array, where a P&O algorithm was used for the MPPT. In addition, the required transfer functions related to PV voltage control, DC-bus voltage control, battery converter current control and voltage source inverter (VSI) current control, were also presented. However, the authors did not consider the SOC limits of the battery.

It must be stressed here that all the above studies, which include research in stability analysis, have assumed a unified controller for the design of the bidirectional DC-DC

converters, in which the two modes (boost and buck) were controlled in a complementary fashion. Therefore, the design concerned the boost-mode operation of the converter. On the contrary, the following studies made a different control structure for each mode of operation (boost and buck).

Song et al. [31] proposed an algorithm for a grid-connected residential 10kWh battery, considering the daily load profile, PV generation and the SOC of the battery. The authors presented the required system controllers (MPPT, inverter current control and charging/discharging mode controllers for the bidirectional converter). The design of the controllers was not presented, and the PI tuning parameters were not given or explained. However, their aim was to present the power management of the charging/discharging mode of the battery, where the battery was charged overnight and discharged during the day.

Aktas et al. [32] proposed a grid-connected PV system with hybrid energy storage. A limitation in this work is that the storage topology was semi-active, where the supercapacitor was passively connected to the DC-bus, while the battery was connected to the DC-bus through a bidirectional DC-DC converter. Thus, the battery was allowed to have different voltage levels from the DC-bus, resulting in reduced size and higher flexibility and adjustability of the battery. On the other hand, the supercapacitor was required to be relatively large to keep DC-bus voltage levels stable, resulting in higher cost requirements. Moreover, the control structure of the battery bidirectional converter was made according to the mode of operation (boost or buck). Finally, a proposed smart energy management algorithm introduced some limitations on battery SOC, the lowest battery power level, the lowest acceptable PV power produced level, and the lowest power level at which a load can receive energy from the battery and the PVs. An extended version of the previous work was presented in [33] by the same authors. The same semi-active system topology was examined for the battery and supercapacitor. A comprehensive explanation was given of the proposed operation modes for the energy management of the system. However, the same limitations on the size and use of the supercapacitor remain as in [32].

From the above literature review, one can clearly state that, depending on the application and the system configuration and complexity, there is a plethora of power management and control methods that can be developed. In Table 1.1, the above as well as other

published studies related to our research are summarized. It is worth noting that none of these studies consider the self-consumption and/or self-sufficiency factor of the building together with the utilization of the hybrid storage, in contrast to the present study. Here, a novel dynamic PMA is proposed for such a model to make better use of the generated PV power, the battery-supercapacitor storage, the building load and the grid. A detailed small-signal analysis is performed for the bidirectional DC-DC converter and the single-phase inverter. Note that the stability analysis is done for both the boost and the buck modes of operation of the battery and the supercapacitor converters, which can lead to more accurate tuning of the controllers. The DC-bus voltage is regulated by the single-phase inverter, where a reference output current is extracted using a phase-locked loop (PLL) for grid synchronization. Also, the battery and the supercapacitor charging/discharging currents are controlled by the battery and the supercapacitor bidirectional converters, respectively, by consideration of the battery SOC and the supercapacitor SOC. Finally, it should be noted that none of the tabulated studies below contain the complete set of features and functions that the present Thesis deals with.

Table 1.1: Summary of related work in the literature

Ref.	System	Topology	Control strategy	MPPT	Storage modeling	Stability analysis	Key points
[18]	PV/battery/supercapacitor	Grid-connected DC load AC load	PI (voltage & current control) with LPF	N/A	–	–	- Increased cost and power loss due to large number of converters required for the modular topology of battery-supercapacitor
[19]	PV/battery/supercapacitor	Off-grid DC load	PI (voltage & current control) with LPF + rate limiter + compensation factor	✓	–	✓	- No consideration of the SOC of the battery and supercapacitor - Better control of the charge/discharge rates of the battery current due to rate limiter
[20]	PV/battery/supercapacitor	Off-grid DC load	PI (voltage & current control) with LPF + compensation factor	✓	–	✓	- No consideration of the SOC of the battery and supercapacitor - Better control of the charge/discharge rates of the battery current due to rate limiter
[21]	PV/battery/supercapacitor	Grid-connected Islanded DC load AC load	PI (voltage & current control) with LPF Hysteresis (current control)	✓	–	–	- The control algorithm maintained the DC-bus at 200 V (for high power dc loads) and at 48 V (for low power dc loads) - PMA for grid-connected and islanded mode
[22]	PV/battery/supercapacitor	Grid-connected Islanded DC load AC load	PI (voltage & current control) with LPF + rate limiter Hysteresis (current control)	✓	–	✓	- PMA for grid-connected and islanded mode based on the peak pricing mode
[23]	PV/battery/supercapacitor	Off-grid DC load AC load	PI (current control) Fuzzy (voltage control) with LPF	✓	–	✓	- PI/fuzzy control strategy improved the dynamic stress and the peaks in current of the battery

Ref.	System	Topology	Control strategy	MPPT	Storage modeling	Stability analysis	Key points
[24]	PV/battery/ supercapacitor	Off-grid DC load	PI (voltage & battery current control) with LPF Sliding mode (supercapacitor current control)	✓	✓	✓	- PMA includes off-MPPT mode if battery is fully charged for DC-bus voltage control
[25]	PV/battery/ supercapacitor	Off-grid DC load	PI (voltage control) Sliding mode (current control) with LPF + rate limiter + compensation factor	✓	✓	✓	- PMA includes off-MPPT mode if battery is fully charged for DC-bus voltage control - Battery and supercapacitor models from Simulink library
[26]	PV/battery	Grid-connected AC load	PI (current control) Hysteresis (current control)	Incremental conductance	✓	–	- Calculation of proper battery size, based on the average consumption, efficiency and SOC limits - Dual polarization model for battery modeling - Economic assessment showed 87.2% reduction in the annual electricity bill
[27]	PV/battery/ supercapacitor	Off-grid DC load	PI (voltage & current control) with LPF	✓	✓	–	- Modeling of battery (CIEMAT model) and supercapacitor (two branches model)
[28]	PV/battery/ supercapacitor	Off-grid DC load	PI (voltage & current control) with LPF	✓	✓	–	- Modeling of battery (CIEMAT model) and supercapacitor (two branches model) - Comparative simulation of battery-only and battery-supercapacitor system. Results shown that supercapacitors reduce battery stress by reducing peaks in battery current
[29]	PV/battery/ supercapacitor	Off-grid DC load	PI (voltage & current control) Fuzzy logic + LPF	✓	✓	–	- Modeling of battery (CIEMAT model) and supercapacitor (two branches model) - Fuzzy logic for managing the power flow keeping the SOC limits of battery and supercapacitor

Ref.	System	Topology	Control strategy	MPPT	Storage modeling	Stability analysis	Key points
[30]	PV/battery	Grid-connected AC load	PI (voltage & current control)	P&O	✓	✓	- Modeling of battery (Thevenin equivalent) - No consideration of the SOC of the battery
[31]	PV/battery	Grid-connected AC load	PI (voltage & current control)	P&O	–	–	- Different control structure for boost and buck mode - Battery is charging during the night and discharging during the day
[32] & [33]	PV/battery/ supercapacitor	Grid-connected AC load	PI (voltage & current control) Hysteresis (current control)	P&O	–	–	- Different control structure for boost and buck mode - Passive connection of supercapacitor (size must be large to keep the DC-bus voltage levels stable)
[34]	PV/battery	Grid-connected AC load	PI (voltage control) K factor (current control) PR (voltage & current control)	✓	✓	✓	- Different control structure for boost and buck mode - Generic battery model from Simulink library - Floating interleaved buck-boost converter model
[35]	PV/battery/ flywheel	Grid-connected AC load	N/A	N/A	✓	–	- Battery as primary storage system and flywheel for peak-shaving, power peaks and fluctuations
[36]	PV/battery	Grid-connected Islanded AC load	N/A	P&O	–	–	- PMA considering the load power, PV power, battery SOC, grid availability and peak load period
[37]	PV/battery	Grid-connected Islanded DC load AC load	PI (voltage & current control)	Incremental conductance	–	–	- Comprehensive control and power management system (CAPMS) with both DC and AC buses, in grid-connected and islanded mode
[38]	PV/ supercapacitor	Grid-connected	PI (voltage & current control)	Incremental conductance	–	–	- Fault ride through and power fluctuation minimization using supercapacitors

Ref.	System	Topology	Control strategy	MPPT	Storage modeling	Stability analysis	Key points
[39]	PV/battery	Grid-connected AC load	PI (power, voltage & current control) Lead-lag compensator (PV voltage control)	Incremental conductance	✓	✓	- Generic battery model from Simulink library - Residential battery for potential participation in primary frequency regulation of grid
[40]	PV/battery/ supercapacitor	Grid-connected Islanded DC load AC load	PI (power & voltage control) Hysteresis (current control)	Incremental conductance	–	–	- No consideration of the lower SOC limit of the battery
[41]	Wind turbine/ battery/ supercapacitor	Off-grid DC load	PI (voltage & current control) + LPF	✓	–	✓	- Supercapacitor absorbs abrupt increase of wind power during gust period
[42]	PV/ wind turbine/ battery/ supercapacitor	Off-grid DC load	PI (voltage & current control)	P&O	–	–	- PMA keeps DC-bus voltage constant and power balance by off-MPPT and dump load methods
This study	PV/battery/ supercapacitor	Grid-connected AC load	PI (voltage & current control) with LPF + rate limiter + compensation factor	P&O	✓	✓	- Modeling of battery (dual polarization model) and supercapacitor (two branches model) storage - Average modeling approach (for converters and inverter) - Different control structure for boost and buck-mode - Comparative simulation of battery-only and battery-supercapacitor system. Results showed that supercapacitors can reduce battery stress by reducing peaks in battery current - Novel local PMA for increased PV & storage self-consumption and self-sufficiency of the building

1.3 Objectives and contributions of the Thesis

Energy storage is the key element in regards to the distributed renewable generation. Specifically, residential storage can increase PV self-consumption, manage peaks on demand and reduce electricity bills. Moreover, residential storage may solve several problems related to the stability, quality and reliability of the grid. In addition, battery-supercapacitor hybrid storage comprises both high-power and high-energy technologies, resulting in extended battery lifetime because the supercapacitor is utilized for high-frequency variations and this relieves battery stress. Therefore, a major challenge is the management of the generated and demanded power, ensuring an effective power sharing between the PV, the hybrid storage, the load and the grid.

The main contributions of this Thesis can be summarized as follows:

- A novel and customized dynamic filtration-based PMA for the building is developed. Specifically, the proposed algorithm prioritizes the utilization of the generated PV and battery-supercapacitor instead of the grid, reducing the peaks in generation or demand, and increasing the PV self-consumption and the self-sufficiency of the building. For instance, the grid supplies power only if the PVs and the battery are insufficient to cover the load needs, and it absorbs power only if the produced PV power is larger than the load power, and the battery is fully charged.
- Each part of the model is fully analyzed and developed from the ground up, with no black boxes. Specifically, the PV array is mathematically analyzed based on the equivalent circuit of the one-diode PV cell. Also, three different Maximum Power Point Tracking (MPPT) methods are examined and compared. Moreover, each converter is mathematically modeled based on the averaged model. In addition, the battery is modeled based on the dual polarization (2nd-order RC) battery cell circuit. The supercapacitor model is developed based on the two branches equivalent circuit of the supercapacitor cell.
- A fully active parallel configuration is used for the battery-supercapacitor hybrid storage, where the battery is the main storage technology. The supercapacitor provides a supportive function to the battery by handling rapid changes occurring within 0.2 seconds.

- A detailed small-signal ac analysis is considered for the design of the controllers for the two bidirectional converters of the battery and supercapacitor. Stability analysis is performed for both the boost and the buck mode of operation for the battery and supercapacitor converters, resulting in more accurate tuning of the controllers.
- A detailed small-signal ac analysis is performed for the design of the DC-bus voltage controller, where a reference output current is obtained for the current controlled voltage source inverter (CCVSI).
- The proposed model is developed and simulated using the MATLAB/Simulink software based on mathematical analysis and average modeling. The mathematical modeling approach provides flexibility and adjustability to the parameters of a model. Despite examining the averaged model of the converters, the system dynamics and the small ripple signals that occur are captured as well. The switching ripple can be negligible in a well-designed converter. It is also worth noting that the simulation time of the system with the averaged model is dramatically decreased compared to the switching model.

1.4 Outline of the Thesis

Chapter 2 presents an extensive review with regard to renewable energy (Section 2.1), energy storage technologies (Section 2.2), grid-scale storage applications (Section 2.3), hybrid storage technologies (Section 2.4) and different configurations of a grid-connected PV system with hybrid energy storage (Section 2.5).

In Chapter 3, the mathematical analysis and modeling of each part of the proposed system is presented. Each Section is divided into two sub-Sections, namely the mathematical analysis part and the modeling part, where at first sight the theory is analyzed and then the Simulink model is presented. First, the mathematical analysis and modeling behind the PV array is examined in Section 3.1. After that, three different MPPT techniques are compared in Section 3.2, concluding with the best choice for our needs. Section 3.3 includes the mathematical analysis of the DC-DC boost converter. Furthermore, Sections 3.4 and 3.5 examine the battery and supercapacitor mathematical models, respectively, whereby the proper sizing of each storage technology is calculated. The bidirectional

DC-DC converter investigation is presented in Section 3.6, where a detailed small-signal analysis of the converter is examined. In Section 3.7, the DC-AC voltage source inverter is studied, where the impact of the output current variation on the DC-bus voltage is determined by the small-signal analysis of the inverter. Moreover, Section 3.8 presents the system controllers and the stability analysis of each controller. Specifically, the stability analysis and design of the controllers for the battery and supercapacitor converters are performed in sub-Section 3.8.1, while the calculation of the DC-link capacitance and the DC-bus voltage is done in sub-Section 3.8.2. Sub-Section 3.8.3 examines the design of the DC-bus voltage controller and the phase-locked loop (PLL) for the calculation of the reference output current of the inverter, so that the output current injected into the grid is in phase with the grid voltage (unity power factor). Section 3.9 deals with the PMA for battery-only (sub-Section 3.9.1) and battery-supercapacitor storage (sub-Section 3.9.2), for increasing the PV self-consumption and self-sufficiency of the building. Specifically, for the battery-supercapacitor PMA, twelve (12) different cases are identified, depending on the amount of generated PV power, the amount of the required load power and the availability of energy in the battery and the supercapacitor.

Chapter 4 presents the results of the complete proposed model in long-term and short-term operations. Specifically, the PV system with battery-only application is examined in Section 4.1, in long-term operation of 24 hours. For the same scenario, a comparison of the performance of the battery-only and the battery-supercapacitor application is performed in Section 4.2. Also, in Section 4.3, the short-term operation (10–30 seconds) is studied for the PV system with hybrid storage application under Excess Power Mode (EPM) and Deficit Power Mode (DPM), in order to investigate the dynamic response of the system and verify all possible cases of PMA. Finally, conclusions and possible future directions are given in Chapter 5.

2 Theoretical Background

2.1 Renewable energy

Renewable Energy is essentially the energy that comes from natural resources, which are non-depletable and free, and they do not pollute the environment and can replace the conventional fuels to produce electricity, heat water or an area, or replace fuel to off-grid energy service. Examples of the renewable energy sources are the sunlight, the wind, the tides, the waves and the geothermal heat. Typical examples of renewable technologies that are applicable for building design are photovoltaics (PVs) and solar thermal collectors for hot water (from sunlight), wind turbines (from wind) and geothermal heat pumps.

2.1.1 Solar Energy

Solar energy, among all RES, can be considered as the most promising, widely available and essential resource for countries like Cyprus, especially for domestic applications. Most of RES come directly or indirectly from the sun. There are currently three ways to use the energy from the sun: passive heat, solar thermal and photovoltaic energy. Generally, solar energy can be converted easily into heat via solar thermal systems or into electricity via PVs and concentrated solar power (CSP) systems.

2.1.1.1 Solar Photovoltaic Energy

Solar photovoltaic is one of the most growing technologies in the world with a growth rate of 35–40% per year. The first use of solar PV cells was in the 1950s, when these were first developed in the space industry to be used on satellites. In the 1970s, applications for PV cells started the off-grid use for rural electrification and for communications. The first steps for domestic and industrial installation followed in the 1990s [8], [9], [43]–[46].

As seen in Figure 2.1, by the end of 2017, the global installed PV capacity was 409 GW. In 2018, the global installed PV capacity was 512 GW and by the end of 2019 the capacity reached 627 GW. The top countries in relation to installed PV cumulative capacity in 2019, were China, the United States, Japan, Germany and India [47], [48].

Due to the rapid increase in manufacturing scale in the past decade, solar PV technology costs have drastically decreased. Consequently, in sunny countries the solar thermal electricity is competitive against oil-fueled electricity production. Some recent research studies on PV systems focus on thin-film solar cells, which are composed of thin layers of photovoltaic material on glass or stainless-steel substrates. The common disadvantage of the thin-film modules is the low efficiency [8], [9], [43]–[46].

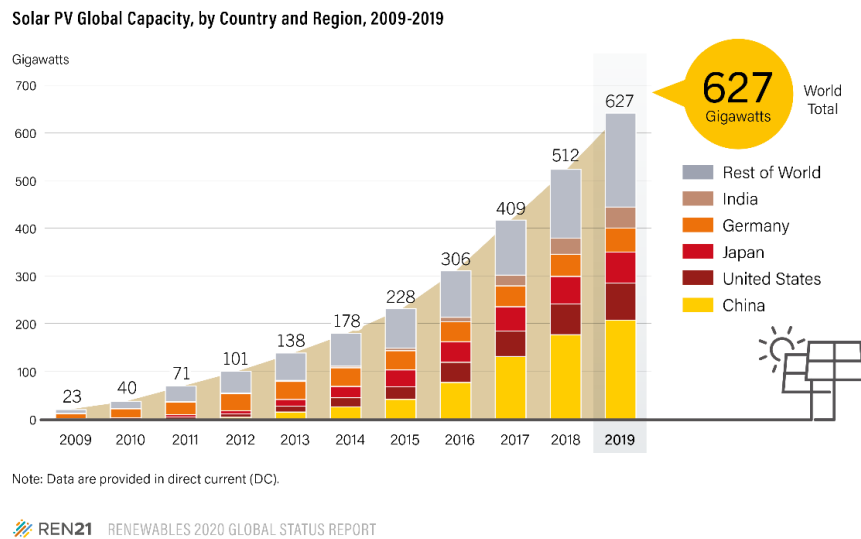


Figure 2.1: Solar PV Global installed capacity, by country [47]

2.1.1.2 Concentrated Solar Power (CSP)

Concentrated Solar Power (CSP) technologies produce electricity by concentrating direct-beam solar irradiance to heat liquid, solid or gas, which are then used for electricity generation. The first steps in developing CSP plants were made near 1984 in the USA with solar energy generating systems. Currently, the majority of the installed CSP plants are based on parabolic trough systems. CSP systems use lenses or mirrors to concentrate sunlight into a smaller area. Parabolic trough solar thermal systems use mirrors to focus sunlight on thermally efficient tubes that contain a heat transfer fluid. Once the fluid reaches the temperature of 390°C, it pumps through the heat exchangers to produce superheated steam that drives a conventional turbine generator to produce electricity [9], [43]–[46].

In 2018, the global installed capacity for CSP plants reached 5.5 GW, with Spain being the global leader in existing CSP capacity with 2.3 GW, followed by the United States

with just over 1.7 GW. These two countries accounted for about 75% of the global installed capacity in 2018 [48]. In 2019, the global installed capacity for CSP plants reached 6.2 GW (Figure 2.2), where five countries added new capacity during 2019: Israel (242 MW), China (200 MW), South Africa (100 MW), Kuwait (50 MW) and France (9 MW) [47].

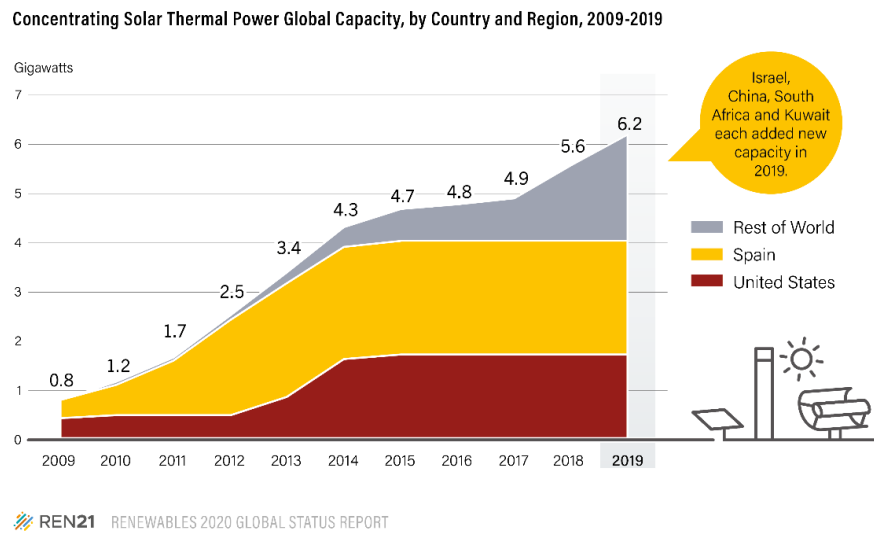


Figure 2.2: CSP Global installed capacity, by country [47]

2.1.1.3 Solar thermal heating and cooling

Solar heating and cooling technologies utilize the sunlight to collect thermal energy for residential, commercial or industrial applications, such as providing hot water, cooling and heating an area, or heating a pool. Solar energy collectors are the major component of any solar thermal system. These collectors transform solar radiation into internal energy of the transport medium [43], [44].

As seen in Figure 2.3, in 2019 the global capacity of glazed (flat plate and vacuum tube technology) and unglazed collectors was decreased for the first time to 479 GW_{th}. This happened because China did not meet the capacity of the systems that were retired during 2019. China again led the world for new installations of glazed and unglazed collectors, accounting for 73% of cumulative world capacity. Not including China, global capacity increased 3% to an estimated 148 GW_{th} in 2019, up from 144 GW_{th} in 2018 [47].

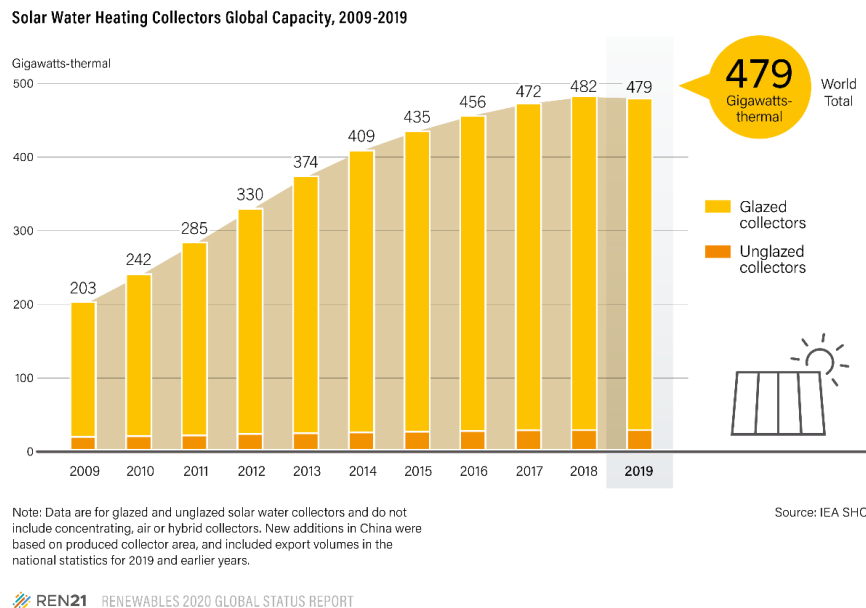


Figure 2.3: Solar water heating collectors Global installed Capacity [47]

2.1.2 Photovoltaic Module

Photovoltaic module is a technology for the conversion of sunlight into electricity. In other words, when a PV module is exposed to solar radiation, it generates direct current without any noise or impact to the environment. PV modules can be connected in series and/or in parallel, forming photovoltaic arrays. Additionally, PV modules contain series and/or parallel connections of PV cells. These cells are basically semiconductor diodes whose p-n junction is exposed to sunlight, as seen in Figure 2.4 [49], [50]. The photons' energy from sunlight breaks the bond of the electron, forcing it to pass its bandgap and moving it to the conduction band [51]. The n-type layer can emit electrons while the p-type layer can absorb electrons. At the interface of the two layers (p-n junction) there is electric field. This potential difference is created by the excited electrons.

There are many photovoltaic materials used at present, such as monocrystalline, polycrystalline and amorphous silicon, cadmium telluride and copper indium/gallium selenide/sulfide. Among all the above, silicon-based systems are the most commonly used and established materials. Monocrystalline silicon cells, which are the most commercially used, have higher efficiency than polycrystalline silicon cells. The efficiency of monocrystalline silicon cells is about 14–19% compared to that of polycrystalline silicon

cells which is about 11–13%. However, monocrystalline silicon cells have a slower production process and are costlier compared with polycrystalline silicon cells. Amorphous silicon cells are used in thin film technologies and they have very low efficiency (about 8%) [46], [52], [53].

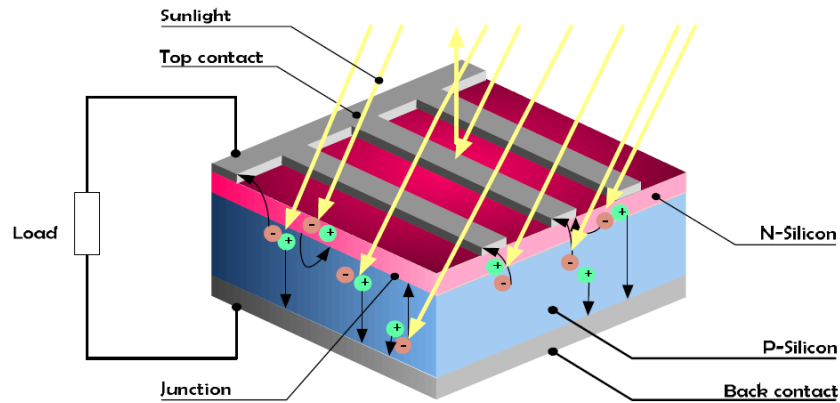


Figure 2.4: Structure of a silicon PV cell [54]

2.2 Energy Storage³

The penetration of renewable energy technologies causes major problems to the stability of the electrical grid. This happens because renewable energy production cannot be predicted accurately, as it relies on weather conditions such as sunlight and wind. For instance, when the clouds suddenly appear or the wind stops blowing then the energy production from photovoltaics and wind turbines will be decreased dramatically. Thus, energy storage can allow energy to be stored during high renewable generation or low demand periods, and to be used during low renewable production or high demand periods [55]. Along with the fluctuations of the renewable energy technologies production, storage is important for power and voltage smoothing. Energy storage is also important for energy management, frequency regulation, peak shaving, load leveling, seasonal storage and standby generation during a fault. Thus, storage technologies have currently gained an increased attention and have become more than a necessity [43].

³ Section 2.2 contains material from published paper [56]

The various storage technologies are in different stages of maturity and are applicable in different scales of capacity [56]. Pumped Hydro Storage is suitable for large-scale applications and accounts for 96% of the total installed capacity in the world, with 169 GW in operation (Figure 2.5). Following, thermal energy storage has 3.2 GW installed power capacity, in which the 75% is deployed by molten salt thermal storage technology. Electrochemical batteries are the third most developed storage method with 1.63 GW global power capacity, followed by electromechanical storage with 1.57 GW global installed power capacity. Finally, a promising energy storage technology is that of hydrogen, which accounts for a small share compared to the above storage groups, with almost 15 MW global installed storage capacity [10], [57]–[59].

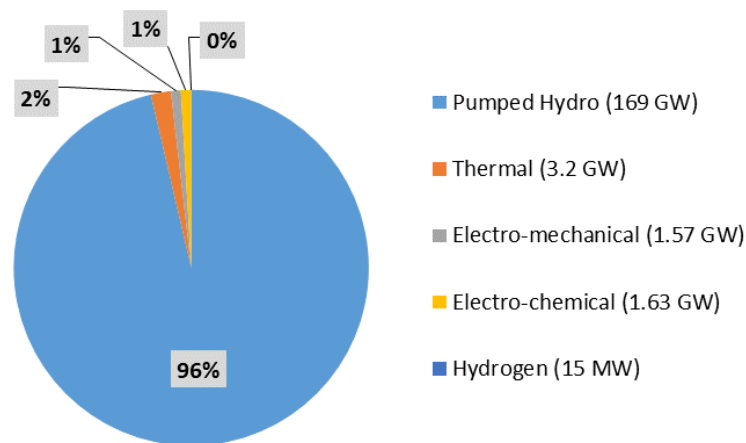


Figure 2.5: Global energy storage power capacity by technology group until 2017

Figure 2.6 presents the current global storage shares of electrochemical and electromechanical technologies. Regarding the electromechanical storage, flywheels and compressed air are the most developed storage technologies with storage capacities of 930 MW and 640 MW respectively. However, the storage capacity of flywheel and compressed air storage is concentrated in only three large projects. Lithium-ion batteries account for the largest share of the installed power capacity, with 1.12 GW in operation. The remaining electrochemical technologies are the sodium-based batteries (220 MW), capacitors (80 MW), the lead-acid batteries (80 MW), the flow batteries (47 MW) and the nickel-based batteries (30 MW) [10], [57]–[59].

This Section analyses all storage technologies, particularly those for electricity generation. Specifically, an updated overview of Pumped Hydro Storage (PHS),

Compressed Air Energy Storage (CAES), several types of batteries (lead-acid, nickel-based, sodium-based, lithium-ion, metal-air, redox flow), Hydrogen Storage, Thermal Energy Storage (TES), Superconducting Magnetic Energy Storage (SMES), Flywheel Energy Storage (FES) and Supercapacitors is performed. The following review presents an updated comprehensive overview of the above storage technologies, focusing on their functionalities and characteristics with graphical representation of their operation.

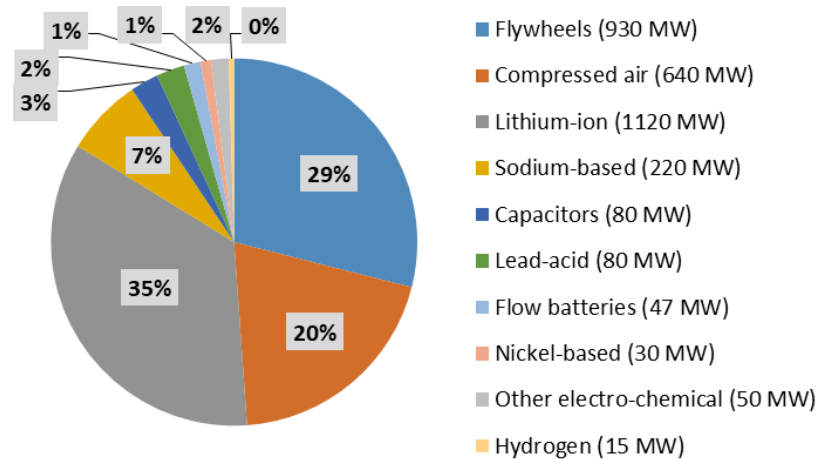


Figure 2.6: Global energy storage power capacity shares in MW of several storage technologies until 2017

For clarity, a brief explanation of several key terms regarding the characteristics of energy storage technologies is given in the sequel. Firstly, the self-discharge rate indicates the percentage of discharge during a period that a storage method is either not in use or in an open-circuit condition. The response time of a storage method is the duration of time for the transition from no discharge state to full discharge state. Furthermore, the cycle life of a storage method is the total number of charge-discharge cycles before it becomes unusable for an application (e.g., when its capacity is reduced dramatically). Additionally, the Depth-of-Discharge (DoD) is the amount (or percentage) of rated capacity that has been used from a battery. On the other hand, the State-of-charge is the complement of Depth-of-Discharge and represents the percentage of the remaining capacity in the battery [60], [61]. Finally, a Control and Power Conditioning System (C-PCS) is presented in most of the figures of the energy storage technologies. A Power Conditioning System is a bi-directional system for conversion of power between the grid side and the storage

side. The current produced by most of the storage technologies is direct (DC), thus a conversion to alternating current (AC) is necessary to follow the grid requirements (voltage value, phase, frequency) for connection to the grid [62], [63].

Electrical Energy Storage (EES) is a process of converting electrical energy into other forms of energy that can be stored for converting back into electrical energy when needed. One can categorize the storage technologies by storage duration (long-term, short-term storage), by the kind of storage (electrical, mechanical, chemical, thermal, etc.) or by other criteria like capital cost, capacity, efficiency and environmental impact. Figure 2.7 shows a classification of Energy Storage technologies by the form of stored energy.

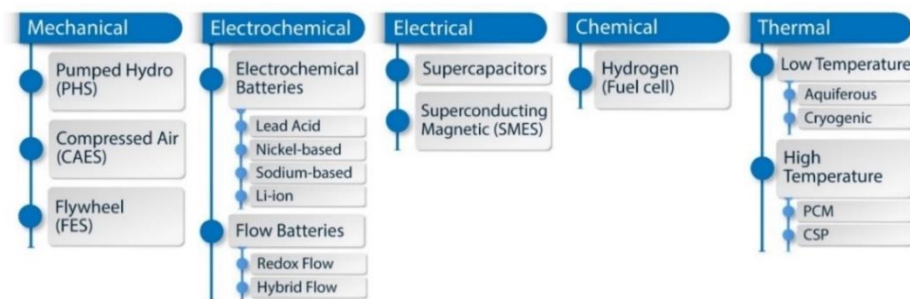


Figure 2.7: Classification of energy storage technologies by the form of stored energy

2.2.1 Pumped Hydro Storage (PHS)

Pumped Hydro Storage (PHS) is one of the most popular, common and mature methods of storage. PHS is considered as a large-scale energy storage. The first large-scale station for PHS was built in 1929, in Hartford, USA [55]. Currently there are globally over 300 PHS plants with a total installed capacity of 169 GW. The largest PHS plant has a capacity of 3 GW and duration of 10 hours at rated power. It was built by the end of 1985 at Virginia, USA [58]. The functionality of PHS is simple. A quantity of water is stored with a large difference in water level (hence, potential energy is present). The water can either flow from upper to lower level or be pumped from the lower to the upper level. During a period of electricity demand, water from the upper reservoir is released and activates the turbines for electricity generation. When there is no need for electricity, the water is pumped to the upper reservoir [64].

As shown in Figure 2.8, the PHS system consists of two reservoirs in different levels and a unit to pump water to the upper reservoir in order to convert electricity to potential energy, as mentioned above. Also, there is a turbine to generate electricity when needed. The amount of stored energy is proportional to the quantity of water that can be stored and the height difference between the two levels ($E=mgh$). The lower reservoir can be the open sea or a lake, but it must be near a hill, natural or man-made [55], [65]. Poullikkas [66] states that in order for a PHS to become economically viable, there is a rule of thumb that requires the head to be in excess of 300 m.

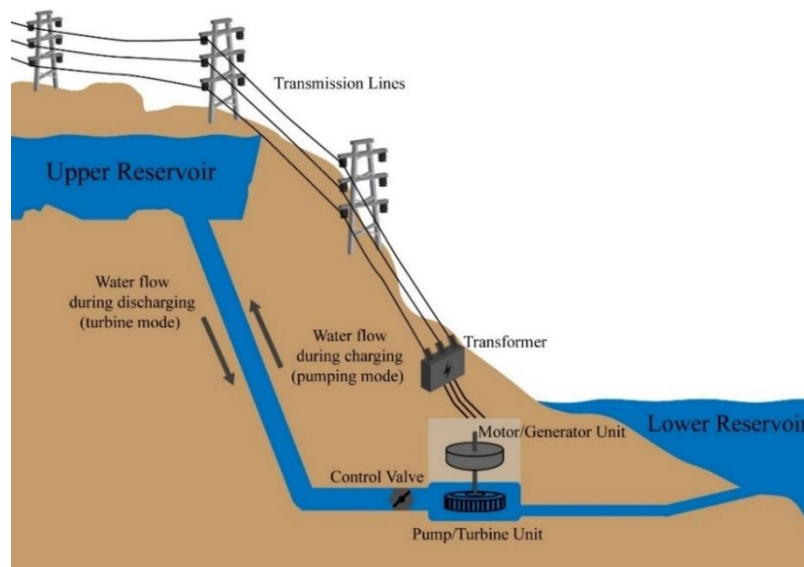


Figure 2.8: A typical diagram of PHS system

Among the advantages of PHS are the relatively high efficiency (65–85%), the long lifetime (30–60 years) and the fast response time (< 1 min). In addition, there can be large power capacity (100–1000 MW), long storage period and low cycle cost (\$0.1–1.4/kWh/cycle). The drawbacks include long project lead time (around 10 years), large land area, high capital cost (\$500–4600/kW) and environmental impact (due to the cutting of trees). Finally, the difficulty of finding a topographically suitable area with large water capacity is a major disadvantage [55], [66]–[68].

Morabito et al. [69] examined a set-up of a pump as turbine (PAT) in micro-PHS. PAT is a pump in reverse mode and can replace the pump and turbine into a single device [70]. Regarding the maintenance, it is mentioned that PAT has many advantages compared to custom-made turbines. Also, regarding the economic side, PATs are profitable in the

power range of 1 to 500 kW and perform capital payback periods of about two years or less. In the same study, a pilot project of a micro-PHS plant using PAT in Froyennes, Belgium is simulated [69].

2.2.2 Compressed Air Energy Storage (CAES)

In CAES systems the excess energy is stored mechanically by compressing air in natural or mechanically formed caverns. In the most usual designs the air from the atmosphere is used [71]. CAES is classified as a long-term energy storage method because it can reserve or supply power for days. It is not an independent system and has to be associated to a gas turbine plant. When there is excess energy, or the electricity demand is low, the compressor stores air into a sealed volume to a high pressure. During peak loads or when the electricity price is high, the high-pressured air goes through a turbine to generate power [72]. A typical power capacity of CAES plant ranges between 100–300 MW. Currently, there are only two large-scale CAES plants in operation: one in Huntorf, Germany, since 1978 (290 MW) and one in Alabama, USA, since 1991 (110MW) [73]–[75]. The total global deployment of CAES has currently reached 640 MW, however it is expected that by the end of 2020 two large-scale CAES plants will be operated with total capacities of 317 MW (Tennessee Colony, Texas, United States) and 300 MW (San Joaquin County, California, United States) [10], [58].

Figure 2.9 presents a schematic diagram of a basic CAES system. Firstly, it consists of a motor (for charging) and a generator (for discharging). Furthermore, there is an air compressor with an air cooler for economic compression and reduction of moisture content of the compressed air. Next, there is a recuperator (to preheat the air from cavern) and a low and a high-pressure turbine. The container for storing compressed air is located underground, as mentioned above. Finally, there are equipment controls and auxiliaries, i.e., fuel storage and heat exchanger units [55], [65]. Although the equipment used in CAES plants is mature and well proven, CAES plants lack the maturity of some other EES systems.

Some benefits of this system are similar to PHS systems; high power capacity, long energy storage duration (> 1 year), relatively quick start up and high efficiency (70–80%). Additionally, it requires a significant low capital cost (\$400–800/kW), it has

approximately 40 years lifetime and it creates little surface environmental problems due to the underground storage. Also, the self-discharge rate of the system is very low (0.5%/day). On the other hand, CAES systems have low energy density (12 kWh/m³) [67], [68], [76].

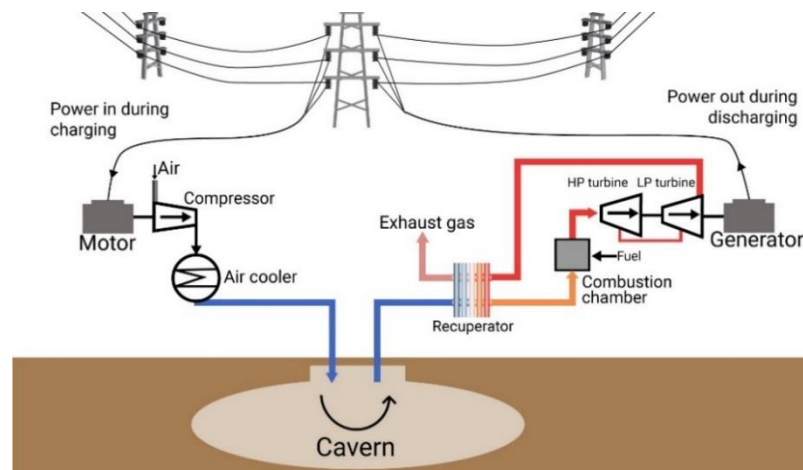


Figure 2.9: A typical diagram of a CAES system

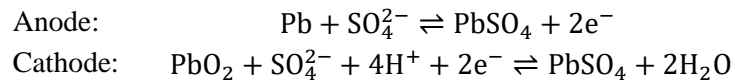
An improvement of CAES technology has been proposed over the last years, attracting research attention. The Advanced Adiabatic CAES (AA-CAES) is operated at the expansion mode, by integrating thermal storage. The stored energy in the cavern is converted into electrical energy with no need of a combustion process. In other words, the heat created from compression process is stored and used to reheat the air during expansion. Thus, the overall efficiency of the system is higher than the conventional CAES and fuel consumption is eliminated. An AA-CAES system is considered a promising technology because of its higher efficiency, the environmental friendliness and its reduced costs [10], [72], [77]. The first AA-CAES plant was built in 2016 in the Swiss Alps near the city of Biasca with a 500 kW capacity and autonomy of 4 hours. An unused tunnel is used as the air storage cavern and a packed bed of rocks is used for thermal storage, placed inside the pressure cavern. The overall efficiency of the plant is estimated at about 63–74% [58], [78].

2.2.3 Batteries

Batteries are the most popular and mature energy storage devices. They are classified as long-term energy storage devices. They can connect in series and/or parallel combination to increase their power capacity to be compatible with different applications. There are two main categories of batteries: electrochemical and redox flow batteries. Electrochemical batteries can store energy by creating electrically charged ions using chemical reactions between positive and negative plates. In other words, during charging the electricity (direct current) is converted to chemical energy, and during discharging the chemical energy is converted back to electricity (flow of electrons in direct current form) [79].

2.2.3.1 Lead-acid batteries

Lead-acid batteries are the most mature (invented in 1859) and widely used rechargeable electrochemical devices in vehicles and in stationary equipment. The anode is made of metallic lead (Pb), the cathode is made of lead dioxide (PbO₂) and the electrolyte is sulfuric acid (H₂SO₄) (Figure 2.10). The chemical reactions at the anode and cathode of lead-acid battery are:



The rated voltage of a lead-acid cell is 2V and its lifetime is between 3–12 years [80]. Lead-acid batteries are low cost devices (\$150–500/kWh), have relatively high efficiency (65–80%) and are reliable and suitable for power quality and spinning reserve applications. Furthermore, their response time is fast (< 5 ms) and they have small daily self-discharge rate (< 0.3%/day). Among their disadvantages are the low energy density (25–45 Wh/kg), the low specific power (180–200 W/kg), the limited cycle life (200–1800 cycles), the high maintenance requirements and some environmental impacts (they emit explosive gas and acid fumes). Also, they are slow to charge and they have poor low temperature performance, so they require a thermal management system. It is not recommended to completely discharge the lead-acid batteries (because their lifetime depends on the cycle Depth-of-Discharge), so it is necessary to install a larger battery bank to keep the battery life constant. Furthermore, lead-acid batteries are expensive

devices for RES because of their maintenance and replacement costs [55], [65], [67], [74], [81].

Cho et al. [82] presented an advanced lead-acid system with a split design for the negative electrode, known as ultra-battery, as demonstrated in Figure 2.11. This system uses a Pb electrode connected in parallel with a modified carbon electrode as the negative electrode, with one PbO₂ electrode as the positive electrode [83]. This new configuration provides a high capacity and significantly longer cycle life (17000 cycles) compared to the traditional lead-acid battery. The capital cost for the ultra-battery system is higher than the typical lead-acid battery, but it is possible to reduce the cost by increasing the scale of production [82]. In 2012 at the island of Maui, Hawaii, a 10 MW advanced lead-acid system was operated to support grid needs and provide ramp control and frequency regulation [58].

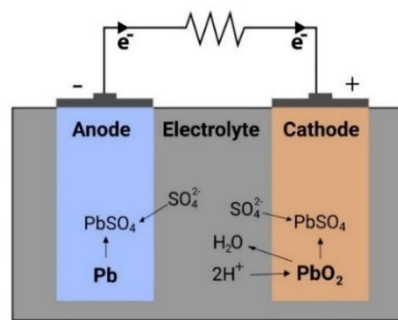


Figure 2.10: Lead–acid battery storage with chemical reactions during discharge

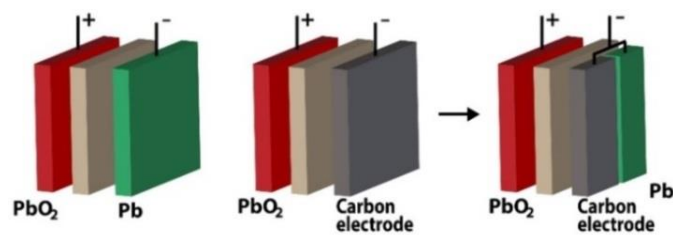
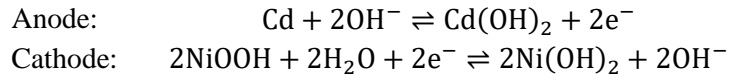


Figure 2.11: Schematic of the advanced lead-acid battery (ultra-battery)

2.2.3.2 Nickel-based batteries

Nickel cadmium (NiCd) batteries are also mature devices since they have been used commercially since 1915. They use nickel hydroxide and metallic cadmium as the two

electrodes and an aqueous alkaline solution as the electrolyte [80]. The following formulas describe the chemical reactions at the anode and cathode of NiCd battery:



They are reliable and do not require high maintenance cost. They are the only batteries capable of performing well even at low temperatures (from -20 to -40 °C). Their advantages are their high energy density (50–75 Wh/kg) and their long cycle life (2000–2500 cycles). Some barriers of the NiCd type are the toxic heavy metals (cadmium and nickel) used and the environmental harm they cause [84]. Moreover, their lifetime and maximum capacity decrease dramatically if the battery is repeatedly recharged after being partially discharged (memory effect). The cost of NiCd batteries is relatively high (\$800–1500/kWh), their unit voltage is about 1.0–1.3 V and their energy efficiency is between 60–70%. Nickel cadmium batteries are not heavily used commercially and it seems that they will not be used for future large-scale energy storage applications [64], [67], [76], [81]. NiCd batteries have been prohibited for consumer use within the EU since 2006 and are used only for stationary applications [85].

Nickel-metal hydride (NiMH) batteries are similar to the NiCd batteries except that the material used for electrodes is a hydrogen-absorbing alloy instead of cadmium (Figure 2.12) [86]. The chemical reactions at the anode and cathode for the NiMH battery are:

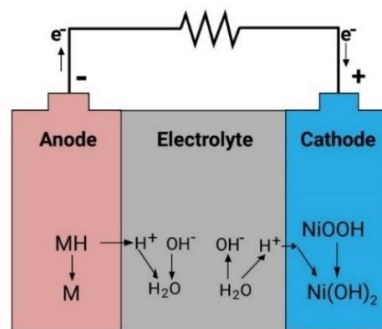
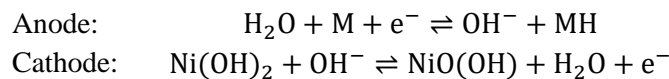


Figure 2.12: NiMH battery storage reaction diagram during discharge

They first appeared commercially around 1995 to replace NiCd batteries. Their specific energy is moderate (70–80 Wh/kg) but their energy density is high (170–420 Wh/L).

Additionally, they do not get affected so much from the memory effect and they are more environmentally benign than NiCd batteries. However, NiMH batteries have a low energy efficiency (65–70%) [65], [67], [81], [85].

2.2.3.3 Sodium Sulfur (NaS) batteries

Sodium Sulfur (NaS) batteries were introduced in the 1960s. They are considered as one of the most promising solutions for large-scale stationary EES applications. Some of their applications include load leveling, power quality, peak shaving and renewable energy management and integration. The NaS battery system is constructed in a tubular design (Figure 2.13). The anode is made of sodium (Na), the cathode is made of sulfur (S) and the solid electrolyte is made from beta alumina [62]:

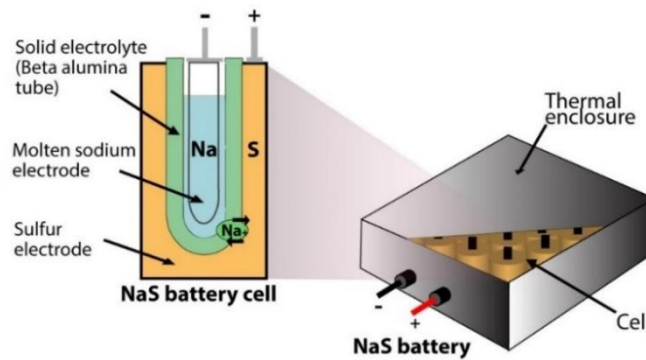
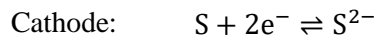
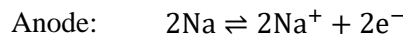


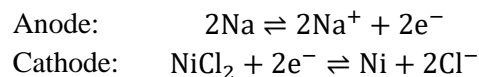
Figure 2.13: Schematic of a NaS battery

The cell reactions normally require a temperature of 300–350 °C to ensure that the electrodes (Na and S) are in liquid state, leading to a high reactivity. At 350 °C the NaS battery exhibits a voltage of 2.07 V until 60–75% of the discharge process. After that, the voltage starts to decrease linearly to 1.78 V at the end of the discharge. The lifetime of a NaS battery is about 10–15 years. The desirable features of NaS batteries include relatively high energy density (150–240 Wh/kg), high power density (150–240 W/kg) and high rated capacity (up to 244.8 MWh). In addition, they have low maintenance needs, high energy efficiency (75–90%), long cycle life (2500–4500 cycles) and very fast response time (<5 ms). The battery also uses inexpensive, non-toxic materials with high

recyclability (about 99% recyclable). However, NaS batteries have some limitations regarding the high annual operating cost (\$80/kW/year), the high initial capital cost (\$300–500/kWh or \$1000–3000/kW) and some safety problems (if both electrodes come into direct contact at high temperature, fires and explosions occur). In addition to that, a need of an extra system is required to ensure its operating temperature and sodium corrosion problem. The research and development focuses mainly on enhancing the cell performance indices and decreasing or eliminating the high temperature operating constrains [65], [67], [68], [81], [82], [87], [88].

2.2.3.4 Sodium Nickel Chloride (NaNiCl) batteries

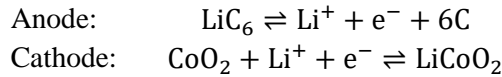
The sodium nickel chloride (NaNiCl) battery (also known as ZEBRA battery) is similar to the sodium sulfur (NaS) battery. It is commercially available since 1995 and was intended to solve some development issues that NaS battery was experiencing at the time. It uses nickel chloride (NiCl₂) as the positive electrode, liquid sodium as the negative electrode and ceramic electrolyte to separate the electrodes:



A sodium nickel chloride battery is a high temperature system (250–350 °C) with higher cell voltage (2.58 V) than a NaS battery. Among the advantages of such batteries are their better safety characteristics, their less corrosive properties, their good pulse power capability, the fact that they are cell maintenance free and very low self-discharge, and their relatively high cycle life. Their limitations with respect to NaS batteries are their low energy density (100–120 Wh/kg) and their low power density (150–200 W/kg). Sodium nickel chloride batteries tend to develop low resistance when faults occur and this is why cell faults in serial connections only result in the loss of the voltage from one cell, instead of a premature failure of the complete system. They have been successfully implemented almost exclusively for electric vehicle applications. The related research nowadays focuses on hybrid electric vehicles and on storing renewable energy for load leveling and industrial applications. However, very few companies have been involved in the development of this technology and produce this type of battery, therefore its potential is limited [55], [81], [85], [87], [88].

2.2.3.5 Lithium-ion (Li-ion) batteries

Lithium-ion (Li-ion) batteries were commercialized by Sony in 1991. The cathode is composed of lithium-based compounds (e.g., LiCoO_2 , LiMnO_2 , LiFePO_4) and the anode is made from graphitic carbon (C). The electrolyte is normally a non-aqueous liquid organic solvent mix with dissolved lithium salts (Figure 2.14). The chemical reactions of the Li-ion battery with lithium cobalt oxide cathode (LiCoO_2) are:



Lithium ion cells have a nominal voltage of around 3.7 V. At present, lithium battery technology has achieved significant penetration into the portable consumer electronics and especially in laptop and mobile systems [89], [90]. Furthermore, it is making the transition into hybrid and electric vehicle applications and has opportunities in grid storage as well [91].

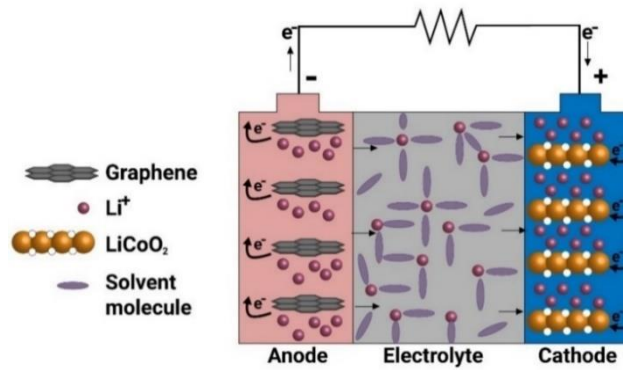


Figure 2.14: Schematic of a lithium-ion battery

The recent related research on Li-ion batteries focuses on cost reduction (which is about \$600–2500/kWh) by the use of cheaper materials, lifetime increase and reduction of high flammability risk. Their advantages compared with NiCd and lead-acid batteries are the higher energy density (80–200 Wh/kg) and energy efficiency (90–97%), the lower self-discharge rate (< 5%/month) and the extremely low maintenance required. In addition, lithium ion batteries have fast response time (< 5 ms), high power density (500–2000 W/kg), wide operating temperatures (–20 to 60 °C for charge and –40 to 65 °C for discharge) and more than 1000–10000 life cycles. Unfortunately, the lifetime of lithium ion batteries is temperature dependent and for that reason they are unsuitable for back-up

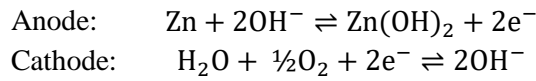
applications where they may become completely discharged. Another drawback is the safety issue due to the metal oxide electrodes, which are thermally unstable and can decompose at raised temperatures, releasing oxygen and thermal energy. Therefore, to minimize this safety problem, lithium ion batteries are equipped with a monitoring unit to avoid over-charging and over-discharging. Furthermore, there is a maximum charge and discharge current limit on most packs [55], [65], [81], [82], [85], [88].

There are several material combinations and various types of lithium-based batteries [92]. During the last few years, graphene has been considered as a promising material that will change dramatically the li-ion battery field and bring a huge improvement in their performance. It is flexible, almost transparent, environmentally friendly, lightweight and the most impermeable and strongest material ever tested. Also it has excellent thermal conductivity (3000 W/m/K) and high theoretical specific surface area (2630 m²/g) [10], [87], [93]. Adding graphene at a lithium-ion battery's anode improves the battery's performance and increases its energy density and cycle life [94]. Moreover, incorporating hybrid materials with graphene at the cathode can enhance several characteristics of the battery. Specifically, graphene can be combined with Vanadium Oxide at the lithium-ion cathode to achieve fast charge and discharge characteristics. Furthermore, enhancing a lithium iron phosphate (LiFePO₄) cathode with graphene can increase the battery's storage capacity, improve the charging time and decrease its weight [95], [96]. An increased attention on the integration of graphene has been paid by electric vehicles companies, but there is no any official announcement by the companies yet [97], [98]. Graphene is also an attractive material for electronics companies. On November 2017, a team of researchers at the Samsung Advanced Institute of Technology developed the "graphene ball" [99]. This invention provides improved cycle life, increased capacity and fast charging capability (five times faster charging speeds than standard lithium-ion batteries). However, there is no commercial large-scale production so far. R&D is intensive, and the future of graphene-based batteries is definitely huge.

2.2.3.6 Metal-air batteries

Metal-air battery can be categorized as a special type of fuel cell using metal instead of fuel and air as the oxidant. A metal-air battery consists of the anode made of metal (e.g., lithium, aluminium, or zinc) and the cathode from porous carbon structure connected to an air supply, as seen from Figure 2.15. The electrolyte is often a good OH-ion (metal-

ion) conductor and it can be in a liquid form or a solid polymer membrane. The reaction is electrochemical and only oxygen is needed from air [55], [82]:



There are various metal air battery chemical couples. One of them is the lithium-air battery, which has a theoretical specific energy of 11140 Wh/kg, however the high reactivity of lithium with air and humidity can cause fire. At present, only zinc-air (Zn-air) batteries are technically feasible with an energy density near 470–650 Wh/kg. Metal-air technology offers high energy density, reasonable cost levels and it is environmentally friendly. However, the electrical recharging is difficult and inefficient (50% efficiency) with a life of a few hundred cycles and a limited operating temperature range (0–50 °C). Although rechargeable metal-air batteries are still under development, there are some developers producing them [55], [65], [82], [85].

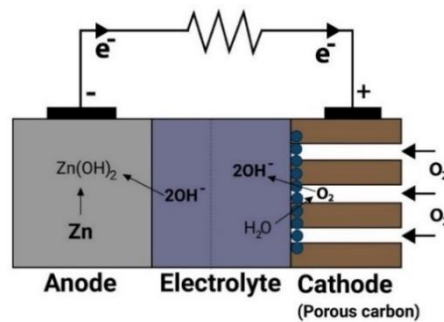


Figure 2.15: Metal-air (Zn-air) battery storage during discharge

2.2.3.7 Flow batteries

Flow batteries are relatively new and promising storage systems and are considered as long-term energy storage devices for large-scale applications. They convert electrical energy into chemical potential energy by charging two liquid electrolyte solutions and releasing the stored energy. The electrolytes are stored externally in tanks/reservoirs and pumped through the electrochemical cell that converts chemical energy directly to electricity and vice versa (Figure 2.16). It is very easy to replace or increase the amount of the electrolytes, thus their capacity is easily scalable. Flow batteries have two sets of electrolytes which are pumped through separate loops and are separated by a microporous separator or an ion conducting membrane. The operation is based on reduction-oxidation

reactions of electrolytes. During charging, the one electrolyte is oxidized at the anode and the other electrolyte is reduced at the cathode. During discharging, a reverse process occurs. Flow batteries can be used in a wide range of stationary applications. They overcome the disadvantages of typical electrochemical batteries, in which the electrochemical reactions create solid compounds that are stored directly on the electrodes causing limited storage capacity [81], [100], [101].

Redox flow technology offers significant benefits such as no self-discharge rate, no degradation for deep discharge, long lifetime and low maintenance requirements. On the negative end, it requires high investment cost and it has technical development issues. Redox flow battery is an attractive technology for large-scale EES systems (10kW–10MW) considering all the above benefits. Many researchers and manufacturers are offering flow batteries for stationary applications because of their positive characteristics regarding the self-discharge rate, the energy costs, the cycle life and the response time. However, further effort must be made to improve their performance and efficiency [55], [102]. Some types of flow batteries that have been developed over the past few years are the vanadium redox flow batteries (VRB), the polysulfide bromide batteries (PSB), and the zinc-bromine batteries (ZBR).

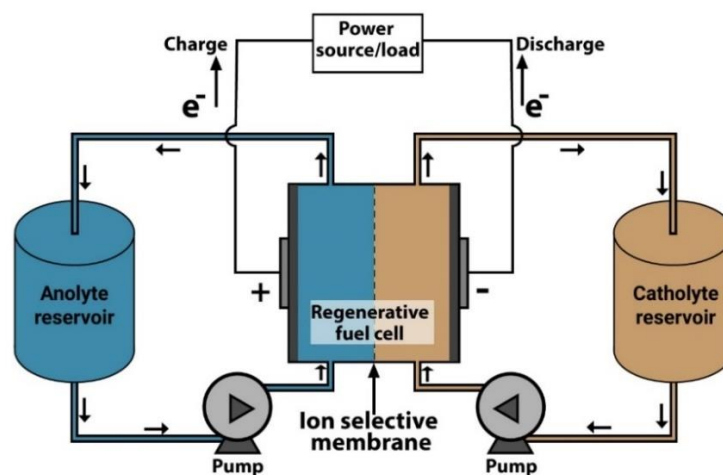
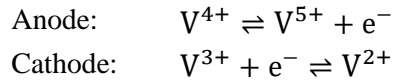


Figure 2.16: Schematic of a flow battery

Vanadium redox batteries (VRB)

VRB is the most studied and mature type of flow batteries. The cell voltage is about 1.4–1.6 V. All chemical reactions are based on the transfer of electrons between vanadium

ions in different oxidation states. Specifically, at the negative electrode V^{3+} is converted to V^{2+} during charging and during discharging V^{2+} ions are reconverted back to V^{3+} ions. A similar reaction happens at the positive electrode. During charging and discharging, H^+ ions are exchanged between the two electrolyte reservoirs through the ion conductive membrane [81], [83], [103]. The chemical reactions are expressed by:

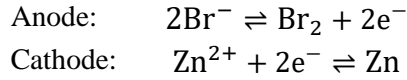


Among all these types of flow batteries, vanadium redox batteries have some attractive benefits, such as better efficiency (75–85%), longer cycle life (12000–14000 cycles), better safety and lower operating cost and maintenance. Also, they do not get affected by deep discharges or if are left completely discharged for a long period. VRB are suitable for various applications, most of them are focused on stationary applications because they require large amount of space due to their low energy density (10–50 Wh/Kg). For instance, they can be used for power quality, load leveling applications and UPS devices. VRB have been installed and tested in various locations for different applications [77], [82]. Uhrig et al. [104] states that for large capacities VRB can be competitive candidates compared to lithium-ion batteries regarding the economic viability. According to the Department of Energy (DOE) database [58], the larger power plant of VRB is located at Minamihayakita Transformer Station in Abira-Chou, Hokkaido, Japan. The power capacity of the plant is 15 MW and can provide power for 4 hours. Finally, in 2016 the China National Energy Administration approved a VRB system of 200MW capacity to be built in Dalian, China. It is estimated that it will be operated by the end of 2018 and will be the world's largest battery plant. The energy storage station will provide peak-shaving as well as grid stabilization [10], [58]. Concluding, flow batteries and especially VRB are definitely the future technologies for stationary applications.

Zinc-bromine (ZBR) batteries

Zinc-bromine batteries are classified as a type of hybrid flow batteries. As shown in Figure 2.16, one reservoir is used to store the electrolyte for the positive electrode reactions and the other one for the negative electrode reactions. Both electrolytes are aqueous solutions of zinc-bromide ($ZnBr_2$). During charge cycle, zinc is plated from electrolyte solution to negative electrode surface. At the positive electrode surface,

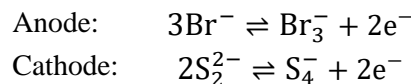
bromide is converted to bromine and it is stored in the electrolyte tank. Therefore, zinc is electroplated onto conductive electrodes, while bromine is formed. During the discharge cycle, zinc dissolves in the electrolyte, thus a reverse process occurs [81], [83], [105]. The chemical reactions at the anode and cathode are described by:



ZBR batteries have similar features with VRB. However, ZBR batteries have relatively higher energy density (30–85 Wh/Kg) compared to VRB. Their cell voltage is about 1.8 V with discharge duration of up to 10 hours. Additionally, they are applicable for seasonal storage due to the low self-discharge rate and the allowance to keep the battery fully discharged (100% DoD) without any damage [55]. According to DOE database [58], the larger power plant of ZBR batteries is located in Astana, Kazakhstan with a rated power of 25 MW and energy capacity of 100MWh. The system is estimated to have 20 years lifetime and can withstand 15000 charge and discharge cycles. The rest of the ZBR battery operational power plants are limited in the range of 10kW–1MW [58].

Polysulfide Bromide batteries (PSB)

PSB batteries are based on the electrochemical reactions between two salt-based electrolytes; sodium bromide (for the positive electrode) and sodium polysulfide (for the negative electrode). The cell voltage is about 1.5 V. The polymer membrane separates the two electrolytes and allows only the interchange of positive sodium ions. During the charge process, bromide ions (Br^-) are transformed into tribromide ions (Br_3^-) at the positive electrode, while dissolved sodium particles (S_4^{2-}) are reduced to sulfide ions (S_2^{2-}). During discharging, a reverse process occurs [81], [102]. The chemical reactions at the anode and cathode are expressed by:



This type of flow battery has relatively low efficiency of about 60–75% because of the pumping requirements. Also, in a case of a reservoir failure, toxic bromine gas is rejected leading to a negative environmental impact. PSB batteries are suitable for voltage and frequency regulation applications because of their fast response time [77], [83]. Currently, there does not exist any large-scale plant of PSB batteries [58]. Regenesys Technologies had tried to build a PSB battery plant in a station in the UK of 15 MW power capacity.

However, due to several financial and engineering constraints the plant remained uncompleted [81].

2.2.4 Hydrogen Energy Storage - Fuel Cells

A fuel cell is an electrochemical cell that converts a fuel (chemical energy) into electricity. The cell consists of two electrodes on both sides of an electrolyte (Figure 2.17). When the fuel (e.g., hydrogen) is fed to the anode and an oxidant (air or oxygen) is fed to the cathode, then a potential difference occurs between the two electrodes. The chemical equation is given by: $2\text{H}_2 + \text{O}_2 \rightarrow 2\text{H}_2\text{O} + \text{energy} + \text{heat}$, where electrical and heat energy are released during the process. Most of the cell types can perform the reverse process (regenerative or reversible fuel cell). The reversible fuel cell combines the functions of an electrolyzer and a fuel cell into one device. When a current is applied, the device acts as an electrolyzer producing hydrogen and oxygen from water. When applying a load, the device behaves as a fuel cell and generates electricity from hydrogen. In other words, when electricity is needed, the stored hydrogen can be used to feed the fuel cell [71]. That is, during off-peak hours electrolysis produces hydrogen, which can be stored to generate electricity during peak hours.

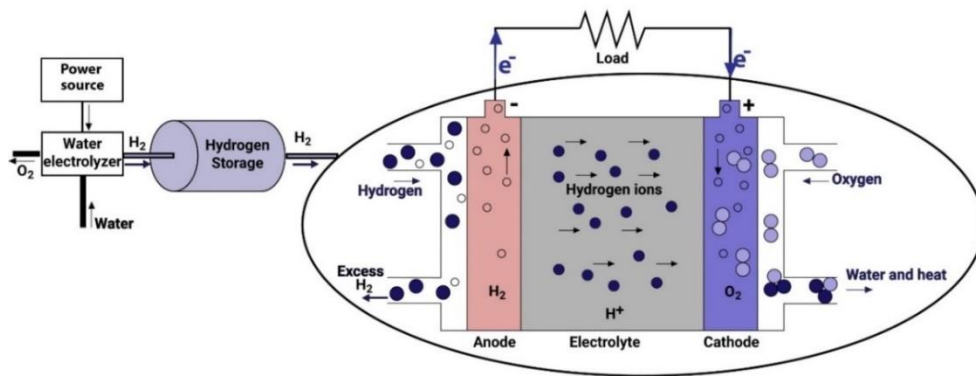


Figure 2.17: Topology of fuel cell and hydrogen storage

Hydrogen fuel cells can be characterized as long-term storage devices. Some of their benefits include high energy density (300–1200 Wh/kg), modular design, low maintenance needs, low toxic emissions, low noise and vibrations, almost zero daily

parasitic loss, easy installation and low maintenance cost. Moreover, they can be transportable, highly versatile, compatible with a lot of types of fuels and suitable for small and large-scale applications. Hydrogen fuel cells have about 15 years lifetime with more than 20000 charge and discharge cycles respectively. However, hydrogen fuel cells remain a very expensive method of storage (\$2–15/kWh) and suffer from high storage cost (\$500–10000/kW) and low efficiency (20–50%). Cost reduction and durability improvement are essential to deploy hydrogen energy storage in large-scale applications [55], [64], [67], [68], [81].

At present, there are four main types of technologies of hydrogen storage, two of which are more mature and developed:

- The pressurized hydrogen method that depends on high materials permeability to hydrogen and their stability under pressure (200–350 bar).
- The second type of technology is based on the use of metal hydrides as storage mediums that relies on the excellent hydrogen absorption properties of these compounds. These compounds are capable of absorbing the hydrogen and restoring it when required. They have low equilibrium pressure at room temperature. This type of technology is safe for use at low pressure and it is compact because of the high-volume absorption capacities of the hydrides. However, a thermal management system is required because the absorption of hydrogen is an exothermic reaction, while desorption of hydrogen is endothermic [65], [68].
- The liquid hydrogen storage, which is limited at present. This is due to its properties, the cost of the materials that are used in the manufacturing of the tank and the very low temperature that is required (-253°C) [106]. Among the drawbacks of this method are the leaks from the unavoidable thermal losses, which lead to pressure increase inside the tank and the self-discharge of the tank that reach 3%/day or 100%/month.
- The fourth type is based on the use of carbon nanofibers, and is currently under research. However, there are many types of materials that are in the research stage depending on the temperature or the pressure of the hydrogen [65], [68].

2.2.5 Thermal Energy Storage (TES)

Thermal Energy Storage (TES) systems can store heat using different means in insulated repositories for later use in many industrial and residential applications, like space heating or cooling, hot water production or electricity generation. TES can be simply defined as the temporary storage of thermal energy at low or high temperatures. Thermal storage systems are deployed for the overcoming of the mismatch between demand and supply of thermal energy and thus they are important for the integration of RES. A typical TES system consists of a storage medium in a tank, a chiller or a built-up refrigeration system, piping, pumps and controls [68].

TES technology can be divided into two categories based on the temperature level of stored thermal energy: the low temperature TES and the high temperature TES.

Low temperature TES is developed for commercial and industrial buildings for heating, cooling and water boiling. The low temperature TES technologies that are currently being used are the following:

(i) *Aquiferous low temperature TES*, where water is cooled or iced by a refrigerator during off-peak hours and stored for later use during peak hours. The amount of stored cooling energy depends on the temperature difference between the chilled/iced water stored in the tank and the returning warm water from the heat exchanger. This technology is applicable for peak shaving commercial and industrial cooling loads during daytime [55].

(ii) *Cryogenic energy storage (CES)*, where cryogen (e.g., liquid air or liquid nitrogen) is generated by off-peak power from RES. When electricity is needed, heat from the environment boils the cryogen and using cryogenic heat engine, electricity is released. Meanwhile, the wasted heat from the flue gas can be used to provide direct cooling and refrigeration. CES does not require significant capital cost per unit energy, is benign to the environment, it has high energy density (100–200 Wh/kg) and has long storage period. Apart from the benefits, CES has low efficiency (40–50%). CES is expected to be used for future grid power management [55], [81].

High temperature TES is developed within solar thermal energy applications and plays vital role in renewable energy technologies and heat recovery. The high temperature TES technologies that are currently in use or are being under development are the following:

(i) *Concrete storage*. This type of technology uses concrete or castable ceramics to store energy at high temperatures for parabolic trough power plants. The heat transfer fluid can be a synthetic oil [55].

(ii) *Phase Change Materials (PCM)*. They are materials that can change phase, usually solid to liquid, at constant temperature. Latent heat is the energy exchanged during a phase transition, where there is no change of temperature during energy transfer. During accumulation, the bulk material shifts from solid to liquid and during discharge the liquid transfers back to solid. The heat transfer between the thermal collector and the environment are made through a heat transfer fluid (e.g., sodium hydroxide). This type of technology can be utilized for long-term seasonal storage. The advantage of latent heat storage is its capacity to store large amounts of energy in a small volume with a minimal temperature change as the change of phase is done at constant temperature, which allows efficient heat transfer [55], [76], [85], [107].

(iii) *Molten salt storage and Room Temperature Ionic Liquids*. They are organic salts with negligible vapor pressure and a melting temperature below 25 °C. They can also be stored at high temperatures (many hundreds of degrees) without decomposing [55]. Concentrated Solar Power (CSP) systems use the sunlight to produce heat. The heat energy can be stored easily before conversion to electricity and eventually provide electrical energy by a conventional plant. CSP plants consist of two functionality parts: one that converts solar energy into heat and another that converts heat into electrical energy [73], [108]. An example of a CSP plant is shown in Figure 2.18. When there is sunlight, cold salt at about 265 °C is pumped from the cold temperature storage tank to the solar power tower. Hot salt at around 550°C is generated by the concentrated solar beams at the receiver of the solar tower and then, it is used to produce steam in a steam turbine for electricity generation. Also, any additional hot salt is stored in a high temperature storage tank to be used during the night to generate additional electricity [109]. However, some CSP plants use molten salt as the heat transfer fluid in the solar collector. Instead of a power tower, they use parabolic troughs to focus sunlight onto a receiver pipe, through which the molten salt circulates [110], [111].

The CSP has power capacity between 10 kW (for small applications) to 200 MW (for grid connection applications). When CSP plant is equipped with thermal storage this is considered as a long-term energy storage method because it can store energy for several

hours. For example, they can produce electricity from heat even on cloudy days or after sunset. In other words, when production is required after sunset, the stored heat is released into the steam cycle and the plant continues to produce electricity. Additionally, the losses in thermal storage cycles of CSP systems are much less than other energy storage technologies (e.g., PHS, batteries). Thus, the thermal storage in CSP is more effective and less costly. The main disadvantages of CSP are the risk of the liquid salt to freeze at relatively low temperatures (265 °C) and the risk of salt decomposition at higher temperatures [73], [108], [112]. Kuravi et al. [113] listed several operational solar thermal power plants with integrated storage, including their characteristics regarding the type, storage medium, power plant capacity and storage duration capacity.

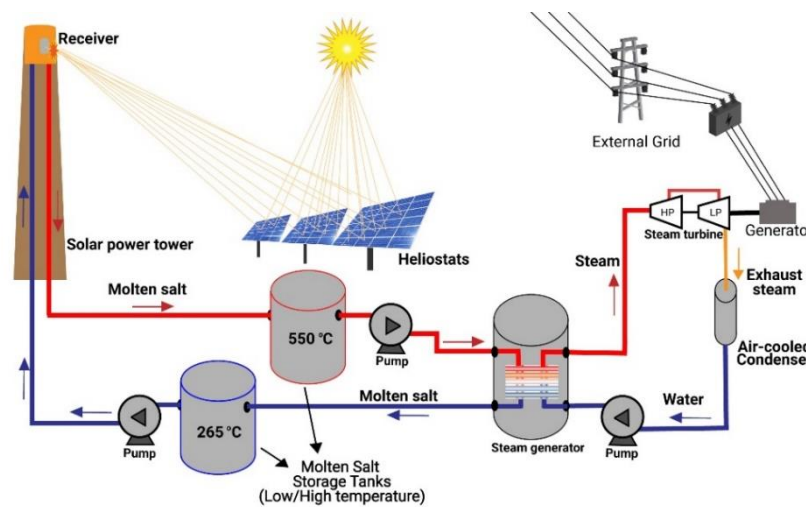


Figure 2.18: CSP plant with thermal energy storage

2.2.6 Superconducting Magnetic Energy Storage (SMES)

Superconducting Magnetic Energy Storage (SMES) is a relatively new technology method that first induces DC current into a coil of a superconducting wire and then stores electrical energy in a magnetic field. There are no resistive losses nor any need for energy conversion to other forms [64]. When the wire reaches a temperature of $-270\text{ }^{\circ}\text{C}$, the phenomenon of superconductivity occurs. As shown in Figure 2.19, the main components of SMES are the superconducting unit, the refrigeration system and a power conversion system. The energy stored can be calculated as $E = LI^2/2$, where L is the inductance of the coil and I is the current passing through [55], [114].

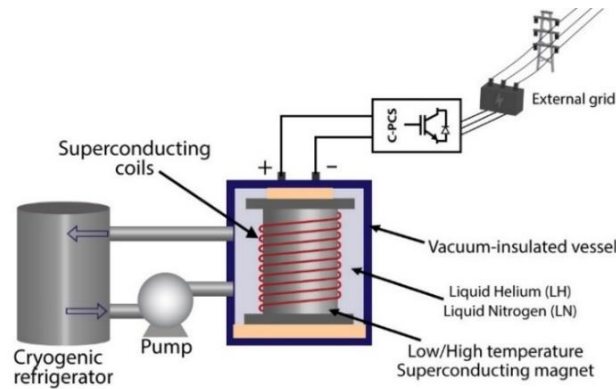


Figure 2.19: SMES system

SMES is a short-term energy storage method with an extremely high operational cost (\$1000–10000/kWh) [115]. The response time is fast, which makes the SMES suitable for stability applications. Moreover, SMES is a reliable method and has high energy efficiency (90–95%). Also, the lifetime of the superconducting coil is high, although there is mechanical stress in the components leading to material fatigue [68], [76].

2.2.7 Flywheel Energy Storage (FES)

The energy stored in a flywheel is in the form of kinetic energy of a rotating mass. It acts as a motor during charging, and as a generator from the rotational energy during discharging. The energy that can be stored is calculated as $E = J\omega^2/2$, where J is the moment of inertia and ω the angular velocity. The faster the flywheel rotates the more energy it stores [116]. Flywheel storage is considered as a short-term storage method, since the discharge time is from some minutes to 1 hour [73], [74]. There are two types of flywheel, the lower speed (up to 6000 rpm) and the higher speed (up to 60000 rpm). Low speed flywheels have specific energy near 10–30 Wh/kg and they are made of steel rotors and conventional bearings. High speed flywheels can achieve specific energy of 100 Wh/kg because of the light weight and high strength composite rotors [64].

Figure 2.20 shows the flywheel storage system, which consists of the motor/generator, the two magnetic bearings that rotate a mass in order to decrease friction at high speed and the vacuum to reduce wind shear. A flywheel storage device shares some attractive qualities such as long lifetime (15–20 years), long cycle life (10000–100000 cycles) and

high efficiency (90–95%). However, flywheels have a high self-discharge (~20% per hour), so they do not constitute an adequate device for long-term energy storage. In addition to that, as mentioned above, the energy density is low and the capital cost is high [64], [65], [68], [117].

Nowadays, the largest flywheel storage system is the EFDA JET Fusion Flywheel at Culham Science Centre, Oxfordshire, UK with total a power capacity of 400 MW. This power is available for 30 seconds, every 20–30 minutes for frequency regulation and on-site power generation [58].

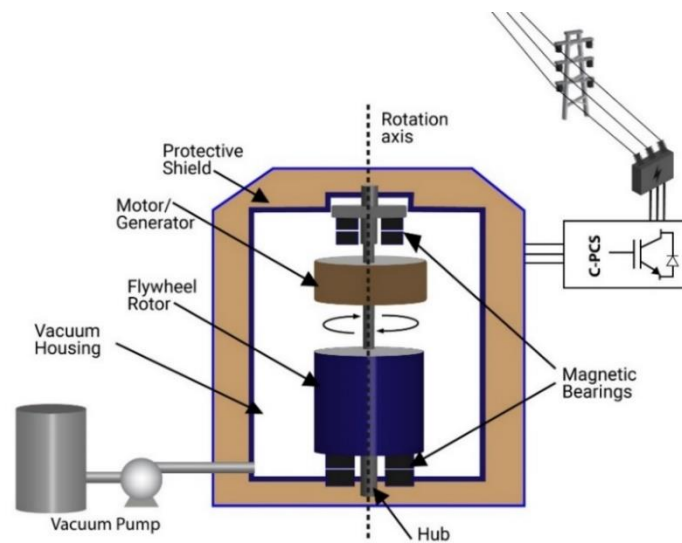


Figure 2.20: The flywheel storage system

2.2.8 Supercapacitors/Ultracapacitors

Supercapacitors, also known as electrochemical double layer capacitors or ultracapacitors, are relatively new energy storage devices. Energy storage is achieved with no chemical reaction, in the form of an electric field between two electrodes. The main difference between supercapacitors and conventional capacitors is that the supercapacitors have a very high energy density, because they have a larger electrode surface area coupled with a much thinner electrical layer between the electrode and the electrolyte. They both follow the same principle, except that supercapacitors have an electrolyte ionic conductor instead of an insulating material, in which ion movement is made along a conducting electrode with a large specific surface (Figure 2.21) [65], [76].

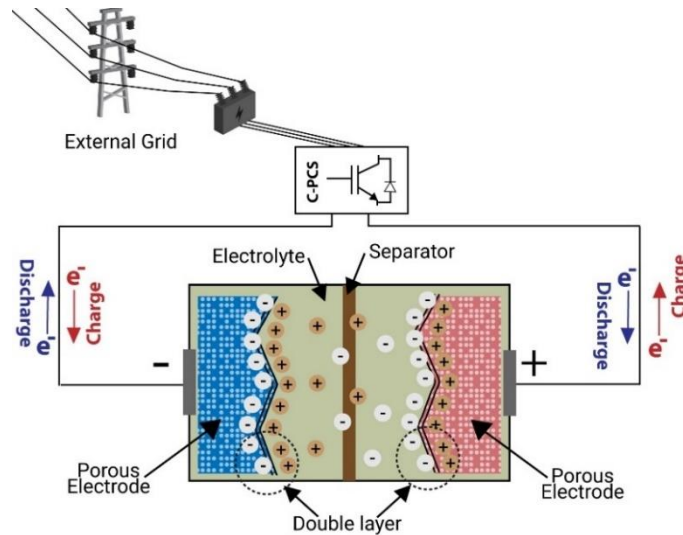


Figure 2.21: Supercapacitor cell

The electrodes are usually made of porous carbon or any other high surface area material. Recent technological progresses have allowed carbon aerogels and carbon nanotubes to be used as electrode material. The electrolyte is organic (which allows a nominal voltage of up to 3V) or aqueous (whose nominal voltage is limited to 1 V). The function of the supercapacitor is simple; during charging, the electrically charged ions in the electrolyte are being moved towards the electrodes of opposite polarity due to the electric field between the charged electrodes [65]. Due to the low voltage resistance between the terminals of the supercapacitor, which is up to 3 V per element, supercapacitors are built up with modules of single cells connected in series or in a combination of series and parallel connections. The module voltage is typically 200–400 V. Single cells have a capacitance of 350–2700 F [64]. The energy stored in the supercapacitors can be calculated as $E = CV^2/2$, where C is the capacitance and V is the voltage across the cell or module [118].

Supercapacitors exhibit some favorable characteristics when compared with other energy storage devices. Firstly, they have high energy efficiency (85–98%), long life cycle (> 100000 cycles), high power density (500–5000 W/kg) and very fast response time (< 5 ms). Moreover, they are environmentally friendly, as no thermal heat or hazardous substances are released during their discharge. Also, they have high tolerance to deep discharges and an extremely low internal resistance. Some of their drawbacks are the very short charge and discharge time (from some seconds up to some minutes), the low energy

density (0.1–5 Wh/kg) and the high cost (\$300–2000/kWh). Finally, their lifetime is up to 20 years and they have a high self-discharge rate (14% per month) [55], [65], [67].

An interesting project (Endesa STORE: La Palma Project) was constructed in 2013 in the Canary Islands to improve the reliability and operation of the grid. The supercapacitors are integrated in a conventional power plant and are able to respond to fast events (for up to 6 seconds) and to keep the frequency at an acceptable range. The same project also implemented two other plants of lithium-ion batteries (1 MW/ 3 MWh) and flywheels (0.5 MW/ 5 kWh) located also at the Canary islands [58].

2.2.9 Comparison of all storage methods

The choice of the ideal storage method to be used depends on several factors: the amount of energy or power to be stored (small-scale or large-scale), the time for which this stored energy is required to be retained or to be released (short-term or long-term), spacing, portability, environmental issues, energy efficiency, cost, and so forth. For instance, PHS and CAES are used in stationary large-scale applications. Also, flywheels and supercapacitors are suitable for short-term applications, such as a brief auxiliary power supply due to an unexpected interruption. Further, CAES and flow batteries are a good choice for peak-hour load leveling when high energy storage is required (many MWh). Additionally, lithium-ion batteries are very efficient, but expensive for remote area applications. Although flow batteries are considered as a promising storage solution because they are scalable, they are still in the developing stage. Some other promising battery solutions are the lithium-ion batteries and NaS batteries. The following tables contain the characteristics of all storage methods. A comparison of all energy storage technologies by their power rating, autonomy at rated power, energy and power density, lifetime in cycles and years, energy efficiency, response time, capital cost, self-discharge rate and maturity is presented.

Table 2.1: Comparison of the various storage methods (except batteries)

Storage Technology	Power Rating (MW)	Discharge time at rated power	Specific Energy (Wh/kg)	Specific Power (W/kg)	Cycle Life (cycles)	Lifetime (years)	Energy Efficiency (%)	Maximum DoD (%)	Response time	Power Capital Cost (\$/kW)	Energy Capital Cost (\$/kWh)	Self-Discharge rate (%/day)	Maturity
PHS	100–5000 [55]	hours–days [59]	0.5–1.5 [55]	–	10000–30000	30–60 [67]	65–85 [67]	95 [121]	min	500–4600 [123]	5–430 [59]	0.01 [10]	Mature
			1–2 [85]		[119]		80–100 [120]	100 [122]		700–2000 [124]			
					50000 [10]								
CAES	5–300 [80]	hours–days [73]	30–60 [55]	–	8000–12000	20–40 [55]	70 [68]	70 [121]	sec–min	400–800 [67]	40–80 [120]	0.5 [10]	Commercialized
					[55]		80 [74]			50–150 [125]			
					50000 [10]								
Hydrogen fuel cell	0.001–50 [126]	minutes–hours [59]	300–1200 [127]	500+ [55]	20000+ [81]	5–20 [119]	20–50 [55]	90 [121]	< 5 ms	500–10000 [67]	2–15 [102]	Almost zero [55]	Developing
						5–15 [55]	30–40 [67]	40–60 [120]					
TES (high temperature)	0.1–300 [68]	hours [81]	80–200 [55]	10–30 [55]	–	5–40 [68]	30–60 [55]	–	Not for rapid response	100–400 [81]	3–130 [128]	0.05–1 [55]	Developed
						5–15 [55]	< 60 [73]			3500–7000 (CSP) [73]			
SMES	0.1–10 [129] < 100 [59]	seconds–30 minutes [59]	0.5–5 [55]	500–2000 [55]	100000+ [130]	20–30 [67]	90–95 [123]	100 [76]	5 ms	200–300 [55]	1000–10000 [55]	10–15 [67]	Developing
Flywheel	0.01–10 [125]	seconds–minutes [86]	10–30 (low speed) [55]	400–1500 [77]	10000–100000 [67]	15–20 [67]	90–95 [67]	75 [120]	seconds	110–330 [126]	1000–5000 [81]	100 [65]	Developed
	0.1–20 [59]		100 (high speed)				70–95 [119]	100 [131]				55–100 [67]	
Supercapacitors	0.01–1 [132]	seconds–minutes [59]	0.1–5 [133]	800–2000 [76]	100000+ [55]	10–20 [67]	85–98 [65]	75 [120]	< 5 ms	100–300 [55]	300–2000 [125]	0.5 [65]	Developing
			2.5–15 [55]	500–5000 [55]	500000 [65]	20+ [55]	5 [76]						

Table 2.2: Comparison of various battery storage technologies

Battery Storage Technology	Power Rating (MW)	Discharge time at rated power	Specific Energy (Wh/kg)	Specific Power (W/kg)	Cycle Life (cycles)	Lifetime (years)	Energy Efficiency (%)	Maximum DoD (%)	Response time	Power Capital Cost (\$/kW)	Energy Cost (\$/kWh)	Self-Discharge rate (%/day)	Maturity
Lead-acid Battery	0–20 [67]	seconds–hours [80]	25–45 [134]	180–200 [102]	200–1800 [81]	3–12 [88]	65–80 [67]	60–70 [121]	< 5 ms	300–600 [67]	150–500 [125]	0.1–0.3 [67]	Mature
				75–300 [55]	500–1000 [55]	5–15 [55]	75–85 [135]						
NiCd Battery	0–40 [81]	seconds–hours [80]	50–75 [67]	150–300 [55]	2000–2500 [67]	10–20 [55]	60–70 [135]	100 [91]	< 5 ms	500–1500 [136]	800–1500 [80]	0.2–0.6 [55]	Mature
NiMH battery	0.01–1 [86]	Hours [86]	70 [137]	175 [137]	< 1800 [65]	15 [137]	65–70 [65]	60–70 [91]	< 5 ms	600–1800 [86]	200–729 [128]	0.4–1.2 [86]	Commercialized
			80 [65]	200–1500 [86]	500 [137]	64 [138]	960–1800 [86]						
NaS battery	0.15–10 [139]	seconds–hours [80]	85 [137]	150–240 [67]	2500–4500 [67]	10–15 [55]	75–90 [67]	90 [122]	< 5 ms	1000–3000 [139]	300–500 [80]	0.05 [10]	Commercialized
NaNiCl(ZEBRA) Battery	0–0.3 [129]	seconds–hours [80]	100–120 [55]	150–200 [55]	2500+ [55]	10–14 [55]	90 [135]	75–85 [140]	< 5 ms	150–300 [55]	100–345 [128]	5 [10]	Commercialized
							80 [141]						
Lithium-ion Battery	0.1–50 [102]	minutes–hours [125]	80–150 [65]	500–2000 [65]	~4500 [87]	5–15 [55]	90–97 [81]	80 [91]	< 5 ms	1200–4000 [55]	600–2500 [129]	0.1–0.3 [55]	Commercialized
			75–200 [55]	1800 [137]	1000–10000 [142]	5–20 [142]	95–99 [142]	85–90 [122]			1200–4000 [143]		
Metal-air (Zn-air) battery	0–1 [87]	seconds–24+ hours [80]	110–420 [133]	100 [129]	100–300 [55]	0.17–30 [128]	~50 [133]	90 [122]	< 5 ms	1750–1900 [145]	10–60 [55]	0.005–0.01 [128]	Developing
Vanadium Redox flow Battery (VRB)	0.3–15 [68]	seconds–10 hours [55]	10–50 [146]	166 [81]	12000–14000 [147]	5–20 [10]	75–85 [67]	100 [120]	< 5 ms	600–1500 [139]	150–1000 [86]	0.15 [10]	Developed
											600–1500 [143]		
Zinc-bromine Flow battery (ZBR)	0.05–10 [81]	seconds–10 hours [55]	75–85 [67]	100 [81]	2000+ [67]	5–20 [10]	75–80 [67]	100 [120]	< 5 ms	700–2500 [55]	340–1350 [87]	Almost zero [144]	Developed
			30–50 [55]	45 [137]	10000 [87]	60–65 [87]	400 [144]						
Polysulfide Bromide battery (PSB)	0.1–15 [81]	seconds–10 hours [55]	15–30 [81]	–	2000 [77]	10–15 [83]	60–75 [77]	100 [120]	20 ms [83]	700–2500 [55]	150–1000 [55]	Almost zero [81]	Developing

2.3 Energy Storage Applications ⁴

The widespread growth of the renewable energy technologies creates stabilization or quality problems to the grid. Moreover, when the wind is not blowing, or it is cloudy wind turbines and photovoltaic systems are not able to produce electricity respectively. The electric power system must keep in balance the real-time generation and load. Consequently, energy storage is required to provide smooth and uninterrupted electricity. EES technologies cover a wide spectrum of applications to the power network such as: (i) helping in meeting peak electrical demands, (ii) providing seasonal storage, (iii) regulating power, voltage and frequency, (iv) improving power quality and reliability, (v) supporting the smart grids, (vi) providing energy management, (vii) mitigating the fluctuations of renewable source power generation, (viii) reducing electrical energy import during peak hours and smoothing power demand, and (ix) providing standby power generation when a fault appears [120], [148]. Case studies, performed by Hoff et al. [149], showed that the addition of a storage for local load control and for emergency load protection are beneficial to the economics of customer-sited photovoltaic systems. Figure 2.22 classifies the energy storage applications by the needs concerning energy, power and discharge time duration [150]. Most of the energy storage applications in the figure are explained in this Section.

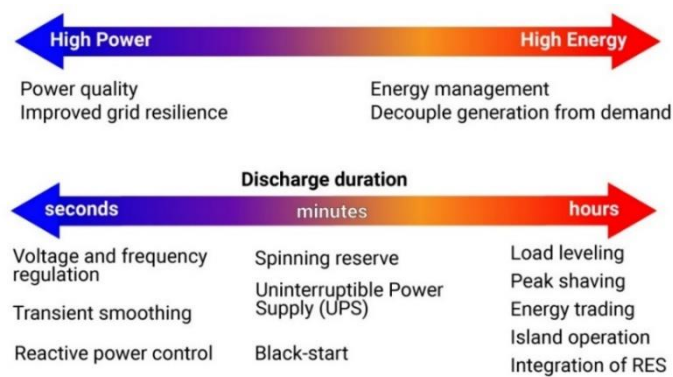


Figure 2.22: Energy Storage Applications by the needs in energy, power and discharge time duration

⁴ Section 2.3 contains material from published paper [56]

Additionally, Figure 2.23 summarizes all storage technologies by their power capacity and the duration for which this power can be relieved. The values for the power rating and the discharge time come from Table 2.1 and Table 2.2. This comparison is useful when considering which technologies are best for providing certain applications. For instance, Figure 2.23 summarizes three application categories; (i) uninterruptible power supply (UPS), frequency and power quality, (ii) transmission and distribution (T&D) grid support and load shifting, and (iii) energy (bulk power) management [151]. Nourai [152] presented all storage methods and compared them with several characteristics. Also, Luo et al. [81] provided an overview of current and potential EES options for multiple applications.

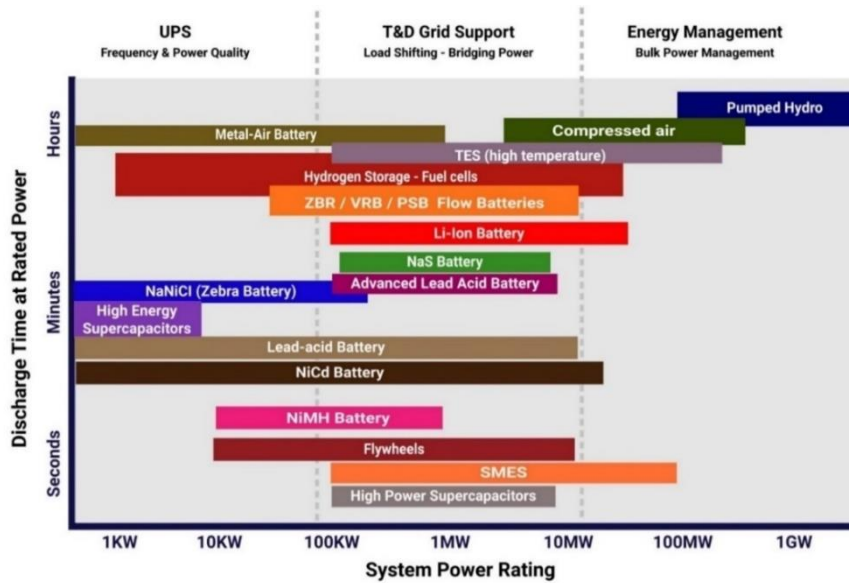


Figure 2.23: Energy Storage Technologies by power capacity and discharge time

A brief explanation of the applications (grid-scale and customer-sited) that energy storage can provide is given below, with reference to the suitable technologies for each application.

- **Power Quality**

Power quality concerns the ability of the grid to supply a clean and stable power flow acting as a perfect power supply that is always available, with a pure noise-free sinusoidal wave shape, within voltage and frequency tolerances [153]. The flow of reactive power and the presence of transients and harmonics in the network are the common contributors to voltage instability and interference on the voltage waveform.

All these can affect the performance of some sensitive parts of equipment. Therefore, EES technologies can ensure a power quality improvement with a fast response time, high cyclability and a reasonable cost. Flywheels, supercapacitors and batteries contain all the above characteristics. Also, SMES may be a good choice [67], [68], [81], [133]. Seo et al. [154] suggested supercapacitors for power quality control strategies in photovoltaic and wind turbine systems. Also, simulations confirmed that supercapacitors can smooth the fluctuations caused by wind speed and irradiance variations.

- **Frequency regulation**

When the power consumption exceeds the generated power, due to increased customer usage or reduced generating capacity in the grid, the increased load on the generators will cause them to slow down and since the generators are synchronous machines, the grid frequency will also decrease. Similarly, if the consumption suddenly falls below the power generated or more generating capacity is switched into the network, the generator will speed up and the grid frequency will increase. Keeping the grid frequency and voltage within strict limits is essential for maintaining the stability of the grid. This requires access to very fast response means. A rapid drop of frequency may cause several problems, even a system collapse. Frequency support requires power to be delivered for a very short duration. The technologies that are capable for both regulation and power quality are the flywheels, SMES, batteries and supercapacitors. Supercapacitors have very fast response time, although their energy density is low. Delivering an instantaneous and consistent power supply can be an elusive goal. Yet without it, grid frequency regulation is impossible and frequency regulation remains one of the primary economic drivers for grid-scale storage today [67], [68], [81], [133].

- **Peak shaving**

Peak shaving is the way of changing the pattern of energy supply so that the generation of energy for consumption during the hours of peak demand is shifted to off-peak periods. In other words, the energy is stored when there is excess in renewable energy production and it is released to the grid during periods of high demand (Figure 2.24). The storage technology must be scalable and able to provide energy for some minutes to some hours. Currently, the most applicable technologies are PHS, CAES, electrochemical batteries, flow batteries and hydrogen fuel cells. Batteries are capable

because of their fast response and the long duration of energy supply [67], [68], [81], [133], [155]. Senjyu et al. [156] proposed a model for leveling the power of photovoltaic array with battery storage, calculating the optimal size of the battery to minimize the capital cost. According to Toledo et al. [157] sodium sulfur (NaS) batteries are suitable for peak shaving applications in photovoltaic systems.

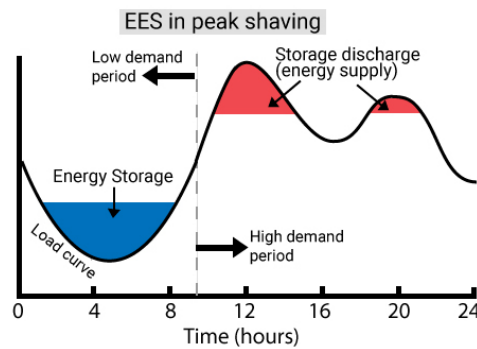


Figure 2.24: Energy storage load profile in peak shaving

- **Load leveling**

Load leveling is the rescheduling of the loads to limit the requirements during periods of high demand and to increase the production of energy during off-peak periods for immediate storage and subsequent use during high demand periods (Figure 2.25). The storage technology must be able to provide energy for some minutes to some hours. As for the case of peak shaving, the most applicable technologies are PHS, CAES, electrochemical batteries, flow batteries and hydrogen fuel cells [67], [68], [81], [133], [155].

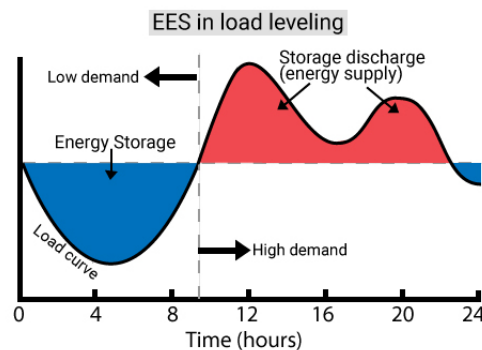


Figure 2.25: Energy storage load profile in load leveling

- **Load following**

Energy storage can provide support in the following load changes of electricity demand. In other words, storage can act as an energy source or sink in response to both load and generating capacity changes. Most types of storage can also respond much more quickly than typical rotary generators when more or less output is needed for load following. Similarly, they can usually operate at partial output levels with relatively modest performance penalties. On the downside, storage systems cannot supply power indefinitely and the duration of supply is limited by the storage capacity [67], [68], [81], [133].

- **Seasonal storage**

Seasonal storage requires high energy capacity and low self-discharge rates. Also, an advantage can be the efficiency and the power density. The selected storage technology for seasonal storage should be able to store energy for days to months, to compensate for a longer-term supply disruption or seasonal variability on the supply and demand sides of the energy system. For example, an underground TES system may store heat in the summer to use it in the winter. For this case, PHS, CAES, hydrogen fuel cells and flow batteries are more technically acceptable. However, PHS has low energy density and this may cause unacceptable changes to water levels. Also, hydrogen fuel cells have low efficiency and for this reason may be unsuitable [67], [68], [81], [123], [133].

- **Integration of Renewable energies**

The main problem with RES is that they are intermittent and thus they may be available when they are not needed and may not be available when they are needed. Unfortunately, the power output from these sources cannot be accurately predicted or controlled by grid operators. Thus, most renewable energy installations such as wind farms and solar arrays would better be utilized with the use of storage. For instance, Zahedi [158] proposed a solar photovoltaic combined with battery and supercapacitor. Depending on the application, renewable energy installations may use a variety of storage technologies [67], [68], [81], [133].

- **Black-start**

EES can provide a start-up from a shutdown condition to a system without taking power from the grid. This happens in case the system fails to provide energy therefore units are unable to restart [159]. This application requires a storage system with a fast response time, thus batteries and supercapacitors are suitable methods. An example of

an installed EES is a CAES plant in Huntorf, Germany, providing black-start to nuclear units near the North Sea [81], [129].

- **Spinning reserve**

In the case of a fast increase in generation or a fast decrease in load demand, energy storage systems can provide spinning reserve for the prevention of unexpected problems in the grid. In other words, spinning reserve is the unused capacity that can be activated by decision of the system operator and which is provided by devices that are synchronized to the grid and can affect the active power. Such systems must respond immediately, with the ability to maintain the output for some minutes up to a few hours. Some suitable storage methods are the flywheels, the batteries, the SMES and the flow batteries. Also, some other promising technologies are the CAES and PHS systems [125]. Spinning reserve is also helpful in isolated systems. Several studies examined the spinning reserve functionality using batteries and flow batteries in wind power plants [102].

- **Emergency back-up power generation**

In the case of a network failure, energy storage systems can act as emergency suppliers to provide adequate power until the system be restored [160]. For this case, rapid response time storage technologies are needed with relatively long duration of discharge time. The most suitable technologies are batteries, flow batteries and flywheels [67], [68], [81], [133]. Masaud et al. [73] state that CAES are able to provide backup electricity during long blackouts.

- **Uninterruptible Power Supply (UPS)**

In the case of a power interruption or a power surge then EES must provide power to the system. UPS systems react immediately by providing energy for some minutes up to two hours. They are designed to automatically provide emergency power with no delay in case of an interruption or unacceptable situation of the grid supply. UPS is applicable in fire protection systems, security systems and in computers and servers, where the data must be protected. The most suitable technologies are batteries, flywheels and supercapacitors [81], [150], [161].

- **Time-Of-Use (TOU) bill management**

Energy storage could be employed to help the end-users to time-shift their demand from peak hours to off-peak hours, and thus reduce their electricity bill by purchasing low-priced electricity. In other words, energy storage could absorb energy when the demand

and the electricity price are low, and be used later when the demand and electricity price are high. The storage technology is applied behind-the-meter and can benefit both the end-user and the grid operators. The most suitable storage technologies for this application are batteries, and some promising technologies are flow batteries, flywheels, SMES and supercapacitors [81], [83], [159].

- **Increased PV self-consumption**

The PV self-consumption application is suitable to prosumers when no promotion of renewables integration is available or any favorable export tariffs are applied. Self-consumption has become widespread in Germany and Australia, where feed-in-tariff levels for residential PV customers have dropped below the retail rate, forcing prosumers to maximize the amount of generated PV power they consume on-site. Typically, batteries are the most suitable technology for this application [26], [62], [162].

2.4 Hybrid Energy Storage (HES) ⁵

Hybrid energy storage refers to the integration of two or more different storage technologies into a system. This is achieved by combining the advantages and characteristics of different storage methods to achieve specific requirements and improve the whole system performance. The combination of energy and power rating, life cycle, duration of discharge period and other characteristics cannot be satisfied by the simple EES technology. Among all storage technologies, SMES, supercapacitors, flywheels and high-power batteries have high power rate and short discharge duration. Contrarily, PHS, CAES, hydrogen fuel cells and high energy batteries have high energy rates and long duration of storage. It is necessary to choose an appropriate combination of energy storage systems to follow the system requirements [163]–[167]. Below a review of the current combinations of EES is presented.

- **CAES-TES**

The first large pilot power plant, ADELE, uses adiabatic CAES and TES technologies for better efficiency (about 70%), preventing fossil fuel consumption. It is planned to

⁵ Section 2.4 contains material from published paper [56]

have a 1 GWh storage capacity and 200 MW of power generation with an autonomy of 5 hours. The aim of the plant is the optimization and smooth interaction of the individual energy sources, especially of wind power. The project is designed to be built in Germany, but it is on hold due to non-technical reasons [58], [168].

- **CAES-Supercapacitor**

Lemofouet and Rufer [169] presented a hybrid energy storage system using CAES and supercapacitors for maximum system efficiency. The CAES system provides energy and long storage periods while supercapacitors offer power smoothing. Additionally, Martinez et al. [170] proposed a similar hybrid system and provided the dynamic modeling and control algorithm of the system.

- **CAES-Flywheel**

Zhao et al. [171] studied the hybrid storage of an adiabatic CAES and the flywheel storage system for a wind power plant. The stochastic and intermitted nature of the wind leads to power fluctuations that can be eliminated through hybrid energy storage. The design and parametric analysis of the system is carried out to examine the effects of several parameters, such as the ambient conditions, inlet temperature of compressor, storage cavern temperature and maximum and minimum pressures of storage cavern.

- **Fuel cell-SMES**

Sander and Gehring [172] proposed the LIQHYSMES hybrid plant to solve several problems that are caused by the increased contribution of RES to the grid. The plant uses the high volumetric energy density of liquid hydrogen to provide long-term storage for large-scale stationary applications. Furthermore, the integration of SMES achieves short-term applications, such as load balancing. Another interesting back-up system for renewable generation was designed by researchers in Japan, combining a SMES system (cooled with liquid hydrogen) with a hydrogen fuel cell system [173].

- **Fuel cell-Supercapacitor**

There are many studies concerning the hybrid storage of hydrogen fuel cells and supercapacitors. Some researches focus on the application to electric vehicles while others examine the integration of RES. Thounthong et al. [174] proposed a control strategy of hybrid fuel cell-supercapacitors for electric vehicles. The polymer electrolyte membrane (PEM) fuel cell acts as the main power source and the supercapacitors as the auxiliary power source for electric vehicles. Furthermore, a hybrid PEM fuel cell-supercapacitor system for stand-alone residential applications was examined by

Uzunoglu and Alam [175]. Mathematical and dynamic electrical models were proposed and simulated. The combination of fuel cells and supercapacitors may increase the energy efficiency of the system, reduce the cost of fuel cell technology, and improve fuel usage. Apart from the above studies, there are various researches in the literature regarding the hybridization of fuel cells and supercapacitors for several control strategies [176], [177] or for power and energy management applications [178], [179].

- **Fuel cell-Battery**

The combination of fuel cell and battery is one of the most studied hybrid storage system. Many researchers propose the fuel cell-battery hybrid storage for RES integration (mostly by photovoltaics and wind turbines) and distributed generation [180]. Several types of batteries combined with fuel cells are depicted, namely lead-acid [181], [182], lithium-ion [183] and flow batteries [184]. However, increased attention is also paid on automotive applications and on electric vehicles for powertrain performance improvements. For this case, lithium-ion batteries [185], [186], lead-acid batteries [187] and sodium nickel chloride (ZEBRA) batteries [188] were studied.

- **Battery-Flywheel**

Flywheels provide high power for a short period of time with high efficiency and high cycle life. Briat et al. [189] examined the design and the integration of a flywheel storage system into an electric vehicle power train. They proposed a method to improve the system performance by keeping the battery power within rated levels for charges and discharges, while flywheel provides or recovers the energy during acceleration or braking, respectively. In addition, an application of battery-flywheel storage system for power stabilization on a large-scale wind farm was studied in [190]. The combination of battery and flywheel can also be applied on a UPS system [191] or on aerospace applications [192]. Moreover, a stand-alone house with RES and battery-flywheel storage system is depicted in [131], in which the authors proved the economic and technical feasibility of the system. Finally, Barelli et al. [35] provided a dynamic analysis of a hybrid battery-flywheel storage system coupled to a photovoltaic plant and a residential load. The authors considered the effect of components sizing, the power flow control management and the different weather conditions. As a result, this hybridization allowed load management, peak shaving, power quality improvement and enhanced life of the battery.

- **Battery-SMES**

The utilization of a battery and SMES technologies leads to various advantages, such as high efficiency, fast response time, high power and energy density and high cycle life. However, a SMES system requires the use of a refrigeration system that is an expensive solution. Therefore, the SMES is limited to some stationary applications like renewable power generation [193]–[195] and railway supply substations [196]. Specifically, Cansiz et al. [195] proposed a hybrid system using lithium-ion battery and SMES into an interconnected microgrid operation. The authors examined a case of a fault, in which the SMES responds immediately to maintain the voltage of the system, and battery is switched on when the fault remains and the SMES cannot supply enough power.

- **Battery-Supercapacitor**

There are many researchers who propose the use of batteries and supercapacitors together. This combination offers high storage capacity and a very fast response time [197]. Kanchev et al. [198] proposed an energy management method in a building with photovoltaic arrays and a hybrid storage. Specifically, excess energy from photovoltaics is stored in batteries and the local real-time power control is achieved by supercapacitors. Liu et al. [199] proposed a control strategy in a wind power system, using batteries and supercapacitors to relieve battery stress and extend the lifetime of the battery. Zhang et al. [200] presented an application of a battery-supercapacitor hybrid storage in a microgrid. Furthermore, some researchers proposed a hybrid system (battery-supercapacitor) for electric vehicles for better performance, higher efficiency and extended battery life [201]–[203]. Zhang et al. [204] indicated some control strategies using batteries and supercapacitor bank to provide transient power and peak load requirement. Finally, regarding the types of batteries used, Wang et al. [205] proposed flow batteries (VRB) for a 1 MW photovoltaic plant connected to the grid.

2.5 Configurations of a grid-connected PV system with hybrid energy storage (HES)

Photovoltaic systems are classified into two categories depending on their grid dependency, namely the stand-alone or off-grid systems, and the grid-connected systems (Figure 2.26). The simplest stand-alone PV system is that of a PV module with

a DC load, such as a water pump. If there is a need of a continuous supply, then a storage system or a fossil-fuel generator is required. Stand-alone PV systems are usually oversized in order to withstand the worst-case scenarios of solar generation. The grid-connected systems are either decentralized or centralized. The decentralized grid-connected PV systems are mostly installed on rooftops or integrated near a building and usually have “small” power ranges. The centralized grid-connected PV systems are large scale systems and are connected directly to medium or high voltage grid [52], [206].

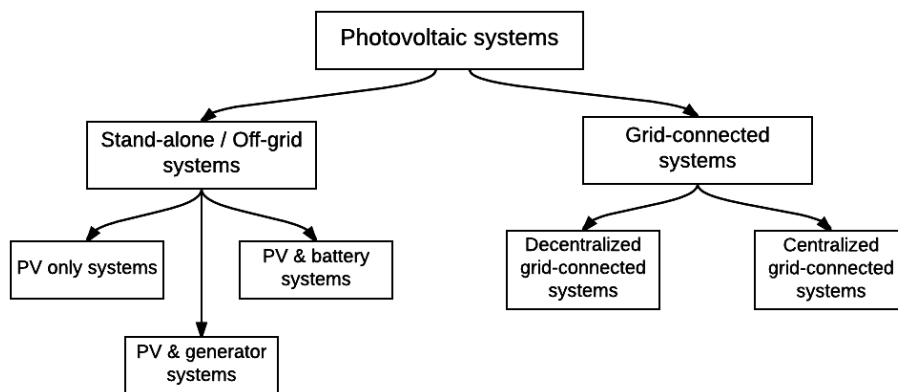


Figure 2.26: Classification of PV systems

This study focuses on the grid-connected rooftop solar PV systems. A typical example of a grid-connected rooftop PV system (without storage) is shown in Figure 2.27. When there is sunlight, a connection of PV modules produces electricity (DC). A maximum power point tracking (MPPT) algorithm finds the maximum power for the operation of the PV system during variations of solar irradiance and ambient temperature. Additionally, a DC-DC converter ensures that its output DC voltage is always greater than the grid peak voltage. Moreover, a DC-AC inverter provides an AC voltage that meets the grid requirements for connection and synchronization; the voltage magnitude and the frequency must be equal with that of the grid and the phase sequence between the system and the grid must be the same [207]. The consumption of the building is satisfied from either the PV, and/or the low voltage grid, providing an efficient power flow between the aforementioned sources and the building load. Over the last few years, there has also been an opportunity for a communication between the PV system and the grid through the smart meters. The smart grid can carry a two-way flow of electricity

and information to communicate and respond to events that occur in the grid, such as a transformer failure. Thus, the smart grid provides flexibility and reliability. In addition, a significant benefit of the smart grid is the real-time pricing for a smoothed and shaped demand profile, instead of a full-of-peaks profile. Therefore, a communication between the prosumer and the utility operator can be efficiently achieved [208], [209].

Furthermore, a storage method can be applied to a system for various functions, such as voltage smoothing, peak shaving, emergency backup generation, smart grid support and building energy management. It may also contain a bidirectional DC-DC converter and a controller to prevent overcharging or over-discharging, ensuring a better performance of the storage system [210]. In addition, hybrid energy storage can be integrated to achieve different applications. There are several storage technologies that may be used in a PV system. The hybridization of the battery-supercapacitor can be integrated into the existing system to achieve several solutions in renewable energy integration and grid support. Specifically, some of the benefits of the hybrid storage are the combination of both high energy and power rating, the increased life cycle, the duration of discharge period (short-term or long-term) and other features that cannot be satisfied by the single storage technology [211].

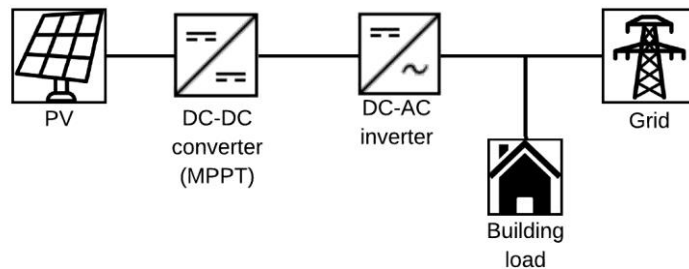


Figure 2.27: Block diagram of a basic grid-connected rooftop PV system

There are several topologies regarding the connection of hybrid energy storage technologies in the system of Figure 2.27. A type of connection is that of the AC-coupled system, where the connection between the PV and the storage is applied on the common AC-bus. This type of connection requires an inverter on the storage side, and therefore the storage expandability is easier [212]–[214].

This Section is focused on the DC-coupled systems, where storage element is connected to the common DC-bus of the system. The DC-coupled systems are more efficient and

have fewer components than the AC-coupled systems. However, the expandability is limited and they are more expensive in case of an upgrade in storage capacity [214].

Some configurations proposed in the literature for such systems include passive, active or a combination of both topologies [215], [216]. The passive configuration in parallel connection of both storage technologies is shown in Figure 2.28. The terminal voltage of the battery and supercapacitor is the same with that of the DC-bus, as they are directly connected in parallel. The passive topology has as advantage the simplicity and the ease of implementation with no complicated control devices. On the other hand, the power sharing between the storage devices and the PV system is not controlled and the DC-bus voltage is not regulated and varies depending on the battery voltage range. Therefore, the battery and supercapacitor cannot be always operated at their maximum power point [27], [167], [217].

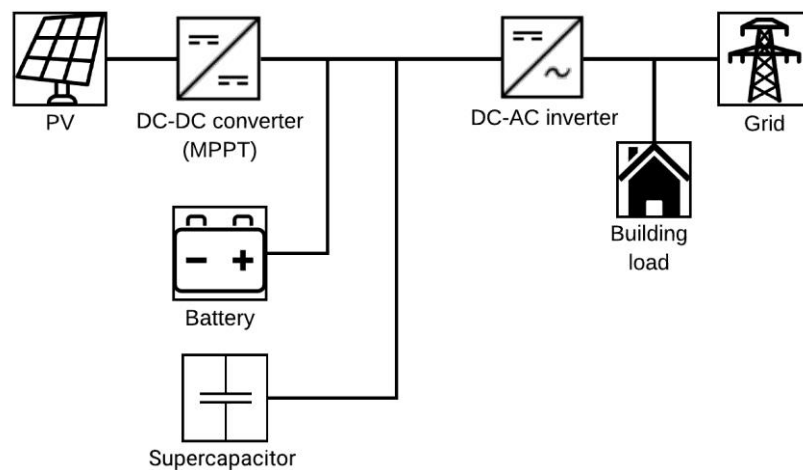


Figure 2.28: Passive topology of the rooftop PV system with HES

Figure 2.29 presents a battery semi-active topology, where the battery can be controlled through a bidirectional DC-DC converter, and the supercapacitor is passively connected. The bidirectional DC-DC converter allows the battery to have different voltage levels than the DC-bus, resulting to higher flexibility and adjustability of the battery. The supercapacitor size must be relatively large in order to keep the DC-bus voltage levels stable, resulting to higher cost requirements [217].

Another semi-active topology is that of Figure 2.30, where the battery is passively connected in parallel and the supercapacitor is connected through a bidirectional DC-

DC converter [203]. Therefore, the supercapacitor can be utilized more and controlled, and its voltage is allowed to vary over a wider range, resulting in higher volumetric efficiency. In addition, the supercapacitor can be controlled to absorb/release short-term high frequency variations, while the battery can manage the long-term energy requirements [27], [167], [217].

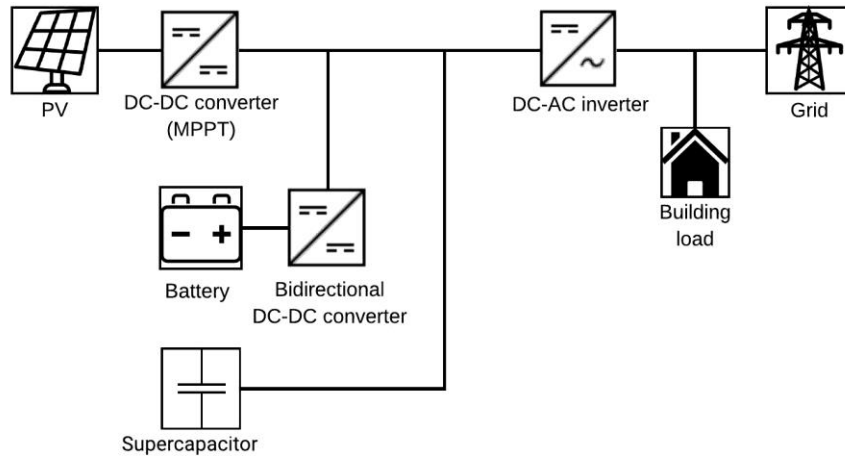


Figure 2.29: Battery semi-active topology of the rooftop PV system with HES

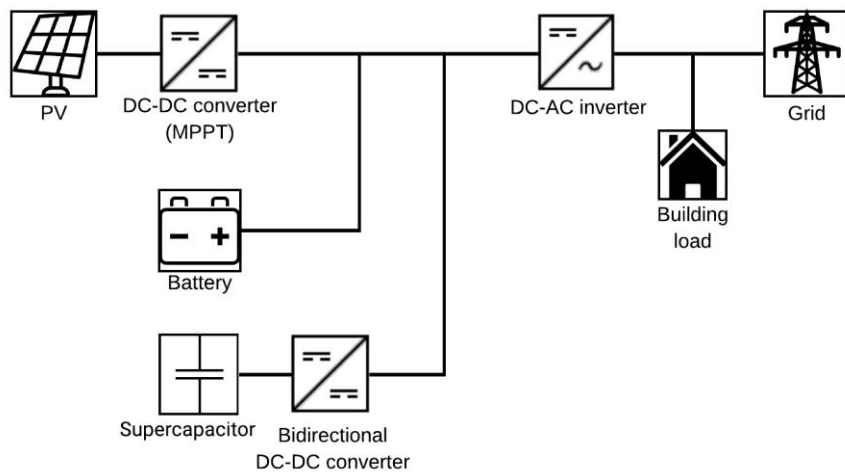


Figure 2.30: Supercapacitor semi-active topology of the rooftop PV system with HES

The fully active parallel configuration is presented in Figure 2.31, where both storage technologies are controlled through two individual bidirectional DC-DC converters. Each converter allows the storage to have different voltage levels on the battery/supercapacitor side, and regulated voltage on the common DC-bus side. This topology

solves all the drawbacks associated with the supercapacitor and battery voltage variations and efficiency problems. However, the fully active topology is more expensive and complex to implement [27], [167], [217]. This method is widely examined and discussed by researchers who propose different energy management algorithms [199], [201], [204], [205].

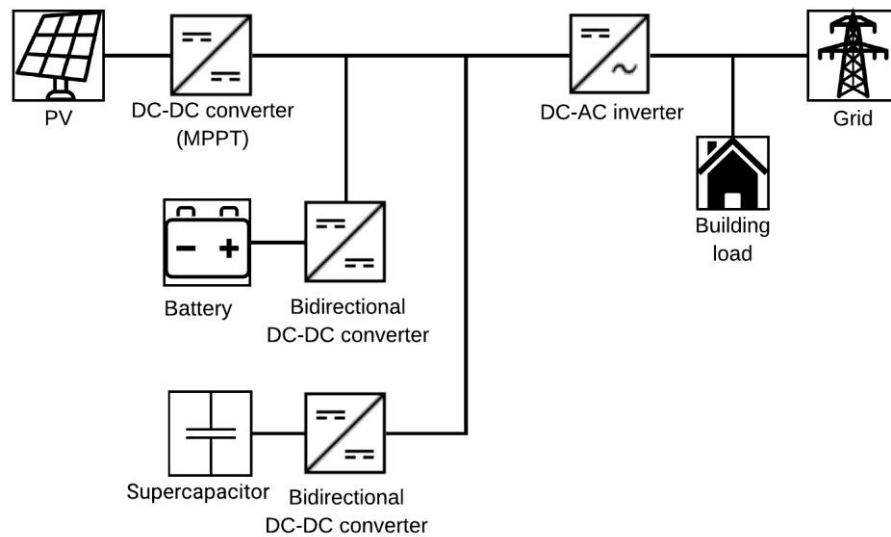


Figure 2.31: Fully active topology of the rooftop PV system with HES

3 Grid-connected PV system in buildings: mathematical analysis and simulation modeling

Figure 3.1 presents the block diagram of the proposed grid-connected PV system with battery-supercapacitor hybrid energy storage. In Figure 3.2 the architecture of the system under investigation is also presented. The system can be adjusted to different weather conditions and synchronized with the utility grid. A 3 kW_p PV array is connected to a DC-DC boost converter to step-up the output PV voltage at 400 V, regardless of changes in solar irradiance and temperature. A Maximum Power Point Tracking (MPPT) control provides the maximum power point for the operation of the PV system, which is achieved using the Perturbation and Observation (P&O) method. A 10 kWh lithium battery pack is considered suitable for our needs while a 50.6 Wh supercapacitor pack is enough for our system's requirements. The battery is modeled based on the dual polarization (2nd-order RC) battery cell circuit, while the supercapacitor model is developed based on the two branches equivalent circuit of the supercapacitor cell. An active parallel configuration is used for the battery-supercapacitor model for better utilization of the storage technologies and higher efficiencies. The battery and supercapacitor packs are connected to the common 400 V DC-bus through two bidirectional DC-DC converters. This topology allows the battery and supercapacitor modules to have different voltage levels and their power flow to be controlled separately. A single-phase DC-AC inverter is designed to convert the DC power from the DC-link into the AC form for grid interconnection. Since the system is grid-connected, the inverter is responsible for the DC-bus voltage control. In order to maintain the DC-bus voltage stable near the reference value of 400 V, a voltage controller is used, where a reference magnitude for the grid current, and hence for the inverter output current is obtained. Also, a PLL is used so that the output current injected to the grid be in phase with the grid voltage (unity power factor).

The electricity demand of the building is satisfied through the PV system, the energy storage system, and/or the low voltage grid. A novel dynamic PMA is proposed for this model to make better use of the generated PV power, the battery-supercapacitor storage, and the building load. Specifically, the proposed algorithm focuses on the use of generated PV power and storage (instead of the grid), reducing the peaks in generation or demand, and increasing the self-consumption and self-sufficiency of the building.

Also, the hybridization of battery-supercapacitor reduces battery stress and extends battery lifetime.

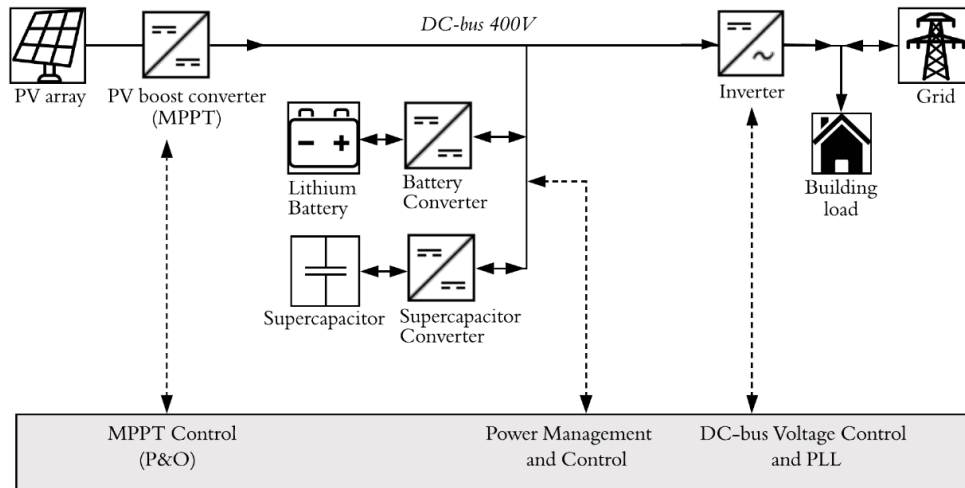


Figure 3.1: Block diagram of the proposed grid-connected PV system with battery-supercapacitor hybrid storage

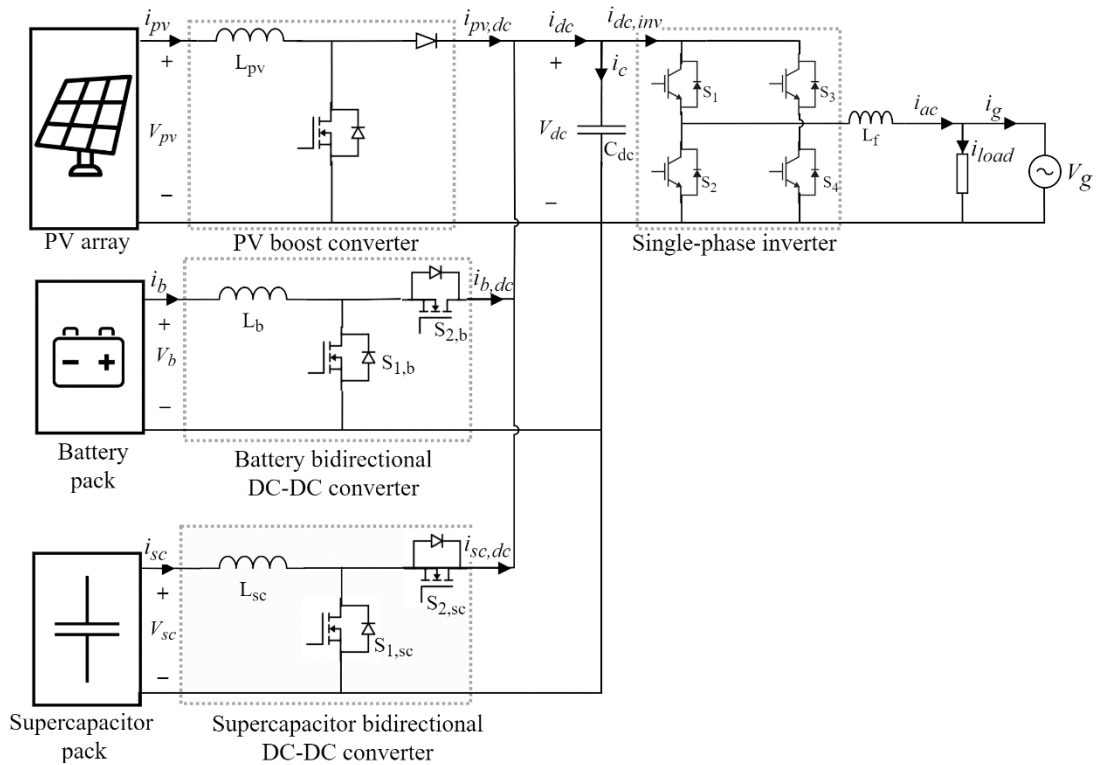


Figure 3.2: Architecture of the proposed grid-connected PV system with battery-supercapacitor hybrid storage

The proposed model is developed and simulated using MATLAB/Simulink software based on mathematical analysis and average modeling.

The mathematical modeling approach provides flexibility and adjustability to the parameters of a model. Moreover, mathematical modeling is used when a customized and complex model can only be designed and expressed by equations, or when a specific technology is not available from a software (e.g., a PV module, a specific type of battery or supercapacitor). Additionally, in engineering, it is sometimes preferred to model a specific behavior of a system and to neglect other insignificant phenomena. It should also be noted that a mathematical model can be easily understood and accepted by all engineers, applied mathematicians and other scientists who have no knowledge or ease of electrical circuits [218], [219].

It must be stressed that the averaged model of all converters is examined here (PV boost converter, battery and supercapacitor bidirectional converters, voltage source grid inverter). However, the system dynamics and the small ripple signals that occur are captured, to ensure model accuracy. According to [220], the effect of the high switching frequency of the converters is insignificant on the DC-bus, because the DC-link capacitor mitigates the double line frequency produced. Moreover, one should note that the simulation time of the system with the averaged model is decreased dramatically compared to the switching model, especially for long-term operation with a significant number of converters [220]–[223]. Finally, as the switching ripple can be negligible in a well-designed converter [224], the switching ripples are ignored and the small-signal variations are modeled, where the frequency is much smaller than the switching frequency. Therefore, the average modeling combines fast simulation speed, and accurate modeling performance as the system dynamics are considered [225].

3.1 PV array ⁶

3.1.1 Theory and mathematical analysis

Figure 3.3 presents the equivalent circuit of the one-diode PV cell. It consists of a current source in parallel with diode and two resistors. There is also a more detailed model of PV modules, known as the two-diode model [226], [227]. The value of series resistance R_s is usually very small, with that of the shunt resistance R_p being very large [228].

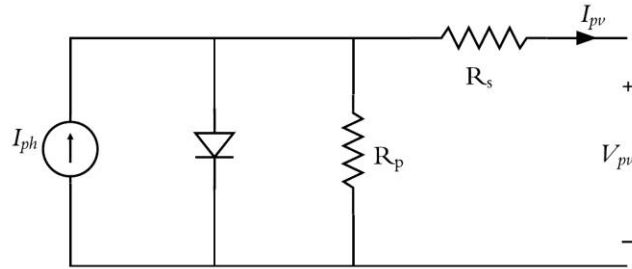


Figure 3.3: Equivalent circuit of the one-diode PV cell

The module photocurrent, I_{ph} , can be calculated by:

$$I_{ph} = [I_{sc} + K_i (T_c - T_{ref})] * \left(\frac{G}{G_{ref}}\right) \quad (1)$$

where I_{sc} is the short-circuit current [A], K_i is the temperature coefficient of the short-circuit current [A/K], T_c is the module temperature [K], G is the irradiation [W/m^2], $T_{ref} = 298$ K and $G_{ref} = 1000$ W/m^2 .

The reverse saturation current, I_o , is given by [226], [229]:

$$I_o = \frac{I_{sc} + K_i (T_c - T_{ref})}{e^{\left[\frac{q[V_{oc} + K_v(T_c - T_{ref})]}{N_s A k T_c}\right]} - 1} \quad (2)$$

where K_v is the temperature coefficient of the open-circuit voltage [V/K], $k = 1.381 \times 10^{-23}$ J/K is Boltzmann's constant and $q = 1.602 \times 10^{-19}$ C is the electron charge. The diode ideality factor A depends on the PV cell technology; e.g., for polycrystalline silicon cells $A = 1.3$ [230]. The number of cells in a module in series connection is presented with N_s .

⁶ Section 3.1 contains material from published papers [241], [314]

Using Kirchhoff's Current Law, the output current of the PV module, I_{pv} , is given by:

$$I_{pv} = I_{ph} - I_o \left(e^{\frac{q(V_{pv} + R_s I_{pv})}{N_s A k T_c}} - 1 \right) - \frac{V_{pv} + R_s I_{pv}}{R_p} \quad (3)$$

Some common graphs for PV modules are the P-V and I-V curves, as shown in Figure 3.4. The I-V curve results from equation (3), where the short-circuit current exists at zero output voltage and the open-circuit voltage exists at zero output current. Also, there is no generated power in short-circuit and open-circuit operation. A significant point on P-V curve is the maximum power point, P_{mp} , at a voltage V_{mp} and a current I_{mp} .

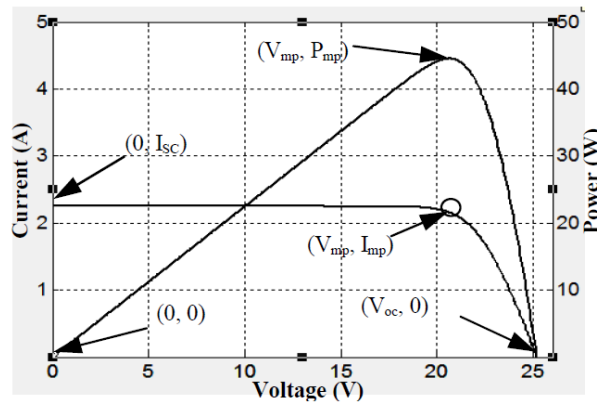


Figure 3.4: Output characteristics of a PV module [226]

- **Effects of Solar Irradiance variation**

Solar irradiance affects mostly the generated photocurrent and thus the output power. Less change is presented on open-circuit voltage. This is reasonable because photocurrent is proportional to the irradiance (Equation (1)). In other words, the increase of irradiance causes increase on both short-circuit current and output power [231]–[233].

- **Effects of Temperature variation**

Moreover, another significant factor for PV module operation is the temperature. A variation on temperature affects mostly the open-circuit voltage, and less the short-circuit current. An increase on temperature causes small increase on short-circuit current and decrease on both output power and open-circuit voltage [231]–[233].

3.1.2 Modeling and simulation

The studied model consists of 12 modules with a total power capacity of 3 kW_p (two parallel strings of six PV modules in series). The electrical characteristics are given in Table 3.1, some are taken from a manufacturer's datasheet [234] and the rest from [50] and [235]. The parameters are given under Standard Test Conditions (STC) with a module temperature of 298 K (25°C) and an irradiance of 1000 W/m².

Table 3.1: Electrical characteristics of photovoltaic module

Rated Power	250 W
Short-circuit current (I_{sc})	8.61 A
Open-circuit voltage (V_{oc})	37.41 V
Temperature coefficient of I_{sc} (K_i)	0.0032 A/K or A/°C
Temperature coefficient of V_{oc} (K_v)	-0.1230 V/K or V/°C
Series Resistance (R_s)	0.22 Ω
Shunt Resistance (R_p)	415 Ω
Number of cells in series (N_s)	60
Diode ideality factor (A)	1.3

The studied PV model takes as inputs the ambient temperature T_c on the module, the solar irradiance G , and the array voltage. The PV array subsystem encloses the PV module (Figure 3.5).

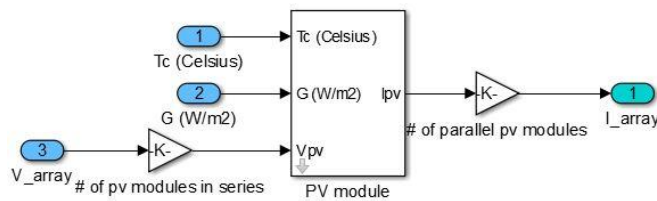


Figure 3.5: Inside the PV array subsystem

The output current of the PV module is calculated using equation (3), as shown in Figure 3.6. In order to calculate the PV module voltage, the array voltage is divided by the number of the modules in series connection (strings of 6 PV modules in series).

Moreover, the output current of the PV module is multiplied by the number of the modules connected in parallel (2 strings in parallel), in order to calculate the output PV array current.

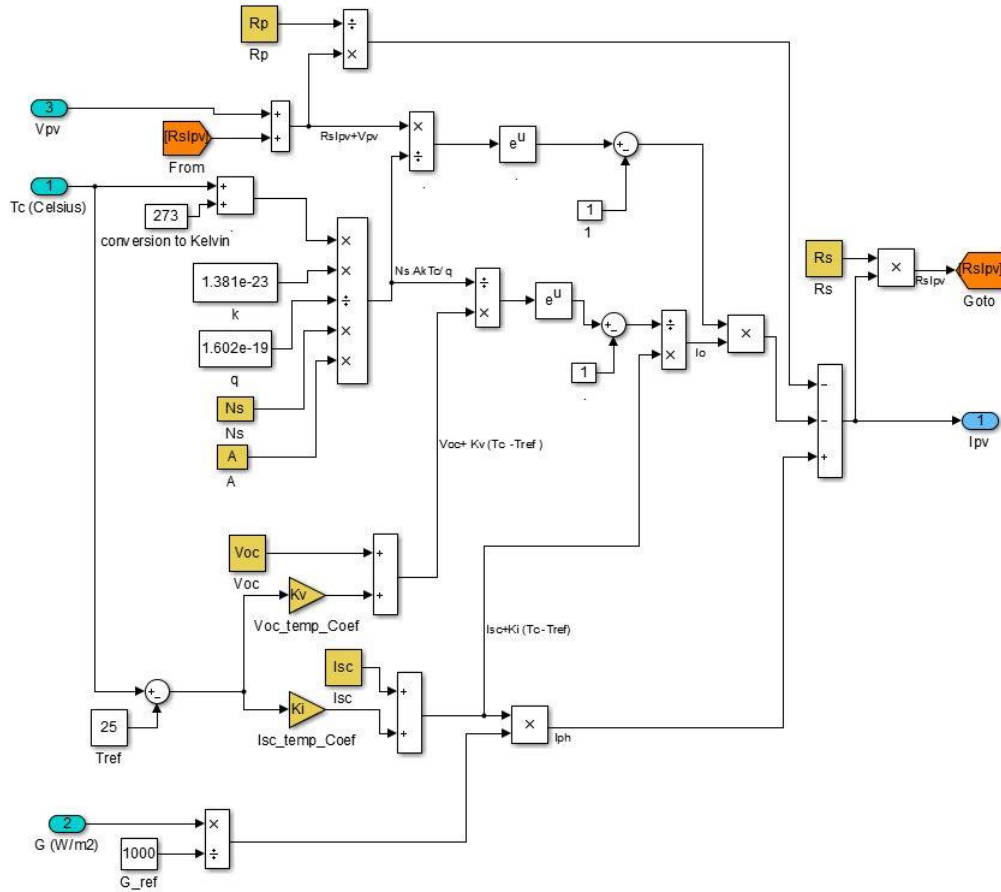


Figure 3.6: Calculation of output current of PV module I_{pv}

A preliminary simulation of the PV array subsystem is performed in order to verify that the model responds correctly to the changes in ambient temperature and solar irradiance. First, a constant ambient temperature of 25°C is applied and a variable solar irradiance of 1000 W/m², 800 W/m², 600 W/m², 400 W/m² and 200 W/m² is considered. The results are presented in Figure 3.7 and Figure 3.8. As expected, the change in solar irradiance affects mostly the generated PV current and therefore the output power. On the other hand, a relatively less impact is presented on the open-circuit voltage. A second simulation has been examined having a constant solar irradiance of 1000 W/m² and a fluctuating ambient temperature of 0°C, 25°C, 45°C and 60°C. As expected, the increase in temperature caused small increase in short-circuit current and decrease in both output

PV power and open-circuit voltage (see Figure 3.9 and Figure 3.10). The increase in solar irradiance causes increase in both short-circuit current and output power, while the increase in temperature causes a decrease in both output PV power and open-circuit voltage.

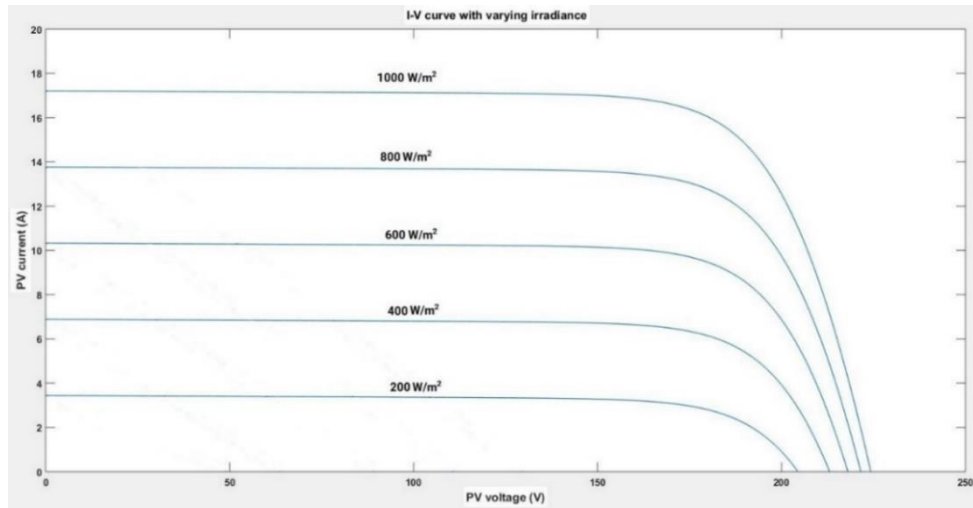


Figure 3.7: I-V curve with varying irradiance at 25°C

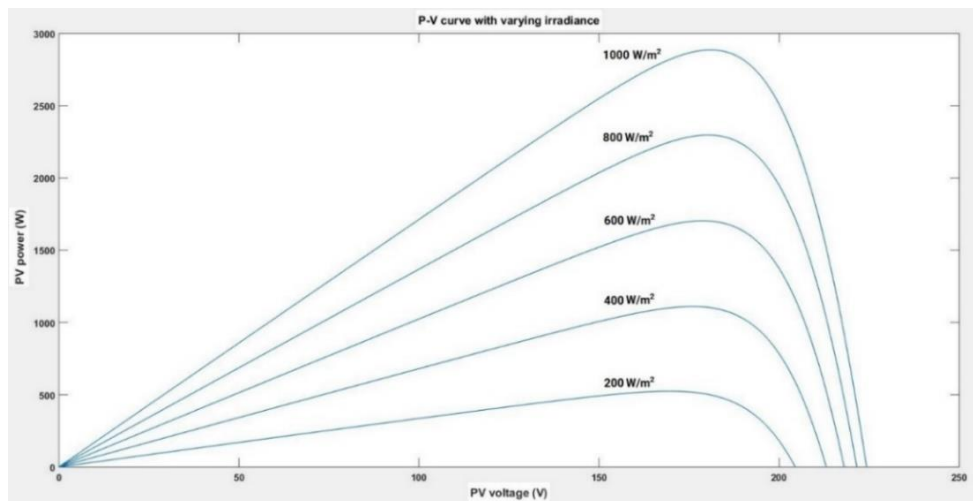


Figure 3.8: P-V curve with varying irradiance at 25°C

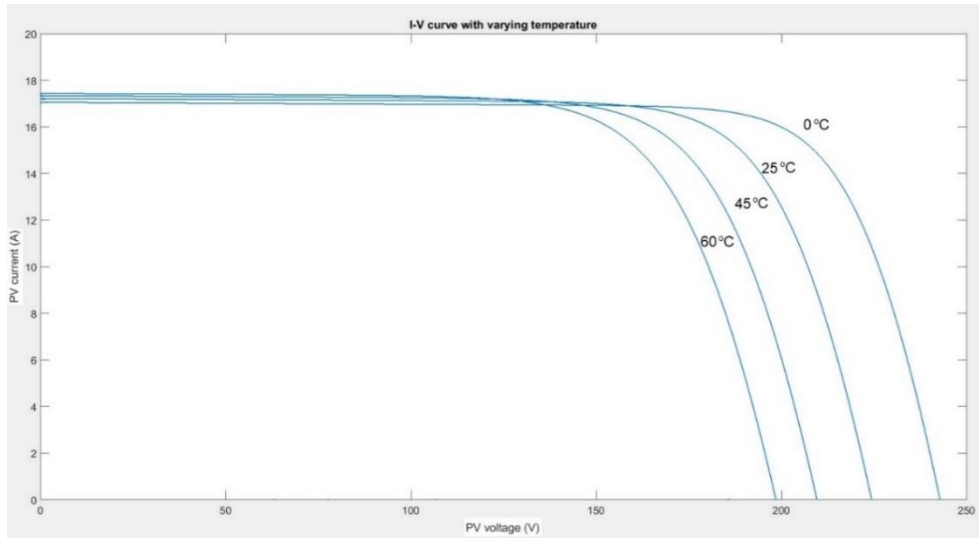


Figure 3.9: I-V curve with varying temperature at 1000 W/m^2

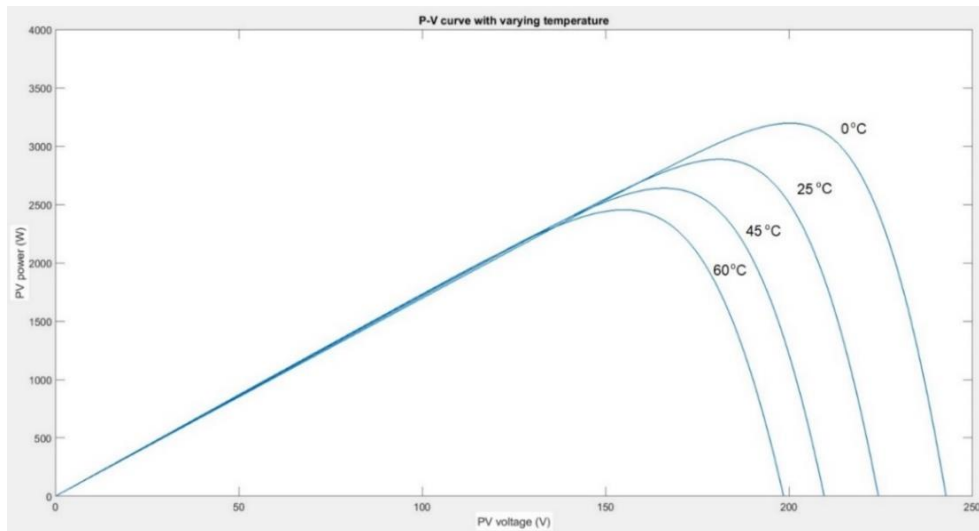


Figure 3.10: P-V curve with varying temperature at 1000 W/m^2

3.2 Maximum Power Point Tracking (MPPT) ⁷

3.2.1 Theory and mathematical analysis

Maximum Power Point Tracking (MPPT) techniques are very significant, as one can improve the efficiency of the PV model through them. There are many methods of

⁷ Section 3.2 contains material from published papers [241], [314]

MPPT, such as the Perturbation and Observation (P&O), the incremental conductance, the Fractional Open-Circuit Voltage, the Fractional Short-Circuit Current, the fuzzy logic control and the Ripple Correlation Control. All the above vary in complexity, cost, popularity, convergence speed, hardware requirements and efficiency levels [52], [236]–[239]. In this study, Perturbation and Observation (P&O), incremental conductance and fuzzy logic control are examined.

3.2.1.1 Perturbation and Observation (P&O)

Perturbation and Observation algorithm, also known as a hill climbing method, is one of the most commonly used methods due to its ease of implementation. As can be seen in Figure 3.11, the slope of the curve is zero at the maximum power point (MPP), positive on the left side of the MPP (increasing power region) and negative on the right side of the MPP (decreasing power region). Therefore, the following algorithm will be repeated and oscillated until the MPP is reached. The oscillation can be minimized by reducing the step-size of the perturbation, but this slows down the process reaching the MPP [238].

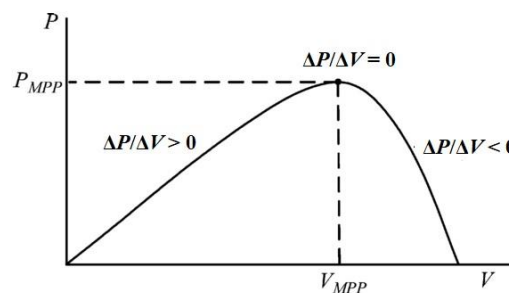


Figure 3.11: Characteristic P - V curve of a photovoltaic array

In Figure 3.12 there is a flowchart of our implementation based on the P&O algorithm. There are many modifications of the conventional P&O method. For instance, a variable step-size can be used instead of a fixed step for perturbation [239]. Also, the independent variable for perturbation can be the converter duty cycle [240] or the array current [241].

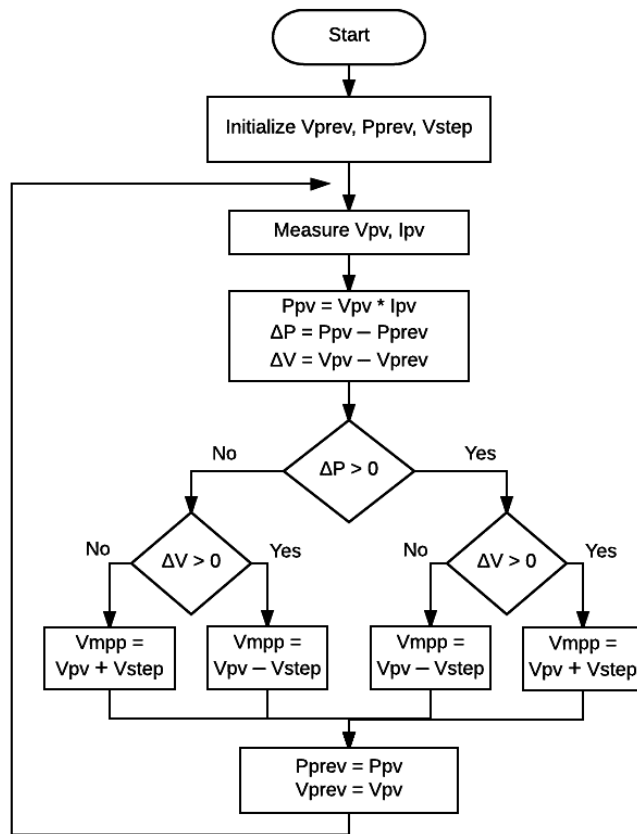


Figure 3.12: Flowchart of the P&O algorithm

3.2.1.2 Incremental Conductance

This technique is also considered as a hill climbing method. The MPP can be tracked by comparing the instantaneous conductance I/V to the incremental conductance $\Delta I/\Delta V$ (Figure 3.13).

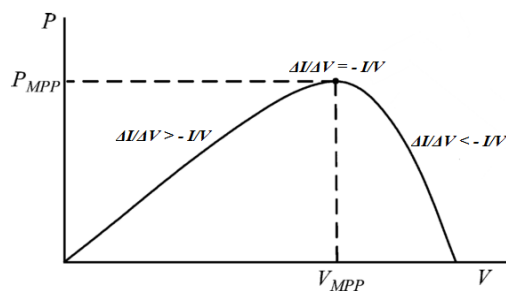


Figure 3.13: Characteristic P - V curve of a photovoltaic array

In other words, the solution of equation (4) is zero at the MPP, positive on the left side of the MPP and negative on the right side of the MPP.

$$\frac{dP}{dV} = \frac{d(IV)}{dV} = I + V \frac{dI}{dV} \cong I + V \frac{\Delta I}{\Delta V} \quad (4)$$

The flowchart of the incremental conductance algorithm is shown in Figure 3.14. The incremental conductance algorithm is as efficient and simple as the P&O algorithm. Additionally, a variable step-size can be used to improve the response time, accuracy and performance of the system, but the cost may be higher due to the increased complexity of the control system [242].

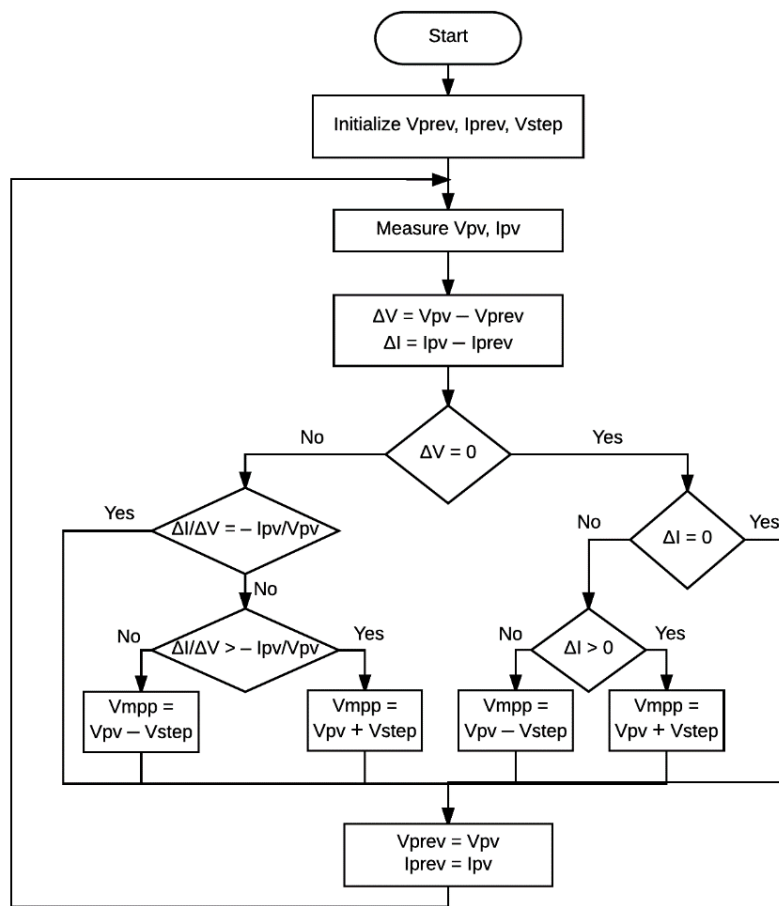


Figure 3.14: Flowchart of the Incremental Conductance algorithm

3.2.1.3 Fuzzy Logic

Fuzzy logic is one of the most sufficient control techniques for MPPT, which has attracted many researchers in the last years. Fuzzy Logic controllers do not need an

accurate mathematical model and can work with imprecise inputs. They have also the ability to handle nonlinear systems and control unstable systems [243].

The basic structure of any fuzzy logic controller is shown in Figure 3.15 and consists of the following stages: fuzzification, rule base and inference engine, and defuzzification. The studied model takes as inputs the change in the array voltage (ΔV_{pv}) and the change in the array power (ΔP_{pv}). The output of the controller is the variation of the array voltage (ΔV_{ref}). It must be noted that different fuzzy input and output variables can be used [244]. For example, P - V slope and variation of P - V slope are some of the most common inputs, while converter duty cycle is used more often for output variable [245].

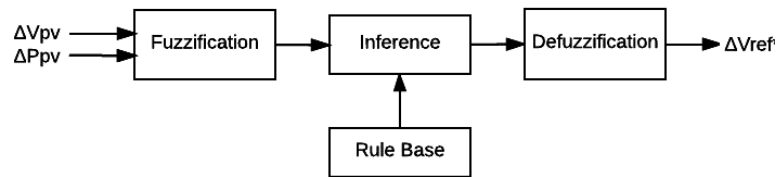


Figure 3.15: Fuzzy Logic controller diagram

In the fuzzification stage, numerical input variables are converted into linguistic variables, such as NB (Negative Big), NS (Negative Small), ZE (Zero), PS (Positive Small) and PB (Positive Big) using basic fuzzy subset [246]. Each of them is described by a triangular-shaped membership function (Figure 3.16). An alternative case may be also a Gaussian-shaped membership function [247]–[248].

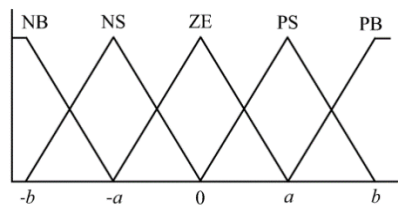


Figure 3.16: Membership function for inputs and output of fuzzy logic controller

The fuzzy inference engine processes the inputs according to the rules base table (Table 3.2) and produces the linguistic output. Figure 3.17 presents the nine regions according to the voltage and power variation, and it shows how the rules base table was filled. The basic concept was derived from hill climbing method. For example, regions 1 and 9

represent the case that the operating point is located on the left side of the MPP. Regions 2 and 8 correspond to zero change in power, while regions 4 and 6 show zero change in voltage. Moreover, regions 3 and 7 represent the case that the operating point is located on the right side of the MPP. Finally, in region 5 the power and voltage remain the same, so MPP is reached.

The defuzzification stage is used to convert the output linguistic variable back to numerical variable. The centroid method, which is the most prevalent one, is used for defuzzification. The resulting output ΔV_{ref} is then added to the previous value of voltage to get the new value of the array voltage. This value of voltage is going back as input to the PV array.

Table 3.2: Fuzzy logic rules base table

ΔP_{pv} \ ΔV_{pv}	NB	NS	ZE	PS	PB
NB	PS	PS	ZE	NS	NS
NS	PB	PS	ZE	NS	NB
ZE	NB	NS	ZE	PS	PB
PS	NB	NS	ZE	PS	PB
PB	NS	NS	ZE	PS	PS

↑ 1
↑ 2
↑ 3

↓ 7
↓ 4
↓ 8
↓ 5
↓ 9
↓ 6

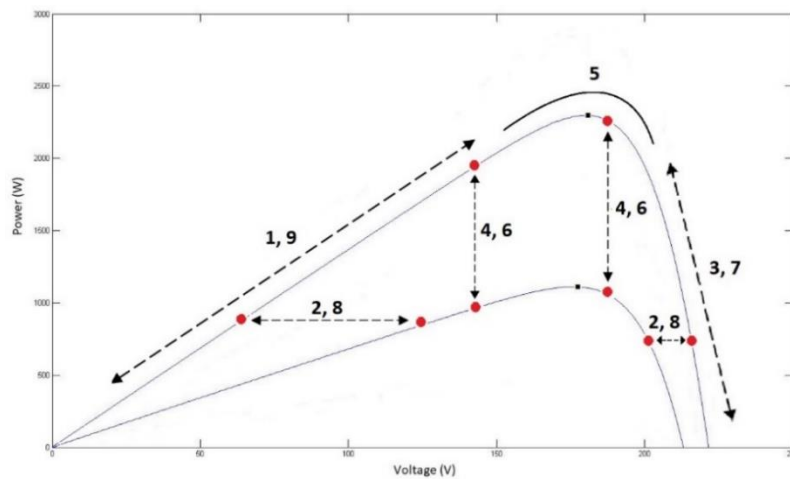


Figure 3.17: Characteristic P - V curve of a photovoltaic array, showing the nine regions according to voltage and power variation

3.2.2 Modeling and simulation

The P&O and incremental conductance algorithms are implemented in Simulink using a MATLAB code. The representation of the PV array model with the P&O algorithm is shown in Figure 3.18. The model representation in the case of the incremental conductance algorithm is similar with that of the P&O algorithm.

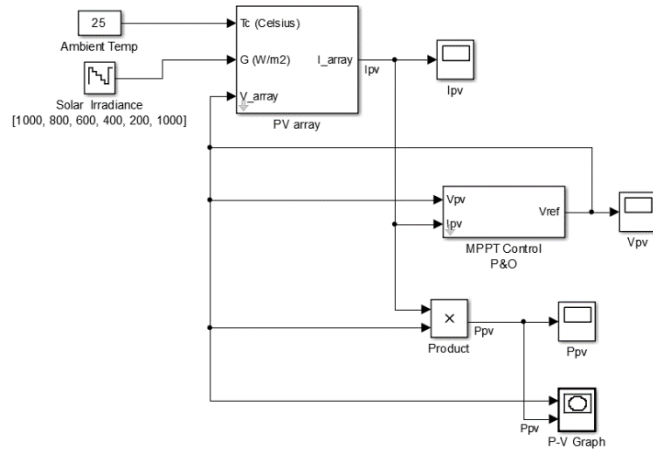


Figure 3.18: PV system with P&O control in Simulink

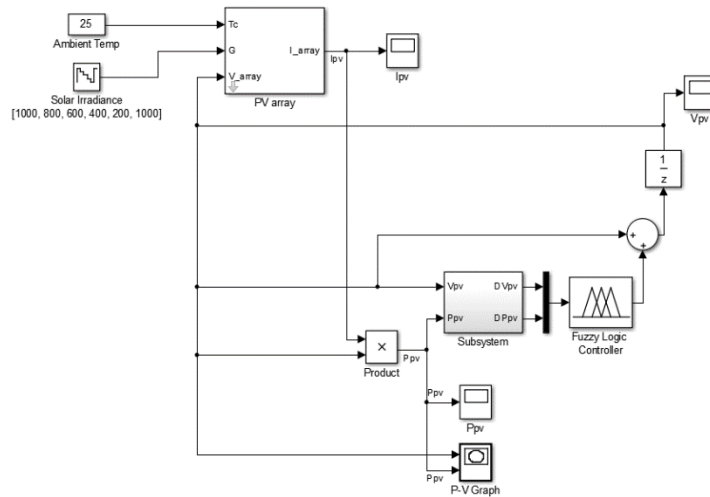


Figure 3.19: PV system with Fuzzy logic control in Simulink

Figure 3.19 shows the Simulink PV model for the case of the Fuzzy Logic control. Using the Fuzzy Logic Designer in MATLAB, membership functions (Figure 3.20) and relevant rules (Figure 3.21) are set. Finally, Figure 3.22 displays the output surface map of the system, which shows the dependency of the output (DV_{ref}^*) on the inputs (DV_{pv} , DP_{pv}) of the fuzzy logic controller.

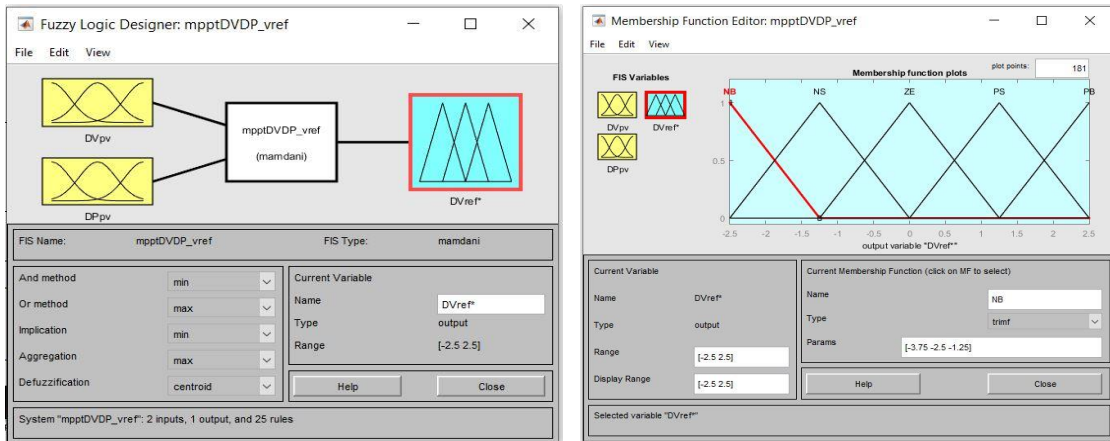


Figure 3.20: Fuzzy logic designer and membership function editor

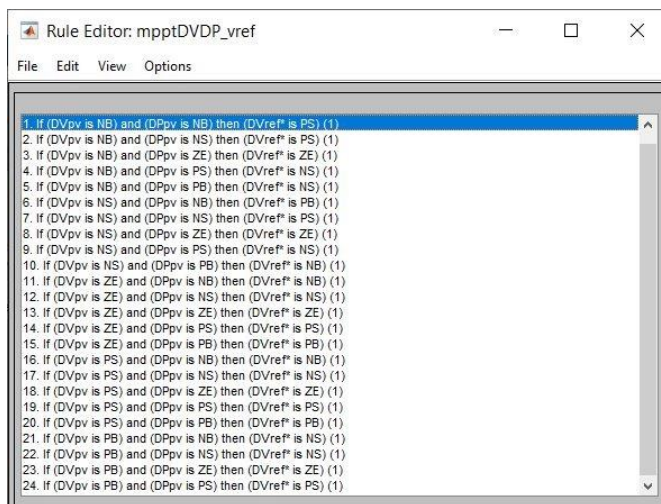


Figure 3.21: Fuzzy logic rule editor

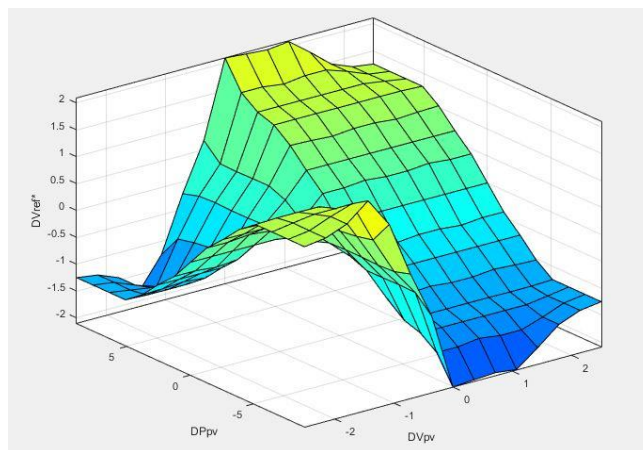


Figure 3.22: Surface viewer for the fuzzy logic controller

First, a simulation of the three MPPT methods is performed to check which method is the most accurate and responsive to irradiance variations. Solar irradiance level changes of 1000 W/m^2 , 800 W/m^2 , 600 W/m^2 , 400 W/m^2 , 200 W/m^2 and 1000 W/m^2 , with 0.1 seconds duration time of each level, are assumed. A constant temperature of 25°C is also considered. Although in reality the solar irradiance does not change as fast as in the simulation, fast weather variations are studied so as to observe graphically in a practical (comprehensive) scale the response time that each method needs to reach the MPP.

The PV voltage, current and power are shown in Figure 3.23, Figure 3.24 and Figure 3.25, respectively, for the three different studied MPPT techniques. Concerning the P&O algorithm, the corresponding voltage, current and power are reached in all cases, and there is an oscillation until the next change of irradiance. The oscillation is more obvious for the case of the voltage representation (Figure 3.23). The incremental conductance method has the same features and results with that of the P&O method. On the other hand, the fuzzy logic controller reacts much faster to variations of irradiance and no oscillations exist.

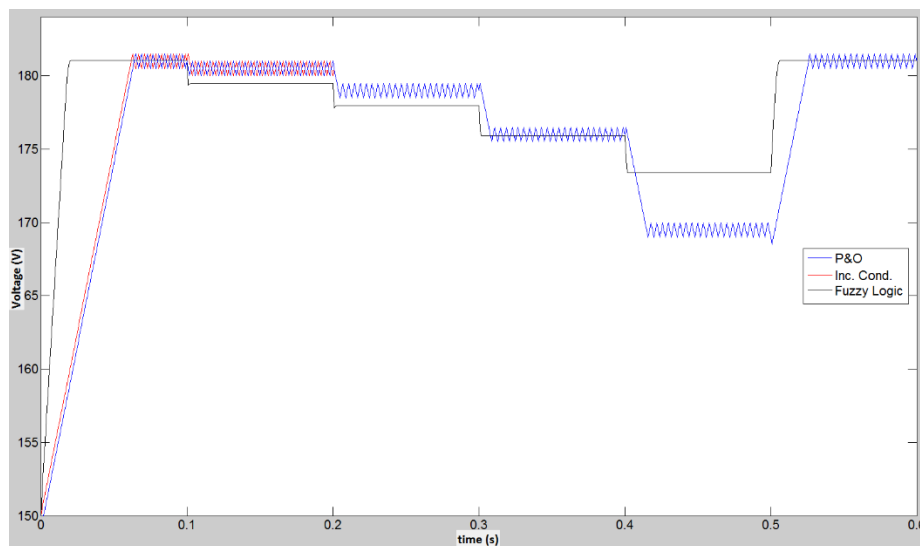


Figure 3.23: PV array voltage for P&O (blue), incremental conductance (red) and fuzzy logic (black) control

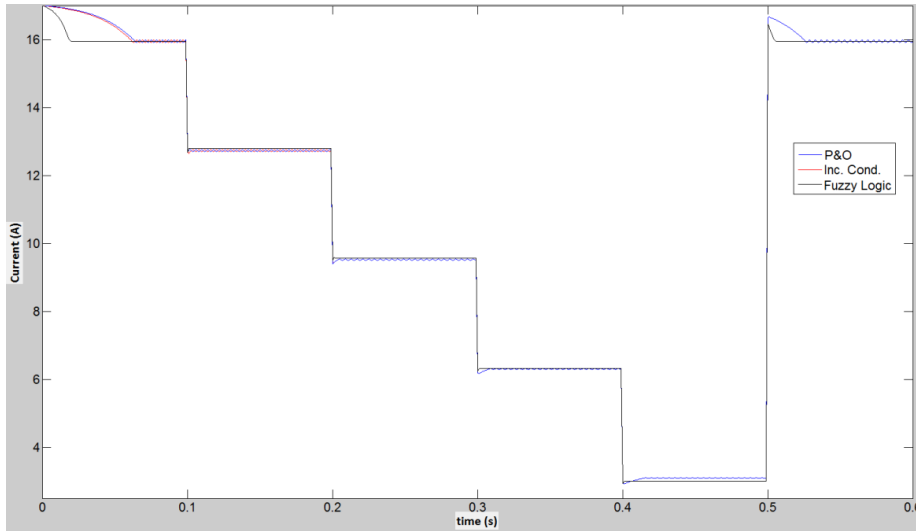


Figure 3.24: PV array current for P&O (blue), incremental conductance (red) and fuzzy logic (black) control

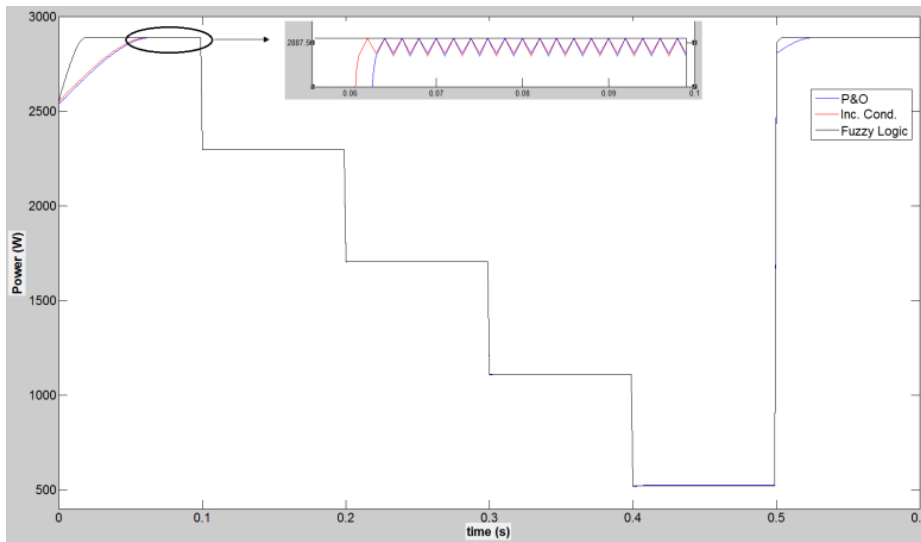


Figure 3.25: PV array power for P&O (blue), incremental conductance (red) and fuzzy logic (black) control

Table 3.3 includes several simulation results regarding the transition of the solar irradiance from 200 W/m^2 to 1000 W/m^2 at $t = 0.5 \text{ s}$. One can notice that the fuzzy logic method exhibits certain advantages over the P&O and incremental conductance methods. Specifically, P&O and incremental conductance methods can reach the MPP after 98 ms while fuzzy logic control tracks the MPP after 8 ms. Also, fuzzy logic method presents

no oscillations at the steady state period and can track the system to higher power values than the other two methods, leading to higher performance and efficiency.

Regarding the parameters for P&O and incremental conductance method, the step voltage (V_{step}) is defined to be 0.5 V. The step-size in these methods must be increased so that their corresponding tracking speed matches that of the fuzzy logic method. For the case of the transition of the solar irradiance from 200 W/m² to 1000 W/m² (see Table 3.3), the voltage step-size must be increased to 1.5 V to reach the tracking time of 8 ms. However, the use of this large step-size would result into increased oscillation and limited accuracy and efficiency of the model.

The results show that the hill climbing methods, namely the P&O and incremental conductance, may fail under rapidly changing climatic conditions. On the other hand, Fuzzy Logic control can track the system to the MPP very fast and accurately, even during rapid variations of atmospheric conditions. Moreover, the P&O and incremental conductance algorithms present small oscillations around the MPP at the steady state period, thus energy losses appear. If a smaller perturbation size is used, then the MPP will be reached more slowly.

Table 3.3: Comparison table of studied MPPT methods

	P&O	Incremental Conductance	Fuzzy Logic
P_{MPP}	2886.95 W	2886.95 W	2887.55 W
V_{MPP}	181 V	181 V	181.06 V
I_{MPP}	15.95 A	15.95 A	15.948 A
Tracking time	98 ms	98 ms	8 ms

Although P&O has limitations on convergence time and oscillations, it remains the most simple and commonly used method for MPPT, as it does not require special hardware requirements. Also, its accuracy and efficiency are very satisfactory. Furthermore, incremental conductance has increased hardware requirements compared to the P&O algorithm. Concluding, fuzzy logic has more advantages with regard to the desired MPPT

goals than the other two methods, although exhibiting drawbacks with regard to cost requirements and implementation complexity.

For the present study, the P&O algorithm is chosen due to its simplicity and the acceptable range of response, as in real conditions the variations in solar irradiance are much slower than the convergence time of the P&O algorithm. A final simulation for the P&O method is performed. In the following three figures the representation of the P-V, P-I and I-V curves is given respectively. The curves derived by the P&O algorithm are represented by solid lines, where one can observe that the MPP is efficiently reached in all cases.

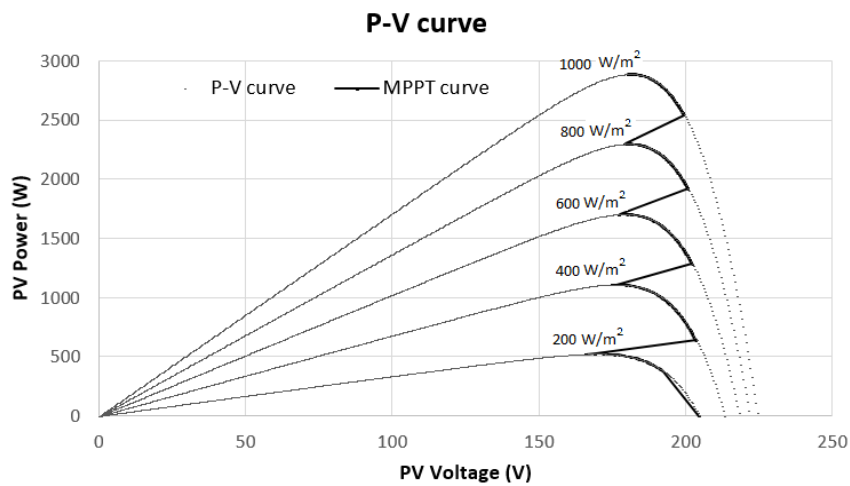


Figure 3.26: P-V curve (dashed line) and MPPT P-V curve (solid line) for different values of irradiance

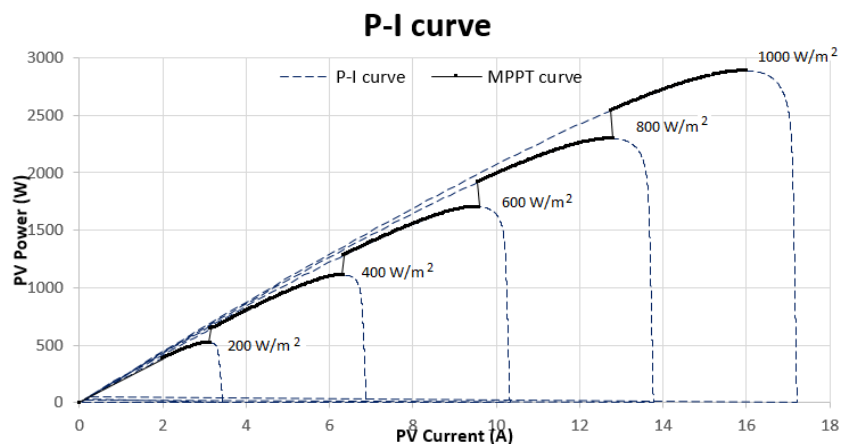


Figure 3.27: P-I curve (dashed line) and MPPT P-I curve (solid line) for different values of irradiance

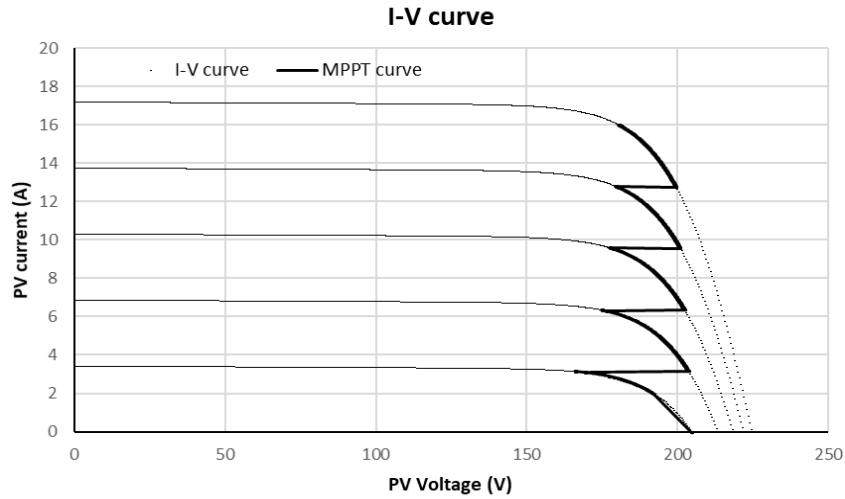


Figure 3.28: I-V curve (dashed line) and MPPT I-V curve (solid line) for different values of irradiance

3.3 DC-DC Boost Converter ⁸

3.3.1 Theory and mathematical analysis

A DC-DC boost converter is important to our system, since the input voltage of the DC-AC inverter must be always greater than the grid peak voltage and balanced at 400 V. The maximum voltage that the studied PV array can reach is about 230 V. Therefore, the boost converter is essential for providing the MPP for the operation of the PV system and maintaining a constant voltage at the output of the converter, greater than the grid peak voltage of 325 V.

The studied electrical circuit of the DC-DC boost converter is given in Figure 3.29. A continuous conduction mode (CCM) of operation is assumed. The duty cycle D represents the time that the switch S_1 is ON, while D' ($D' = 1 - D$) corresponds to the time that the switch is OFF.

⁸ Section 3.3 contains material from published paper [241]

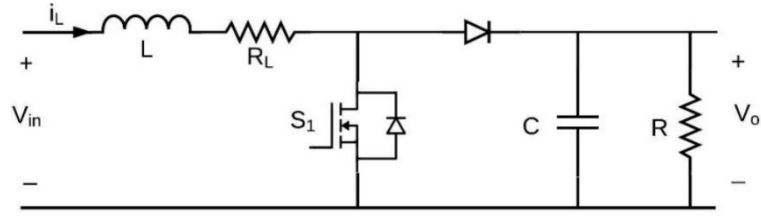


Figure 3.29: Circuit of a DC-DC boost converter

Implementing an averaged model of the converter, it is better to consider switching losses and conduction losses, in order to have a more accurate model. The switching loss current parameter, I_{sw} , describes the current loss during ON/OFF transitions, due to the high switching frequency. During the switching ON/OFF transitions, very large instantaneous power loss can occur in the semiconductor device (e.g., MOSFET). Although the duration of the switching times is short, the resulting average power loss can be significant. Switching losses are proportional to the switching frequency, and not strongly dependent on output power [224], [249].

In addition, conduction loss appears due to voltage drop across inductor winding resistance and across power semiconductor switches when are ON. In practice, inductors exhibit power loss due to copper loss (wire resistance) and due to core loss (hysteresis and eddy current losses in the magnetic core). In this model, R_L corresponds to the inductor winding resistance, which is connected in series with the inductor. Conduction losses depend strongly on the output power [224], [249].

Taking into consideration the above losses, the steady-state equations between the duty cycle (D) and the output voltage (V_o) and inductor current (I_L) are given by:

$$V_o = \frac{V_{in} - I_L R_L}{D'} \quad (5)$$

$$I_L = \frac{I_o + I_{sw}}{D'} \quad (6)$$

Thus, the equations regarding the inductor current and the output voltage of the converter are derived as follows [218], [250]–[253].

$$\frac{dI_L}{dt} = \frac{1}{L} (V_{in} - I_L R_L - V_o D') \quad (7)$$

$$\frac{dV_o}{dt} = \frac{1}{C} (I_L D' - \frac{V_o}{R} - I_{sw}) \quad (8)$$

3.3.2 Modeling and simulation

The Simulink averaged model of the DC-DC boost converter is shown in Figure 3.30. The input parameters of the model are the inductor current and the input voltage of the PV array ($V_{in} = V_{pv}$), where both variables are locked on the MPP of operation. Also, the output voltage ($V_o = V_{dc}$) is considered as known parameter because the voltage control on the common DC-bus is analysed in sub-Sections 3.8.2 and 3.8.3.

For this study, the inductor winding resistance, R_L , is 50 m Ω , and the switching loss current, I_{sw} , is 10 mA.

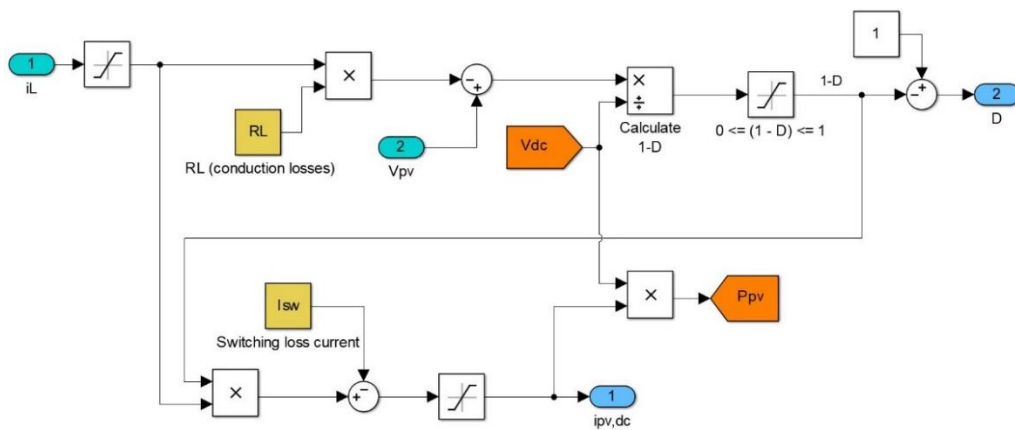


Figure 3.30: Averaged model of DC-DC boost converter

3.4 Battery storage⁹

3.4.1 Theory and mathematical analysis

Battery packs include battery modules, with each battery module containing several battery cells in series, parallel, or series and parallel configuration. Battery cells are connected in series to achieve higher pack voltage, while parallel cells connection is used to achieve higher current and power capability and consequently higher pack capacity [254]. In order to create a battery pack, it is essential to analyse and model the battery cell. There is a variety of different battery models to use [255]. Four commonly used models regarding the equivalent circuit of the battery cell are:

⁹ Section 3.4 contains material from published paper [211]

- (i) The ideal model is the simplest model with a voltage source only, in which all the internal parameters are ignored.
- (ii) The linear model consists of an ideal battery with an open-circuit voltage and an equivalent series resistance. However, this model ignores the varying characteristics of the battery's internal impedance with the varying state-of-charge (SOC) and electrolyte concentration.
- (iii) The Thevenin equivalent model consists of an open-circuit voltage V_{oc} , an internal resistance R_s , a capacitance C_p and an overvoltage resistance R_p [256].
- (iv) The dual polarization model (2nd-order RC model) is an improvement of Thevenin's equivalent model that was proposed by Chen et al. [257]. It contains an open-circuit voltage V_{oc} , an internal resistance R_s and two RC networks, as shown in Figure 3.31. The RC circuits correspond to the internal charge distribution of the battery, while the series resistance R_s represents the internal losses of the battery. The open circuit voltage V_{oc} is the internal voltage of the battery and depends on the SOC [26]. The left-hand circuit in Figure 3.31 is designed to track the SOC of the battery. The studied dual polarization model comprises both steady state and transient response behavior.

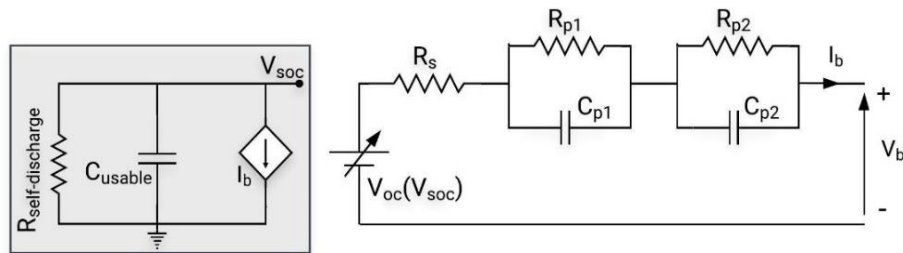


Figure 3.31: Dual polarization battery cell circuit

Figure 3.32 contains all the typical characteristic curves of the battery in which battery parameters can be calculated. The calculation of all battery parameters is presented and analyzed in the following sub-Sections 3.4.1.1 – 3.4.1.5.

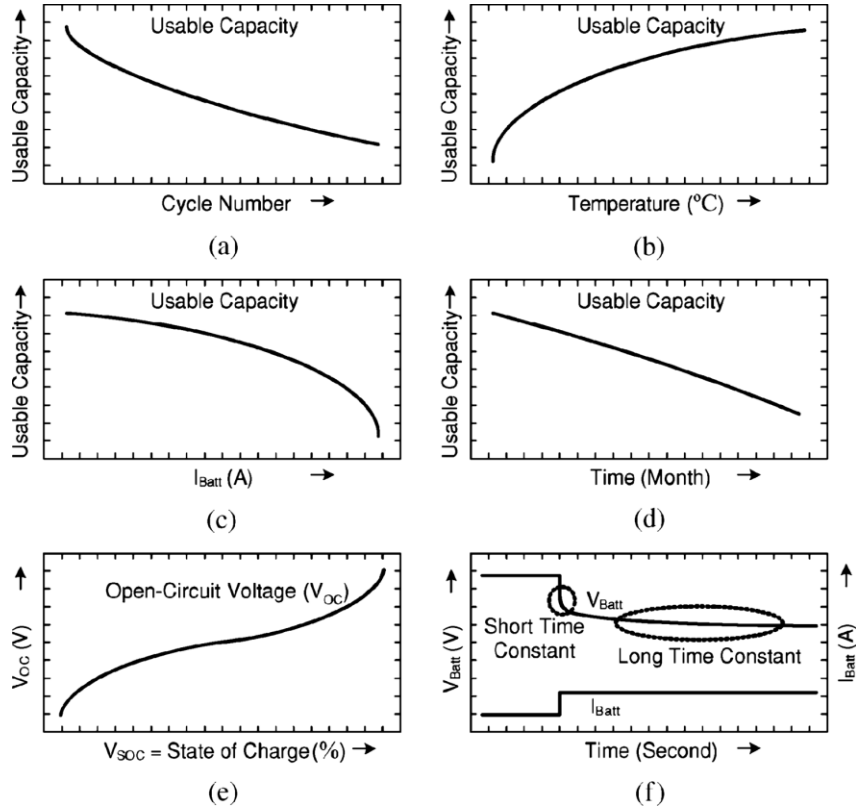


Figure 3.32: Battery characteristic curves of usable capacity with respect to: (a) cycle number, (b) temperature, (c) battery current, (d) storage time, as well as (e) open-circuit voltage V_{oc} versus SOC, and (f) transient response to a step load current event [257]

3.4.1.1 Usable capacity calculation

The usable capacity of the battery (C_{usable} in Coulombs) represents the charge that a battery can store. Specifically, it is the nominal battery capacity in Ah (C_{init}) multiplied by cycle number-dependent correction factor ($f_1(N)$, see Figure 3.32(a)) and temperature-dependent correction factor ($f_2(T)$, see Figure 3.32(b)) [257].

$$C_{usable} = 3600 \cdot C_{init} \cdot f_1(N) \cdot f_2(T) \quad (9)$$

For simplicity, usable capacity is assumed not to be affected so much from the temperature, and therefore $f_2(T)$ can be set to 1. Regarding the capacity fading because of the battery cycle number, the cycle number-dependent correction factor $f_1(N)$ can be calculated as below:

$$f_1(N) = 1 - (k_1 \sqrt{N}) \quad (10)$$

where N is the cycle number and $k_1 = 4.5 \times 10^{-3}$ [258].

As can be seen from expression (9), the usable capacity does not depend on current variation. The current dependence of usable capacity shown in Figure 3.32(c), presents the variation of capacity for different SOC values at the end of discharge time for different battery currents. During the charge or discharge event, a current-controlled current source I_b can charge or discharge the capacitor (C_{usable}), and therefore the V_{soc} changes dynamically, as shown on the left circuit of Figure 3.31. The resistor $R_{self-discharge}$ represents the energy losses when the battery is left unused for a long time, which is usually ignored for a lithium-ion battery. Finally, usable capacity is decreased with time when no load is connected to the battery, as shown in Figure 3.32(d) [257].

3.4.1.2 *Voc and SOC_b calculation*

The SOC of the battery is the ratio of its current capacity to its nominal capacity. The nominal capacity is the maximum amount of charge that a battery can store. The relationship between V_{oc} and SOC is shown in Figure 3.32(e). A third-order polynomial relationship between V_{oc} and SOC is presented below:

$$V_{oc}(SOC_b) = a_0 + a_1 \cdot SOC_b + a_2 \cdot SOC_b^2 + a_3 \cdot SOC_b^3 \quad (11)$$

where a_0 , a_1 , a_2 and a_3 are constant values. For instance, the parameters of the Panasonic NCR18650PF lithium-ion battery cell, examined and tested in [259], are used: $a_0 = 3.2416$, $a_1 = 1.3905$, $a_2 = -1.3781$ and $a_3 = 0.9206$. Moreover, the SOC_b equation during charging/discharging is expressed by [260], [261]:

$$SOC_b = SOC_{b,0} - \frac{1}{C_{usable}} \int I_b dt \quad (12)$$

where $SOC_{b,0}$ is the initial SOC of the battery ($0 \leq SOC_b \leq 1$), and I_b is the battery current which is assumed positive during discharging and negative during charging.

3.4.1.3 *Transient response*

When a step load current is presented, the battery voltage reacts slowly with time (Figure 3.32(f)). The two RC networks in Figure 3.31 are responsible for the transient response. Specifically, series resistance R_s is responsible for the instantaneous drop of the voltage, while the two RC networks are responsible for the following short-time and long-time transient response, as they are circled in the Figure 3.32(f) [257].

3.4.1.4 RC calculation

The values of R_s , R_{p1} , R_{p2} , C_{p1} and C_{p2} depend on the battery current and SOC. Nonlinear curves behavior can be used as depicted by [257]. The following general functions correspond to the RC parameters related to SOC:

$$R_s = b_0 e^{-b_1 \cdot SOC_b} + b_2 \quad (13)$$

$$R_{p1} = c_0 e^{-c_1 \cdot SOC_b} + c_2 \quad (14)$$

$$C_{p1} = d_0 e^{-d_1 \cdot SOC_b} + d_2 \quad (15)$$

$$R_{p2} = g_0 e^{-g_1 \cdot SOC_b} + g_2 \quad (16)$$

$$C_{p2} = h_0 e^{-h_1 \cdot SOC_b} + h_2 \quad (17)$$

where b_i , c_i , d_i , g_i , h_i ($i = 0, 1, 2$) are constant values. The RC parameters can be calculated in Simulink using a look-up table based on their variations behavior using the SOC_b as input. It is observed that when the SOC is 20–100%, these parameters remain almost constant. Therefore, for simplicity these parameters are assumed to remain constant with SOC, where the following values are used [259]: $R_s = 0.0314 \Omega$, $R_{p1} = 0.0181 \Omega$, $C_{p1} = 1712 \text{ F}$, $R_{p2} = 0.0281 \Omega$ and $C_{p2} = 55257 \text{ F}$.

3.4.1.5 Voltage drop on RC networks

Additionally, each RC network has a voltage drop V_{pi} expressed by:

$$\frac{dV_{pi}}{dt} = \frac{I_b}{C_{pi}} - \frac{V_{pi}}{R_{pi}C_{pi}} \quad (18)$$

where $i = 1, 2$ correspond to the first and second RC network respectively [262]. Therefore, the battery voltage V_b is calculated as follows:

$$V_b = V_{oc} - V_{p1} - V_{p2} - I_b R_s \quad (19)$$

3.4.2 Modeling and simulation

Based on the above analysis of the lithium-ion battery cell, the Simulink model is shown in Figure 3.33. The model is based on the behavior of the 2nd-order RC battery cell model. The battery parameters are taken from [259], in which a Panasonic NCR18650PF lithium-ion battery cell was tested. The studied battery has a nominal

capacity of 2900 mAh and a nominal voltage of 3.6 V. The calculation of capacity fading due to the charge/discharge cycle number of the battery is based on equations (9)–(10).

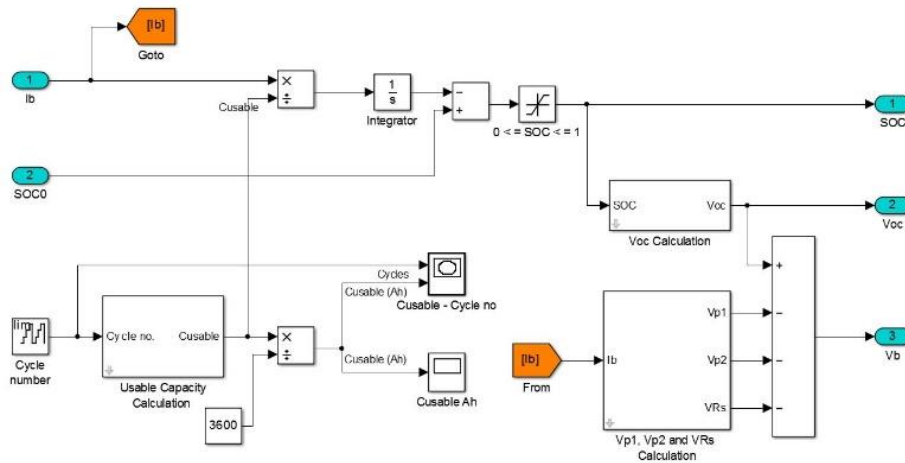


Figure 3.33: Battery cell 2nd-order RC model

Additionally, Figure 3.34 presents the calculation of series voltage and RC parallel networks voltages, based on equation (18). Finally, the subsystem of the V_{oc} calculation in Figure 3.33 contains a third-order polynomial evaluation block based on expression (11).

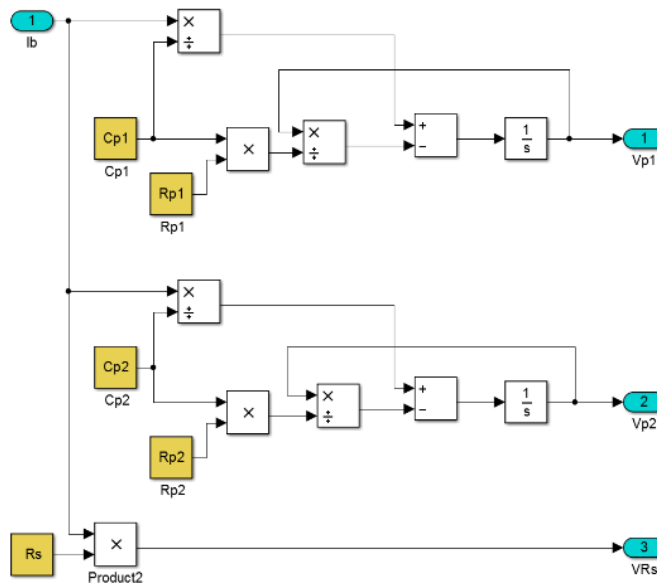


Figure 3.34: Subsystem calculation of series voltage and RC parallel networks voltages

The following results were obtained based on the Simulink battery model of Figure 3.33 [211]. The relationship between V_{oc} and SOC is presented in Figure 3.35, in which the form is similar to Figure 3.32(e) and corresponds to the third-order polynomial in equation (11).

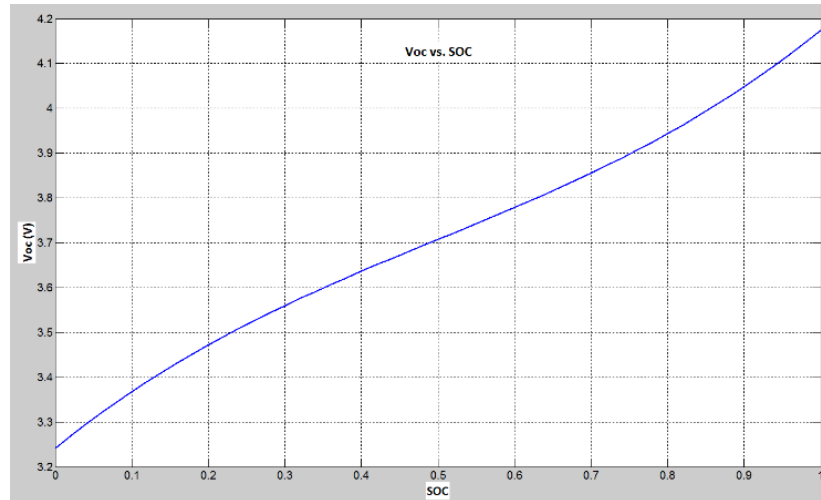


Figure 3.35: Varying curve of V_{oc} with SOC

To verify that the model responds to charge and discharge events, a pulse discharge current of 1.5 A (0.5C) is set (Figure 3.36), assuming that the battery is initially fully charged ($SOC_0 = 1$). As can be seen from Figure 3.37, at the end of discharge period, the battery is not fully discharged ($SOC = 0.38$). Also, at that moment the battery voltage is about 3.52 V (Figure 3.38). Moreover, during the resting period the battery voltage curve (Figure 3.38) contains a linear part and an exponential part. The linear part corresponds to the behavior of the battery due to the internal resistance R_s , while the exponential part shows the dynamic behavior of the battery (RC networks). Regarding the capacity fading due to ageing effect, Figure 3.39 represents the decreasing of the usable capacity because of the increase in the cycle number of the battery. The decreasing effect has a similar shape with that of Figure 3.32(a) and also complies with that of the manufacturer's datasheet.

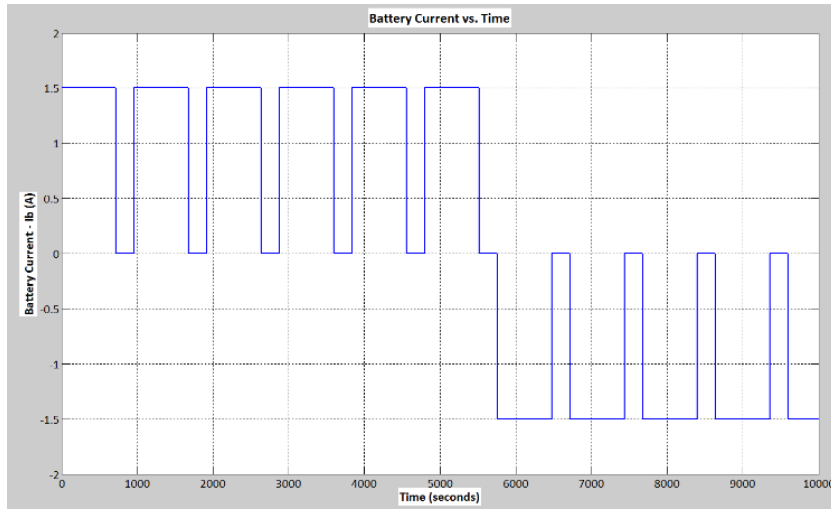


Figure 3.36: Battery pulse discharging/charging current with time

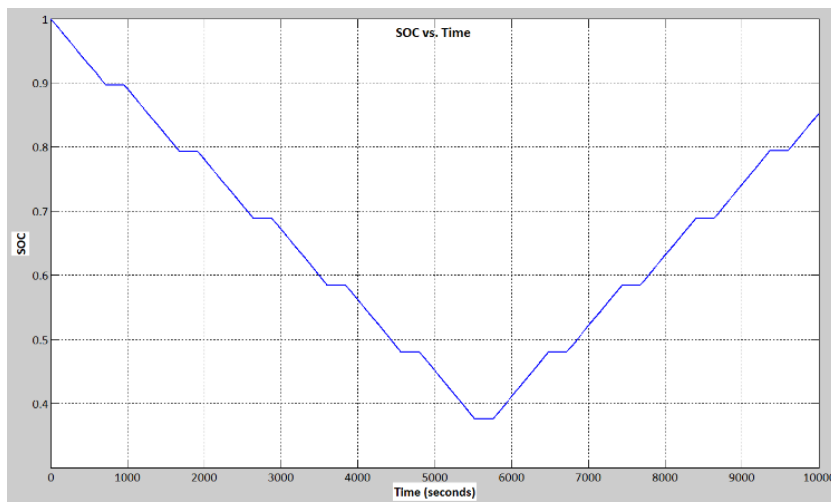


Figure 3.37: Battery SOC with time

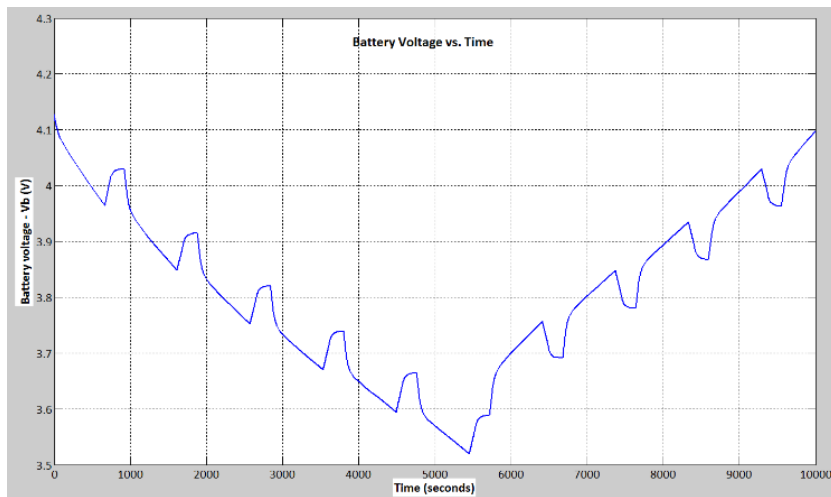


Figure 3.38: Battery voltage during discharging/charging with time

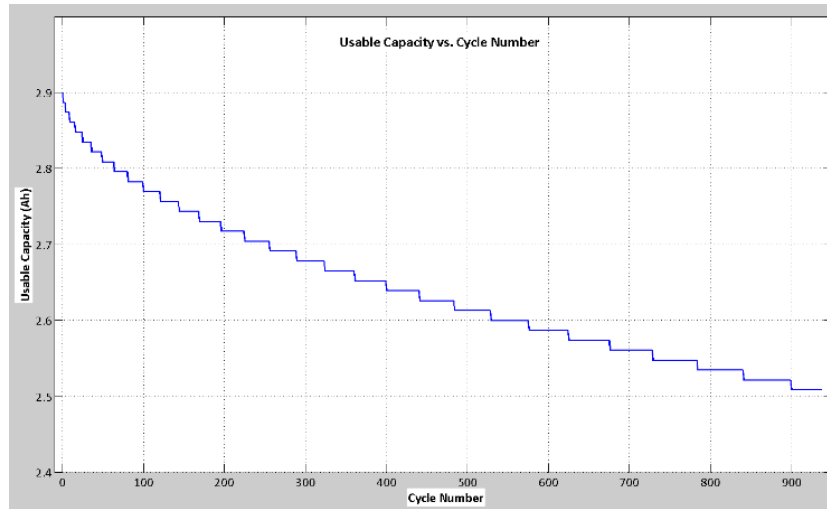


Figure 3.39: Usable Capacity vs. cycle number

3.4.3 Battery pack sizing

In order to define the appropriate size of the battery storage system in a grid-connected building with PV system, the average electricity consumption of a typical household is assessed. Typically, an energy efficient household has an average electricity consumption of about 4000 kWh/year, or about 11 kWh/day. Moreover, several factors are considered, such as storage capacity for good matching between generation and consumption (60% of average daily consumption), minimum battery SOC to avoid battery degradation (20–30%) and battery efficiency (90%). Considering all the above, a battery storage capacity of about 9.5–10.5 kWh was shown to be sufficient for covering the needs of such residential applications [26].

In this study a 10 kWh battery pack is chosen, consisting of 69 parallel strings of 14 cells placed in series formation (see Figure 3.40). Each cell has a nominal capacity of 2.9 Ah and a nominal voltage of 3.6 V. Therefore, a 10 kWh battery pack with a nominal capacity of 200 Ah and a nominal voltage of 51.2 V is considered. Similar batteries exist in industry for residential applications [263], [264].

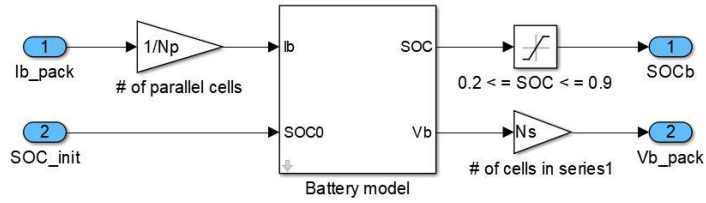


Figure 3.40: Battery pack subsystem in Simulink

3.5 Supercapacitor Storage ¹⁰

3.5.1 Theory and mathematical analysis

Supercapacitors have low cell voltage resistance between their terminals (up to 3 V) and hence they are built up with modules of single cells connected in series or in a combination of series and parallel connections [64]. The circuit of the supercapacitor cell is shown in Figure 3.41, where the two branches model that consists of the main branch and the slow branch, is examined [27].

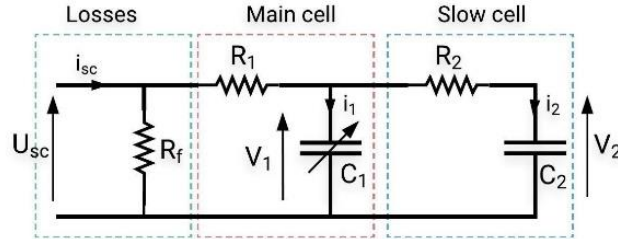


Figure 3.41: Two branches equivalent circuit of a supercapacitor cell

The main branch corresponds to the immediate response of the supercapacitor during the charge or discharge event in the time range of seconds. In the main branch, R_1 is the series resistance and represents the waste power for internal heating on charging and discharging (m Ω). The capacitor C_1 depends on the voltage V_1 as expressed in equation (20), where C_0 is the constant capacitance in Farads (F) and C_v is the constant parameter (F/V) [161], [265].

$$C_1 = C_0 + C_v V_1 \quad (20)$$

¹⁰ Section 3.5 contains material from published paper [211]

The slow branch determines the internal energy distribution at the end of the charge or discharge cycle in the time range of minutes. The parallel resistance R_f describes the leakage current when the supercapacitor is in standby mode ($k\Omega \times 10^2$). This self-discharge property can be neglected for fast charge and discharge cycles [266]. Equation (21) represents the voltage V_{sc} of the supercapacitor pack,

$$V_{sc} = N_s U_{sc} = N_s \left(V_1 + R_1 \frac{I_{sc}}{N_p} \right) \quad (21)$$

where N_s and N_p are the number of supercapacitor cells in series and parallel connection, respectively. Also, U_{sc} is the cell voltage and I_{sc} is the current of the supercapacitor pack. Concerning the slow cell, the voltage V_2 can be expressed by [28]:

$$V_2 = \frac{1}{C_2} \int i_2 dt = \frac{1}{C_2} \int \frac{1}{R_2} (V_1 - V_2) dt \quad (22)$$

The voltage V_1 across the capacitor C_1 on the main cell is given by:

$$V_1 = \frac{-C_0 + \sqrt{C_0^2 + 2C_v Q_1}}{C_v} \quad (23)$$

where Q_1 is the instantaneous charge of C_1 and can be calculated by:

$$Q_1 = C_0 V_1 + \frac{1}{2} C_v V_1^2 \quad (24)$$

A useful indicator of the level of charge stored into the supercapacitor is the SOC. The easiest method to calculate the SOC of the supercapacitor is based on the ampere-hour equation:

$$SOC_{sc} = SOC_{sc,0} - \frac{1}{3600 C_{sc,Ah}} \int I_{sc} dt \quad (25)$$

Where $SOC_{sc,0}$ is the initial SOC of the supercapacitor, $C_{sc,Ah}$ is the capacity of the supercapacitor in Ah, which can be calculated by [267]:

$$C_{sc,Ah} = \frac{C_{sc} V_{max}}{3600} \quad (26)$$

where C_{sc} is the rated capacitance of the supercapacitor in Farads, and V_{max} is the maximum voltage of the supercapacitor (i.e., the rated voltage).

3.5.2 Modeling and simulation

Regarding this study, all electrical parameters of the supercapacitor cell (Maxwell BCAP3000) are given as $R_1 = 0.29 \text{ m}\Omega$, $C_0 = 2100 \text{ F}$, $C_v = 623 \text{ F/V}$, $R_2 = 1.92 \text{ }\Omega$ and $C_2 = 172 \text{ F}$ [161]. The supercapacitor has a rated voltage of 2.7 V and a rated capacitance of 3000 F . Therefore, its capacity is 2.25 Ah (see equation (26)).

The supercapacitor cell model in Simulink is presented in Figure 3.42, where $N_s = N_p = 1$. Note here that the supercapacitor current, I_{sc} , is assumed to be positive during discharging and negative during charging.

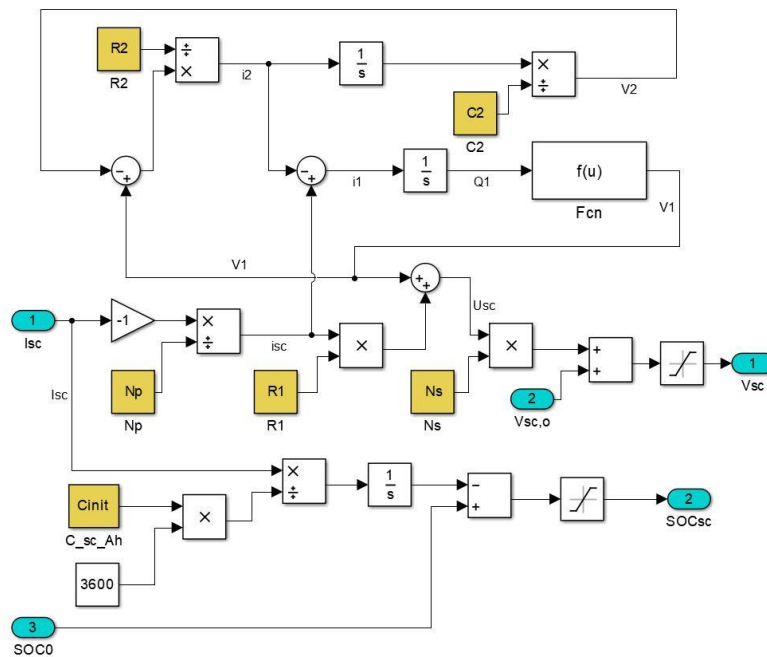


Figure 3.42: Simulink model of supercapacitor pack

The simulation results of the supercapacitor model are shown in Figure 3.43, Figure 3.44 and Figure 3.45, based on the Simulink model of Figure 3.42. Firstly, a constant current of -200 A charges the supercapacitor for about 40 s until it reaches the rated voltage. During the period of $55\text{--}70 \text{ s}$, the supercapacitor is at rest ($I_{sc} = 0 \text{ A}$). After that, a constant current of 200 A discharges totally the supercapacitor. At the beginning of discharging, an initial slight voltage drop of 59 mV is observed. This happens due to the internal resistance R_1 of the supercapacitor ($\Delta V = I_{sc}R_1$).

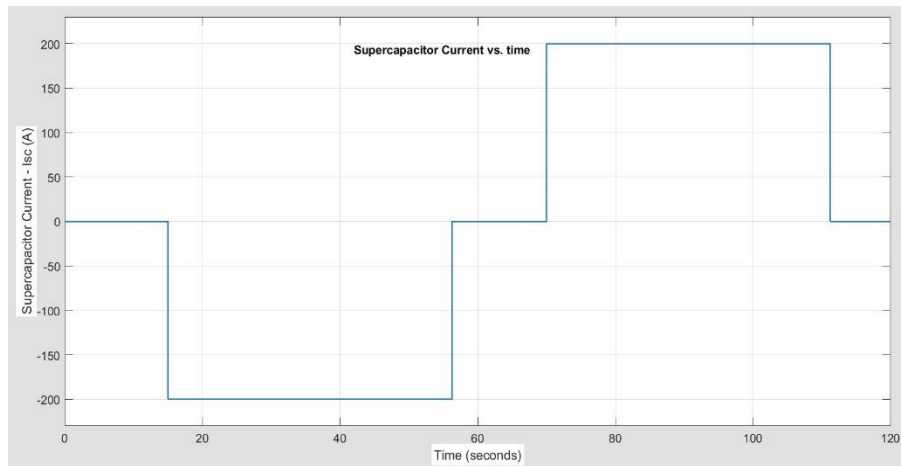


Figure 3.43: Supercapacitor charging/discharging current with time

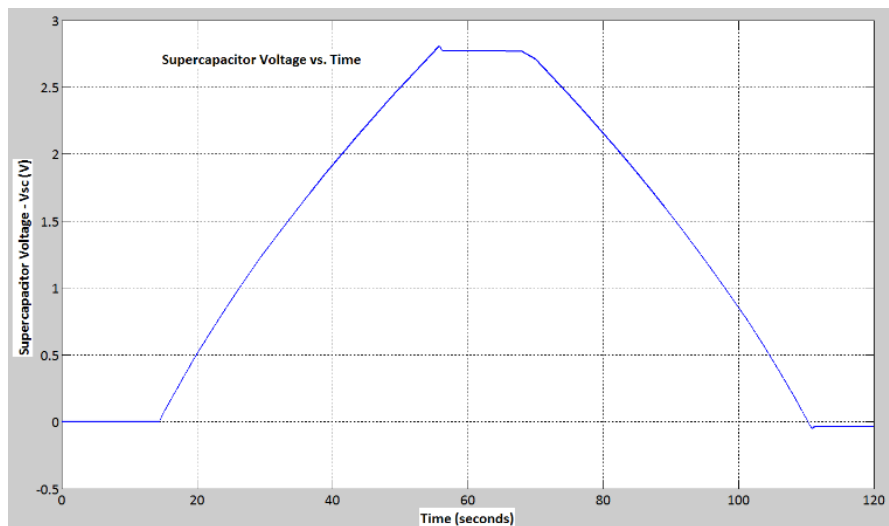


Figure 3.44: Supercapacitor charging/discharging voltage with time

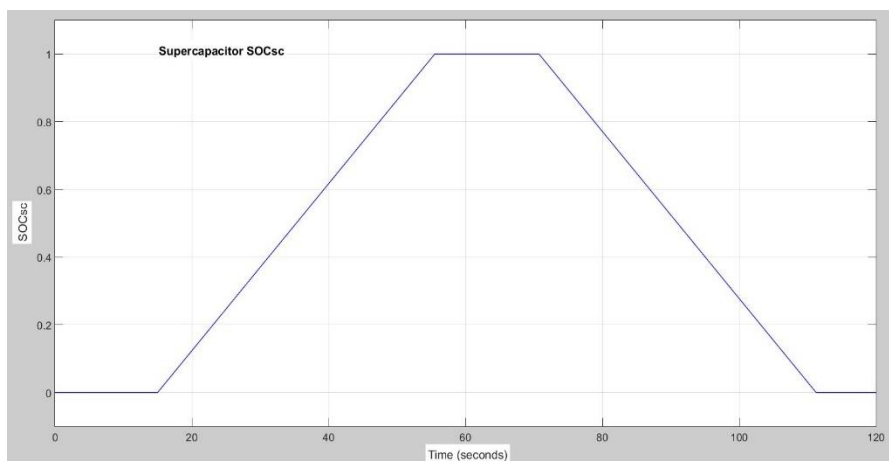


Figure 3.45: Supercapacitor SOC with time

3.5.3 Supercapacitor pack sizing

The DC voltage for the supercapacitor pack is assumed to be about 64 V. Hence, 24 cells in series connection are needed to achieve the voltage of 64.8 V, because each supercapacitor cell has a voltage of 2.7 V. As the supercapacitor is considered a high-power storage device, it is assumed that the supercapacitor pack must be able to supply/absorb a maximum power of 9 kW for 20 seconds, and therefore the required energy is calculated to be 50 Wh, or 180 kJ. Note that it is usually not allowed to utilize 100% of the energy stored in the supercapacitor pack. A typical voltage window considered for supercapacitors is between $V_{max}/2$ and V_{max} , hence it is assumed that the pack can be discharged from its rated voltage of 64.8 V to about 35 V (i.e., $V_{max}= 64.8$ V, $V_{min}= 35$ V) [268], [269]. Therefore, the equivalent capacitance, C_{eq} , of the supercapacitor pack can be calculated as [161], [270]:

$$E_{sc} = \frac{1}{2} \eta_{sc} C_{eq} (V_{max}^2 - V_{min}^2) \quad (27)$$

where E_{sc} is the energy stored in the supercapacitor (in J) and η_{sc} is the efficiency of the supercapacitor. Assuming an efficiency of 98%, the equivalent capacitance is calculated to be about 123.5 F. Each supercapacitor cell has a capacitance of 3000 F, hence the module of 24 cells in series has a total equivalent capacitance of 125 F. Therefore, the stored energy of about 50.6 Wh is enough for the requirements of our system [161], [271]. Concluding, the supercapacitor pack consists of 24 cells in series ($N_s = 24$ and $N_p = 1$) and has an equivalent capacitance of 125 F, and it can store 50.6 Wh of energy.

3.6 Bidirectional DC-DC Converter ¹¹

3.6.1 Theory and mathematical analysis

The bidirectional DC-DC converter is a combination of a boost and buck converter, where the proper mode is selected by an appropriate control algorithm. Such a converter

¹¹ Section 3.6 contains material from submitted paper [315]

is used to charge and discharge the battery and the supercapacitor, where the corresponding duty cycles d_1 and d_2 of the transistors S_1 and S_2 , respectively, are determined by the appropriate controllers. The electrical circuit of the bidirectional DC-DC converter is presented in Figure 3.46, where L is the inductance of the converter (either in boost or buck mode), C_1 is the capacitance on the boost-mode operation, C_2 is the capacitance on the buck-mode operation, V_b is the lower voltage (e.g., battery side) and V_{dc} is the common DC-bus voltage [272]–[274].

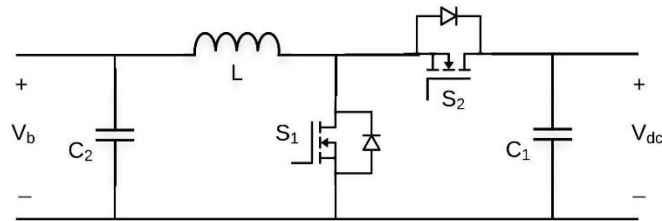


Figure 3.46: Bidirectional DC-DC converter circuit

In the sequel, a step-by-step power stage modeling is presented for the case of the boost and the buck modes of operation of the bidirectional converter. This process is done for the modeling of the converter and the design of the controller. The first part examines the steady-state operation of the converter. An essential part for the design of the control is the determination of the dynamic behavior of a converter. In other words, how the small variations of the inputs near the steady-state value affect the output of the converter. The switching ripple is considered as negligible in a well-designed converter that operates in a CCM. Therefore, the switching ripples are ignored and only the ac variations are modeled, where the frequency is much smaller than the switching frequency. The goal here is to predict this low-frequency part, which allows us to design the controller of the converter [224].

Classical control theory applies only to linear time-invariant (LTI) single-input single-output (SISO) systems, and it is not appropriate for the more demanding dynamic analysis of a nonlinear time-variant system. Therefore, for the latter case, it is necessary to develop a process that allows one to overcome the problems related to time-variation and nonlinearity of the switching process of the converter [275]. To this end, the necessary steps to be followed are graphically represented in Figure 3.47. The resulting

small-signal model is a LTI model in which all the standard circuit analysis techniques can be applied. To construct this, the nonlinear time-variant signal is averaged over one switching period, thus assuming that the switching ripples of the state variables are equal to zero as their time variance is removed. After that, the model is linearized by removing all the nonlinearities that incurred by the averaging process. Therefore, a linear time-invariant small signal model is produced, describing the time-domain dynamics at the presence of small-signal excitation. Finally, the time-domain small-signal model is transformed into a frequency-domain (s-domain) small-signal model. This conversion provides the transfer functions of power stage dynamics, which are required for the stability analysis [276]–[279].

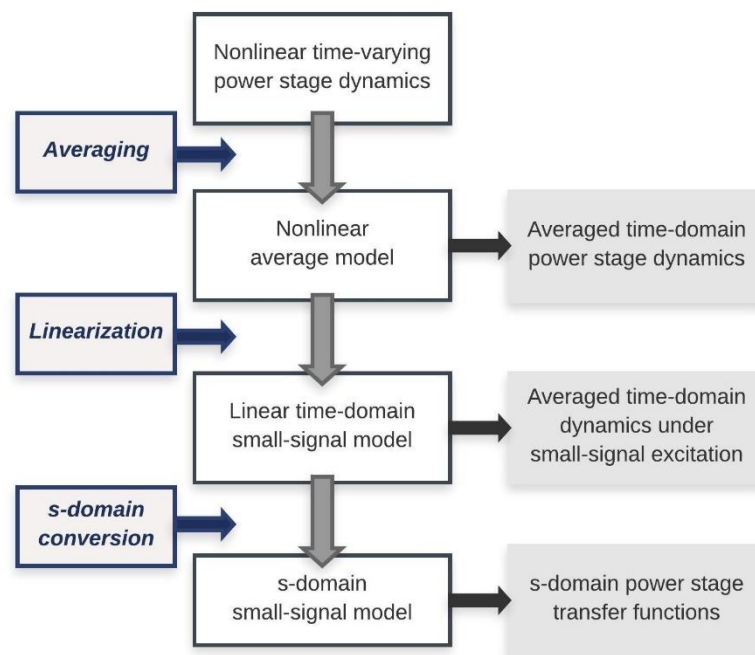


Figure 3.47: Steps of power stage modeling

3.6.1.1 Boost-mode operation

The boost-mode is applied for the discharging process of the storage (battery or supercapacitor) system. Figure 3.48 shows the circuit of the boost-mode converter, where the direction of the inductor current is from the lower voltage side to the higher voltage side [280]–[282]. The capacitance of the boost-mode is assumed equal with that of the buck-mode, hence $C_1 = C_2 = C$. The boost-mode operation is activated when S_1

operates periodically, while S_2 is switched off. The duty cycle D_1 is the ratio of the time that the switch S_1 is ON to the switching period, and determines the steady-state output voltage and current values based on the equations (28)–(29).

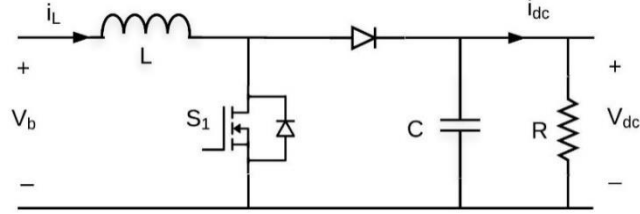


Figure 3.48: Circuit of the boost-mode converter

$$V_{dc} = \frac{V_b}{1 - D_1} \quad (28)$$

$$I_{dc} = (1 - D_1)I_L \quad (29)$$

The averaged large signal inductor current, i_L , and the DC-bus output voltage, v_{dc} , in a CCM operation can be found using the equations below.

$$\frac{di_L}{dt} = \frac{1}{L}(v_b - (1 - d_1)v_{dc}) \quad (30)$$

$$\frac{dv_{dc}}{dt} = \frac{1}{C}((1 - d_1)i_L - i_{dc}) \quad (31)$$

or, in state-space matrix form,

$$\begin{bmatrix} \frac{di_L}{dt} \\ \frac{dv_{dc}}{dt} \end{bmatrix} = \begin{bmatrix} 0 & -\frac{(1 - d_1)}{L} \\ \frac{(1 - d_1)}{C} & -\frac{1}{RC} \end{bmatrix} \begin{bmatrix} i_L \\ v_{dc} \end{bmatrix} + \begin{bmatrix} 1 \\ 0 \end{bmatrix} \frac{1}{L} [v_b] + \begin{bmatrix} 0 \\ -\frac{1}{C} \end{bmatrix} [i_{dc}] \quad (32)$$

where L is the inductance of the converter, C is the capacitance of the converter, R is the output resistance, v_b is the input voltage (e.g., battery voltage) and i_{dc} is the output current of the converter. Each parameter in the equations above must be expanded to include the dynamics produced by the inductors and capacitors of the converter. Thus, the input voltage and the duty cycle ($v_b(t)$, $d_1(t)$) can be represented by the sum of their quiescent values (V_b , D_1) and small ac variations in time ($\hat{v}_b(t)$, $\hat{d}_1(t)$).

$$v_b(t) = V_b + \hat{v}_b(t) \quad (33)$$

$$d_1(t) = D_1 + \hat{d}_1(t) \quad (34)$$

These time varying inputs produce perturbations in the dynamic variables. Hence, one can write:

$$i_{dc}(t) = I_{dc} + \hat{i}_{dc}(t) \quad (35)$$

$$v_{dc}(t) = V_{dc} + \hat{v}_{dc}(t) \quad (36)$$

$$i_L(t) = I_L + \hat{i}_L(t) \quad (37)$$

where the output current, output voltage and inductor current ($i_{dc}(t)$, $v_{dc}(t)$, $i_L(t)$) are represented by the sum of their quiescent values (I_{dc} , V_{dc} , I_L) and small ac variations in time ($\hat{i}_{dc}(t)$, $\hat{v}_{dc}(t)$, $\hat{i}_L(t)$). In addition, the ac variations are assumed to be relatively small in magnitude compared to the dc quiescent values.

$$|\hat{v}_b(t)| \ll |V_b|, |\hat{d}_1(t)| \ll |D_1|, |\hat{i}_L(t)| \ll |I_L|, |\hat{v}_{dc}(t)| \ll |V_{dc}|, |\hat{i}_{dc}(t)| \ll |I_{dc}| \quad (38)$$

Thus, equations (30)–(31) can be linearized by expanding and separating the steady-state terms and small-signal terms. From the inductor current equation (30), yields:

$$\frac{d(I_L + \hat{i}_L(t))}{dt} = \frac{1}{L} [(V_b + \hat{v}_b(t)) - (V_{dc} + \hat{v}_{dc}(t))(1 - (D_1 + \hat{d}_1(t)))] \quad (39)$$

or, upon collecting relevant terms,

$$L \left(\frac{dI_L}{dt} + \frac{d\hat{i}_L(t)}{dt} \right) = \underbrace{(V_b - V_{dc}D_1')}_{dc \text{ terms}} + \underbrace{(\hat{v}_b(t) + V_{dc}\hat{d}_1(t) - \hat{v}_{dc}(t)D_1')}_{1st \text{ order ac terms (linear)}} + \underbrace{(\hat{v}_{dc}(t)\hat{d}_1(t))}_{2nd \text{ order ac terms (nonlinear)}}$$

where $D_1' = 1 - D_1$. The above equation consists of (i) the *dc terms*, which are dc values only, (ii) the *1st-order ac terms (linear)*, which contain products of a dc term with an ac term, and (iii) *2nd-order ac terms (nonlinear)*, which contain products of two ac terms – time-varying signals – (hence, they are nonlinear in time). One can then neglect the 2nd-order small ac quantities, as, following assumptions (38), they are much smaller in magnitude than the 1st-order ac terms. Moreover, the dc terms on the right-hand side are equal to the dc terms on the left-hand side of the equation, by definition in steady-state analysis. Since I_L is a constant (dc) term, its derivative is zero ($\frac{dI_L}{dt} = 0$), and hence the sum of the dc terms on the left-hand side is equal to zero. Therefore, the sum of the dc terms on the right-hand side are also zero. Consequently, the remaining terms of the

inductor current equation are only the linear first order terms. Equation (40) represents the small-signal linearized equation for the inductor current variations.

$$\frac{d\hat{i}_L(t)}{dt} = \frac{1}{L} \left(-D_1' \hat{v}_{dc}(t) + V_{dc} \hat{d}_1(t) + \hat{v}_b(t) \right) \quad (40)$$

The same process can be followed in the case of the output capacitor voltage. From the output voltage equation (31), yields:

$$\frac{d(V_{dc} + \hat{v}_{dc}(t))}{dt} = \frac{1}{C} \left[(I_L + \hat{i}_L(t))(1 - (D_1 + \hat{d}_1(t))) - (I_{dc} + \hat{i}_{dc}(t)) \right] \quad (41)$$

or, upon collecting relevant terms,

$$C \left(\frac{dV_{dc}}{dt} + \frac{d\hat{v}_{dc}(t)}{dt} \right) = \underbrace{(I_L D_1' - I_{dc})}_{dc \text{ terms}} + \underbrace{(\hat{i}_L(t) D_1' - I_L \hat{d}_1(t) - \hat{i}_{dc}(t))}_{1st \text{ order ac terms (linear)}} + \underbrace{(-\hat{i}_L(t) \hat{d}_1(t))}_{2nd \text{ order ac terms (nonlinear)}}$$

In the same way, the 2nd-order small ac quantities are neglected. Since V_{dc} is a constant (dc) term, its derivative is zero ($\frac{dV_{dc}}{dt} = 0$), and hence the sum of the dc terms on the right-hand side is also equal to zero. Consequently, the remaining terms of the capacitor voltage equation are only the linear 1st-order terms. Equation (42) represents the small-signal linearized equation for the output voltage variations.

$$\frac{d\hat{v}_{dc}(t)}{dt} = \frac{1}{C} \left[D_1' \hat{i}_L(t) - I_L \hat{d}_1(t) - \hat{i}_{dc}(t) \right] \quad (42)$$

Combining the derived equations (40) and (42) in state-space matrix form, yields:

$$\begin{bmatrix} \frac{d\hat{i}_L(t)}{dt} \\ \frac{d\hat{v}_{dc}(t)}{dt} \end{bmatrix} = \begin{bmatrix} 0 & -\frac{D_1'}{L} \\ \frac{D_1'}{C} & -\frac{1}{RC} \end{bmatrix} \begin{bmatrix} \hat{i}_L(t) \\ \hat{v}_{dc}(t) \end{bmatrix} + \begin{bmatrix} \frac{1}{L} & 0 & \frac{V_{dc}}{L} \\ 0 & -\frac{1}{C} & -\frac{I_L}{C} \end{bmatrix} \begin{bmatrix} \hat{v}_b(t) \\ \hat{i}_{dc}(t) \\ \hat{d}_1(t) \end{bmatrix} \quad (43)$$

The next step is to define the state vector $\hat{\mathbf{x}}(t)$, which includes all the state variables, and the input vector $\hat{\mathbf{u}}(t)$, which contains all the independent inputs. Also, the output vector $\hat{\mathbf{y}}(t)$ is defined as a linear combination of the state vector and the input vector. Hence, the state-space averaged model of the boost converter is given by the system of equations (44) below.

$$\hat{\mathbf{x}}(t) = \begin{bmatrix} \hat{i}_L(t) \\ \hat{v}_{dc}(t) \end{bmatrix}, \quad \hat{\mathbf{u}}(t) = \begin{bmatrix} \hat{v}_b(t) \\ \hat{i}_{dc}(t) \\ \hat{d}_1(t) \end{bmatrix}, \quad \hat{\mathbf{y}}(t) = \begin{bmatrix} \hat{v}_{dc}(t) \\ \hat{i}_L(t) \end{bmatrix} \quad (44)$$

The above vectors in state-space equation form are written as:

$$\dot{\hat{\mathbf{x}}}(t) = \mathbf{A} \hat{\mathbf{x}}(t) + \mathbf{B} \hat{\mathbf{u}}(t) \quad (45)$$

$$\hat{\mathbf{y}}(t) = \mathbf{C} \hat{\mathbf{x}}(t) + \mathbf{D} \hat{\mathbf{u}}(t) \quad (46)$$

where \mathbf{A} , \mathbf{B} , \mathbf{C} and \mathbf{D} are the state equation matrices and are derived from (43).

$$\mathbf{A} = \begin{bmatrix} 0 & -\frac{D_1'}{L} \\ \frac{D_1'}{C} & -\frac{1}{RC} \end{bmatrix}, \mathbf{B} = \begin{bmatrix} \frac{1}{L} & 0 & \frac{V_{dc}}{L} \\ 0 & -\frac{1}{C} & -\frac{I_L}{C} \end{bmatrix}, \mathbf{C} = \begin{bmatrix} 0 & 1 \\ 1 & 0 \end{bmatrix}, \mathbf{D} = \begin{bmatrix} 0 & 0 & 0 \\ 0 & 0 & 0 \end{bmatrix} \quad (47)$$

The next step is the conversion of the time-domain small-signal model into a frequency-domain (s-domain) small-signal model. Taking Laplace transforms (with zero initial conditions) and solving for $\hat{\mathbf{X}}(s)$ in equation (45), yields:

$$\hat{\mathbf{X}}(s) = (s\mathbf{I} - \mathbf{A})^{-1} \mathbf{B} \hat{\mathbf{U}}(s) \quad (48)$$

Substituting equation (48) into the Laplace transform of equation (46), yields:

$$\hat{\mathbf{Y}}(s) = \mathbf{C} (s\mathbf{I} - \mathbf{A})^{-1} \mathbf{B} \hat{\mathbf{U}}(s) \quad (49)$$

The last step is to export the small signal transfer functions of the boost converter. This research is focused on the input current control, but the small signal transfer functions for the case of output voltage control are also extracted. For the case of the input current control, the remaining independent variables are set to zero ($\hat{v}_b(t) = 0$, $\hat{i}_{dc}(t) = 0$), which requires a reduced matrix $\mathbf{C} = [1 \ 0]$, leading to the normalized form equation (50). For the case of the output voltage control, the remaining independent variables are set to zero ($\hat{v}_b(t) = 0$, $\hat{i}_{dc}(t) = 0$), which requires a reduced matrix $\mathbf{C} = [0 \ 1]$, leading to the normalized form equation (51). This is useful for deriving the transfer function of equation (52) for the output voltage control.

In the control-to-output transfer function in (51) a non-minimum phase system is observed, because of the presence of a RHP (Right Half Plane) zero in the numerator. This RHP zero causes a 90° phase delay resulting to an overall phase variation between 0° and -270° (instead of 0° and -180° on the system with a regular left half plane zero). This phase problem presents considerable difficulties to the design of the voltage feedback of the controller and prevents it from securing a stable operation with a good performance.

$$G_{id}^{bo}(s) = \frac{\hat{i}_L(s)}{\hat{d}(s)} = \frac{2V_{dc}}{RD_1'^2} \left(\frac{1 + s\frac{RC}{2}}{1 + s\frac{L}{RD_1'^2} + s^2\frac{LC}{D_1'^2}} \right) \quad (50)$$

$$G_{vd}^{bo}(s) = \frac{\hat{v}_{dc}(s)}{\hat{d}(s)} = \frac{V_{dc}}{D_1'} \left(\frac{1 - s\frac{L}{RD_1'^2}}{1 + s\frac{L}{RD_1'^2} + s^2\frac{LC}{D_1'^2}} \right) \quad (51)$$

$$G_{vi}^{bo}(s) = \frac{\hat{v}_{dc}(s)}{\hat{i}_L(s)} = RD_1' \left(\frac{1 - s\frac{L}{RD_1'^2}}{2 + sRC} \right) \quad (52)$$

3.6.1.2 Buck-mode operation

The buck-mode is operated for the charging process of the storage. Figure 3.49 presents the circuit of the buck-mode converter. In contrast to the boost-mode operation, the inductor current flows from the higher voltage side to the lower voltage side [283]. The buck-mode operation is activated when S_2 operates periodically, while S_1 is switched off. The duty cycle D_2 is the ratio of the time that the switch S_2 is ON to the switching period, and determines the steady-state output voltage (V_b) and output current (I_b) values as follows.

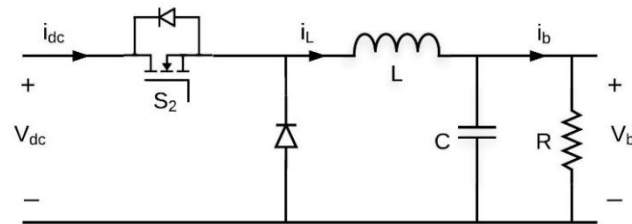


Figure 3.49: Circuit of the buck-mode converter

$$V_b = D_2 V_{dc} \quad (53)$$

$$I_b = \frac{I_{dc}}{D_2} \quad (54)$$

The averaged large signal inductor current, i_L , and the output battery voltage, v_b , are calculated by equations (55)–(56), respectively, and describe the buck-mode operation in a CCM of the converter.

$$\frac{di_L}{dt} = \frac{1}{L}(v_{dc}d_2 - v_b) \quad (55)$$

$$\frac{dv_b}{dt} = \frac{1}{C}\left(i_L - \frac{v_b}{R}\right) \quad (56)$$

or, in matrix form,

$$\begin{bmatrix} \frac{di_L}{dt} \\ \frac{dv_b}{dt} \end{bmatrix} = \begin{bmatrix} 0 & -\frac{1}{L} \\ \frac{1}{C} & -\frac{1}{RC} \end{bmatrix} \begin{bmatrix} i_L \\ v_b \end{bmatrix} + \begin{bmatrix} \frac{d_2}{L} \\ 0 \end{bmatrix} [v_{dc}] \quad (57)$$

The power stage modeling analysis for the buck-mode is similar to that of the boost-mode. Each parameter on the equations above must be expanded to include the dynamics produced by the inductors and capacitors of the converter. Thus, the input voltage and the duty cycle ($v_{dc}(t)$, $d_2(t)$) can be represented as their quiescent values (V_{dc} , D_2) and small ac variations in time ($\hat{v}_{dc}(t)$, $\hat{d}_2(t)$).

$$v_{dc}(t) = V_{dc} + \hat{v}_{dc}(t) \quad (58)$$

$$d_2(t) = D_2 + \hat{d}_2(t) \quad (59)$$

These time varying inputs produce perturbations in the dynamic variables. Hence, one can write:

$$i_L(t) = I_L + \hat{i}_L(t) \quad (60)$$

$$v_b(t) = V_b + \hat{v}_b(t) \quad (61)$$

In addition, the ac variations are assumed to be relatively small in magnitude compared to the dc quiescent values:

$$|\hat{v}_{dc}(t)| \ll |V_{dc}|, \quad |\hat{d}_2(t)| \ll |D_2|, \quad |\hat{i}_L(t)| \ll |I_L|, \quad |\hat{v}_b(t)| \ll |V_b| \quad (62)$$

Thus, the equations (55)–(56) can be linearized by expanding and separating the steady-state terms and small-signal terms. From the inductor current equation (55), yields:

$$\frac{d(I_L + \hat{i}_L(t))}{dt} = \frac{1}{L}[(V_{dc} + \hat{v}_{dc}(t))(D_2 + \hat{d}_2(t)) - (V_b + \hat{v}_b(t))] \quad (63)$$

or, upon collecting relevant terms,

$$L \left(\frac{dI_L}{dt} + \frac{d\hat{i}_L(t)}{dt} \right) = \underbrace{(V_{dc}D_2 - V_b)}_{dc \text{ terms}} + \underbrace{(V_{dc}\hat{d}_2(t) + D_2\hat{v}_{dc}(t) - \hat{v}_b(t))}_{1st \text{ order ac terms (linear)}} + \underbrace{(\hat{v}_{dc}(t)\hat{d}_2(t))}_{2nd \text{ order ac terms (nonlinear)}}$$

As already explained for the case of the boost-mode operation, the 2nd-order small ac quantities are neglected (see assumptions (62)). Since I_L is a constant (dc) term, its derivative is zero ($\frac{dI_L}{dt} = 0$), and hence the sum of the dc terms on the right-hand side is also equal to zero. Consequently, the remaining terms of the inductor current equation are only the linear first order terms. Equation (64) represents the small-signal linearized equation for the inductor current variations.

$$\frac{d\hat{i}_L(t)}{dt} = \frac{1}{L} [-\hat{v}_b(t) + D_2\hat{v}_{dc}(t) + V_{dc}\hat{d}_2(t)] \quad (64)$$

The same process can be followed in the case of the output capacitor voltage. From the output voltage equation (56), yields:

$$\frac{d(V_{dc} + \hat{v}_{dc}(t))}{dt} = \frac{1}{C} \left[(I_L + \hat{i}_L(t)) - \frac{1}{R} (V_b + \hat{v}_b(t)) \right] \quad (65)$$

or, upon collecting relevant terms,

$$C \left(\frac{dV_b}{dt} + \frac{d\hat{v}_{dc}(t)}{dt} \right) = \underbrace{\left(I_L - \frac{V_b}{R} \right)}_{dc \text{ terms}} + \underbrace{\left(\hat{i}_L(t) - \frac{\hat{v}_b(t)}{R} \right)}_{1st \text{ order ac terms (linear)}}$$

The dc terms on the right-hand side are equal to the dc terms on the left-hand side. Since V_b is constant (dc) term, its derivative is zero ($\frac{dV_b}{dt} = 0$), hence the sum of the dc terms on the right-hand side is also equal to zero. Consequently, the remaining terms of the capacitor voltage equation are only the linear first order terms. Equation (66) represents the small-signal linearized equation for the output voltage variations.

$$\frac{d\hat{v}_b(t)}{dt} = \frac{1}{C} \left[\hat{i}_L(t) - \frac{\hat{v}_b(t)}{R} \right] \quad (66)$$

Combining the derived equations (64) and (66) in matrix form, yields:

$$\begin{bmatrix} \frac{d\hat{i}_L(t)}{dt} \\ \frac{d\hat{v}_b(t)}{dt} \end{bmatrix} = \begin{bmatrix} 0 & -\frac{1}{L} \\ \frac{1}{C} & -\frac{1}{RC} \end{bmatrix} \begin{bmatrix} \hat{i}_L(t) \\ \hat{v}_b(t) \end{bmatrix} + \begin{bmatrix} \frac{D_2}{L} & \frac{V_{dc}}{L} \\ 0 & 0 \end{bmatrix} \begin{bmatrix} \hat{v}_{dc}(t) \\ \hat{d}_2(t) \end{bmatrix} \quad (67)$$

The next step is to define the state vector $\hat{\mathbf{x}}(t)$, which includes all the state variables, and the input vector $\hat{\mathbf{u}}(t)$, which contains all the independent inputs. As before, the output vector $\hat{\mathbf{y}}(t)$ is defined as a linear combination of the state vector and the input vector. Hence, the state-space averaged model of the boost converter is given by the system of equations (68) below.

$$\hat{\mathbf{x}}(t) = \begin{bmatrix} \hat{i}_L(t) \\ \hat{v}_b(t) \end{bmatrix}, \quad \hat{\mathbf{u}}(t) = \begin{bmatrix} \hat{v}_{dc}(t) \\ \hat{d}_2(t) \end{bmatrix}, \quad \hat{\mathbf{y}}(t) = \begin{bmatrix} \hat{v}_b(t) \\ \hat{i}_L(t) \end{bmatrix} \quad (68)$$

The above vectors can be written in state-space equation form (see equations (45)–(46)), where matrices A, B, C and D are derived from (67).

$$\mathbf{A} = \begin{bmatrix} 0 & -\frac{1}{L} \\ \frac{1}{C} & -\frac{1}{RC} \end{bmatrix}, \quad \mathbf{B} = \begin{bmatrix} \frac{D_2}{L} & \frac{V_{dc}}{L} \\ 0 & 0 \end{bmatrix}, \quad \mathbf{C} = \begin{bmatrix} 0 & 1 \\ 1 & 0 \end{bmatrix}, \quad \mathbf{D} = \begin{bmatrix} 0 & 0 \\ 0 & 0 \end{bmatrix} \quad (69)$$

As before, the last step is to determine the required small signal transfer functions of the buck converter using Laplace transforms (see equations (48)–(49)). For the case of the input current control, the remaining independent input is set to zero ($\hat{v}_{dc}(t) = 0$) and the required reduced matrix to $\mathbf{C} = [1 \ 0]$, leading to the normalized form equation (70). For the case of the output voltage control, the independent input is set to zero ($\hat{v}_{dc}(t) = 0$) and the required reduced matrix to $\mathbf{C} = [0 \ 1]$, leading to the normalized form equation (71). This is useful for deriving the transfer function of equation (72) for the output voltage control.

$$G_{id}^{bu}(s) = \frac{\hat{i}_L(s)}{\hat{d}(s)} = \frac{V_b}{RD_2} \left(\frac{1 + sRC}{1 + s\frac{L}{R} + s^2LC} \right) \quad (70)$$

$$G_{vd}^{bu}(s) = \frac{\hat{v}_b(s)}{\hat{d}(s)} = \frac{V_b}{D_2} \left(\frac{1}{1 + s\frac{L}{R} + s^2LC} \right) \quad (71)$$

$$G_{vi}^{bu}(s) = \frac{\hat{v}_b(s)}{\hat{i}_L(s)} = \frac{R}{1 + sRC} \quad (72)$$

3.6.2 Modeling and simulation

The bidirectional DC-DC converter averaged model for the battery in Simulink has as inputs the type of the mode (mode=1 for boost-mode, or mode=0 for buck-mode operation), the duty cycle and the input and output voltage. The output of this model is the inductor current, which is compared with a reference inductor current. In Figure 3.50 the Simulink model of the battery bidirectional converter is presented.

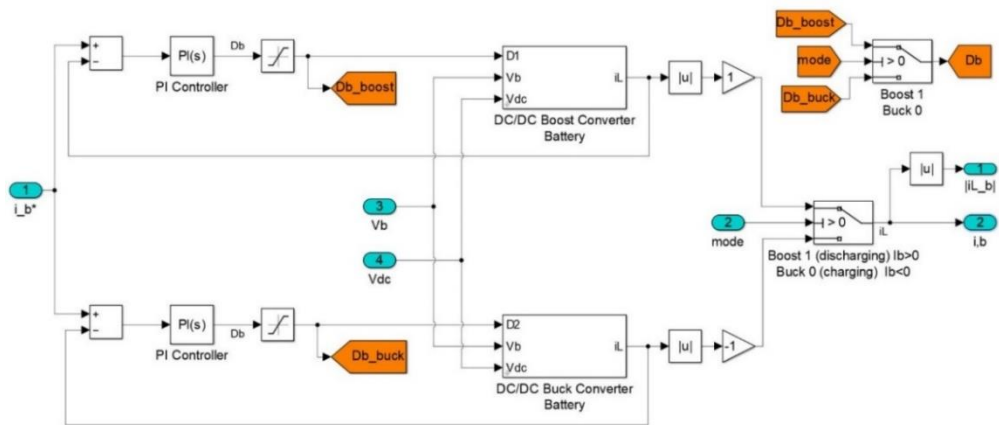


Figure 3.50: Battery bidirectional converter in Simulink

When the bidirectional converter operates as a boost converter (discharging mode), the inputs are the duty cycle D_1 , the battery (or supercapacitor) voltage (input voltage) and the DC-bus voltage (output voltage), while the output is the inductor current. On the other hand, when the bidirectional converter operates as a buck converter (charging mode), the duty cycle D_2 , the DC-bus voltage (input voltage) and the battery (or supercapacitor) voltage (output voltage), while the output is the inductor current. Based on the mode of operation, a final decision on the proper duty cycle and inductor current is made. For the case of the supercapacitor bidirectional converter model, a similar approach is adopted, where the sign of the supercapacitor current defines the mode of operation (sign_sc > 0 for boost-mode, or sign_sc < 0 for buck-mode operation).

3.6.3 Transfer functions and parameters of the bidirectional converter

The model consists of two bidirectional converters, as the configuration of the hybrid storage is fully active. For the case of the battery and supercapacitor converters design,

the system parameters for the simulation are tabulated in Table 3.4. It must be noted here that similar bidirectional converters exist in industry having high efficiencies [284]–[286].

Table 3.4: System parameters for the simulation of the battery and supercapacitor converters

Battery Converter	
Battery voltage (V_b)	60 V
Battery Inductor (L_b)	5 mH
Battery load resistor (R_{L_b}) (virtual)	12 Ω
Supercapacitor Converter	
Supercapacitor voltage (V_{sc})	70 V
Supercapacitor Inductor (L_{sc})	5 mH
Supercapacitor load resistor ($R_{L_{sc}}$) (virtual)	12 Ω
DC-bus parameters	
DC-link Capacitor (C_{dc})	5000 μ F
DC-link load resistor (R_{dc}) (virtual)	50 Ω
DC-bus voltage (V_{dc})	400 V

Moreover, based on the small-signal ac analysis of the previous sub-Section 3.6.1, the derived transfer functions regarding the current control of the battery and supercapacitor are presented in the table below. These transfer functions are used in Section 3.8 for the design of the controllers and the stability analysis.

Table 3.5: Transfer functions of the battery and supercapacitor converters

	Boost-mode	Buck-mode
Battery Converter	$G_{id,b}^{bo}(s) = \frac{\hat{i}_{L,b}(s)}{\hat{d}_b(s)}$ $= \frac{8 \times 10^4 (s + 8)}{s^2 + 4s + 900}$	$G_{id,b}^{bu}(s) = \frac{\hat{i}_{L,b}(s)}{\hat{d}_b(s)}$ $= \frac{8 \times 10^4 (s + 16.67)}{s^2 + 16.67s + 4 \times 10^4}$
Supercapacitor Converter	$G_{id,sc}^{bo}(s) = \frac{\hat{i}_{L,sc}(s)}{\hat{d}_{sc}(s)}$ $= \frac{8 \times 10^4 (s + 8)}{s^2 + 4s + 1225}$	$G_{id,sc}^{bu}(s) = \frac{\hat{i}_{L,sc}(s)}{\hat{d}_{sc}(s)}$ $= \frac{8 \times 10^4 (s + 16.67)}{s^2 + 16.67s + 4 \times 10^4}$

3.7 DC-AC Inverter¹²

3.7.1 Theory and mathematical analysis

The DC-AC inverter is designed to convert the DC power from the DC-link into the AC form for grid interconnection. For this study, a single-phase voltage source inverter (VSI) with H-bridge (full-bridge) topology is considered, as shown in Figure 3.51.

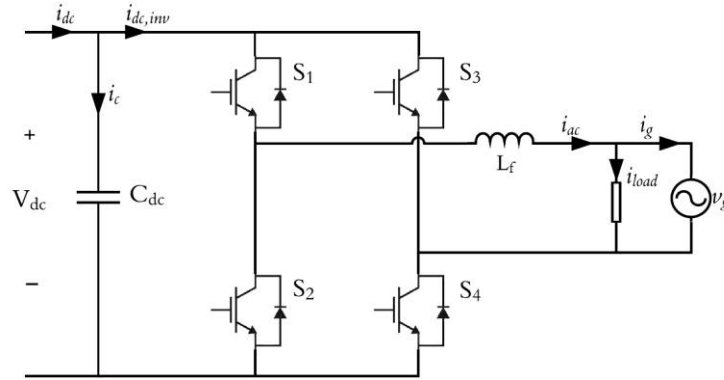


Figure 3.51: Full-bridge grid-side voltage-source inverter circuit

The input voltage of the inverter is the 400 V DC-bus, while the output is connected to the grid through a L-type AC grid-link filter [220], [287], [288]. It must be noted here that a unity power factor is considered, so that the output current of the inverter is in phase with the grid voltage. The AC voltage ($v_{ac}(t)$) and the AC current ($i_{ac}(t)$) equations for the inverter are given below [289]:

$$v_{ac}(t) = \sqrt{2} V_{rms} \sin(\omega t) = V_{ac} \sin(\omega t) \quad (73)$$

$$i_{ac}(t) = \sqrt{2} I_{rms} \sin(\omega t) = I_{ac} \sin(\omega t) \quad (74)$$

where V_{rms} and I_{rms} are the rms values of the inverter output voltage and current, V_{ac} and I_{ac} are the peak values (amplitude) of the inverter output voltage and current, and ω is the grid line frequency.

The power supplied to the AC grid pulsates at twice the AC grid line frequency. This is reasonable, as the instantaneous AC output power, $p_{inv}(t)$, is calculated by [290]:

¹² Section 3.7 contains material from published paper [241] and submitted paper [315]

$$p_{inv}(t) = v_{ac}(t) i_{ac}(t) = V_{rms} I_{rms} [1 - \cos(2\omega t)] = P_{ac} [1 - \cos(2\omega t)] \quad (75)$$

where P_{ac} is the average output power of the inverter. For the production of the AC current, switches operate as pairs of S_1/S_4 and S_2/S_3 . If any other combination occurs, then the output voltage is zero [220], [291], [292]. In order to export the required equations of voltage and current of the inverter model, it is considered that the ON-time of the pair S_1/S_4 is DT_s , while the ON-time of the pair S_2/S_3 is $(1 - D)T_s$. Therefore, one can obtain the following averaged equations of the inverter over a switching period (T_s):

$$V_{ac} = DV_{dc} + (1 - D)(-V_{dc}) = (2D - 1)V_{dc} \quad (76)$$

$$i_{dc,inv} = Di_{ac} + (1 - D)(-i_{ac}) = (2D - 1)i_{ac} \quad (77)$$

where $i_{dc,inv}$ is the input current of the inverter. The inverter control includes a PLL, which is used for the synchronization of the PV system with the grid [293]–[295]. The magnitude of the output current of the inverter is obtained through the voltage controller of the DC-bus [296], [297]. More details regarding the design of the appropriate controller of the inverter are given in sub-Section 3.8.3.

3.7.2 Modeling and simulation

The averaged mathematical model of the single-phase DC-AC inverter is examined [249], as shown in Figure 3.52. It should be noted here that the model in Simulink takes into consideration the parameters for the conduction loss and switching loss, which are ignored here ($R_L = 0 \Omega$, $I_{sw} = 0 \text{ A}$). The inverter is operated as a voltage-source and it is current controlled (CCVSI). Equations (76)–(77) were used to build the Simulink model of the inverter. The appropriate reference output current of the inverter (I_{ref_ac}) is calculated and examined in sub-Section 3.8.3. The grid voltage is 230 V_{rms} with a line frequency of 50 Hz.

In sub-Section 3.8.1 the design and the stability analysis of the required current controllers are performed for the case of the battery and the supercapacitor converters, respectively. In sub-Section 3.8.2, the DC-link capacitance is determined and the required DC-link model is obtained. Finally, sub-Section 3.8.3 presents the design and stability analysis of the DC-bus voltage control loop, where the reference output current of the inverter is obtained.

3.8.1 Battery-supercapacitor hybrid storage system: Design of current controllers and stability analysis

In this sub-Section, the design of the current controllers for the battery and supercapacitor are examined, respectively, where the duty cycle of each converter can be derived [299]–[301]. The proposed feedback loop for the control of each bidirectional DC-DC converter for the case of the battery-supercapacitor hybrid storage is presented in Figure 3.53. Specifically, Figure 3.53(a) corresponds to the supercapacitor current controller loop, while the Figure 3.53(b) presents the block diagram of the battery current controller. Note here that all the feedback sensor gains are assumed to be equal to 1, hence $H_{i,b} = H_{i,sc} = 1$.

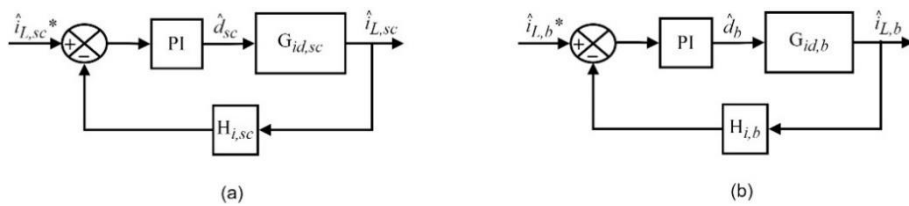


Figure 3.53: Block diagram of the (a) supercapacitor current controller, (b) battery current controller

In order to extend the battery lifetime and relieve the battery stress, supercapacitors are suitable for absorbing/releasing the high frequency variations, while the battery will deal with the low frequencies. In other words, supercapacitor covers the peaks and fluctuations that may occur. The current control of the supercapacitor must be faster than the current control of the battery because the supercapacitor must be faster and track higher frequencies. To this end, the current control loop bandwidth (BW) of the

supercapacitor is set to the limit of $f_{sw}/6$. The battery current control loop BW must be smaller than the BW of the supercapacitor, and therefore its limit is set to $f_{sw}/10$ [19], [20], [23], [302].

- **Boost-mode operation**

The Simulink model of the small-signal feedback control loop for boost-mode operation with battery-supercapacitor storage is shown in Figure 3.54. The model parameters and transfer functions are given in sub-Section 3.6.3.

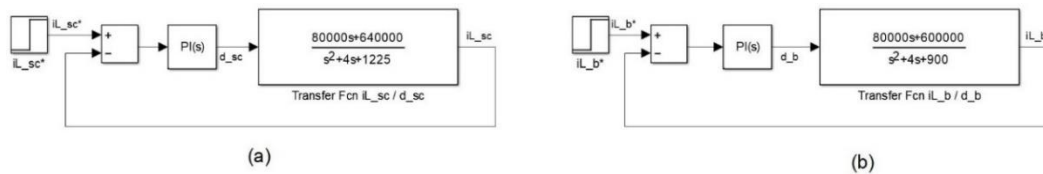


Figure 3.54: Small-signal Simulink model for boost-mode operation for the (a) supercapacitor current controller, (b) battery current controller

- (i) **Design of the supercapacitor current controller (boost-mode)**

The bode plot of the open-loop transfer function with and without compensation for the supercapacitor current control loop design (boost-mode) is shown in Figure 3.55. The bode plot of the uncompensated current control loop (blue line) shows a low gain in the low frequency range, but the loop needs high gain at low frequency. The inverted-zero of the compensator (PI) results to a high gain at low frequencies and reduces the steady-state error of the loop gain. The high-frequency pole cancels the gain of the inverted-zero at the high frequencies [224], [303]. In other words, the compensator contains an integral action in its transfer function, providing high gain in the low frequency range in order to get a perfect tracking of the reference (zero steady-state error). Moreover, it contains high frequency poles to attenuate any produced ripples.

As explained before, to avoid oscillations, the current control loop bandwidth (BW) of the supercapacitor must be limited to $f_{sw}/6$. The switching frequency (f_{sw}) of the supercapacitor converter is set to 10 kHz. Hence, to ensure the stability of the system, the desirable crossover frequency and PM of the current control loop of the

supercapacitor are specified as 10.47 krad/s and 60°, respectively. The PI controller gains for the supercapacitor current control are set to $K_p = 0.113$ and $K_i = 685.58$.

From the bode plot of Figure 3.55 a negative PM (positive feedback), which may lead to instability, is observed. Hence the loop should not have a positive feedback, near the crossover frequency. In this case, the system has a negative GM and negative PM near 60 rad/s, but because the gain is nowhere near unity, the system is stable in this region. At about 10 krad/s, the loop gain is unity (i.e., 0 dB), and the system has a positive PM (negative feedback), hence the system is again, stable in this region.

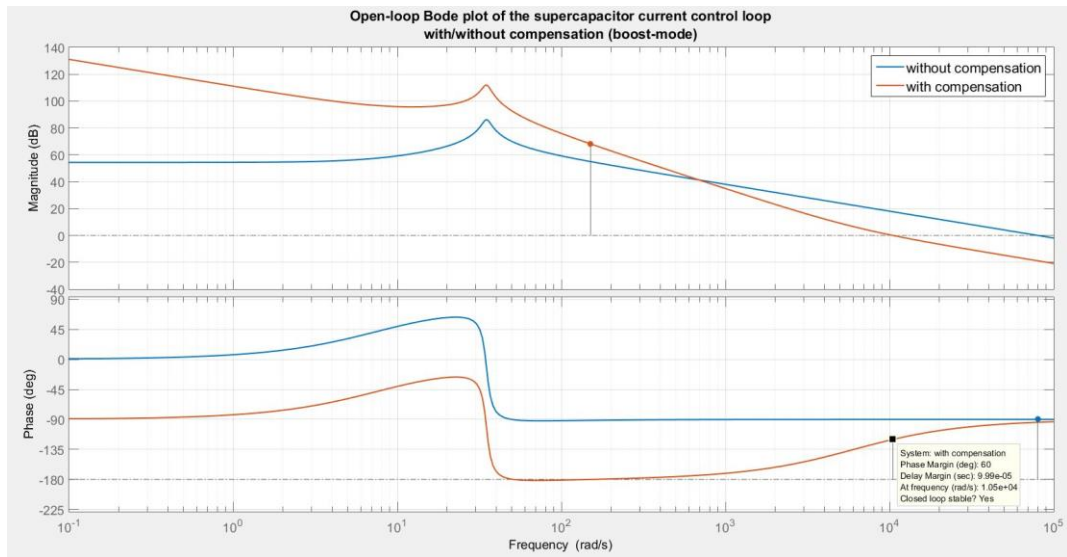


Figure 3.55: Open-loop Bode plot of the supercapacitor current control loop (boost-mode)

(ii) Design of the battery current controller (boost-mode)

The bode plot of the open-loop transfer function with and without compensation for the battery current control loop design (boost-mode) is shown in Figure 3.56. The bode plot has the same PM and GM characteristics with those of the bode plot in Figure 3.55 of the supercapacitor. As explained before, the current control loop BW of the battery must be limited to $f_{sw}/10$. The switching frequency (f_{sw}) of the battery converter is set to 10 kHz. Hence, to ensure the stability of the system, the desirable crossover frequency and PM of the current control loop of the supercapacitor are specified as 6.28 krad/s and 60°, respectively. The PI controller gains are set to $K_p = 0.068$ and $K_i = 246.25$.

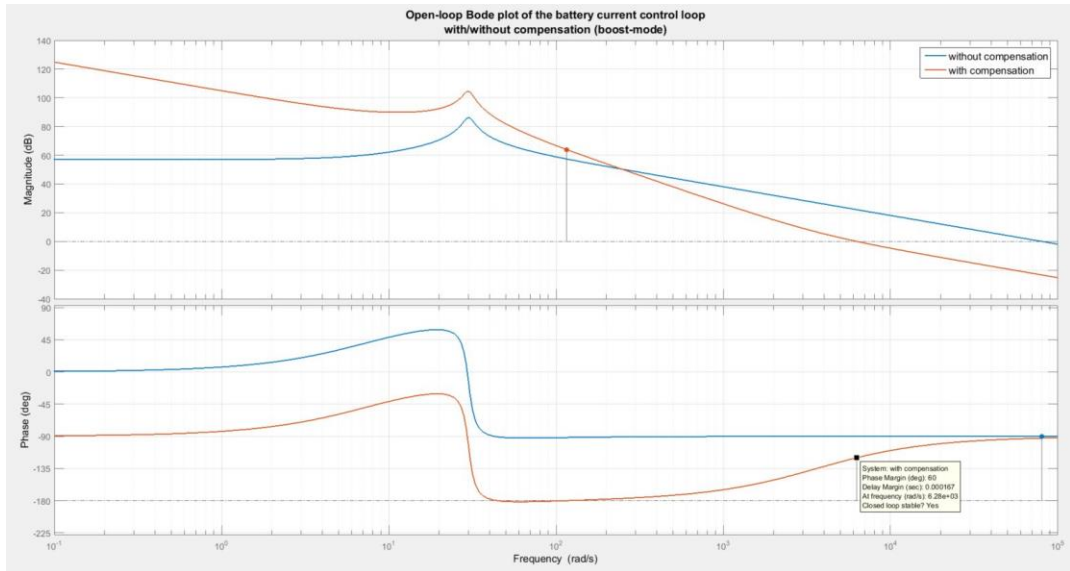


Figure 3.56: Open-loop Bode plot of the battery current control loop (boost-mode)

- **Buck-mode operation**

The Simulink model of the small-signal feedback control loop for buck-mode operation with battery-supercapacitor storage is shown in Figure 3.57. The model parameters and transfer functions are given in sub-Section 3.6.3.

The same process is figured out for the case of the buck-mode operation of the bidirectional converter.

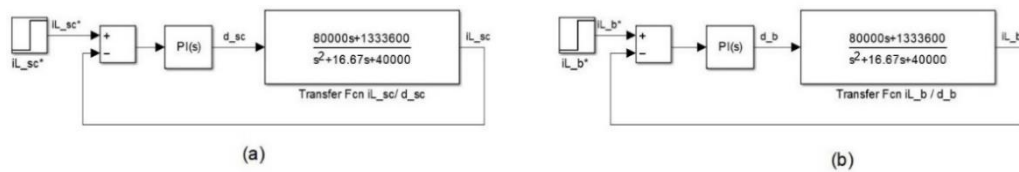


Figure 3.57: Small-signal Simulink model for buck-mode operation for the (a) supercapacitor current controller, (b) battery current controller

(i) **Design of the supercapacitor current controller (buck-mode)**

The Bode plot of the open-loop transfer function with and without compensation for the supercapacitor current control loop (buck-mode) is presented in Figure 3.58. As for the case of the boost-mode, the desirable crossover frequency and PM of the current control loop are specified as 10.47 krad/s and 60°, respectively. The PI controller gains are set to $K_p = 0.113$ and $K_i = 684.88$.

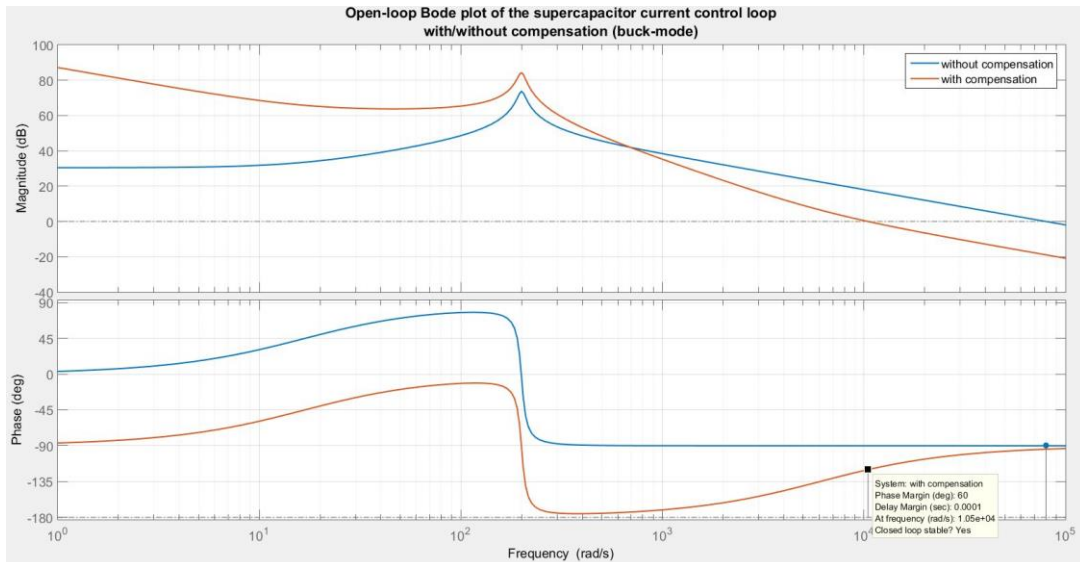


Figure 3.58: Open-loop Bode plot of the supercapacitor current control loop (buck-mode)

(ii) Design of the battery current controller (buck-mode)

The Bode plot of the open-loop transfer function with and without compensation for the battery current control loop (buck-mode) is presented in Figure 3.59. As for the case of the boost-mode, the desirable crossover frequency and PM of the current control loop are specified as 6.28 krad/s and 60°, respectively. The PI controller gains are set to $K_p = 0.068$ and $K_i = 246.24$.

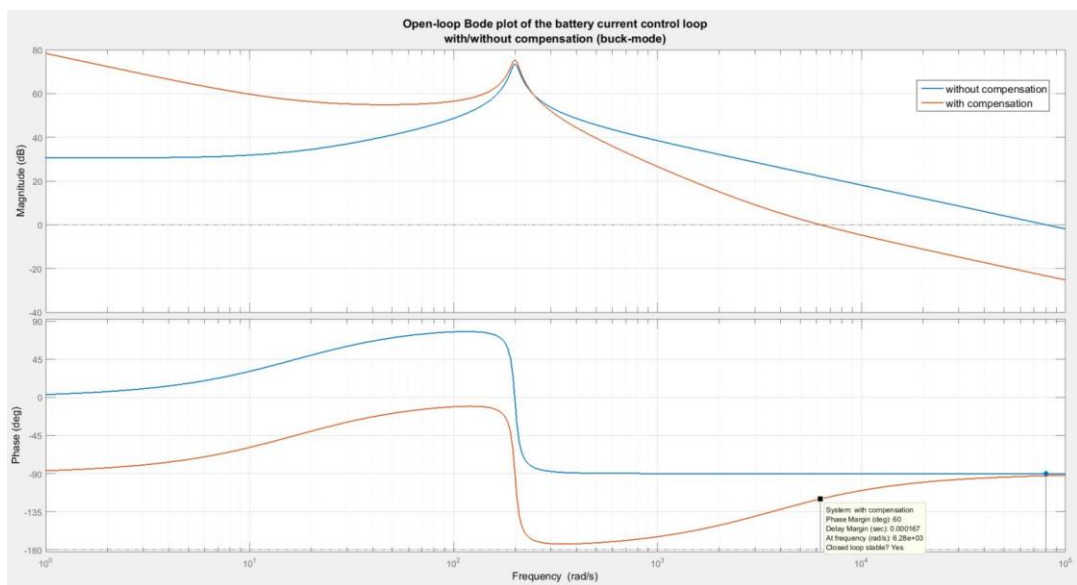


Figure 3.59: Open-loop Bode plot of the battery current control loop (buck-mode)

Concluding, this sub-Section presented the design and stability analysis of the current controllers required for our application. In grid-connected systems, the DC-bus voltage control is employed by the inverter. Therefore, for this system the DC-bus voltage control is performed by the inverter (see sub-Section 3.8.3), and the required reference currents for the current controllers of the battery and supercapacitor converters are exported from the PMA (see sub-Section 3.9.2).

3.8.2 DC-link: Capacitance calculation and dynamics

The common DC-bus is important for the interface between the PV and storage side and the DC-AC inverter side. The role of the DC-link capacitor is to store (filter) the 100Hz energy difference, because the power of the DC-link side (P_{dc}) is constant, but the output power of the inverter (p_{inv}) pulsates at twice the grid frequency, as shown in equation (79) (assuming a lossless inverter) [304], [305].

$$C_{dc}v_{dc}\frac{dv_{dc}}{dt} = P_{dc} - p_{inv} = P_{dc} - P_{ac}[1 - \cos(2\omega t)] \quad (79)$$

The desired DC-link capacitance can be calculated from equation (80):

$$C_{dc} = \frac{P_{ac}}{V_{dc} \omega \Delta V_{dc}} \quad (80)$$

where ΔV_{dc} is the peak-to-peak ripple voltage superimposed over the DC-bus voltage and $\omega = 2\pi f = 100\pi$ [220], [249], [295], [306]. The DC-link capacitor provides balance to the instantaneous power delivered to the grid [290]. If a maximum ripple voltage of about 5 V at 3 kW power is considered, then a minimum capacitance of 4775 μF is required. Hence, a suitable capacitance of 5000 μF is selected for a proper operation.

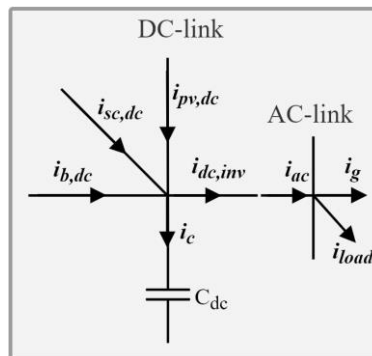


Figure 3.60: Currents balance at DC-link and AC-link

The variation of the DC-link voltage responds to the interaction between the injected current and the extracted current, corresponding to the capacitance of the DC-bus (see equation (81)) [29], [307]. Therefore, Figure 3.60 shows the currents balance on the DC-link, and Figure 3.61 corresponds to the DC-link subsystem in Simulink.

$$C_{dc} \frac{dv_{dc}}{dt} = i_{pv,dc} + i_{b,dc} + i_{sc,dc} - i_{dc,inv} \quad (81)$$

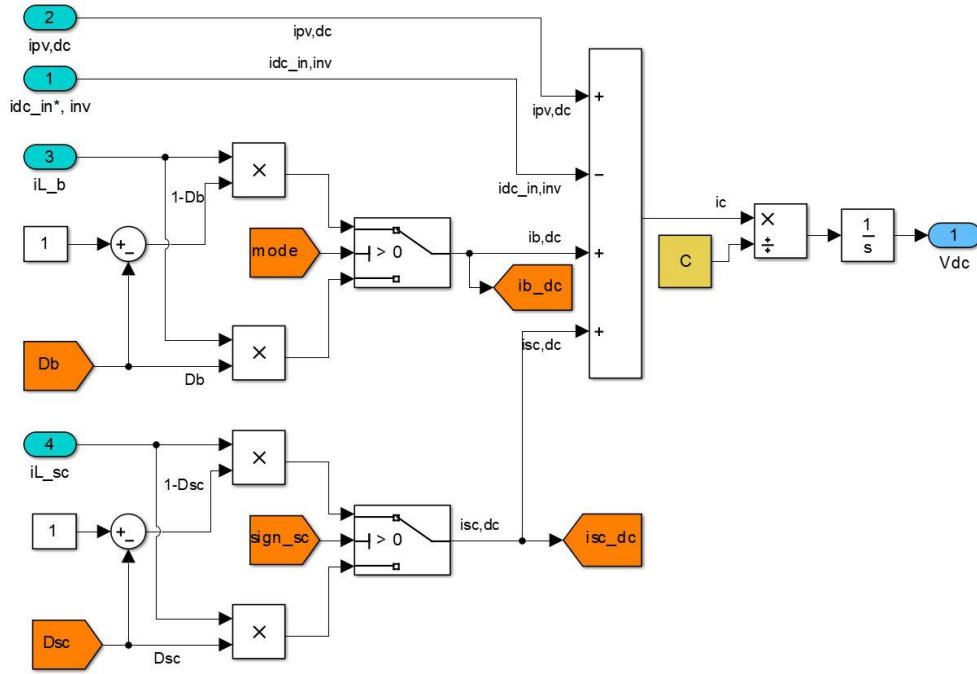


Figure 3.61: DC-link subsystem in Simulink

The dynamics of the DC-bus voltage can be expressed by the following equation (82), related to the input power (P_{dc}) and the average output power of the inverter (P_{ac}) [305]:

$$\frac{d}{dt} \left(\frac{1}{2} C_{dc} v_{dc}^2 \right) = P_{dc} - P_{ac} = P_{dc} - (P_{load} + P_g) = P_{dc} - P_{load} - \frac{v_g i_g}{2} \quad (82)$$

where v_g and i_g are the amplitude of the grid voltage and current (averaged large signals), respectively.

In order to examine the dynamic behavior of the inverter, the parameters of the above equation must be expanded to include the produced dynamics. A small-signal model can be obtained for the steady-state condition in terms of the constant value of the input power of the inverter (P_{dc}) and the constant value of the amplitude of the grid voltage

(V_g). Therefore, for the investigation of the impact of the amplitude of the grid current variation on the average DC-bus voltage, one can neglect P_{dc} and P_{load} . This is done in the framework of a simplified sensitivity analysis, which is sufficient for the study of the impact of the grid current variation on the DC-bus voltage. Thus, the input voltage and the amplitude of the grid current ($v_{dc}(t)$, $i_g(t)$) can be represented by the sum of their quiescent values (V_{dc} , I_g) and small ac variations in time ($\hat{v}_{dc}(t)$, $\hat{i}_g(t)$).

$$v_{dc}(t) = V_{dc} + \hat{v}_{dc}(t) \quad (83)$$

$$i_g(t) = I_g + \hat{i}_g(t) \quad (84)$$

In addition, the ac variations are assumed to be relatively small in magnitude compared to the dc quiescent values:

$$|\hat{v}_{dc}(t)| \ll |V_{dc}|, \quad |\hat{i}_g(t)| \ll |I_g| \quad (85)$$

Thus, equation (82) can be linearized by expanding and separating the steady-state terms and small-signal terms as follows:

$$\frac{d}{dt} \left(\frac{1}{2} C_{dc} (V_{dc} + \hat{v}_{dc}(t))^2 \right) = - \frac{V_g (I_g + \hat{i}_g(t))}{2} \quad (86)$$

or, upon collecting relevant terms,

$$\frac{d}{dt} \left(\underbrace{\frac{1}{2} C_{dc} V_{dc}^2}_{dc \text{ term}} + \underbrace{\frac{C_{dc} V_{dc} \hat{v}_{dc}(t)}{1st \text{ order ac term (linear)}}}_{1st \text{ order ac term (linear)}} + \underbrace{\frac{1}{2} C_{dc} \hat{v}_{dc}^2(t)}_{2nd \text{ order ac term (nonlinear)}} \right) = \underbrace{\left(- \frac{V_g I_g}{2} \right)}_{dc \text{ term}} + \underbrace{\left(- \frac{V_g \hat{i}_g(t)}{2} \right)}_{1st \text{ order ac term (linear)}}$$

The 2nd-order small ac quantities are neglected (see assumptions (85)). Moreover, the dc terms on the right-hand side are equal to the dc terms on the left-hand side and equal to zero (derivative of dc term is zero). Consequently, the remaining terms of the above equation are only the linear first order terms.

$$\frac{d}{dt} (C_{dc} V_{dc} \hat{v}_{dc}(t)) = - \frac{V_g \hat{i}_g(t)}{2} \quad (87)$$

Applying Laplace transforms (with zero initial conditions) in equation (87), yields:

$$s C_{dc} V_{dc} \hat{v}_{dc}(s) = - \frac{V_g \hat{i}_g(s)}{2} \quad (88)$$

Therefore, the required small-signal transfer function of the input voltage by the grid current amplitude is given by equation (89) below [304], [305].

$$G_{vi}(s) = \frac{\hat{v}_{dc}(s)}{\hat{i}_g(s)} = -\frac{V_g}{2C_{dc}V_{dc}s} \quad (89)$$

The above transfer function has negative static gain, showing that any shift from equilibrium can lead the DC-bus voltage to diverge at a rate that corresponds to the static gain of the small-signal model [220]. This transfer function, which is important for the DC-bus voltage control (voltage controller) of the inverter, is examined in the sub-Section 3.8.3.

3.8.3 Inverter control: Design of DC-bus voltage controller and calculation of inverter reference current

In this sub-Section, the DC-bus voltage control and the grid synchronization that are presented in the schematic of Figure 3.62, are examined. As the PV system is grid-connected, the inverter is responsible for the DC-bus voltage control [30], [31], [39], [304], [308]. In order to maintain DC-bus voltage stable near the reference value of 400 V, a voltage controller is used, where a reference magnitude for the grid current, and hence for the inverter output current is obtained, as shown in Figure 3.63.

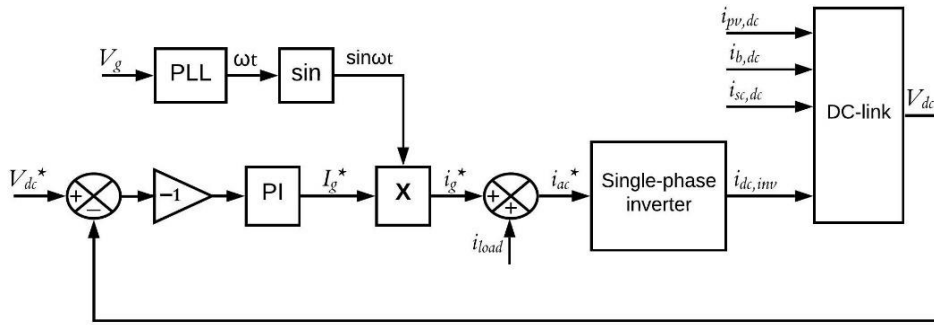


Figure 3.62: Schematic of the inverter control which consists of the DC-bus voltage control and the PLL for the calculation of the inverter reference output current

Regarding the grid synchronization, the task of the inverter is to generate an AC output current in phase with the grid voltage. The PLL circuit provides the reference signal to the inverter, synchronized to the grid frequency. Then, this signal ($\sin\omega t$) is multiplied with the reference signal (output of the PI controller), which corresponds to the reference amplitude of the grid current (see Figure 3.62). Therefore, a reference AC output current

is extracted for the inverter. Through the inverter model, a reference input DC current is obtained (equation (77)) which is used on the DC-link subsystem (see sub-Section 3.8.2). The Simulink model for the DC-bus voltage control and the reference inverter current calculation is presented in Figure 3.64.

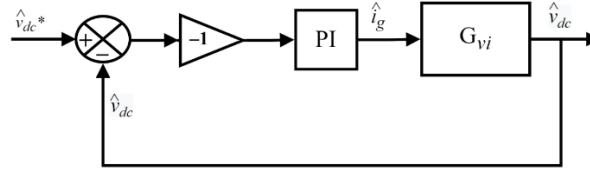


Figure 3.63: Block diagram of the DC-bus voltage control loop

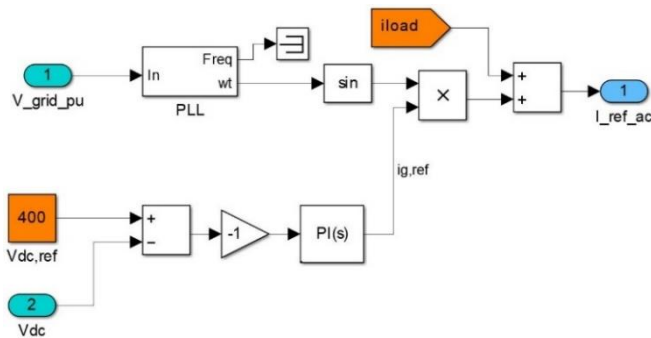


Figure 3.64: Simulink model for the DC-bus voltage control and the reference inverter current calculation

Figure 3.65 shows the small-signal model in Simulink, where the DC-bus voltage control is performed. The required small-signal transfer function was examined previously in sub-Section 3.8.2 and corresponds to equation (89). Assuming that the DC-link capacitance is 5000 μF , the DC-bus voltage is 400 V and the amplitude of the grid voltage is $230\sqrt{2}$ V, then the small-signal transfer function becomes:

$$G_{vi}(s) = \frac{\hat{v}_{dc}(s)}{\hat{i}_g(s)} = -\frac{81.32}{s} \quad (90)$$

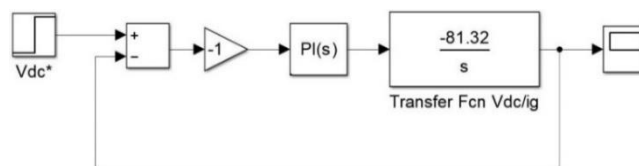


Figure 3.65: Small-signal Simulink model of the DC-bus voltage control loop

The PI controller gains, K_p and K_i , must be tuned and set very accurately with a low crossover frequency to mitigate the double line frequency of 100 Hz on the DC-bus voltage. Therefore, the oscillations in the output current of the inverter are limited [304], [305]. For a crossover frequency of about 40 Hz (or 250 rad/s) and a PM of 65° , the PI controller gains are set to $K_p = 2.79$ and $K_i = 324.81$. The Bode plot of the open-loop transfer function with and without compensation for the DC-bus voltage control loop design is shown in Figure 3.66.

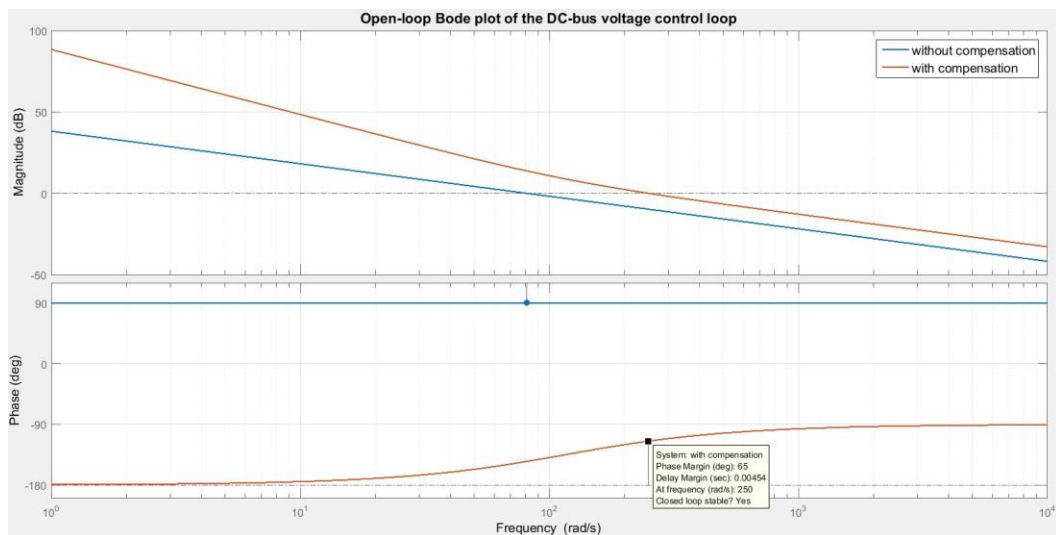


Figure 3.66: Open-loop Bode plot of the DC-bus voltage control loop

3.9 Power management algorithm (PMA)

The most important part of a grid-connected PV system with energy storage is the adopted control scheme and the power management methodology employed to manage the power transfer between the PV system, the storage, the building load and the grid. In this Section a comprehensive description of the proposed PMA, used for a balanced and better utilization of the generated PV power, storage, and building load, is provided.

3.9.1 Battery-only algorithm ¹⁴

3.9.1.1 Theory and mathematical analysis

The block diagram of the proposed grid-connected PV system with battery-only storage is presented in Figure 3.67, where:

- ✓ the MPPT control provides the maximum power point for the operation of the PV system (see Section 3.2)
- ✓ the Power Management maintains the power equilibrium of the system prioritizing the utilization of the PV and the battery
- ✓ the battery bidirectional converter provides the necessary power for the charging/discharging of the battery.
- ✓ the DC-bus voltage control and PLL keeps the voltage stable at 400 V at the DC-bus side and ensures the grid synchronization (see sub-Sections 3.8.2 and 3.8.3)

In this sub-Section, the power management of a battery-only storage system is performed to balance the produced and supplied power with the demanded power.

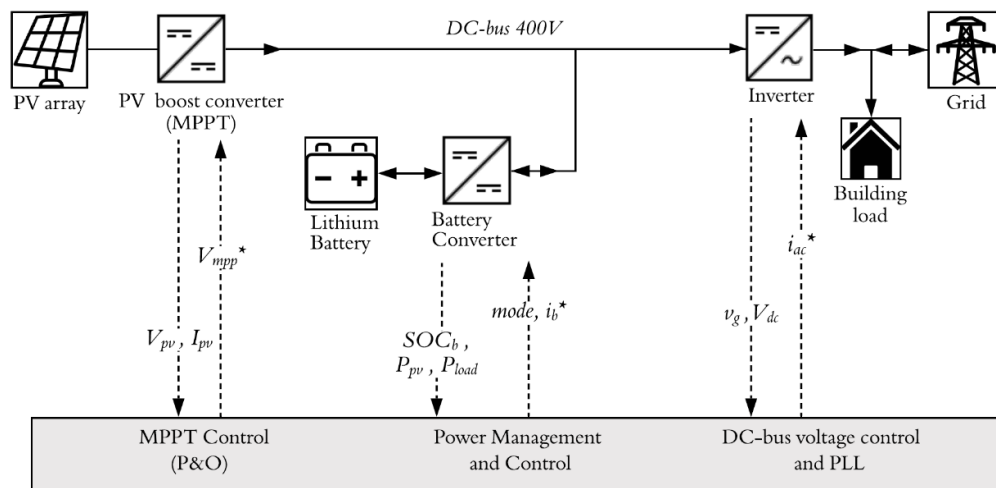


Figure 3.67: Block diagram of the grid-connected PV system with battery-only storage

¹⁴ Sub-Section 3.9.1 contains material from published paper [316]

The PMA is responsible for observing and managing the generated PV power, the SOC of the battery, the load power and the power absorbed from the grid in order to increase the energy self-consumption and self-sufficiency of the building [31], [33], [36]. The battery SOC limits are set to 20–90% in order to avoid deep charging/discharging cycles and extend the battery lifetime.

The flowchart in Figure 3.68 represents the PMA that is adopted in this study for the charging and discharging process of the battery-only storage system. There are two different modes, the Excess Power Mode (EPM) and the Deficit Power Mode (DPM). The EPM represents the period during which the generated PV power is higher than the required load power. During EPM the SOC of the battery is monitored, so that it does not exceed its limits. The DPM corresponds to the period when the generated PV power is lower than the required load power. During DPM the SOC of the battery is monitored, to avoid deep discharging cycles. It should be noted here that the “mode” parameter corresponds to the mode (boost or buck) of the battery converter. In other words, during EPM “mode” is set to zero (mode = 0), which corresponds to the buck-mode (charging mode), and during DPM “mode” is set to one (mode = 1), which corresponds to the boost-mode operation (discharging mode). All possible cases are discussed in detail below.

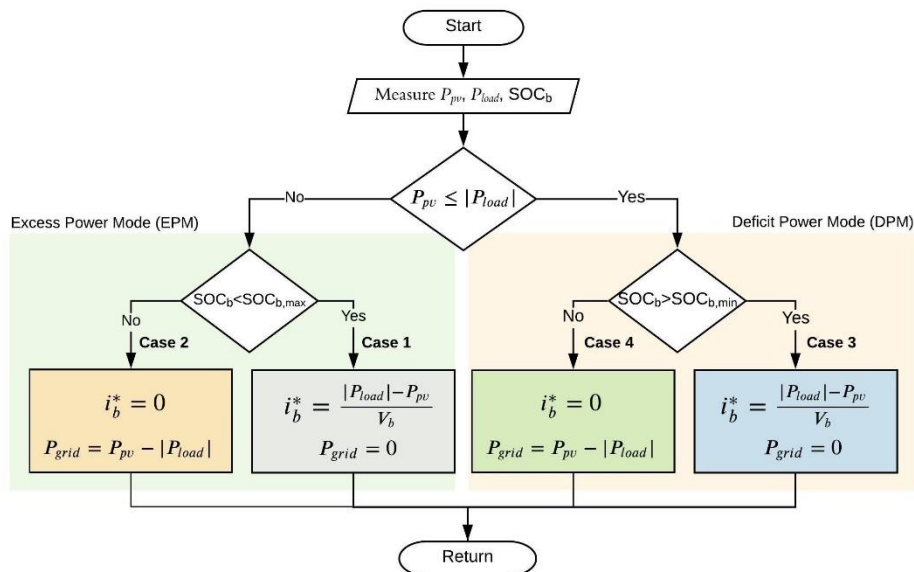


Figure 3.68: Power management flowchart of the battery-only operation

- **Case 1: $P_{pv} > P_{load}$ and $SOC_b < 90\%$ ($mode=0$)**
-

The produced PV power P_{pv} is larger than the load power P_{load} , and thus the excess PV power charges the battery, until the battery reaches its maximum SOC_b limit of 90%. The battery charging current can be calculated from the equation below. Note here that the current has negative value during charging.

$$i_b^* = \frac{|P_{load}| - P_{pv}}{V_b} \quad (91)$$

$$P_{grid} = 0 \quad (92)$$

- **Case 2: $P_{pv} > P_{load}$ and $SOC_b \geq 90\%$ ($mode=0$)**
-

The produced PV power is larger than the load power, and the battery reached the maximum SOC_b limit of 90%. Thus, all the produced PV power is transferred to the load and the grid (P_{grid} is the power injected to the grid). During this period, the battery current is zero.

$$i_b^* = 0 \quad (93)$$

$$P_{grid} = P_{pv} - |P_{load}| \quad (94)$$

- **Case 3: $P_{pv} \leq P_{load}$ and $SOC_b > 20\%$ ($mode=1$)**
-

The produced PV power is smaller than the load power. Therefore, the SOC of the battery must be measured in order to decide whether the required load power will be supplied by the battery or the grid. If the SOC_b is over 20%, then the battery will provide the desired power. For this case, the battery discharging current can be derived from the equation (95).

$$i_b^* = \frac{|P_{load}| - P_{pv}}{V_b} \quad (95)$$

$$P_{grid} = 0 \quad (96)$$

- **Case 4: $P_{pv} \leq P_{load}$ and $SOC_b \leq 20\%$ ($mode=1$)**
-

The produced PV power is smaller than the load power, but the battery SOC reached the minimum limit of 20%. Therefore, the grid will support the PV system for the excess required load power, as shown in equation (98). The battery current for this case is also zero.

$$i_b^* = 0 \quad (97)$$

$$P_{grid} = P_{pv} - |P_{load}| \quad (98)$$

3.9.1.2 Modeling and simulation

The Simulink model of the PMA with battery-only storage is presented in Figure 3.69. It corresponds to the flowchart presented in Figure 3.68 and it is implemented using MATLAB code.

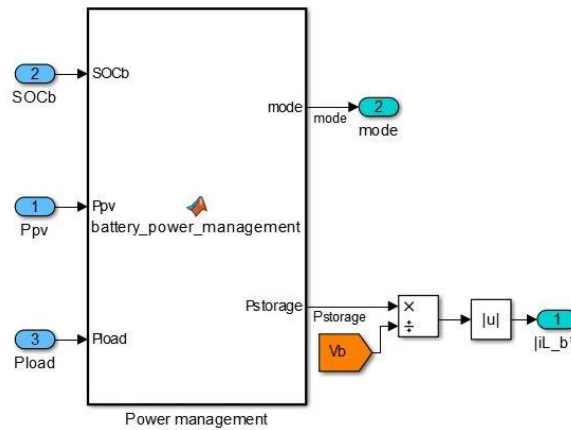


Figure 3.69: PMA for the battery-only operation in Simulink

3.9.2 Battery-supercapacitor hybrid energy storage algorithm ¹⁵

3.9.2.1 Theory and mathematical analysis

The block diagram of the proposed grid-connected PV system with battery-supercapacitor energy storage is presented in Figure 3.70, where:

- ✓ the MPPT control provides the maximum power point for the operation of the PV system (see Section 3.2)
- ✓ the Power Management ensures the effective power sharing between the PV, the hybrid storage, the load and the grid, prioritizing the utilization of the PV and the battery-supercapacitor storage for increased self-consumption and self-sufficiency.

¹⁵ Sub-Section 3.9.2 contains material from submitted paper [317]

- ✓ the battery and supercapacitor bidirectional converters provide the necessary power for charging/discharging. The design of the controllers is examined in sub-Section 3.8.1
- ✓ the DC-bus voltage control and PLL keeps the voltage at the DC-bus stable at 400 V and ensures grid synchronization (see sub-Sections 3.8.2 and 3.8.3)

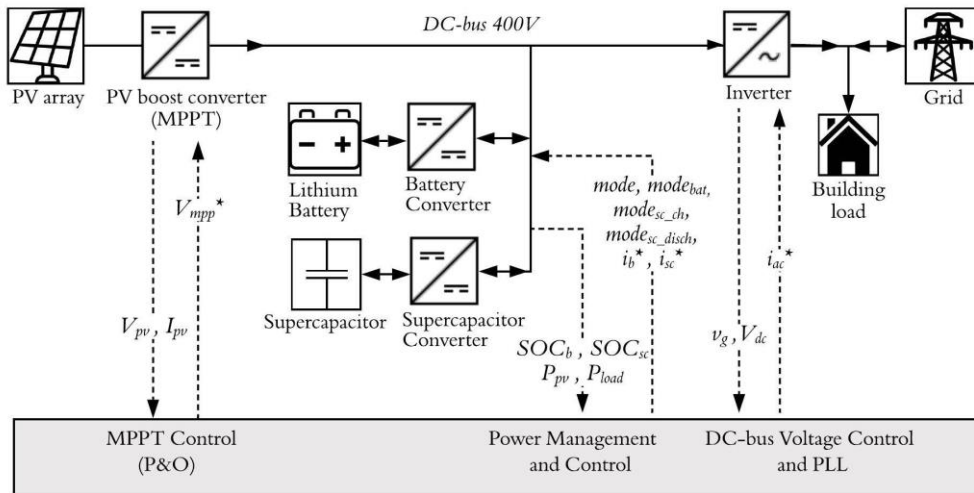


Figure 3.70: Block diagram of the grid-connected PV system with battery-supercapacitor energy storage

The battery-supercapacitor hybridization can relieve battery stress and extend battery lifetime. The electricity demand of the building is satisfied through the PV system, the energy storage system, and/or the grid. In this sub-Section, a local PMA is proposed for the hybrid storage model for a balanced and better utilization of the generated PV power, storage, and building load. Specifically, the proposed algorithm focuses on the availability of storage and produced PV power (instead of grid), reducing the peaks in generation or demand and increasing the self-consumption and self-sufficiency of the building. Therefore, the idea is to provide power to the residential load from the PVs (if available during sunlight) and/or the hybrid storage. If none of the PVs and storage are available, then the grid will supply the required amount of power. The battery is considered to be the main storage element, while the supercapacitor provides a supportive function to the battery or the grid (if the battery is not available). Therefore, the supercapacitor (if available) is activated for charging/discharging by absorbing/supplying high-frequency current variations.

The PMA for the hybrid storage system is responsible for observing the generated PV power, the battery SOC, the supercapacitor SOC and the load power, in order to manage the supplied/absorbed grid power and to increase the energy self-consumption and self-sufficiency of the building. Here the battery SOC operating range is set between 20–90% in order to avoid deep charging/discharging cycles and to extend battery lifetime. Also, it is recommended not to use 100% of the supercapacitor’s stored energy, hence the supercapacitor SOC operating range is set between 50–95% [268], [269].

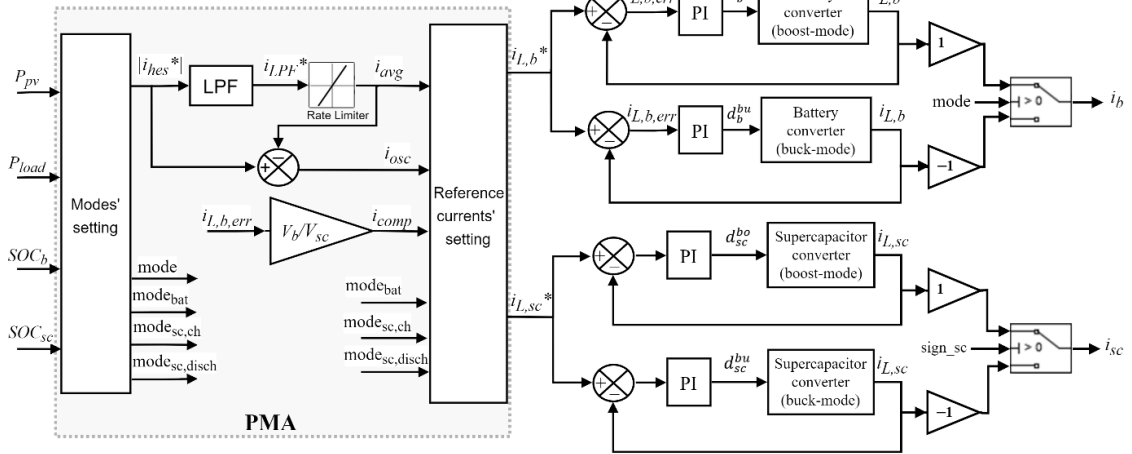


Figure 3.71: Control block diagram of the battery and supercapacitor current calculation through the PMA

As shown in Figure 3.71, the average (low-frequency) current (i_{LPF}^*) of the reference total hybrid current (i_{hes}^*) is extracted using a LPF [309]–[311]. The cut-off frequency of the LPF is chosen to be 5 Hz, so that the supercapacitor responds to variations occurring within 0.2 seconds [22], [312]. A rate limiter is also added to limit the high charging/discharging rates of the battery current, whereby avoiding high transients, and hence the resulting current is the average current (i_{avg}). Then, the difference between the remaining amount (i_{avg}) from the total hybrid current corresponds to the high-frequency component (i_{osc}). The reference inductor current for the battery converter ($i_{L,b}^*$) is calculated based on the availability of PV, battery and supercapacitor (see Table 3.6), and is compared to the actual inductor current ($i_{L,b}$). The remaining error current ($i_{L,b,err}$) passes through a PI controller to generate the appropriate duty cycle (d_b) for the semiconductors of the battery bidirectional converter.

$$i_{LPF}^* = f_{LPF}(i_{hes}^*) \quad (99)$$

$$i_{avg} = f_{RL}(i_{LPF}^*) \quad (100)$$

$$i_{osc} = i_{hes}^* - i_{avg} \quad (101)$$

$$i_{L,b,err} = i_{L,b}^* - i_{L,b} \quad (102)$$

In addition, due to the slow dynamics (regarding battery, controller and converter operation), a compensator was added to the supercapacitor current calculation to compensate for transients that the battery might not instantly track. This helps in a faster DC-bus voltage regulation [312]. Hence, the uncompensated battery power is handled by the supercapacitor, where the compensated current (i_{comp}) is expressed by:

$$i_{comp} = i_{L,b,err} \frac{V_b}{V_{sc}} \quad (103)$$

where V_b is the battery voltage and V_{sc} is the supercapacitor voltage. The reference inductor current for the supercapacitor converter ($i_{L,sc}^*$) is computed based on the availability of PV, battery and supercapacitor (see Table 3.6) and is compared to the actual inductor current ($i_{L,sc}$). The error current passes through a PI controller to generate the appropriate duty cycle (d_{sc}) for the semiconductors of the supercapacitor bidirectional converter.

Based on the mode of operation, a final decision is made on the proper sign of inductor current (see Figure 3.71). Specifically, it is assumed that during discharging (boost-mode) the battery and supercapacitor currents are positive, while during charging (buck-mode) they are negative. Therefore, the battery and supercapacitor currents, i_b and i_{sc} correspond to the input battery and supercapacitor currents.

The flowchart in Figure 3.73 presents the proposed PMA for the process of charging and discharging the hybrid battery-supercapacitor storage system. It should be noted here that the “mode” parameter corresponds to the mode of the battery converter (mode = 1 for boost-mode, mode = 0 for buck-mode). Also, the “mode_{bat}” parameter corresponds to the battery availability for charging/discharging; namely, mode_{bat} = 1 if the battery is available for charging/discharging, whereas mode_{bat} = 0 if the battery SOC limits have been reached. Regarding the charging and discharging mode of the supercapacitor, parameters “mode_{sc,ch}” and “mode_{sc,disch}” are introduced, respectively. If

the supercapacitor is available for charging or discharging, the corresponding modes are set to one, otherwise they are set to zero.

Considering all possible value combinations of the parameters, there are 12 cases that one can deal with, as shown in Table 3.6, which contains conditions on power and SOC along with their respective modes' and reference currents' settings. All cases are discussed in detail below.

Table 3.6: Table of all possible cases with their corresponding modes' and reference currents' setting

Case	Conditions	Modes' setting	Reference Currents' setting
1	$P_{pv} > P_{load}$ $SOC_b < SOC_{b,max}$ $SOC_{sc,min} < SOC_{sc} < SOC_{sc,max}$	mode = 0 mode _{bat} = 1 mode _{sc,ch} = 1 mode _{sc,disch} = 1	$i_b^* = i_{avg}$ $i_{sc}^* = i_{osc} + i_{comp}$ $i_g = 0$
2	$P_{pv} > P_{load}$ $SOC_b < SOC_{b,max}$ $SOC_{sc} \geq SOC_{sc,max}$	mode = 0 mode _{bat} = 1 mode _{sc,ch} = 0 mode _{sc,disch} = 1	$i_b^* = \begin{cases} i_{avg} & , \text{ if } i_{osc} > 0 \\ i_{avg} + i_{osc} & , \text{ otherwise} \end{cases}$ $i_{sc}^* = \begin{cases} i_{osc} + i_{comp} & , \text{ if } i_{osc} > 0 \\ 0 & , \text{ otherwise} \end{cases}$ $i_g = 0$
3	$P_{pv} > P_{load}$ $SOC_b < SOC_{b,max}$ $SOC_{sc} \leq SOC_{sc,min}$	mode = 0 mode _{bat} = 1 mode _{sc,ch} = 1 mode _{sc,disch} = 0	$i_b^* = \begin{cases} i_{avg} + i_{osc} & , \text{ if } i_{osc} > 0 \\ i_{avg} & , \text{ otherwise} \end{cases}$ $i_{sc}^* = \begin{cases} 0 & , \text{ if } i_{osc} > 0 \\ i_{osc} + i_{comp} & , \text{ otherwise} \end{cases}$ $i_g = 0$
4	$P_{pv} > P_{load}$ $SOC_b \geq SOC_{b,max}$ $SOC_{sc,min} < SOC_{sc} < SOC_{sc,max}$	mode = 0 mode _{bat} = 0 mode _{sc,ch} = 1 mode _{sc,disch} = 1	$i_b^* = 0$ $i_{sc}^* = i_{osc}$ $i_g = i_{avg}$
5	$P_{pv} > P_{load}$ $SOC_b \geq SOC_{b,max}$ $SOC_{sc} \geq SOC_{sc,max}$	mode = 0 mode _{bat} = 0 mode _{sc,ch} = 0 mode _{sc,disch} = 1	$i_b^* = 0$ $i_{sc}^* = \begin{cases} i_{osc} & , \text{ if } i_{osc} > 0 \\ 0 & , \text{ otherwise} \end{cases}$ $i_g = \begin{cases} i_{avg} & , \text{ if } i_{osc} > 0 \\ i_{avg} + i_{osc} & , \text{ otherwise} \end{cases}$
6	$P_{pv} > P_{load}$ $SOC_b \geq SOC_{b,max}$ $SOC_{sc} \leq SOC_{sc,min}$	mode = 0 mode _{bat} = 0 mode _{sc,ch} = 1 mode _{sc,disch} = 0	$i_b^* = 0$ $i_{sc}^* = \begin{cases} 0 & , \text{ if } i_{osc} > 0 \\ i_{osc} & , \text{ otherwise} \end{cases}$ $i_g = \begin{cases} i_{avg} + i_{osc} & , \text{ if } i_{osc} > 0 \\ i_{avg} & , \text{ otherwise} \end{cases}$

7	$P_{pv} \leq P_{load}$ $SOC_b > SOC_{b,min}$ $SOC_{sc,min} < SOC_{sc} < SOC_{sc,max}$	$\text{mode} = 1$ $\text{mode}_{bat} = 1$ $\text{mode}_{sc,ch} = 1$ $\text{mode}_{sc,disch} = 1$	$i_b^* = i_{avg}$ $i_{sc}^* = i_{osc} + i_{comp}$ $i_g = 0$
8	$P_{pv} \leq P_{load}$ $SOC_b > SOC_{b,min}$ $SOC_{sc} \geq SOC_{sc,max}$	$\text{mode} = 1$ $\text{mode}_{bat} = 1$ $\text{mode}_{sc,ch} = 0$ $\text{mode}_{sc,disch} = 1$	$i_b^* = \begin{cases} i_{avg} & , \text{ if } i_{osc} > 0 \\ i_{avg} + i_{osc} & , \text{ otherwise} \end{cases}$ $i_{sc}^* = \begin{cases} i_{osc} + i_{comp} & , \text{ if } i_{osc} > 0 \\ 0 & , \text{ otherwise} \end{cases}$ $i_g = 0$
9	$P_{pv} \leq P_{load}$ $SOC_b > SOC_{b,min}$ $SOC_{sc} \leq SOC_{sc,min}$	$\text{mode} = 1$ $\text{mode}_{bat} = 1$ $\text{mode}_{sc,ch} = 1$ $\text{mode}_{sc,disch} = 0$	$i_b^* = \begin{cases} i_{avg} + i_{osc} & , \text{ if } i_{osc} > 0 \\ i_{avg} & , \text{ otherwise} \end{cases}$ $i_{sc}^* = \begin{cases} 0 & , \text{ if } i_{osc} > 0 \\ i_{osc} + i_{comp} & , \text{ otherwise} \end{cases}$ $i_g = 0$
10	$P_{pv} \leq P_{load}$ $SOC_b \leq SOC_{b,min}$ $SOC_{sc,min} < SOC_{sc} < SOC_{sc,max}$	$\text{mode} = 1$ $\text{mode}_{bat} = 0$ $\text{mode}_{sc,ch} = 1$ $\text{mode}_{sc,disch} = 1$	$i_b^* = 0$ $i_{sc}^* = i_{osc}$ $i_g = i_{avg}$
11	$P_{pv} \leq P_{load}$ $SOC_b \leq SOC_{b,min}$ $SOC_{sc} \geq SOC_{sc,max}$	$\text{mode} = 1$ $\text{mode}_{bat} = 0$ $\text{mode}_{sc,ch} = 0$ $\text{mode}_{sc,disch} = 1$	$i_b^* = 0$ $i_{sc}^* = \begin{cases} i_{osc} & , \text{ if } i_{osc} > 0 \\ 0 & , \text{ otherwise} \end{cases}$ $i_g = \begin{cases} i_{avg} & , \text{ if } i_{osc} > 0 \\ i_{avg} + i_{osc} & , \text{ otherwise} \end{cases}$
12	$P_{pv} \leq P_{load}$ $SOC_b \leq SOC_{b,min}$ $SOC_{sc} \leq SOC_{sc,min}$	$\text{mode} = 1$ $\text{mode}_{bat} = 0$ $\text{mode}_{sc,ch} = 1$ $\text{mode}_{sc,disch} = 0$	$i_b^* = 0$ $i_{sc}^* = \begin{cases} 0 & , \text{ if } i_{osc} > 0 \\ i_{osc} & , \text{ otherwise} \end{cases}$ $i_g = \begin{cases} i_{avg} + i_{osc} & , \text{ if } i_{osc} > 0 \\ i_{avg} & , \text{ otherwise} \end{cases}$

Note that $|i_b^| = i_{L,b}^*$ and $|i_{sc}^*| = i_{L,sc}^*$.

- **Case 1: $P_{pv} > P_{load}$, $SOC_b < 90\%$, $50\% < SOC_{sc} < 95\%$**

The produced PV power, P_{pv} , is larger than the load power, P_{load} , and thus the excess PV power charges the battery (mode = 0, mode_{bat} = 1). Also, the supercapacitor is within its minimum and maximum SOC limits, hence it is available for charging/discharging (mode_{sc,ch} = 1, mode_{sc,disch} = 1). The reference battery current corresponds to the low-frequency (average) charging current ($i_b^* = i_{avg}$), while the supercapacitor reference current is the high-frequency part of the charging current plus the compensated error battery current ($i_{sc}^* = i_{osc} + i_{comp}$). Also, the resulting grid current, i_g , is zero.

- **Case 2: $P_{pv} > P_{load}$, $SOC_b < 90\%$, $SOC_{sc} \geq 95\%$**
-

The produced PV power is larger than the load power (mode = 0), SOC_b is lower than its upper limit (mode_{bat} = 1), while the supercapacitor has reached its maximum SOC limit of 95% (mode_{sc,ch} = 0, mode_{sc,disch} = 1). Therefore, the supercapacitor is only available for discharging (where $i_{osc} > 0$), otherwise the reference supercapacitor current is zero. During the period where the battery is charging at an increasing rate, the supercapacitor current is zero and the battery absorbs the high-frequency current oscillations. When the battery charging current decreases (i.e., when the generated PV power decreases and/or the load power increases), the reference current for the battery and supercapacitor must be modified (see Table 3.6), because the supercapacitor is available for discharging. Also, in this case the grid current is zero.

- **Case 3: $P_{pv} > P_{load}$, $SOC_b < 90\%$, $SOC_{sc} \leq 50\%$**
-

In this case, the generated PV power is larger than the load power (mode = 0), SOC_b is lower than its upper limit (mode_{bat} = 1) and the supercapacitor has reached its minimum SOC_{sc} limit of 50% (mode_{sc,ch} = 1, mode_{sc,disch} = 0). Therefore, the supercapacitor is only available for charging (where $i_{osc} < 0$), otherwise the reference supercapacitor current is zero. During the period, if the battery is charging at a decreasing rate, the supercapacitor current is zero and the battery absorbs the high-frequency current oscillations. When the battery charging current increases (i.e., when the generated PV power increases and/or the load power decreases), the reference current for the battery and supercapacitor must be modified (see Table 3.6), because the supercapacitor is available for charging. Also, in this case the grid current is zero.

- **Case 4: $P_{pv} > P_{load}$, $SOC_b \geq 90\%$, $50\% < SOC_{sc} < 95\%$**
-

In Case 4, the generated PV power is larger than the load power (mode = 0), the battery has reached its maximum SOC limit of 90% (mode_{bat} = 0), and the supercapacitor remains between its minimum and maximum SOC limits (mode_{sc,ch} = 1, mode_{sc,disch} = 1). Therefore, the battery is fully charged, and the reference battery current is zero ($i_b^* = 0$). The supercapacitor is available for charging/discharging and absorbs/supplies the high-frequency current oscillations ($i_{sc}^* = i_{osc}$) and the remaining average current is injected into the grid.

- **Case 5: $P_{pv} > P_{load}$, $SOC_b \geq 90\%$, $SOC_{sc} \geq 95\%$**
-

The generated PV power is larger than the load power (mode = 0), and both the supercapacitor and the battery have reached their maximum SOC limits (mode_{bat} = 0, mode_{sc,ch} = 0, mode_{sc,disch} = 1). In other words, the battery is fully charged ($i_b^* = 0$) and the supercapacitor is only available for discharging (where $i_{osc} > 0$), otherwise the reference supercapacitor current is zero. During this period the grid absorbs the remaining power. When the current injected into the grid decreases (i.e., when the generated PV power decreases and/or the load power increases), the reference current for the supercapacitor must be modified (see Table 3.6), because the supercapacitor is available for discharging.

- **Case 6: $P_{pv} > P_{load}$, $SOC_b \geq 90\%$, $SOC_{sc} \leq 50\%$**
-

The generated PV power is larger than the load power (mode = 0). In addition, battery has reached its maximum SOC limit (mode_{bat} = 0), while the supercapacitor has reached its minimum SOC limit (mode_{sc,ch} = 1, mode_{sc,disch} = 0). During this mode, the battery is fully charged ($i_b^* = 0$) and the supercapacitor is fully discharged. Therefore, the supercapacitor is only available for charging (where $i_{osc} < 0$), otherwise the reference supercapacitor current is zero. Also, the grid absorbs the remaining power. During this period, if the grid absorbs power at a decreasing rate, the supercapacitor current is zero, and the grid absorbs the high-frequency current oscillations. If the grid current increases (i.e., when the generated PV power increases and/or the load power decreases), the reference current for the supercapacitor must be modified (see Table 3.6), because the supercapacitor is available for charging.

- **Case 7: $P_{pv} \leq P_{load}$, $SOC_b > 20\%$, $50\% < SOC_{sc} < 95\%$**
-

In Case 7, the load demand is higher than the produced PV power (mode = 1), the battery SOC remains higher than its lower limit (mode_{bat} = 1), and the supercapacitor remains between its minimum and maximum SOC limits (mode_{sc,ch} = 1, mode_{sc,disch} = 1). Therefore, the battery provides the remaining required average current ($i_b^* = i_{avg}$), while the supercapacitor handles the high-frequency part of the discharging current plus the compensated error battery current ($i_{sc}^* = i_{osc} + i_{comp}$). Additionally, the resulting grid current is zero.

- **Case 8: $P_{pv} \leq P_{load}$, $SOC_b > 20\%$, $SOC_{sc} \geq 95\%$**
-

In Case 8, the generated PV power is lower than the load power (mode = 1), the battery SOC remains higher than its lower limit (mode_{bat} = 1), and the supercapacitor has reached its upper SOC limit (mode_{sc,ch} = 0, mode_{sc,disch} = 1). Therefore, the supercapacitor is only available for discharging (where $i_{osc} > 0$), otherwise the reference supercapacitor current is zero. During the period where the battery is discharging at a decreasing rate, the supercapacitor reference current is zero and the battery supplies the load with a current that includes the high-frequency current oscillations. When the battery discharging current increases (i.e., when the generated PV power decreases and/or the load power increases), the reference current for the battery and supercapacitor must be modified (see Table 3.6), because the supercapacitor is available for discharging. In addition, in Case 8 the grid current is zero.

- **Case 9: $P_{pv} \leq P_{load}$, $SOC_b > 20\%$, $SOC_{sc} \leq 50\%$**
-

In this case, the load power is larger than the generated PV power (mode = 1), SOC_b is larger than its lower limit (mode_{bat} = 1) and the supercapacitor has reached its minimum SOC limit of 50% (mode_{sc,ch} = 1, mode_{sc,disch} = 0). Therefore, the supercapacitor is only available for charging (where $i_{osc} < 0$), otherwise the reference supercapacitor current is zero. During the period, if the battery is discharging at an increasing rate, the supercapacitor current is zero and the battery supplies the high-frequency current oscillations. When the battery discharging current decreases (i.e., when the generated PV power increases and/or the load power decreases), the reference current for the battery and supercapacitor must be modified (see Table 3.6), because the supercapacitor is available for charging. Also, during this case the grid current is zero.

- **Case 10: $P_{pv} \leq P_{load}$, $SOC_b \leq 20\%$, $50\% < SOC_{sc} < 95\%$**
-

In Case 10, the generated PV power is lower than the required load power (mode = 1), the battery has reached its minimum SOC limit of 20% (mode_{bat} = 0) and the supercapacitor remains between its minimum and maximum SOC limits (mode_{sc,ch} = 1, mode_{sc,disch} = 1). Therefore, the battery is fully discharged and hence the reference battery current is zero ($i_b^* = 0$). The supercapacitor is available for charging/discharging and absorbs/supplies the high-frequency current oscillations ($i_{sc}^* = i_{osc}$), while the required average current is supplied by the grid.

- **Case 11: $P_{pv} \leq P_{load}$, $SOC_b \leq 20\%$, $SOC_{sc} \geq 95\%$**
-

The load demand is larger than the generated PV power (mode = 1), the battery has reached its minimum SOC limit (mode_{bat} = 0) and the supercapacitor has reached its maximum SOC limit (mode_{sc,ch} = 0, mode_{sc,disch} = 1). In other words, the battery is fully discharged ($i_b^* = 0$) and the supercapacitor is only available for discharging (where $i_{osc} > 0$), otherwise the reference supercapacitor current is zero. During this period, the grid supplies the required power. When the current supplied by the grid increases (i.e., when the generated PV power decreases and/or the load power increases), the reference current for the supercapacitor must be modified (see Table 3.6), because the supercapacitor is available for discharging.

- **Case 12: $P_{pv} \leq P_{load}$, $SOC_b \leq 20\%$, $SOC_{sc} \leq 50\%$**
-

In Case 12, the generated PV power is lower than the load power (mode = 1). In addition, both the battery and the supercapacitor have reached their minimum SOC limits (mode_{bat} = 0, mode_{sc,ch} = 1, mode_{sc,disch} = 0). During this mode, the battery is fully discharged ($i_b^* = 0$). In addition, the supercapacitor is fully discharged, hence it is only available for charging (where $i_{osc} < 0$), otherwise the reference supercapacitor current is zero. Also, the grid supplies the required remaining power to the load. During this period, if the grid supplies power at an increasing rate, the supercapacitor current is zero, and the grid supplies the high-frequency current oscillations. When the grid current decreases (i.e., when the generated PV power increases and/or the load power decreases), the reference current for the supercapacitor must be modified (see Table 3.6), because the supercapacitor is available for charging.

3.9.2.2 Modeling and simulation

The Simulink model of the proposed PMA for the charging and discharging process of the battery-supercapacitor hybrid storage is presented in Figure 3.72. It corresponds to the flowchart presented in Figure 3.73. For simplicity, based on the twelve cases above, general equations for the battery and the supercapacitor reference currents are derived as follows.

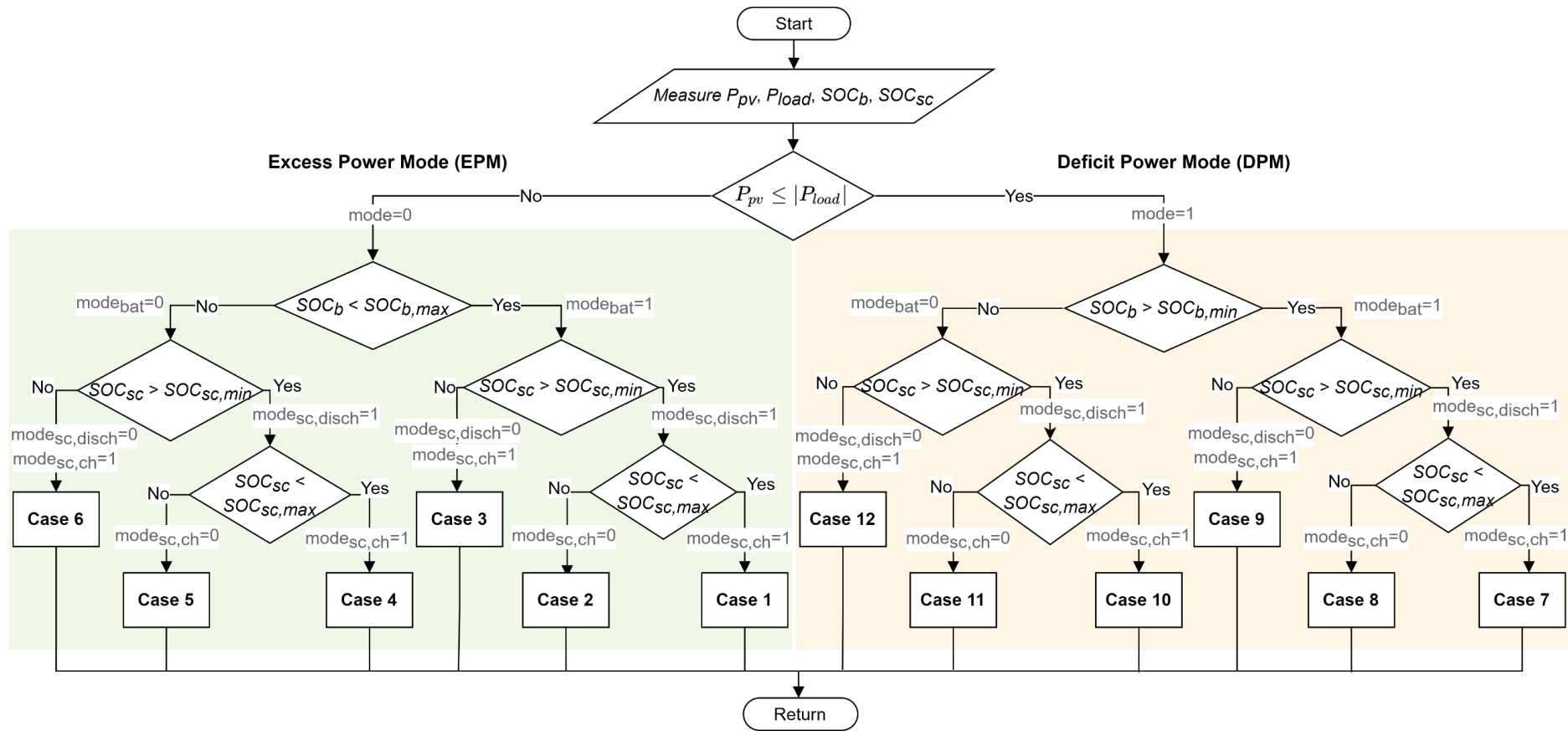


Figure 3.73: PMA for the charging and discharging process of the hybrid battery-supercapacitor storage system

4 Complete Model Results

The complete model of the battery-only storage application in Simulink is presented in Figure 4.1. It consists of a 3 kW_p PV array, a DC-DC boost converter, a MPPT control block (P&O), a single-phase VSI, a 10kWh battery pack and a bidirectional DC-DC converter for the battery.

The complete model of the battery-supercapacitor hybrid storage application in Simulink is presented in Figure 4.2. It contains a 3 kW_p PV array, a DC-DC boost converter, a MPPT control block (P&O), a single-phase VSI, a 10kWh battery pack, a battery bidirectional DC-DC converter, a 50.6 Wh supercapacitor pack and a supercapacitor bidirectional DC-DC converter.

To verify the proper operation of the proposed models, the simulations of the battery-only storage system and the battery-supercapacitor hybrid storage system are performed for different scenarios in long-term operation (24 hours) and short-term operation (10–30 seconds).

For the sake of clarity, it should be noted that the produced PV power is always positive, the load power is always negative, the battery and the supercapacitor power are positive when they supply power and negative when they absorb power, while the grid power is positive when it absorbs power and negative when it supplies power to the system. In addition, the mode for the battery converter is set to zero (mode = 0) during EPM (buck-mode or charging mode), while during DPM the mode of the battery converter is one (mode = 1), which corresponds to the boost-mode operation (or discharging mode). Also, mode_{bat}, mode_{sc,ch} and mode_{sc,disch} represent the availability of the battery and supercapacitor storage, respectively. In other words, when the battery or the supercapacitor are available for charging/discharging, the corresponding mode is one, and when they have reached their maximum/minimum SOC limits the corresponding mode is zero (idle mode).

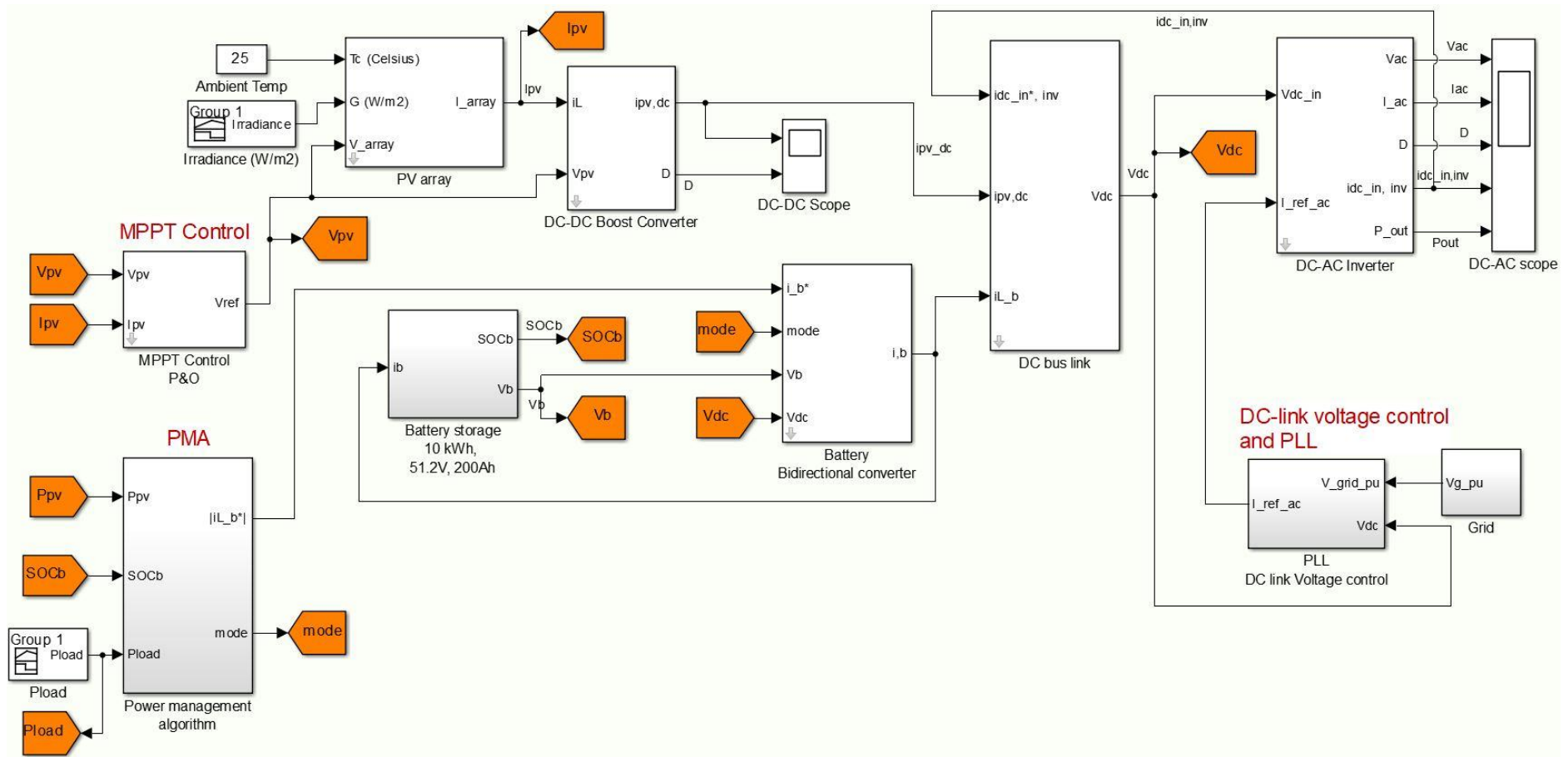


Figure 4.1: Complete model of the grid-connected PV system with battery-only storage in Simulink

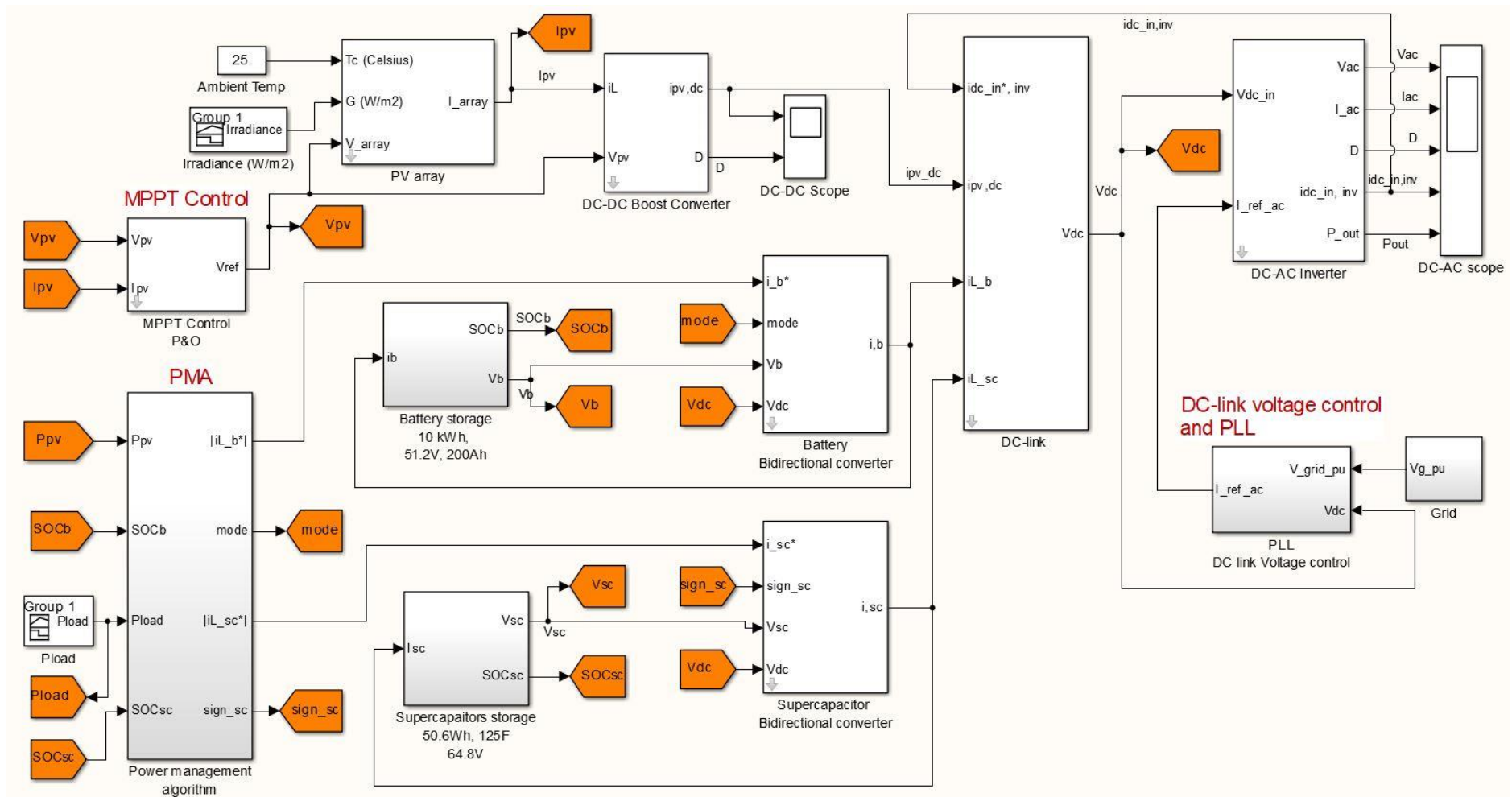


Figure 4.2: Complete model of the grid-connected PV system with battery-supercapacitor hybrid storage in Simulink

4.1 Results for the PV system with battery-only storage in long-term operation

In this scenario, the performance of the system in long-term operation is investigated (24 hours). The initial SOC of the battery is set to 50%. The solar and the load power as well as the results derived from the simulations are presented in Table 4.1.

Also, Figure 4.3 presents the PV power, Load power (average), Battery power and Grid power (average) during the period of 24 hours.

As one can observe from Table 4.1 and Figure 4.3, in the beginning the generated PV power is zero and the load power is 100 W. Therefore, this is Case 3 (as described in sub-Section 3.9.1), where the battery supplies the required power to the load. After the sunrise, the generated PV power is larger than the load power, and hence this is Case 1. During this case, the battery is charging until it reaches its maximum SOC limit of 90% (see Figure 4.4). The battery is fully charged at $t = 10.3$ hours (time 10:18) (Case 2), and all the produced power is transferred to the load and the grid. After that ($t = 13$ hours), the generated PV power is suddenly reduced and the load power is increased, so that the PV power is lower than the load power (Case 3). During this case, the battery starts to discharge having a positive power and current. After one hour ($t = 14$ hours), the generated PV power is increased and becomes larger than the load power, so now the battery is charging again (Case 1). At $t = 15$ hours, the PV power starts decreasing and the load power is now larger than the produced power (Case 3). During this period, the battery is discharging until it reaches its minimum SOC limit of 20%. At $t = 19.1$ hours (time 19:06), the battery is fully discharged (Case 4), hence the grid supports the load for the required power because the PV power is zero.

The above scenario verifies that the model works properly in long-term operation of 24 hours. Moreover, observing Table 4.1, power balance is achieved in all cases. Also, in Figure 4.4, it is observed that the battery current exhibits peaks during the transitions, and hence the battery is stressed. These oscillations can be eliminated by the supercapacitor integration.

Table 4.1: Simulation results of proposed PV system with battery-only storage in long-term operation (24 hours)

	Time (hours)	P_{pv} (W)	P_{load} (W)	P_b (W)	SOC_b	P_{grid} (W)
Case 3	0 – 1	0	-100	100	0.50	0
	1 – 2	0	-100	100	0.49	0
	2 – 3	0	-100	100	0.48	0
	3 – 4	0	-50	50	0.47	0
Case 1	4 – 5	80	-50	-30	0.466	0
	5 – 6	237	-100	-137	0.465	0
	6 – 7	520	-200	-320	0.48	0
	7 – 8	1252	-400	-852	0.51	0
	8 – 9	1932	-500	-1432	0.59	0
	9 – 10	2286	-600	-1686	0.73	0
	10 – 10.3	1696	-800	-896	0.88	0
Case 2	10.3 – 11	1696	-800	0	0.90	896
	11 – 12	2871	-1500	0	0.90	1371
	12 – 13	2667	-2000	0	0.90	667
Case 3	13 – 14	1105	-1500	395	0.89	0
Case 1	14 – 15	1844	-1500	-344	0.89	0
Case 3	15 – 16	1252	-1700	448	0.88	0
	16 – 17	520	-1900	1380	0.80	0
	17 – 18	102	-2500	2398	0.50	0
	18 – 19	0	-2700	2700	0.35	0
	19 – 19.1	0	-3000	3000	0.22	0
Case 4	19.1 – 20	0	-3000	0	0.20	-3000
	20 – 21	0	-3500	0	0.20	-3500
	21 – 22	0	-2000	0	0.20	-2000
	22 – 23	0	-1500	0	0.20	-1500
	23 – 24	0	-200	0	0.20	-200

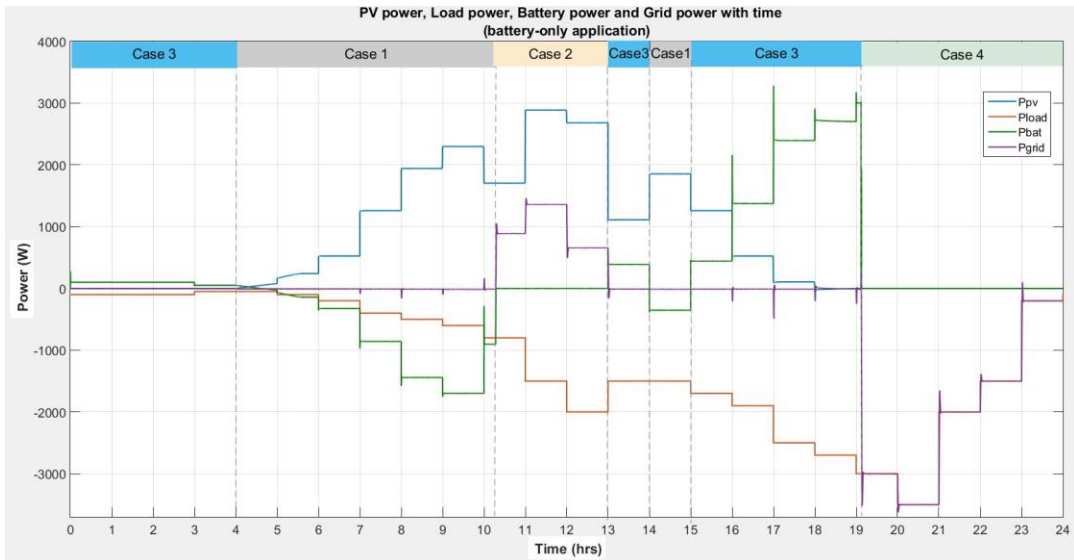


Figure 4.3: PV power (blue), Load power (red), Battery power (green) and Grid power (purple) in long-term operation (24 hours)

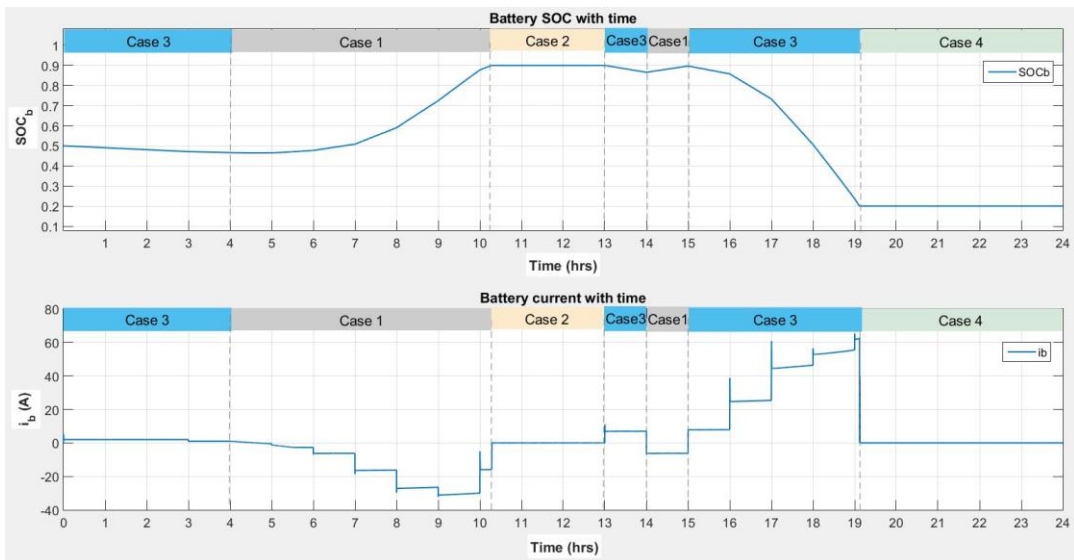


Figure 4.4: Battery SOC and battery current in long-term operation (24 hours)

4.2 Comparison between the battery-only and the battery-supercapacitor hybrid storage system

For this scenario, the effectiveness of the integration of the supercapacitor must be verified. The same scenario as presented in Section 4.1 is considered. Figure 4.5 shows the battery SOC with time for the battery-only and the battery-supercapacitor hybrid storage application. As can be observed, in the case of the battery-only application, the

battery reaches its maximum and minimum SOC limits faster than in the case of the hybrid storage. This is because the battery is more stressed as it absorbs/supplies power with high frequencies (oscillations) during the transitions. This phenomenon can reduce the battery lifetime. Moreover, Figure 4.6 presents the battery current for the battery-only and the battery-supercapacitor hybrid storage application. For the case of the battery-only application, the current exhibits peaks during the transitions. On the other hand, for the case of the hybrid storage, these peaks are eliminated by the supercapacitor. More investigation the supercapacitor can be found in the next Section 4.3.

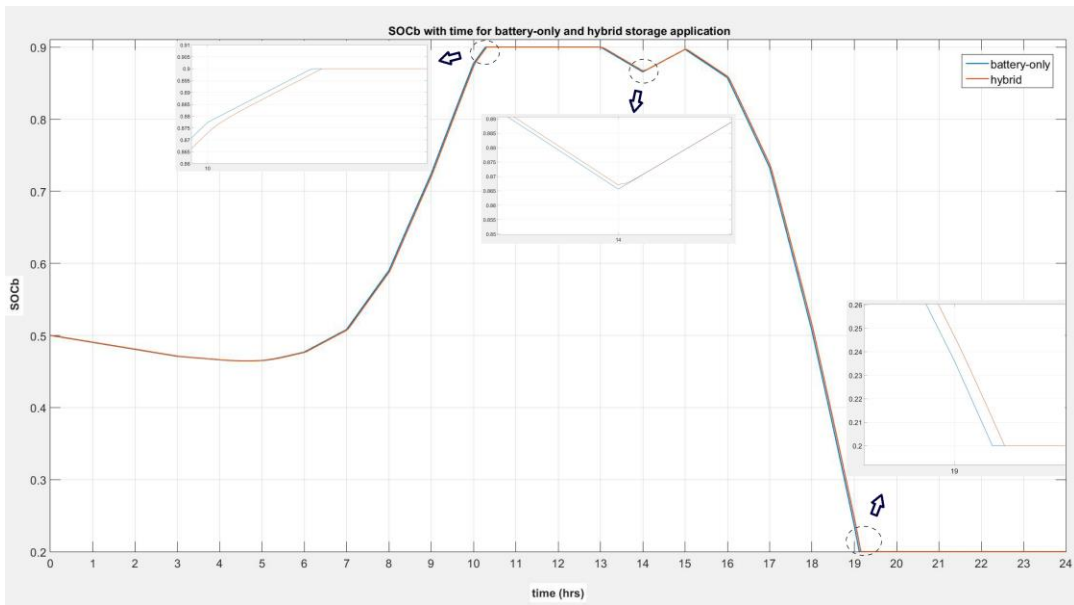


Figure 4.5: Battery SOC for the battery-only (blue) and the hybrid (red) storage application

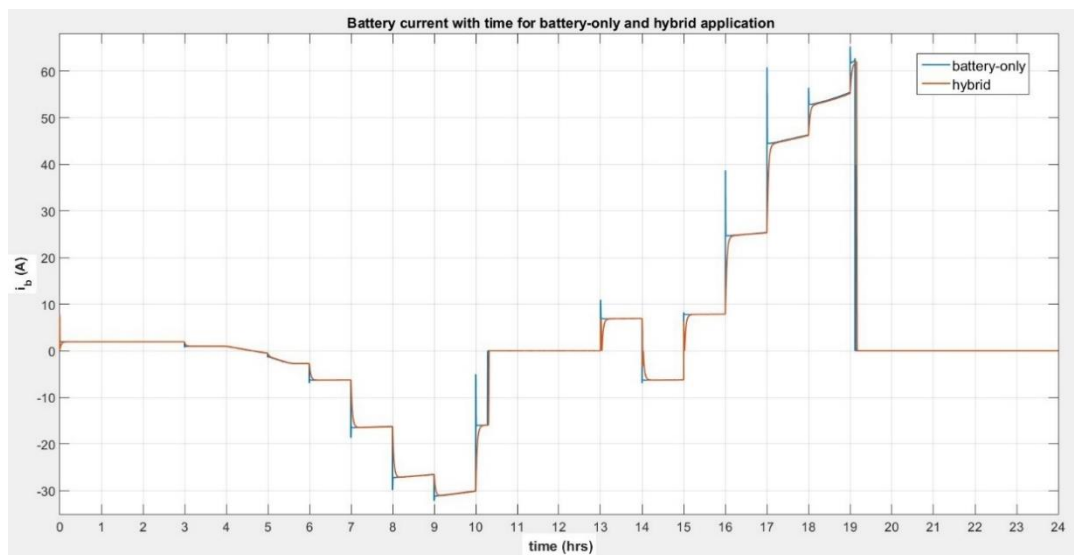


Figure 4.6: Battery current for the battery-only (blue) and the hybrid (red) storage application

4.3 Results for the PV system with battery-supercapacitor hybrid storage in short-term operation

This Section is divided into two parts (sub-Sections), in each of which EPM and DPM are examined respectively, over short time periods (10–30 seconds), in order to verify the operation of the system during sudden changes in solar irradiance (and hence in produced PV power) and in load power. To this end, rapid variations in solar irradiance and/or load are assumed for every second. Furthermore, each mode (EPM and DPM) is divided into two simulation scenarios: (i) when the supercapacitor is near its maximum SOC limit, and (ii) when the supercapacitor is near its minimum SOC limit. Therefore, all cases of the flowchart in Figure 3.73 are investigated.

4.3.1 Excess Power Mode (EPM)

4.3.1.1 Scenario 1: Supercapacitor reaches its maximum SOC limit during EPM

The scenario 1 of the Excess Power Mode (EPM) is carried out here, where in almost all cases the produced PV power is larger than the required load power. The initial SOC of the battery is set to 89.965% ($SOC_b = 0.89965$) and the initial SOC of the supercapacitor to 95% ($SOC_{sc} = 0.95$). Recall that the maximum SOC limits for the battery and supercapacitor are 90% and 95%, respectively. Therefore, in the beginning the supercapacitor is already at its maximum SOC limit, and it is only available for discharging.

The results for the power and SOC, derived from the simulations are presented in Table 4.2. Also, Figure 4.7 shows the PV power, load power (average), battery power, supercapacitor power and grid power (average) over a period of 30 seconds. Additionally, Figure 4.8 shows the mode of the battery converter, as well as the availability modes of the battery and the supercapacitor (charging and discharging), respectively.

As can be seen from Table 4.2 and Figure 4.7, in the beginning ($t = 0\text{--}4$ s) the PV generates electricity, while the load power is zero. Also, the supercapacitor is at its maximum SOC limit. Therefore, this is Case 2 (as described in sub-Section 3.9.2), where the battery is charging and absorbing all the produced PV power. After that ($t = 4$ s), the

PV power remains larger than the load power, and hence the battery is charging. At the same time, the charging rate of the battery has decreased, and hence the supercapacitor is discharging (Case 1). The battery continues charging until it reaches its maximum SOC limit of 90%, at $t = 8.6$ s (Case 4). During this case, the supercapacitor handles the high-frequency oscillations, and the remaining average power is injected into the grid. At $t = 12$ s, the generated PV power decreases and the load power increases, so that the PV power is lower than the load power (Case 7). During this case, the battery is discharging with a positive power. After that (at $t = 16$ s), the generated PV power increases and is larger than the load power, hence the battery is charging again and the supercapacitor is available for charging/discharging (Case 1). During the sudden changes of PV power and/or the load power, the supercapacitor absorbs/supplies the high-frequency power variations, reducing the oscillations in the battery power. Following, at $t = 23.3$ s, the battery reaches its maximum SOC limit (Case 4), hence the grid absorbs the average power difference between the PV and the load power, while the supercapacitor handles the rapid changes that occur within 0.2 seconds. After that, at $t = 27$ s, the supercapacitor reaches its maximum SOC limit (Case 5) and all the produced power is transferred to the load and the grid (with oscillations). During this case, both the battery and the supercapacitor are fully charged, and the supercapacitor is only available for discharging. At $t = 29$ s, the grid power absorption decreases and therefore the supercapacitor can deliver the high-frequency variations and it is discharging (Case 4).

The above scenario, when the supercapacitor is near its maximum SOC limit during EPM, verifies that the model works properly and power balance is achieved in all cases. It can also be noticed that the model reacts very fast and works properly during the mode transitions between EPM and DPM, and vice versa.

Table 4.2: Simulation results of proposed PV system with hybrid storage in EPM (Scenario 1)

	Time (sec)	P_{pv} (W)	P_{load} (W)	P_b (W)	SOC_b	SOC_{sc}	P_{grid} (W)
Case 2	0 – 1	1105	0	-1105	0.89965	0.95	0
	1 – 2	1400	0	-1400	0.89972	0.95	0
	2 – 3	1991	0	-1991	0.89976	0.95	0
	3 – 4	2286	0	-2286	0.89983	0.95	0
Case 1	4 – 5	2579	-1000	-1579	0.89985	0.94996	0
	5 – 6	2579	-1000	-1579	0.89990	0.94996	0
	6 – 7	2871	-800	-2071	0.89995	0.94998	0
	7 – 8.6	2871	-1500	-1371	0.89998	0.94994	0
Case 4	8.6 – 9	2871	-1500	0	0.9	0.94994	1371
	9 – 10	2871	-1500	0	0.9	0.94994	1371
	10 – 11	2871	-2400	0	0.9	0.94988	471
	11 – 12	2871	-2400	0	0.9	0.94988	471
Case 7	12 – 13	2286	-3500	1214	0.89997	0.94978	0
	13 – 14	2286	-3500	1214	0.89994	0.94978	0
	14 – 15	1696	-3500	1804	0.89990	0.94974	0
	15 – 16	1696	-2000	304	0.89989	0.94984	0
Case 1	16 – 17	2286	-2000	-286	0.89990	0.94987	0
	17 – 18	2286	-2000	-286	0.89990	0.94987	0
	18 – 19	2871	-2500	-371	0.89991	0.94988	0
	19 – 20	2871	-2500	-371	0.89992	0.94988	0
	20 – 21	2871	-2500	-371	0.89993	0.94988	0
	21 – 22	2871	-1300	-1571	0.89997	0.94996	0
	22 – 23.3	2286	-1300	-986	0.89999	0.94992	0
Case 4	23.3 – 24	2286	-1300	0	0.9	0.94992	986
	24 – 25	1991	-700	0	0.9	0.94994	1291
	25 – 26	1991	-900	0	0.9	0.94993	1091
	26 – 27	2871	-900	0	0.9	0.94998	1971
Case 5	27 – 28	2871	-200	0	0.9	0.95	2671
	28 – 29	2871	0	0	0.9	0.95	2871
Case 4	29 – 30	2871	-500	0	0.9	0.94997	2371

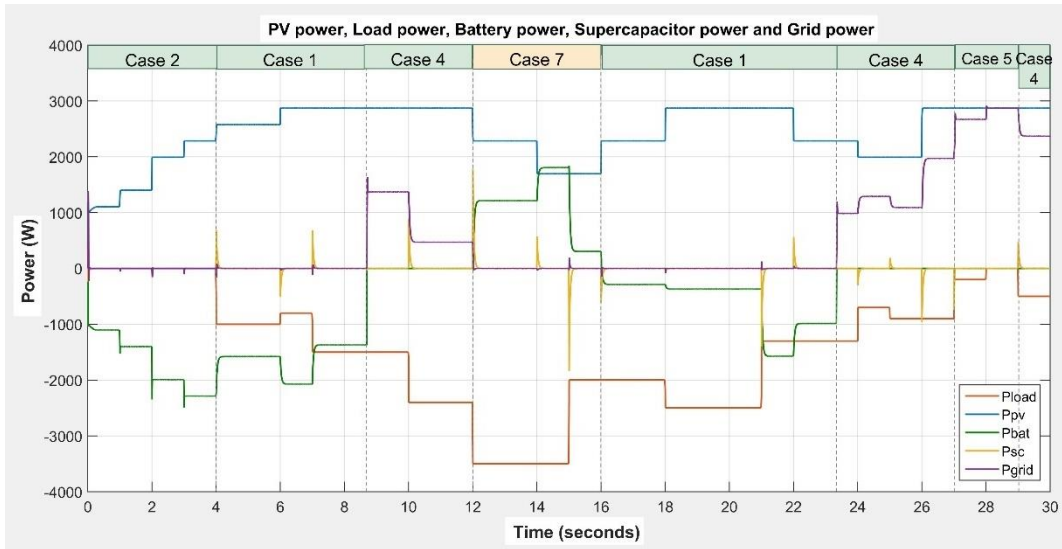


Figure 4.7: PV power (blue), Load power (red), Battery power (green), Supercapacitor power (yellow) and Grid power (purple) (Scenario 1)

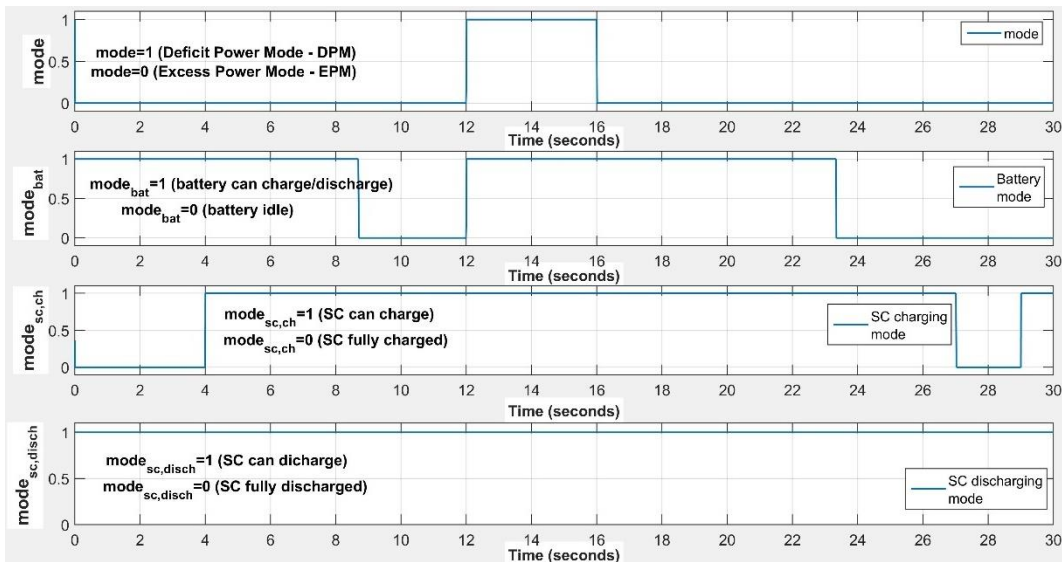


Figure 4.8: Mode of the battery converter, and availability modes of the battery and the supercapacitor (charging and discharging), respectively (Scenario 1)

Figure 4.9 shows the battery and supercapacitor current on the storage side, while Figure 4.10 shows the PV current, battery current and supercapacitor current on the DC-link side. One can observe that during Case 2 ($t = 0-4$ s), where the supercapacitor is idle, the battery current exhibits peaks during the transitions, and hence the battery is stressed. These oscillations are eliminated with the integration of the supercapacitor at $t = 4$ s. Therefore, the supercapacitor handles the rapid changes of current, thus relieving the

battery and extending its lifetime. Next, Figure 4.11 shows the battery SOC and the battery voltage, while Figure 4.12 shows the supercapacitor SOC and the supercapacitor voltage, where both storage methods work properly within their limits.

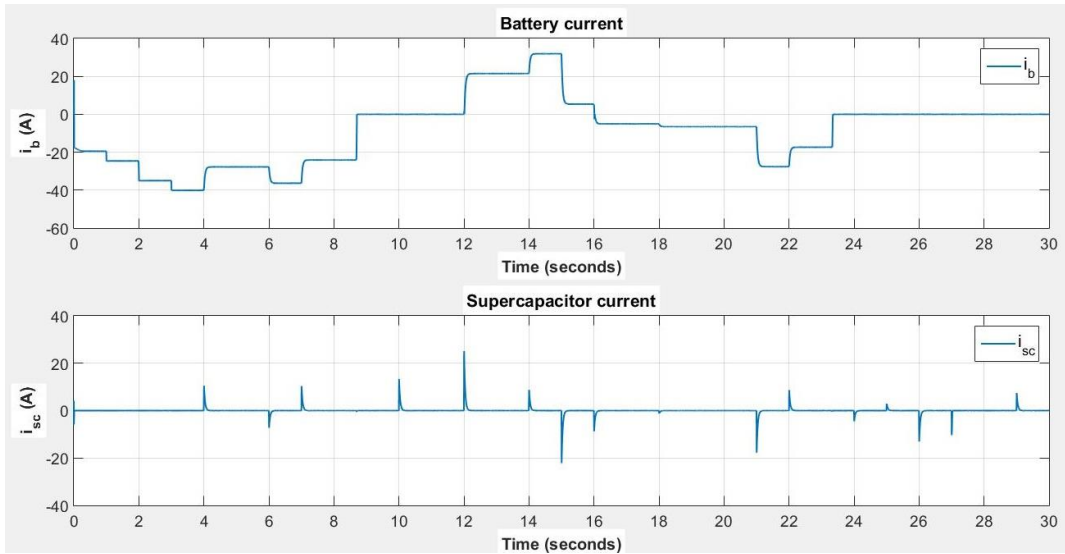


Figure 4.9: Battery current and supercapacitor current (Scenario 1)

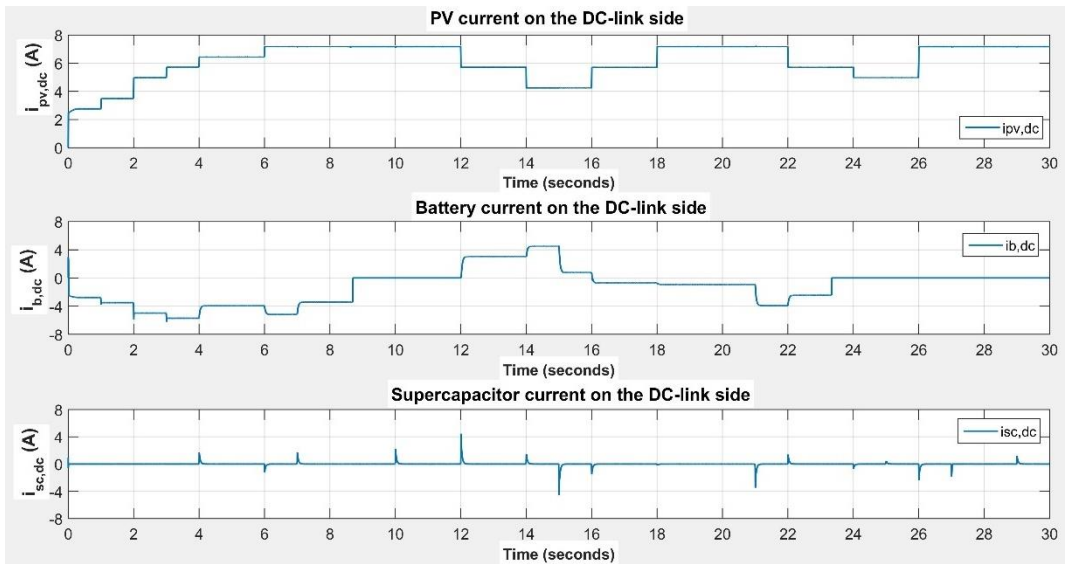


Figure 4.10: PV current, battery current and supercapacitor current on DC-link side (Scenario 1)

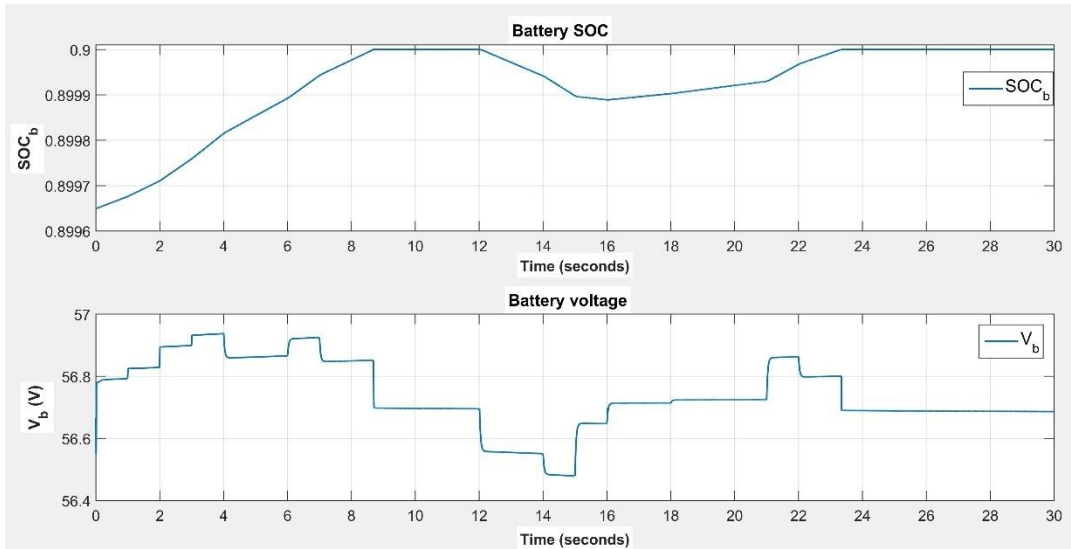


Figure 4.11: Battery SOC and battery voltage (Scenario 1)

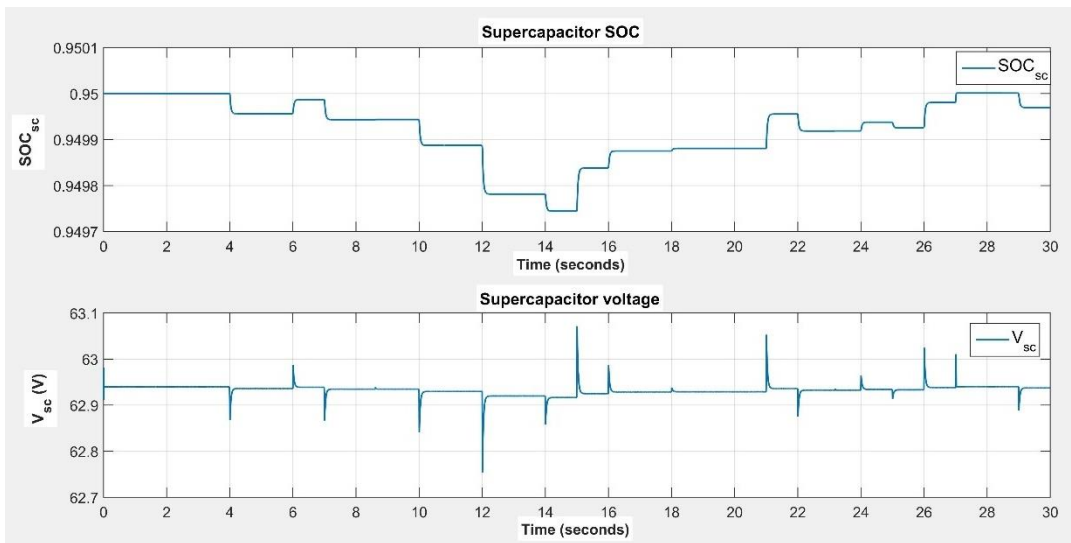


Figure 4.12: Supercapacitor SOC and supercapacitor voltage (Scenario 1)

Another important parameter is the DC-bus voltage, which must be kept stable at 400 V, despite changes in PV power and load power. Observing Figure 4.13, the DC-bus voltage remains stable near 400 V during all different cases, exhibiting a maximum ripple voltage (peak-to-peak) of about 5 V (or $\pm 0.625\%$), which is absolutely acceptable. Moreover, the current controllers on the bidirectional converters of the battery and the supercapacitor provide the corresponding duty cycle for each converter. Specifically, the battery converter operates in buck-mode (battery charging) for almost the whole period of 30 seconds, except for period $t = 12\text{--}16$ s where it operates in boost-mode (battery

discharging). As can be seen in the zoomed view of the duty cycle of the battery converter, during each rapid change, the controller acts extremely fast and provides the required duty cycle to the converter. Also, the supercapacitor converter during the first 0.2 seconds in each transition, operates either in buck-mode or boost-mode. During the remaining period, the supercapacitor absorbs fluctuations around zero. Therefore, the dynamic performance of the system is verified.

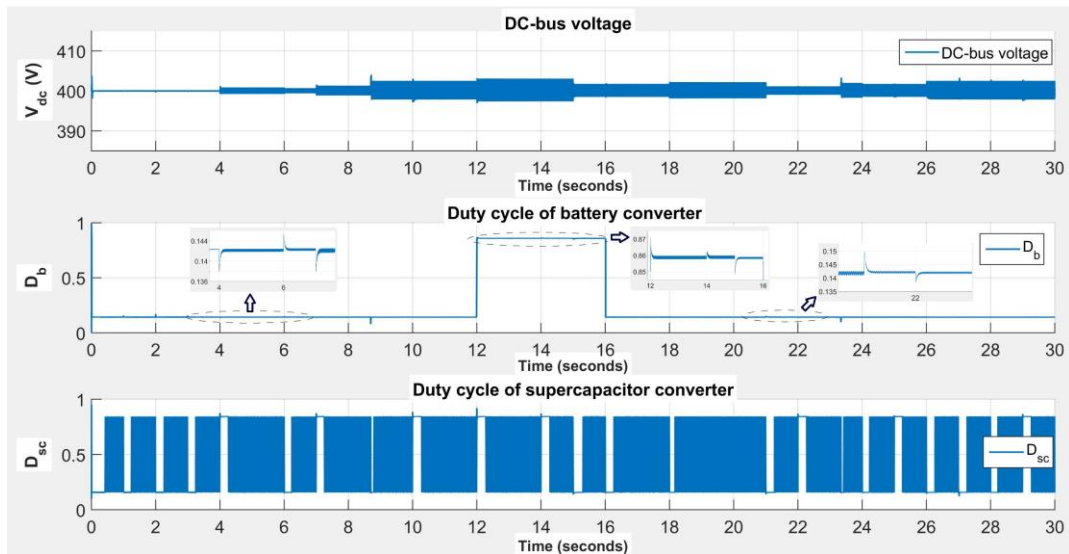


Figure 4.13: DC-bus voltage and duty cycle for the battery and the supercapacitor bidirectional converters, respectively (Scenario 1)

Figure 4.14 corresponds to the currents on the AC side, showing the inverter output current, the load current and the grid current. One can observe that when the supercapacitor is available for charging/discharging, the grid current transitions are smoother. Finally, during the chosen period of 30 seconds, the current balance is verified; the output current of the inverter supplies the load and the excess amount (if any) is injected into the grid.

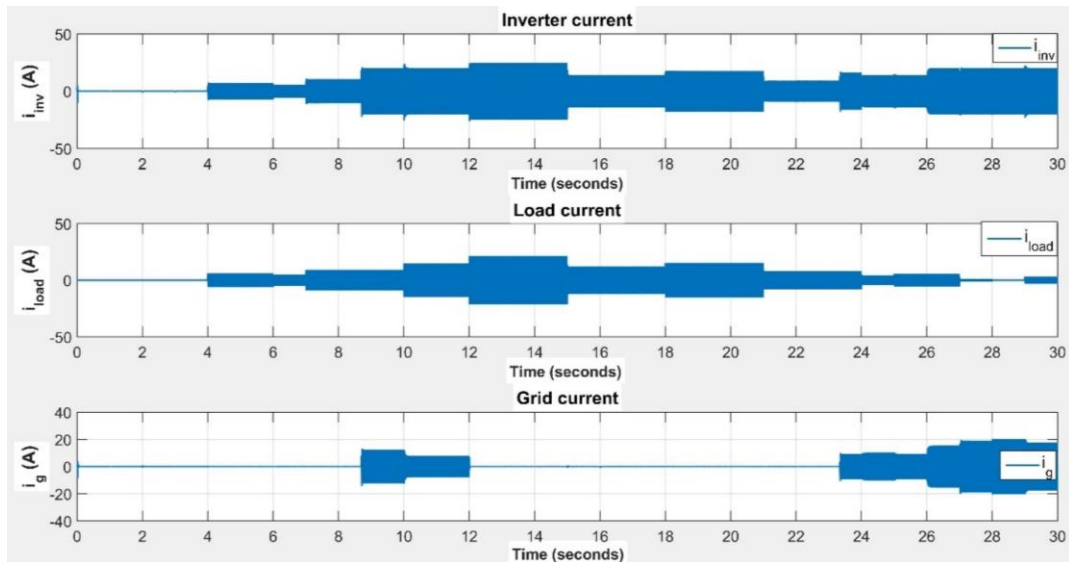


Figure 4.14: Inverter output current, load current and grid current (Scenario 1)

4.3.1.2 Scenario 2: Supercapacitor reaches its minimum SOC limit during EPM

Scenario 2 of EPM is examined here, where in all cases the produced PV power is larger than the required load power. The initial SOC of the battery is set to 89.985% ($SOC_b = 0.89985$) and the initial SOC of the supercapacitor to 49.98% ($SOC_{sc} = 0.4998$). Recall that the maximum SOC limit for the battery is 90% and the minimum SOC limit for the supercapacitor is 50%. Therefore, the supercapacitor is below its minimum SOC limit and is only available for charging.

The power and SOC results derived by the simulations are presented in Table 4.3. Figure 4.15 shows the PV power, load power (average), battery power, supercapacitor power and grid power (average) over the selected period of 10 seconds. Additionally, Figure 4.16 presents the mode of the battery converter, and the availability modes of the battery and the supercapacitor (charging and discharging), respectively.

Observing Table 4.3 and Figure 4.15, in the beginning the PV generates electricity, which is larger than the required load power. Also, the supercapacitor is fully discharged. Therefore, this is Case 3, where the battery is charging and absorbing all the remaining power. During Case 3, if the battery is charging at an increasing rate ($t = 0-3$ s), the battery absorbs the average remaining power and the supercapacitor absorbs the high-frequency component. On the other hand, if the battery is charging at a decreasing rate ($t = 3-4.8$ s),

the supercapacitor is not available for discharging (as it remains below its minimum SOC limit) and the battery absorbs the remaining power along with the power oscillations. After that ($t = 4.8$ s), the PV power remains larger than the load power, the battery reached its maximum SOC limit of 90%, while the supercapacitor is only available for charging (Case 6). During this period ($t = 4.8-8$ s), the grid absorbs the remaining produced power at a decreasing rate, hence the supercapacitor power is zero, and the grid absorbs the high-frequency power variations. At $t = 8$ s, the generated PV power increases, while the load power remains zero. Therefore, the power injected into the grid increases and the supercapacitor absorbs the oscillations, while the average power is injected into the grid (Case 4).

The above scenario verifies that the model works properly during EPM for the selected period of 10 seconds, when the supercapacitor is near its minimum SOC limit. Also, a power balance is achieved in all cases.

Table 4.3: Simulation results of proposed PV system with hybrid storage in EPM (Scenario 2)

	Time (sec)	P_{pv} (W)	P_{load} (W)	P_b (W)	SOC_b	SOC_{sc}	P_{grid} (W)
Case 3	0 – 1	520	-100	-420	0.89985	0.49980	0
	1 – 2	1400	-100	-1300	0.89988	0.49997	0
	2 – 3	1991	-100	-1891	0.89993	0.5	0
	3 – 4	1696	-100	-1596	0.89997	0.5	0
	4 – 4.8	1400	-100	-1300	0.89999	0.5	0
Case 6	4.8 – 5	1400	-100	0	0.9	0.5	1300
	5 – 6	1105	0	0	0.9	0.5	1105
	6 – 7	811	0	0	0.9	0.5	811
	7 – 8	520	0	0	0.9	0.5	520
Case 4	8 – 9	811	0	0	0.9	0.50006	811
	9 – 10	1105	0	0	0.9	0.50011	1105

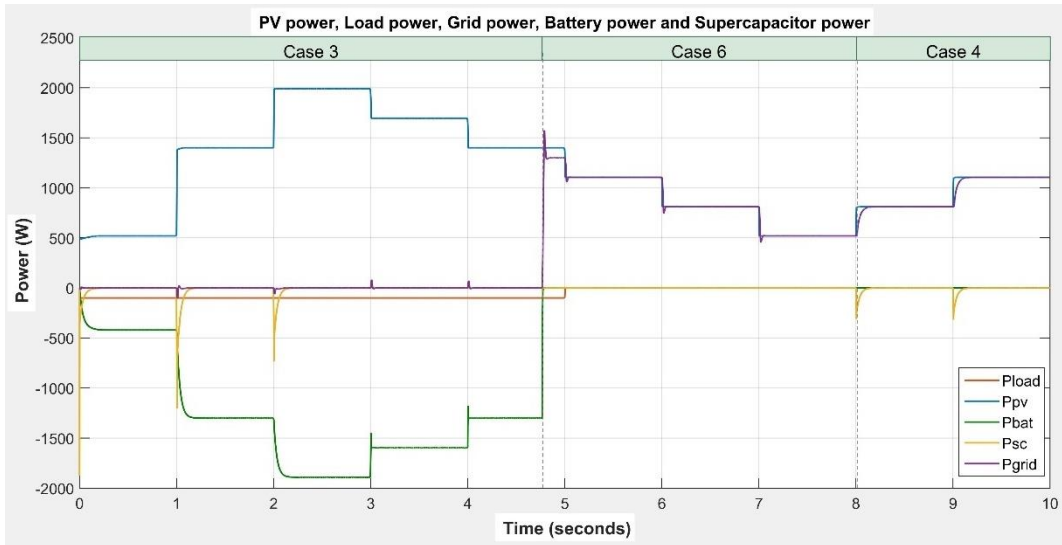


Figure 4.15: PV power (blue), Load power (red), Battery power (green), Supercapacitor power (yellow) and Grid power (purple) (Scenario 2)

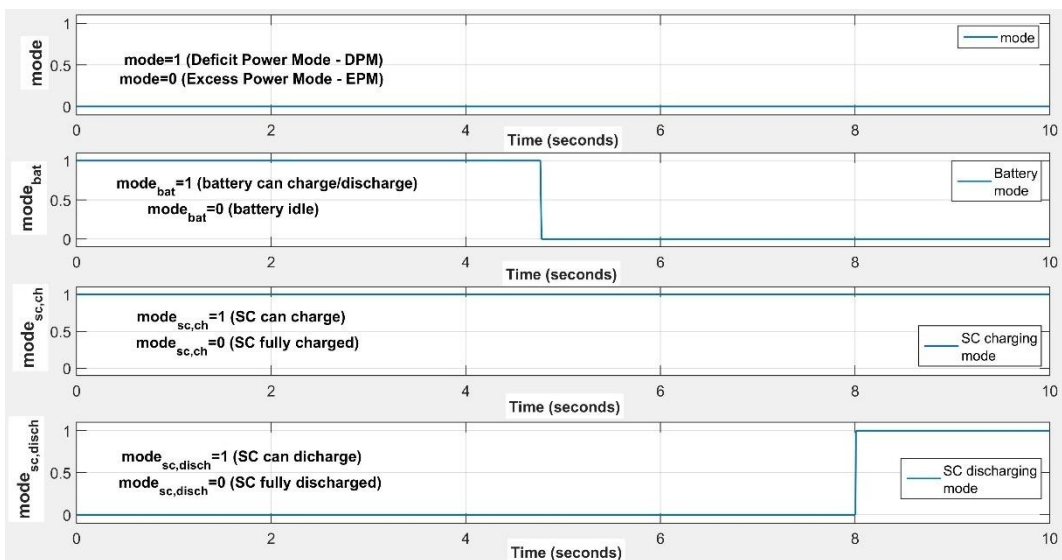


Figure 4.16: Mode of the battery converter, and availability modes of the battery and the supercapacitor (charging and discharging), respectively (Scenario 2)

Figure 4.17 shows the battery and supercapacitor current on the storage side, while Figure 4.18 shows the PV current, battery current and supercapacitor current on the DC-link side. During Case 3 ($t = 0\text{--}3\text{ s}$), where the supercapacitor is available for charging, the battery current transitions are smooth because the current oscillations are eliminated through the supercapacitor. Therefore, the supercapacitor handles the high-frequency current variations, thus relieving the battery and extending its lifetime. After that ($t = 3\text{--}4.8\text{ s}$),

the supercapacitor is idle and the battery current variation is sharp during the transitions ($t = 3$ s, $t = 4$ s), hence the battery is stressed. Next, Figure 4.19 shows the battery SOC and the battery voltage, while Figure 4.20 shows the supercapacitor SOC and the supercapacitor voltage, where both storage methods work properly within their limits.

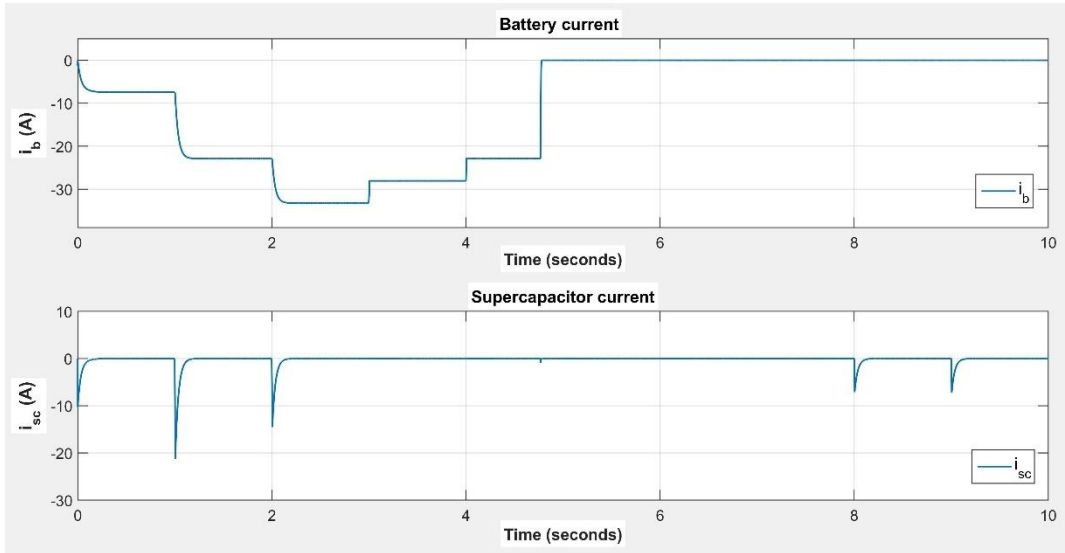


Figure 4.17: Battery current and supercapacitor current (Scenario 2)

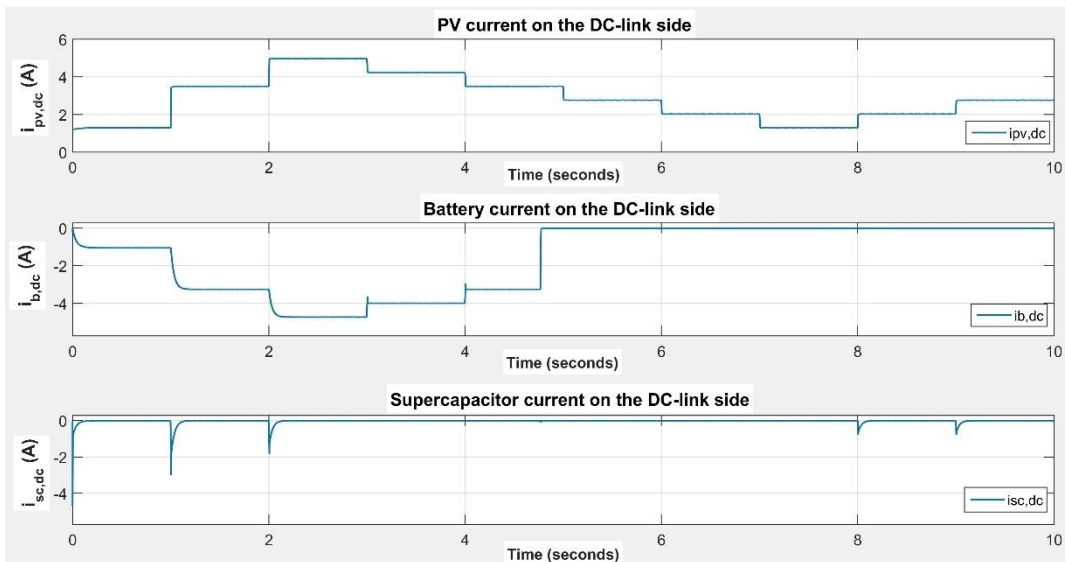


Figure 4.18: PV current, battery current and supercapacitor current on DC-link side (Scenario 2)

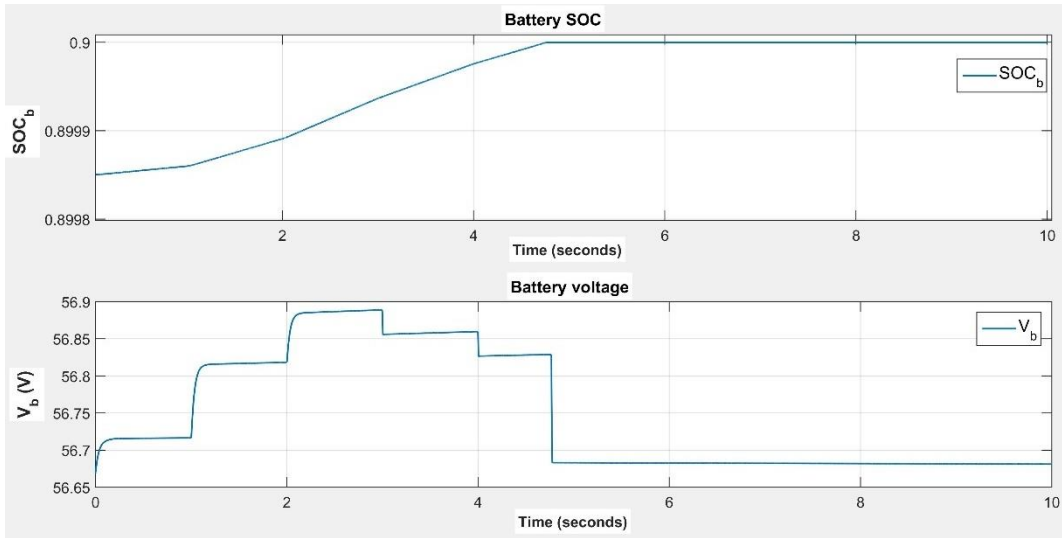


Figure 4.19: Battery SOC and battery voltage (Scenario 2)

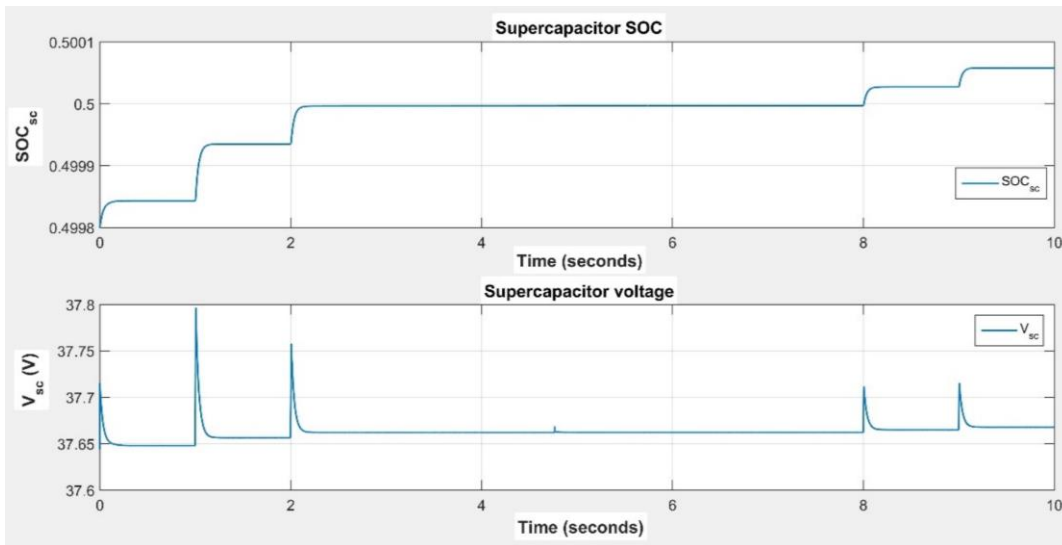


Figure 4.20: Supercapacitor SOC and supercapacitor voltage (Scenario 2)

Observing Figure 4.21, the DC-bus voltage remains stable near 400 V during all different cases, exhibiting a maximum ripple voltage (peak-to-peak) of about 3 V (or $\pm 0.375\%$). Moreover, the current controllers on the bidirectional converters of the battery and the supercapacitor provide the corresponding duty cycle for each converter. Specifically, the battery converter operates in buck-mode (battery charging) during the whole period of 10 seconds. As can be seen in the zoomed view of the duty cycle of the battery converter, during each rapid change the controller acts extremely fast and provides the required duty cycle to the converter. Also, the supercapacitor converter at the beginning of each transition operates either in buck-mode or in boost-mode. During the remaining period,

the supercapacitor absorbs fluctuations around zero. In this way, the dynamic performance of the system is verified.

Figure 4.22 shows the currents on the AC side, namely the inverter output current, the load current and the grid current. The supercapacitor is available for charging, hence the grid current transitions are smoother. Finally, during the selected period of 10 seconds, the current balance is verified; the output current of the inverter supplies the load, and the excess amount (if any) is injected into the grid.

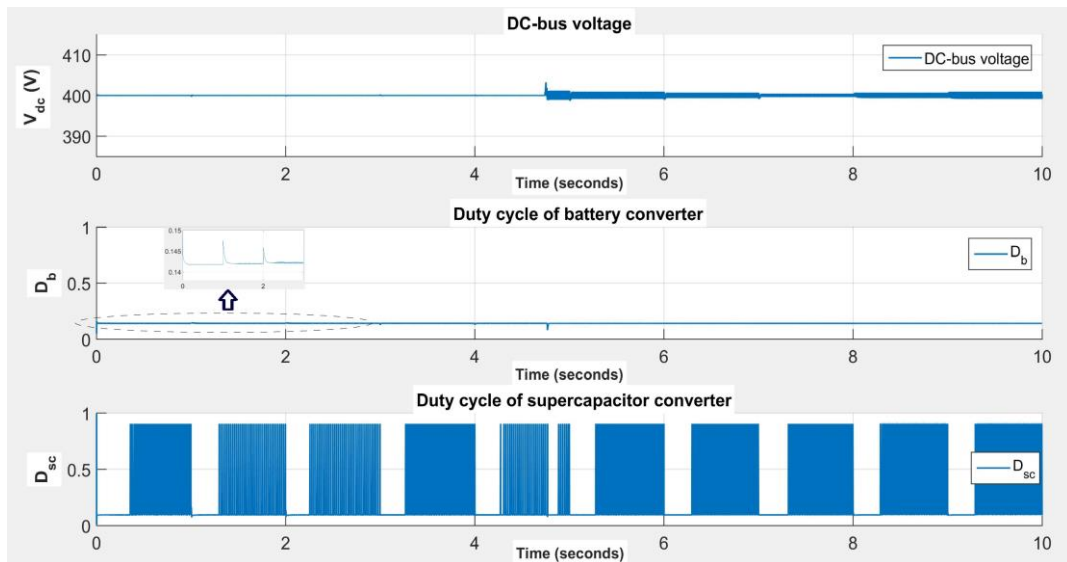


Figure 4.21: DC-bus voltage and duty cycle for the battery and the supercapacitor bidirectional converters, respectively (Scenario 2)

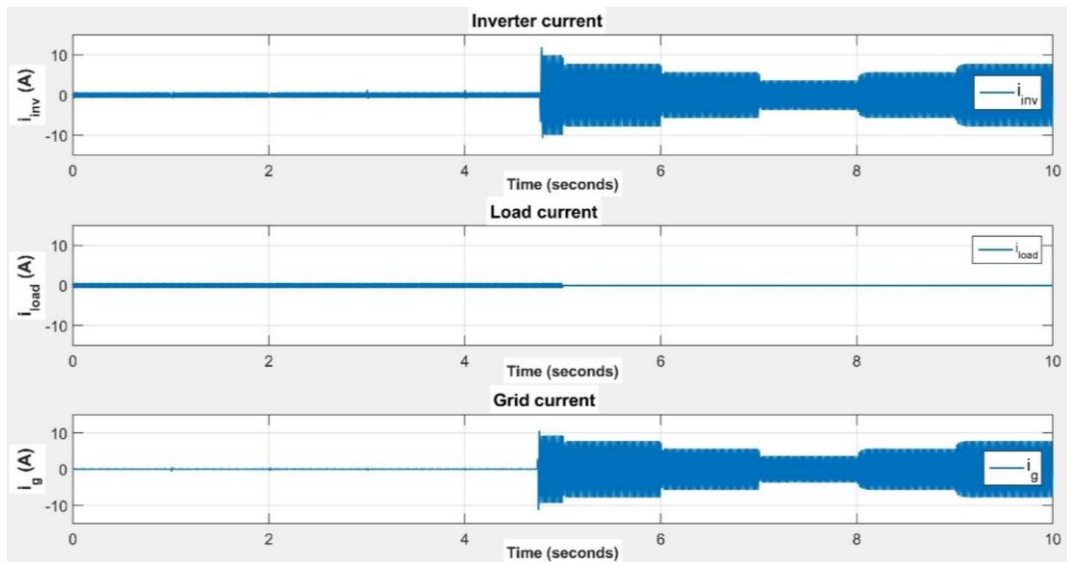


Figure 4.22: Inverter output current, load current and grid current (Scenario 2)

4.3.2 Deficit Power Mode (DPM)

4.3.2.1 Scenario 3: Supercapacitor reaches its minimum SOC limit during DPM

The scenario of DPM is examined, where in almost all cases the produced PV power is smaller than the required load power. The initial SOC of the battery is set to 20.02% ($SOC_b = 0.2002$) and the initial SOC of the supercapacitor to 50% ($SOC_{sc} = 0.50$). Recall that the minimum SOC limits for the battery and the supercapacitor are 20% and 50%, respectively. Therefore, the supercapacitor is already at its minimum SOC limit and is only available for charging.

The power and SOC results derived by the simulations are presented in Table 4.4. Also, Figure 4.23 shows the PV power, load power (average), battery power, supercapacitor power and grid power (average) during the selected period of 30 seconds. Moreover, Figure 4.24 shows the mode of the battery converter and the availability modes of the battery and the supercapacitor (charging and discharging), respectively.

As one can observe from Table 4.4 and Figure 4.23, in the beginning the load power is higher than the PV power. Therefore, this is Case 9, where the battery is discharging and supplying the load with a power equal to the power difference between the load power and the produced PV power. During this period ($t = 0-3$ s), the battery is discharging at an increasing rate, hence the supercapacitor is idle and the battery supplies power with oscillations. After that ($t = 3$ s), the battery discharging power decreases (because the load power decreases), hence this is Case 7, where the supercapacitor is charging. During Case 7 ($t = 3-8.4$ s), the supercapacitor is available for charging/discharging and handles the high-frequency variations, while the battery supplies the average part of the required power. At the same time, the battery continues discharging until it reaches its minimum SOC limit of 20%, at $t = 8.4$ s (Case 10). During Case 10 ($t = 8.4-14$ s), the supercapacitor is available for charging/discharging and absorbs/supplies the high-frequency power oscillations, while the required average power is supplied by the grid. At $t = 14$ s, the load power decreases, so that the PV power is larger than the load power (Case 1). During this case ($t = 14-18$ s), the battery is charging with negative power and the supercapacitor handles the rapid changes. After that (at $t = 18$ s), the generated PV power is smaller than the load power, hence the battery is discharging again and the supercapacitor is available

for charging/discharging (Case 7). Next, at $t = 20.3$ s, the battery reaches its maximum SOC limit (Case 10), hence the grid supplies the average power difference between the PV and the load power, while the supercapacitor handles the high-frequency variations. After that, at $t = 26$ s, the supercapacitor reaches its minimum SOC limit (Case 12), and all the required power is supplied by the grid (with oscillations). During this case, both the battery and the supercapacitor are fully discharged. At $t = 28$ s, the supply of grid power decreases, and therefore the supercapacitor can absorb the high-frequency variations (Case 10).

The above scenario verifies that the model works properly during DPM, when the supercapacitor is near its minimum SOC limit. An effective power sharing is achieved in all cases. It can also be noticed that the model responds extremely fast and operates properly during the transitions between DPM and EPM, and vice versa.

Table 4.4: Simulation results of proposed PV system with hybrid storage in DPM (Scenario 3)

	Time (sec)	P_{pv} (W)	P_{load} (W)	P_b (W)	SOC_b	SOC_{sc}	P_{grid} (W)
Case 9	0 – 1	102	-200	98	0.20020	0.5	0
	1 – 2	102	-1000	898	0.20018	0.5	0
	2 – 3	102	-1500	1398	0.20013	0.5	0
Case 7	3 – 4	102	-1000	898	0.20011	0.50005	0
	4 – 5	520	-1000	480	0.20009	0.50010	0
	5 – 6	520	-1000	480	0.20007	0.50010	0
	6 – 7	1252	-2500	1248	0.20004	0.50002	0
	7 – 8	1252	-2500	1248	0.20002	0.50002	0
	8 – 8.4	1932	-2500	568	0.20001	0.50008	0
Case 10	8.4 – 9	1932	-2500	0	0.2	0.50008	-568
	9 – 10	1932	-3000	0	0.2	0.50003	-1068
	10 – 11	2286	-3000	0	0.2	0.50007	-714
	11 – 12	2286	-3000	0	0.2	0.50007	-714
	12 – 13	1696	-1800	0	0.2	0.50013	-104
	13 – 14	1696	-1800	0	0.2	0.50013	-104
Case 1	14 – 15	2579	-1700	-879	0.20003	0.50024	0
	15 – 16	2579	-1700	-879	0.20005	0.50024	0
	16 – 17	1991	-1700	-291	0.20006	0.50017	0

	17 – 18	1991	-1700	-291	0.20007	0.50017	0
Case 7	18 – 19	1991	-3000	1009	0.20004	0.50004	0
	19 – 20	1991	-3000	1009	0.20002	0.50004	0
	20 – 20.3	1844	-3000	1156	0.2001	0.50002	0
	Case 10	20.3 – 21	1844	-3000	0	0.2	0.50003
Case 10	21 – 22	1844	-2800	0	0.2	0.50005	-956
	22 – 23	2139	-2500	0	0.2	0.50011	-361
	23 – 24	2139	-2500	0	0.2	0.50011	-361
	24 – 25	1844	-2700	0	0.2	0.50006	-856
	25 – 26	1844	-2700	0	0.2	0.50006	-856
	Case 12	26 – 27	1400	-3000	0	0.2	0.5
27 – 28		1400	-3800	0	0.2	0.5	-2400
Case 10	28 – 29	1548	-3100	0	0.2	0.50008	-1552
	29 – 30	1548	-2700	0	0.2	0.50013	-1152

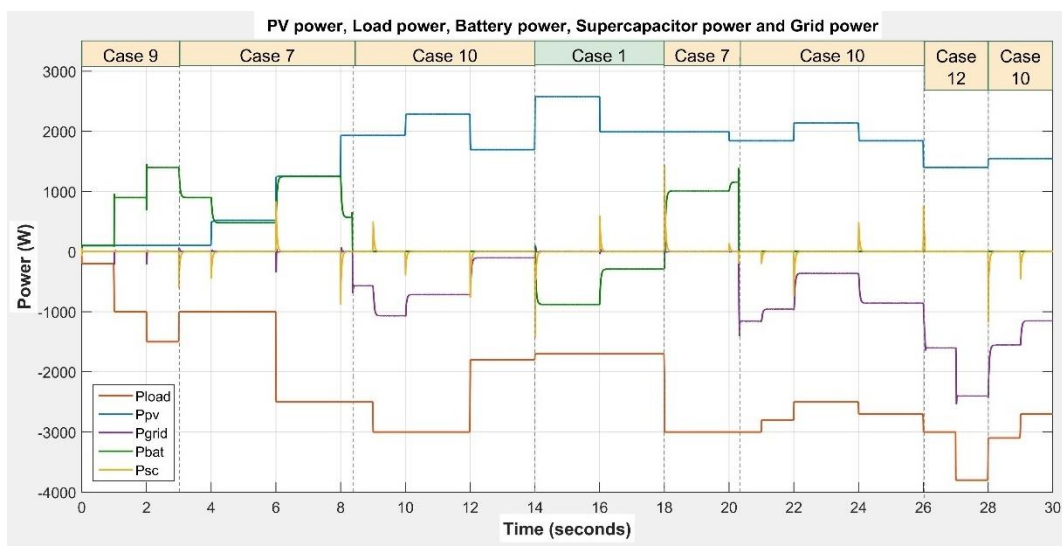


Figure 4.23: PV power (blue), Load power (red), Battery power (green), Supercapacitor power (yellow) and Grid power (purple) (Scenario 3)

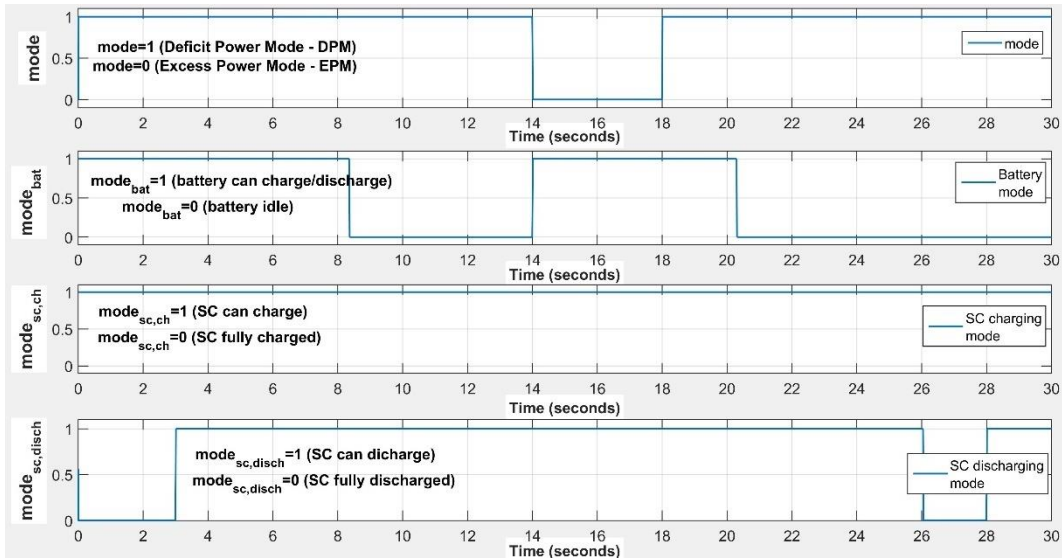


Figure 4.24: Mode of the battery converter, and availability modes of the battery and the supercapacitor (charging and discharging), respectively (Scenario 3)

Figure 4.25 presents the battery and supercapacitor current on the storage side, while Figure 4.26 shows the PV current, battery current and supercapacitor current on the DC-link side. During Case 9 ($t = 0-3$ s), where the supercapacitor is idle, the battery current exhibits peaks during the transitions, and hence the battery is stressed. These oscillations are eliminated with the integration of the supercapacitor at $t = 3$ s. Therefore, the supercapacitor handles the high-frequency current variations, relieving the battery and thus extending its lifetime.

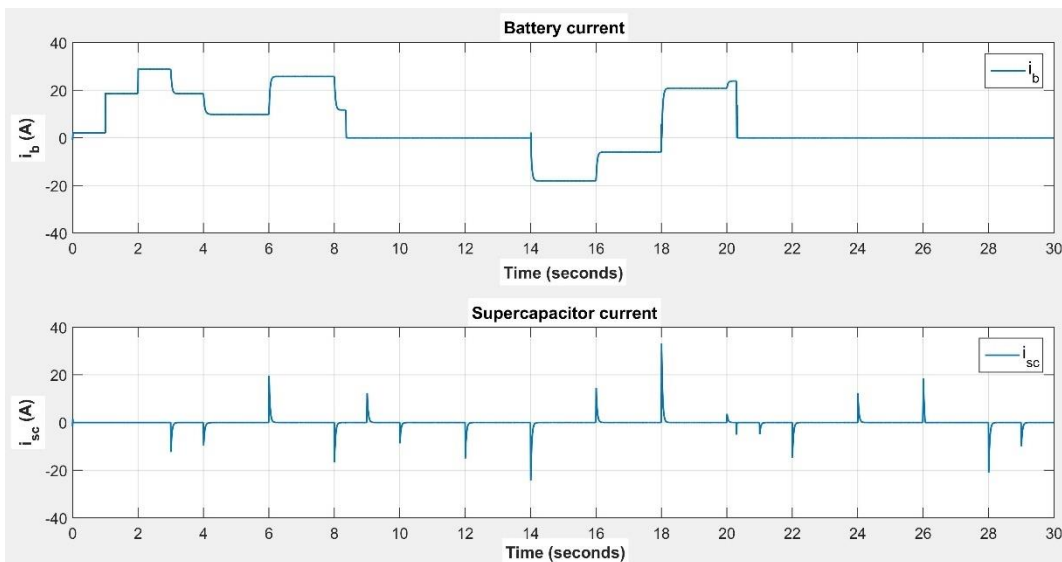


Figure 4.25: Battery current and supercapacitor current (Scenario 3)

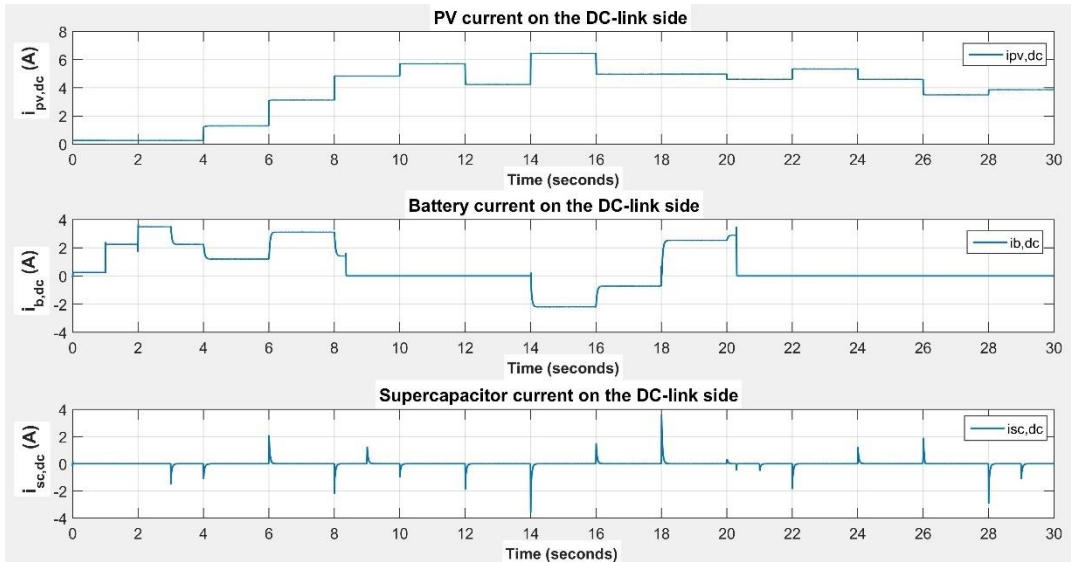


Figure 4.26: PV current, battery current and supercapacitor current on DC-link side (Scenario 3)

Next, Figure 4.27 shows the battery SOC and the battery voltage, while Figure 4.28 shows the supercapacitor SOC and the supercapacitor voltage, where both storage methods work properly within their limits.

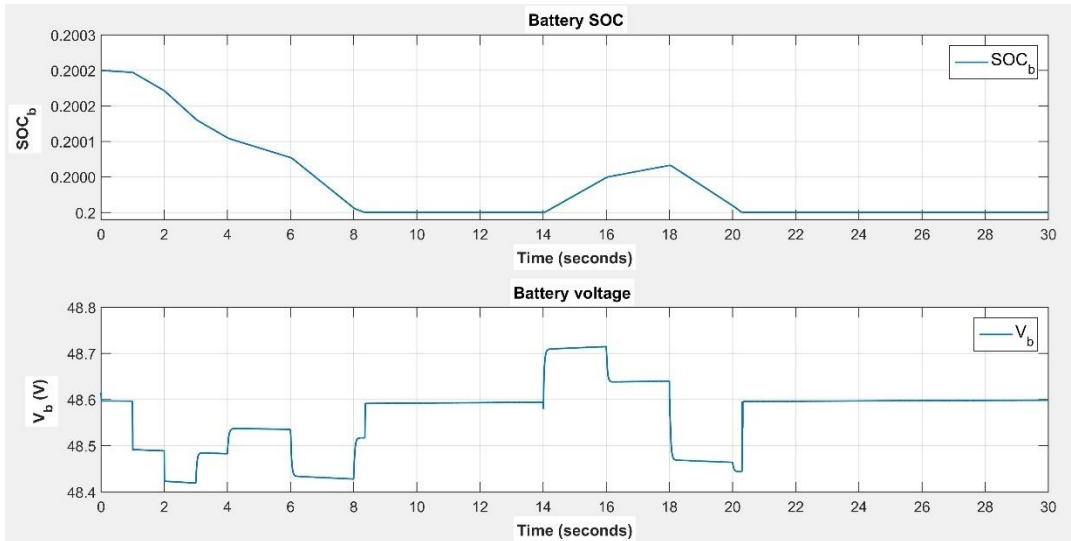


Figure 4.27: Battery SOC and battery voltage (Scenario 3)

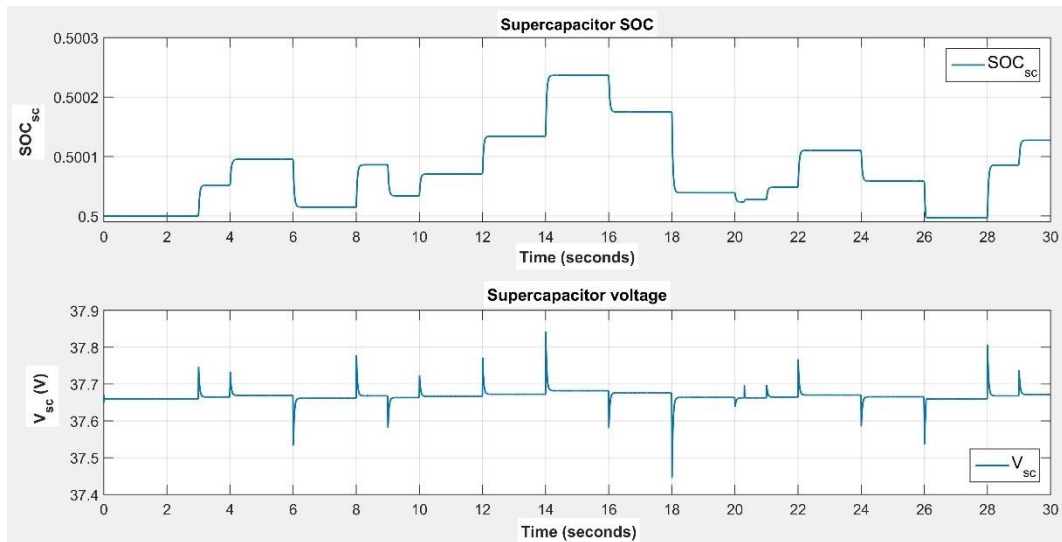


Figure 4.28: Supercapacitor SOC and supercapacitor voltage (Scenario 3)

Observing Figure 4.29, the DC-bus voltage remains stable near 400 V during all different cases, exhibiting a maximum ripple voltage (peak-to-peak) of about 5 V (or $\pm 0.625\%$). Moreover, the current controllers on the bidirectional converters of the battery and the supercapacitor provide the corresponding duty cycle for each converter. Specifically, the battery converter operates in boost-mode (battery discharging) for almost the whole period of 30 seconds, except for the period $t = 14\text{--}18\text{ s}$ where it operates in buck-mode (battery charging). As can be seen in the zoomed view of the duty cycle of the battery converter, during each rapid change the controller acts extremely fast and provides the required duty cycle to the converter. Also, the supercapacitor converter during each transition, operates either in buck-mode or in boost-mode. During the remaining period, the supercapacitor absorbs fluctuations around zero. Therefore, the dynamic performance of the system is verified.

Figure 4.30 shows the currents on the AC side, namely the inverter output current, the load current and the grid current. When the supercapacitor is available for charging/discharging, the grid current transitions are smoother. Finally, during the period of 30 seconds, the current balance is verified; the output current of the inverter along with the grid current (if any) supply the load.

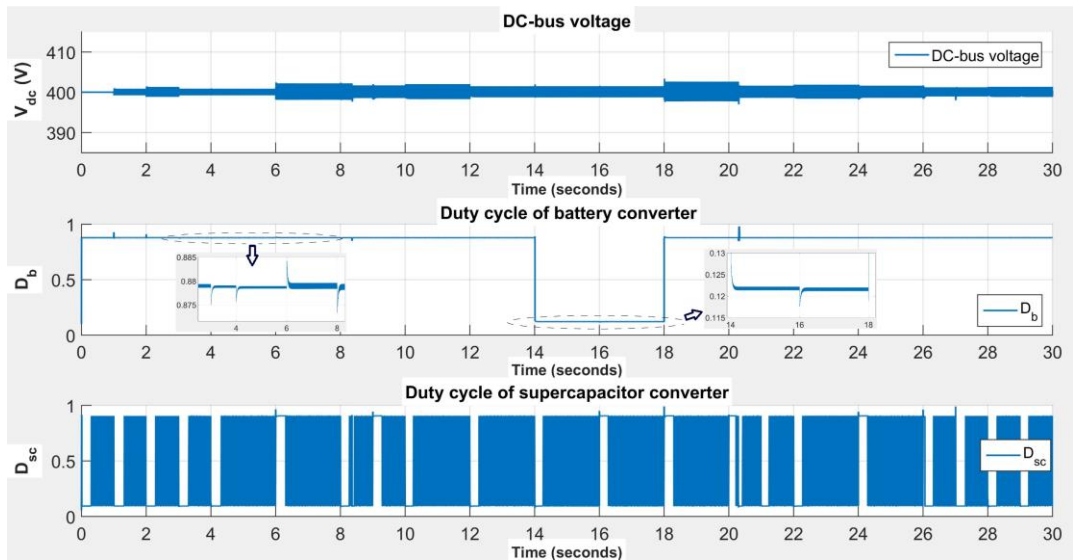


Figure 4.29: DC-bus voltage and duty cycle for the battery and the supercapacitor bidirectional converters, respectively (Scenario 3)

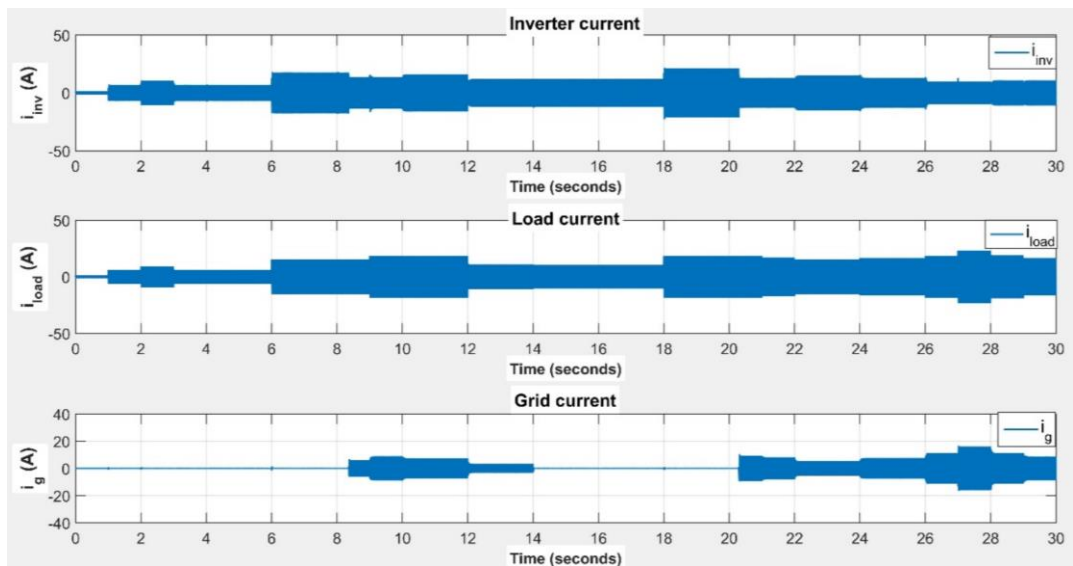


Figure 4.30: Inverter current, load current and grid current (Scenario 3)

4.3.2.2 Scenario 4: Supercapacitor reaches its maximum SOC limit during DPM

Scenario 4 of DPM is examined here, where in all cases the produced PV power is smaller than the required load power. The initial SOC of the battery is set to 20.015% ($SOC_b = 0.20015$) and the initial SOC of the supercapacitor to 95.01% ($SOC_{sc} = 0.9501$). Recall that the minimum SOC limit for the battery is 20% and the maximum SOC limit for the

supercapacitor is 95%. Therefore, the supercapacitor is already above its maximum SOC limit and is only available for discharging.

The power and SOC results derived by the simulations are presented in Table 4.5. Also, Figure 4.31 shows the PV power, load power (average), battery power, supercapacitor power and grid power (average) during the selected period of 15 seconds. Moreover, Figure 4.32 shows the mode of the battery converter and the availability modes of the battery and the supercapacitor (charging and discharging), respectively.

As one can observe from Table 4.5 and Figure 4.31, in the beginning the load power is higher than the PV power. Also, the supercapacitor is above its maximum SOC limit. Therefore, this is Case 8, where the battery is discharging and supplying the load with a power equal to the power difference between the load power and the produced PV power. During this period ($t = 0\text{--}4$ s), the battery is discharging at a decreasing rate, hence the supercapacitor is idle and the battery supplies power with oscillations. After that ($t = 4$ s), the battery discharging power increases, hence this is Case 7, where the supercapacitor is discharging. At $t = 5$ s, the supercapacitor is fully charged (Case 8) and the battery supplies the required power to the load (with oscillations). At the same time, the battery continues discharging until it reaches its minimum SOC limit of 20%, at $t = 7.6$ s (Case 11). During Case 11, the battery is fully discharged, while the supercapacitor is fully charged, and the grid supplies the load with the required power. It is observed that the grid supplies power at a decreasing rate, hence the supercapacitor power is zero and the grid supplies the high-frequency variations. At $t = 12$ s, the generated PV power decreases, so that the required power to the grid increases. This causes the supercapacitor to discharge and support the grid with the high-frequency component in power, while the average required power is supplied by the grid (Case 10).

The above scenario verifies that the model works properly during DPM, when the supercapacitor is near its maximum SOC limit. Also, a power balance is achieved in all cases.

Table 4.5: Simulation results of proposed PV system with hybrid storage in DPM (Scenario 4)

	Time (sec)	P_{pv} (W)	P_{load} (W)	P_b (W)	SOC_b	SOC_{sc}	P_{grid} (W)
Case 8	0 – 1	520	-2000	1480	0.20015	0.9501	0
	1 – 2	520	-1500	980	0.20008	0.95001	0
	2 – 3	520	-1300	780	0.20006	0.95001	0
	3 – 4	520	-1000	480	0.20005	0.95001	0
Case 7	4 – 5	1105	-1800	695	0.20003	0.94999	0
Case 8	5 – 6	1105	-1600	495	0.20002	0.95	0
	6 – 7	665	-900	235	0.20001	0.95	0
	7 – 7.6	665	-900	235	0.20001	0.95	0
Case 11	7.6 – 9	665	-900	0	0.2	0.95	-235
	9 – 10	665	-900	0	0.2	0.95	-235
	10 – 11	1105	-1200	0	0.2	0.95	-95
	11 – 12	1105	-1200	0	0.2	0.95	-95
Case 10	12 – 13	520	-1000	0	0.2	0.94998	-480
	13 – 14	520	-1000	0	0.2	0.94998	-480
	14 – 15	520	-1500	0	0.2	0.94994	-980

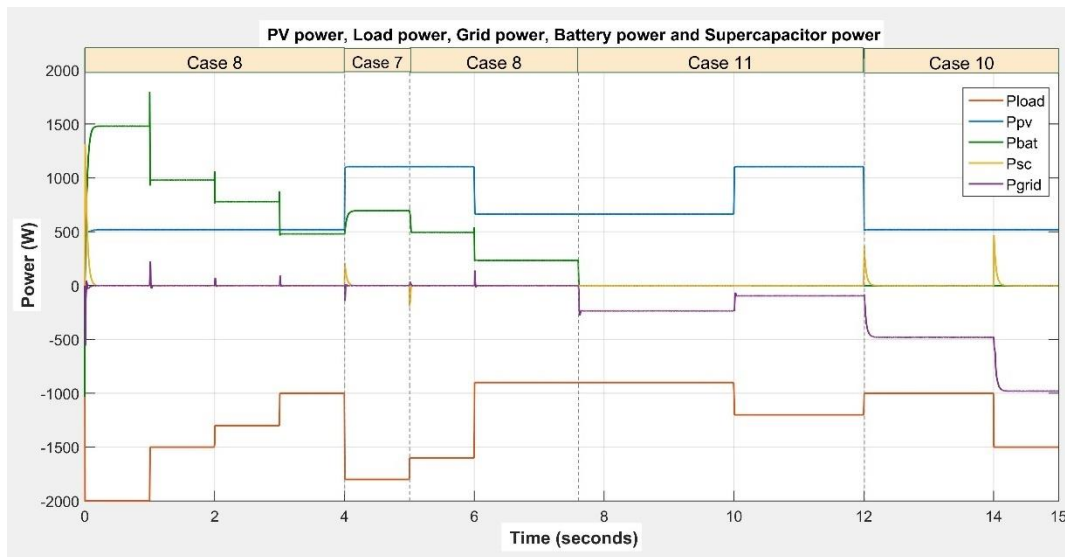


Figure 4.31: PV power (blue), Load power (red), Battery power (green), Supercapacitor power (yellow) and Grid power (purple) (Scenario 4)

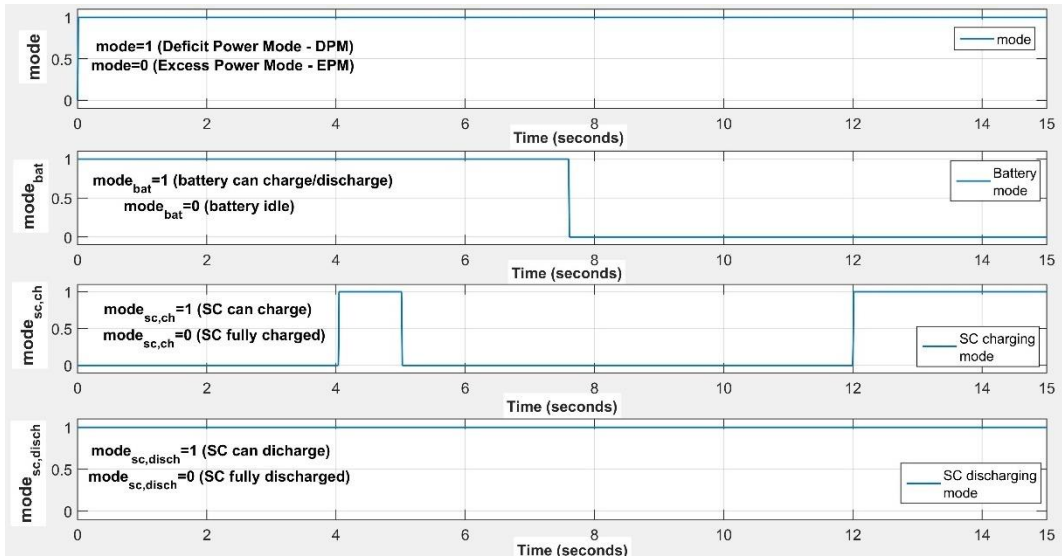


Figure 4.32: Mode of the battery converter, and availability modes of the battery and the supercapacitor (charging and discharging), respectively (Scenario 4)

Figure 4.33 presents the battery and supercapacitor current on the storage side, while Figure 4.34 shows the PV current, battery current and supercapacitor current on the DC-link side. One can observe that during Case 8 ($t = 0-4$ s), where the supercapacitor is idle, the battery current exhibits peaks during the current transitions, and hence the battery is stressed. These oscillations are eliminated with the integration of the supercapacitor at $t = 4$ s. Therefore, the supercapacitor handles the high-frequency variations of current, relieving the battery and thus extending its lifetime.

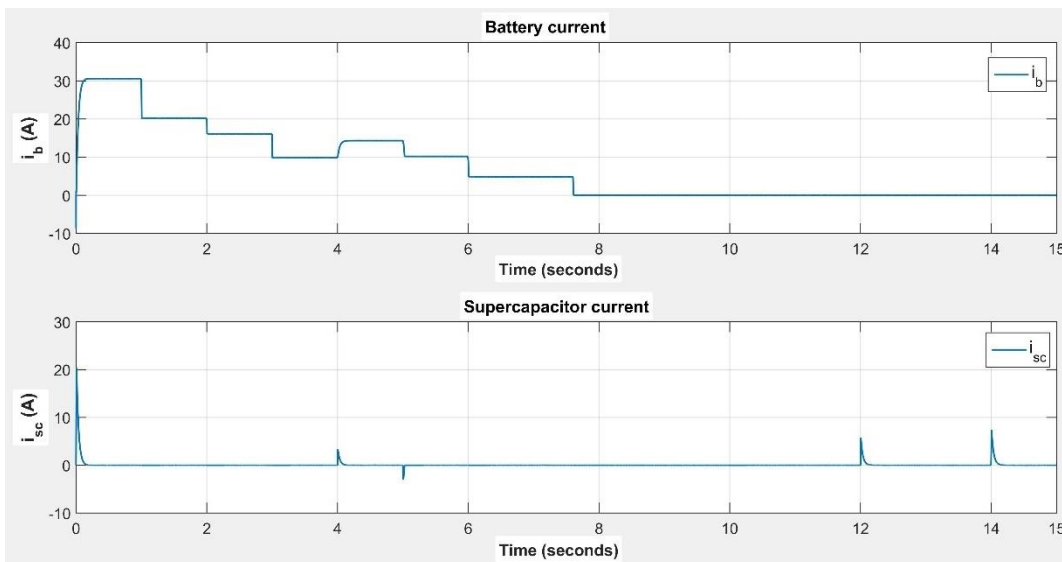


Figure 4.33: Battery current and supercapacitor current (Scenario 4)

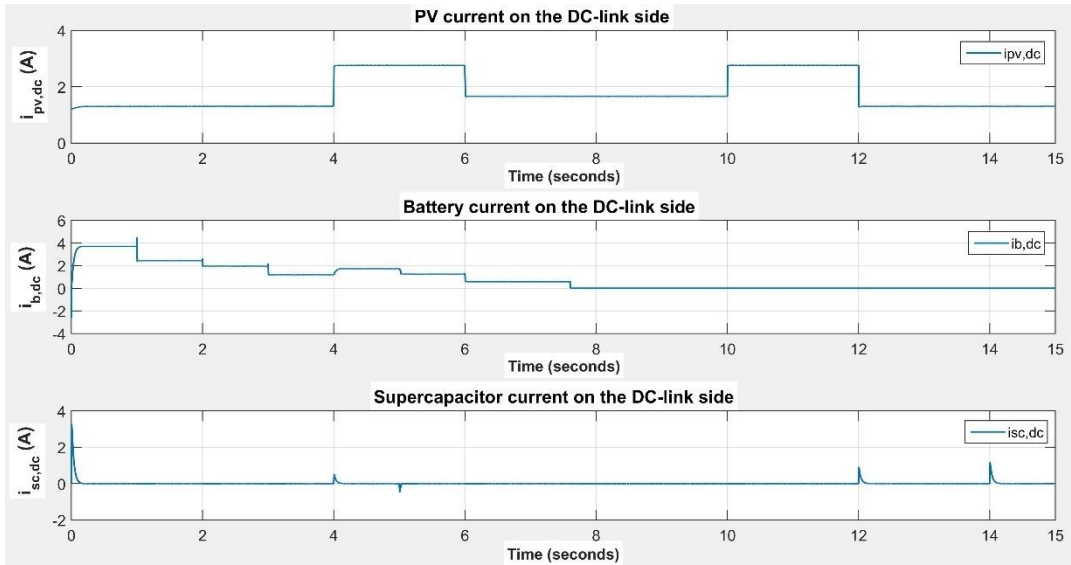


Figure 4.34: PV current, battery current and supercapacitor current on DC-link side (Scenario 4)

Next, Figure 4.35 shows the battery SOC and the battery voltage, while Figure 4.36 shows the supercapacitor SOC and the supercapacitor voltage, where both storage methods work properly within their limits.

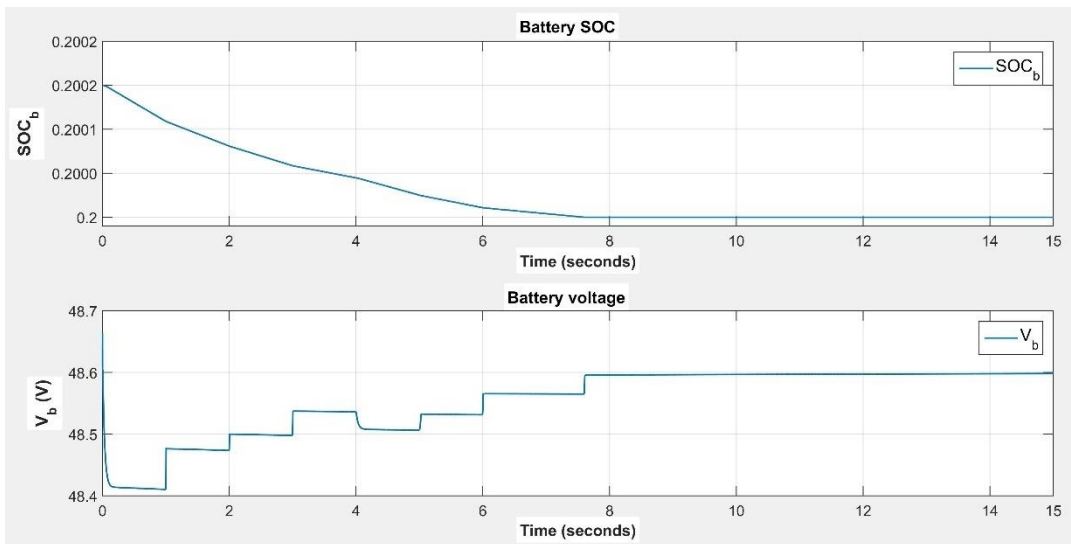


Figure 4.35: Battery SOC and battery voltage (Scenario 4)

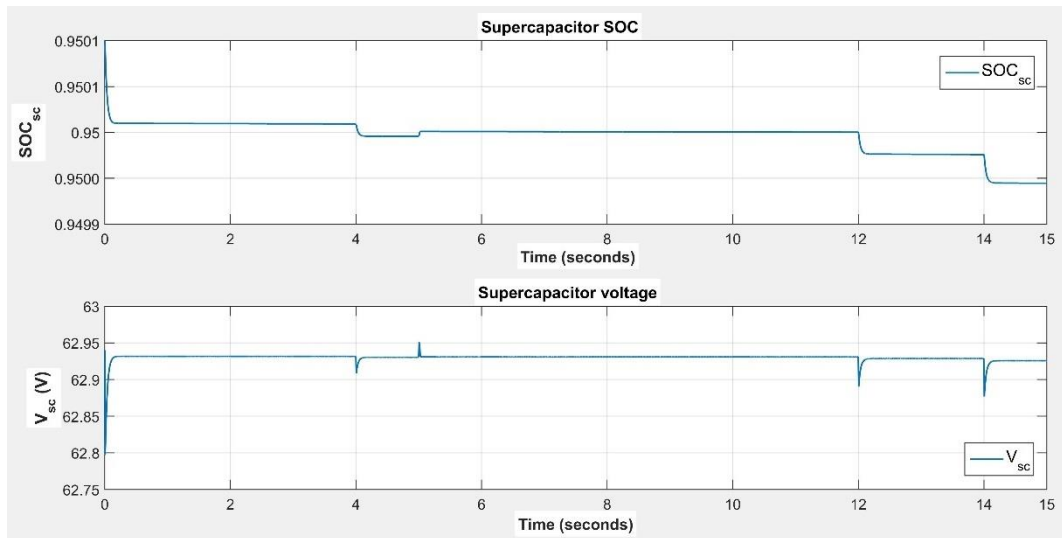


Figure 4.36: Supercapacitor SOC and supercapacitor voltage (Scenario 4)

Observing Figure 4.37, the DC-bus voltage remains stable near 400 V, regardless of rapid changes in PV power and load power, exhibiting a maximum ripple voltage (peak-to-peak) of about 4 V (or $\pm 0.5\%$). Moreover, the current controllers on the bidirectional converters of the battery and the supercapacitor provide the corresponding duty cycle for each converter. Specifically, the battery converter operates in boost-mode (battery discharging) during the whole period of 15 seconds, where the controller acts extremely fast and provides the required duty cycle to the converter. Also, the supercapacitor converter at the beginning of each transition, operates either in buck-mode or in boost-mode. During the remaining period, the supercapacitor absorbs fluctuations around zero. In this way, the dynamic performance of the system is verified.

Figure 4.38 corresponds to the currents on the AC side, namely the inverter output current, the load current and the grid current. When the supercapacitor is available for charging/discharging, the grid current transitions are smoother. Finally, during the selected period of 15 seconds, the current balance is verified; the output current of the inverter along with the grid current (if any) supply the load.

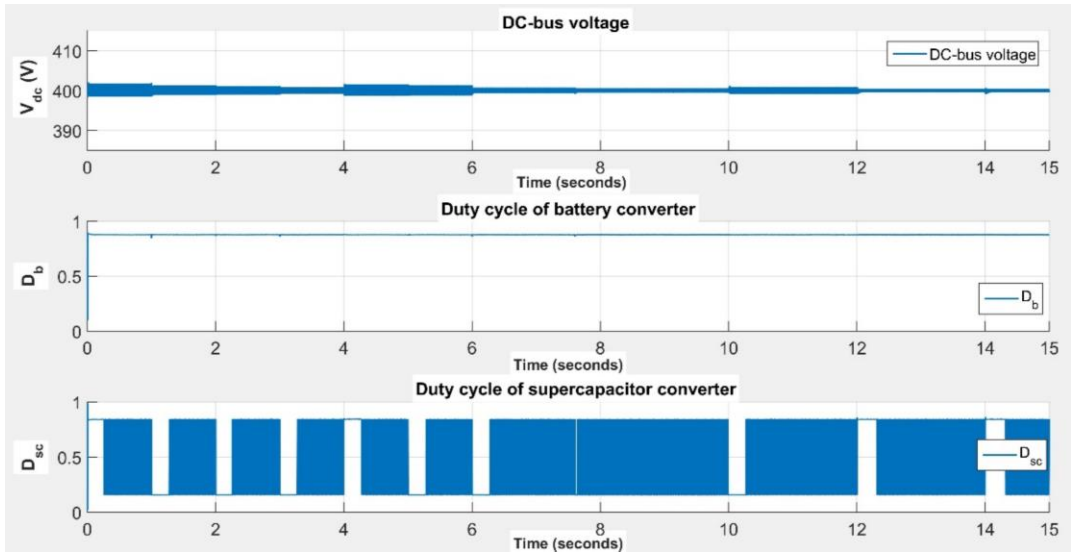


Figure 4.37: DC-bus voltage and duty cycle for the battery and the supercapacitor bidirectional converters, respectively (Scenario 4)

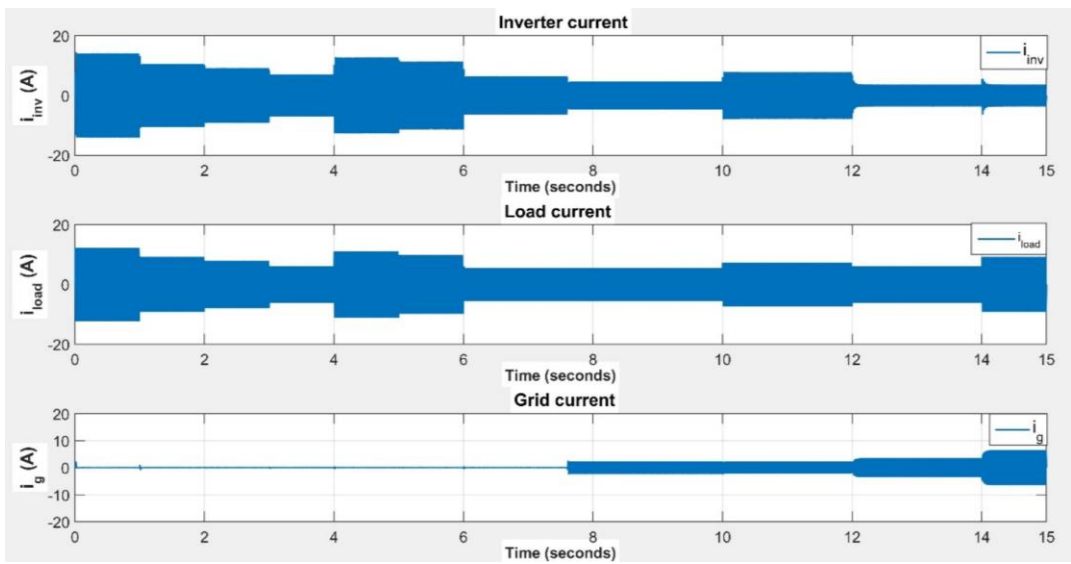


Figure 4.38: Inverter current, load current and grid current (Scenario 4)

5 Conclusions

5.1 Summary

A model containing a 3 kW_p rooftop solar PV system connected to the grid through converters and a battery-supercapacitor hybrid energy storage system was proposed in this Thesis. First, the mathematical analysis and modeling of the PV array, based on the equivalent circuit of the one-diode PV cell, was examined. After that, three different MPPT techniques were compared, resulting in the best choice for our needs, which was the P&O algorithm. Furthermore, the battery and supercapacitor storage models were examined, respectively, where the proper sizing of each storage technology was calculated. Specifically, the battery model was based on the dual polarization (2nd-order RC) battery cell circuit, while the supercapacitor model was based on the two branches equivalent cell circuit. A fully active parallel configuration was selected for the battery and supercapacitor, and a small-signal ac analysis was considered for the design of the current controllers for the two bidirectional DC-DC converters. A stability analysis was conducted for both the boost and the buck mode of operation of the converters, resulting in a more accurate tuning of the controllers. In addition, through the voltage control of the DC-bus, a reference magnitude for the output current of the inverter was obtained. Also, a PLL was used so that the output current injected into the grid be in phase with the grid voltage (unity power factor) and meet the requirements for grid interconnection. Finally, a novel and customized dynamic local PMA was proposed, prioritizing the utilization of the PV and the battery-supercapacitor instead of the grid, and aiming to increase the PV self-consumption and self-sufficiency of the building. Specifically, twelve (12) different cases were identified depending on the amount of generated PV power, the amount of required load power, and the availability of energy in the battery and the supercapacitor.

The simulation results confirmed that the model works properly under different circumstances for both long-term and short-term operation. Specifically, the PV system with battery-only and battery-supercapacitor applications was examined, for long-term operation of 24 hours. The results verified the supportive functioning of the supercapacitor, handling the rapid changes that occur within 0.2 seconds, thus relieving the battery stress and extending the battery lifetime. Also, through the results of the short-

term operation (10–30 seconds), the dynamic performance of the system is verified, observing a fast DC-bus voltage regulation with a very small ripple voltage (a maximum of $\pm 0.625\%$). In conclusion, the proposed model works properly and reacts very fast through several rapid changes in PV generation and in load demand, achieving an increase in self-consumption and self-sufficiency, thus reducing the electricity bill.

It must be emphasized that the proposed model in this Thesis: (i) is of a comprehensive nature, (ii) contains a unique PMA for the proper use of generated and demanded power for increased self-consumption and self-sufficiency of the building, and (iii) provides in general an important step in knowledge.

5.2 Future directions

There are several possible future directions that could be investigated for this model. A possible future study could be the consideration of the islanding condition of the system. When a grid fault occurs, the grid inverter must be disconnected from the grid for security reasons. Therefore, the system must detect this failure and operate in an islanded mode. During this mode, all critical loads must keep receiving energy from the PV (in daylight) and/or the hybrid storage.

Moreover, an interesting integration in the existing model could be the electric vehicle consideration, also known as V2H (vehicle-to-home). Electric vehicles penetration has been growing rapidly in recent years, and their storage capabilities could be a significant key in supporting the needs of a building. The charging and discharging phase of the vehicle can be adjusted depending on the PV generation and building demand, hence the vehicle can act as a controllable load or a backup generator. The management of the V2H will definitely play an important role in the future, especially in promoting the development of smart home energy management techniques and reducing emissions.

Another potential addition in our system could be the integration of the building to several grid support functionalities, such as the primary frequency regulation. The mismatch between generation and demand affects the grid frequency. Even though the contribution of each small system (building) is not significant, the cumulative impact of many systems can be considerable.

Finally, the consideration of several financial aspects could be a valuable improvement for this model. Specifically, considering the technical aspects of the model, the optimization of the storage and PV array sizing concerning the building needs and the time-of-use (TOU) electricity rates could be an important addition to the study. Therefore, a complete technical and economic assessment could give a better understanding of the performance of the system.

Concluding, the proposed model was developed in MATLAB/Simulink, where each part of the model was fully analyzed and customized, with no black boxes, from the ground up. Therefore, the model can be easily extended and adjusted to satisfy several future integrations.

REFERENCES

- [1] EU, “Directive 2010/31/EU of the European Parliament and of the Council of 19 May 2010 on the energy performance of buildings,” *Off. J. Eur. Union*, pp. 13–35, 2010.
- [2] IRENA, “Renewable Energy Roadmap for the Republic of Cyprus,” 2015. [Online]. Available: <http://www.irena.org/EventDocs/Maldives/Maldivesroadmapbackgroundreport.pdf>.
- [3] European Commission, “2030 Climate Target Plan,” *EU climate action & Green Deal*, 2020. https://ec.europa.eu/clima/policies/eu-climate-action/2030_ctp_en (accessed Sep. 23, 2020).
- [4] Republic of Cyprus, “Cyprus’ Integrated national energy and climate plan for the period 2021-2030,” Nicosia, 2020. [Online]. Available: https://ec.europa.eu/energy/sites/ener/files/documents/cy_final_necp_main_en.pdf.
- [5] European Commission, “2050 long-term strategy,” *Climate strategies & targets*, 2020. https://ec.europa.eu/clima/policies/strategies/2050_en (accessed Sep. 23, 2020).
- [6] European Commission, “European Climate Law,” *EU climate action & Green Deal*, 2020. https://ec.europa.eu/clima/policies/eu-climate-action/law_en (accessed Sep. 23, 2020).
- [7] REN21, “Renewables 2017 Global Status Report 2017,” 2017.
- [8] M. Bilgili, A. Ozbek, B. Sahin, and A. Kahraman, “An overview of renewable electric power capacity and progress in new technologies in the world,” *Renew. Sustain. Energy Rev.*, vol. 49, pp. 323–334, 2015.
- [9] F. R. Pazheri, M. F. Othman, and N. H. Malik, “A review on global renewable electricity scenario,” *Renew. Sustain. Energy Rev.*, vol. 31, pp. 835–845, 2014, [Online]. Available: <http://dx.doi.org/10.1016/j.rser.2013.12.020>.
- [10] IRENA, *Electricity storage and renewables: Costs and markets to 2030*. Abu Dhabi: International Renewable Energy Agency, 2017.
- [11] IRENA, *Innovation landscape brief: Behind-the-meter batteries*. Abu Dhabi: International Renewable Energy Agency, 2019.
- [12] M. C. Argyrou, P. Christodoulides, C. C. Marouchos, and G. A. Florides, “Energy storage technologies, nearly Zero Energy Buildings and a short-term storage application,” 2016.
- [13] K. Voss, E. Musall, and M. Lichtmeß, “From Low-Energy to Net Zero-Energy Buildings: Status and Perspectives,” *J. Green Build.*, vol. 6, no. 1, pp. 46–57, 2011.
- [14] W. Pan, “System boundaries of zero carbon buildings,” *Renew. Sustain. Energy Rev.*, vol. 37, pp. 424–434, 2014, [Online]. Available: <http://dx.doi.org/10.1016/j.rser.2014.05.015>.
- [15] D. H. W. Li, L. Yang, and J. C. Lam, “Zero energy buildings and sustainable development implications - A review,” *Energy*, vol. 54, pp. 1–10, 2013, [Online]. Available: <http://dx.doi.org/10.1016/j.energy.2013.01.070>.
- [16] R. Luthander, J. Widén, D. Nilsson, and J. Palm, “Photovoltaic self-consumption in buildings: A review,” *Appl. Energy*, vol. 142, pp. 80–94, 2015, doi: 10.1016/j.apenergy.2014.12.028.
- [17] D. Gudmunds, E. Nyholm, M. Taljegard, and M. Odenberger, “Self-consumption and self-sufficiency for household solar producers when introducing an electric vehicle,”

- Renew. Energy*, vol. 148, pp. 1200–1215, 2020, doi: 10.1016/j.renene.2019.10.030.
- [18] H. Zhou, T. Bhattacharya, D. Tran, T. S. T. Siew, and A. M. Khambadkone, “Composite energy storage system involving battery and ultracapacitor with dynamic energy management in microgrid applications,” *IEEE Trans. Power Electron.*, vol. 26, no. 3, pp. 923–930, 2011, doi: 10.1109/TPEL.2010.2095040.
- [19] S. K. Kollimalla, M. K. Mishra, and N. L. Narasamma, “Design and analysis of novel control strategy for battery and supercapacitor storage system,” *IEEE Trans. Sustain. Energy*, vol. 5, no. 4, pp. 1137–1144, 2014, doi: 10.1109/TSTE.2014.2336896.
- [20] U. Manandhar, N. R. Tummuru, S. K. Kollimalla, A. Ukil, G. H. Beng, and K. Chaudhari, “Validation of Faster Joint Control Strategy for Battery- and Supercapacitor-Based Energy Storage System,” *IEEE Trans. Ind. Electron.*, vol. 65, no. 4, pp. 3286–3295, 2018, doi: 10.1109/TIE.2017.2750622.
- [21] S. Kotra and M. K. Mishra, “Control algorithm for a PV based hybrid microgrid,” in *2015 Annual IEEE India Conference (INDICON)*, 2015, pp. 1–6, doi: 10.1109/INDICON.2015.7443554.
- [22] S. Kotra and M. K. Mishra, “A supervisory power management system for a hybrid microgrid with HESS,” *IEEE Trans. Ind. Electron.*, vol. 64, no. 5, pp. 3640–3649, 2017, doi: 10.1109/TIE.2017.2652345.
- [23] S. Hajiaghasi, A. Salemnia, and M. Hamzeh, “Hybrid energy storage performance improvement in microgrid application,” *9th Annu. Int. Power Electron. Drive Syst. Technol. Conf. PEDSTC 2018*, pp. 392–397, 2018, doi: 10.1109/PEDSTC.2018.8343829.
- [24] P. Singh and J. S. Lather, “Variable structure control for dynamic power-sharing and voltage regulation of DC microgrid with a hybrid energy storage system,” *Int. Trans. Electr. Energy Syst.*, pp. 1–20, 2020, doi: 10.1002/2050-7038.12510.
- [25] P. Singh and J. S. Lather, “Dynamic current sharing, voltage and SOC regulation for HESS based DC microgrid using CPISMTC technique,” *J. Energy Storage*, vol. 30, no. March, p. 101509, 2020, doi: 10.1016/j.est.2020.101509.
- [26] F. M. Vieira, P. S. Moura, and A. T. de Almeida, “Energy storage system for self-consumption of photovoltaic energy in residential zero energy buildings,” *Renew. Energy*, vol. 103, pp. 308–320, 2017, doi: 10.1016/j.renene.2016.11.048.
- [27] Z. Cabrane, M. Ouassaid, and M. Maaroufi, “Analysis and evaluation of battery-supercapacitor hybrid energy storage system for photovoltaic installation,” *Int. J. Hydrogen Energy*, vol. 41, no. 45, pp. 20897–20907, 2016, doi: 10.1016/j.ijhydene.2016.06.141.
- [28] Z. Cabrane, M. Ouassaid, and M. Maaroufi, “Management and control of the integration of supercapacitor in photovoltaic energy storage,” 2017, doi: 10.1109/GECS.2017.8066128.
- [29] Z. Cabrane, M. Ouassaid, and M. Maaroufi, “Battery and supercapacitor for photovoltaic energy storage: A fuzzy logic management,” *IET Renew. Power Gener.*, vol. 11, no. 8, pp. 1157–1165, 2017, doi: 10.1049/iet-rpg.2016.0455.
- [30] N. Saxena, B. Singh, and A. L. Vyas, “Integration of solar photovoltaic with battery to single-phase grid,” *IET Gener. Transm. Distrib.*, vol. 11, no. 8, pp. 2003–2012, 2017, doi: 10.1049/iet-gtd.2016.1455.
- [31] I. B. Song, D. Y. Jung, Y. H. Ji, S. C. Choi, S. W. Lee, and C. Y. Won, “A residential 10kWh lithium-polymer battery energy storage system,” in *8th International Conference on Power Electronics - ECCE Asia: “Green World with Power Electronics”*, ICPE

- 2011-ECCE Asia, 2011, pp. 2625–2630, doi: 10.1109/ICPE.2011.5944747.
- [32] A. Aktas, K. Erhan, S. Ozdemir, and E. Ozdemir, “Experimental investigation of a new smart energy management algorithm for a hybrid energy storage system in smart grid applications,” *Electr. Power Syst. Res.*, vol. 144, pp. 185–196, 2017, doi: 10.1016/j.epsr.2016.11.022.
- [33] A. Aktas, K. Erhan, S. Özdemir, and E. Özdemir, “Dynamic energy management for photovoltaic power system including hybrid energy storage in smart grid applications,” *Energy*, vol. 162, pp. 72–82, 2018, doi: 10.1016/j.energy.2018.08.016.
- [34] M. G. Simões, C. L. Lute, A. N. Alsaleem, D. I. Brandao, and J. A. Pomilio, “Bidirectional Floating Interleaved Buck-Boost DC-DC Converter Applied to Residential PV Power Systems,” in *2015 Clemson University Power Systems Conference (PSC)*, 2015, pp. 1–8.
- [35] L. Barelli *et al.*, “Dynamic Analysis of a Hybrid Energy Storage System (H-ESS) Coupled to a Photovoltaic (PV) Plant,” *Energies*, vol. 11, no. 2, p. 396, 2018, doi: 10.3390/en11020396.
- [36] S. C. Choi, M. H. Sin, D. R. Kim, C. Y. Won, and Y. C. Jung, “Versatile power transfer strategies of PV-battery hybrid system for residential use with energy management system,” *2014 Int. Power Electron. Conf. IPEC-Hiroshima - ECCE Asia 2014*, pp. 409–414, 2014, doi: 10.1109/IPEC.2014.6869615.
- [37] Z. Yi, W. Dong, and A. H. Etemadi, “A unified control and power management scheme for PV-Battery-based hybrid microgrids for both grid-connected and islanded modes,” *IEEE Trans. Smart Grid*, vol. 9, no. 6, pp. 5975–5985, 2018, doi: 10.1109/TSG.2017.2700332.
- [38] M. Y. Worku and M. A. Abido, “Grid-connected PV array with supercapacitor energy storage system for fault ride through,” *Proc. IEEE Int. Conf. Ind. Technol.*, pp. 2901–2906, 2015, doi: 10.1109/ICIT.2015.7125526.
- [39] I. Ranaweera, S. Sanchez, and O. M. Midtgård, “Residential photovoltaic and battery energy system with grid support functionalities,” 2015, doi: 10.1109/PEDG.2015.7223014.
- [40] A. Jahangir, V. Nougain, and S. Mishra, “Control Topology of Hybrid Energy Storage System for AC-DC Microgrid,” in *2018 IEEE International Conference on Power Electronics, Drives and Energy Systems, PEDES 2018*, 2018, pp. 1–5, doi: 10.1109/PEDES.2018.8707682.
- [41] D. M. R. Korada and M. K. Mishra, “Design of composite energy storage system for wind turbine under gust,” 2019, doi: 10.1109/ICPECA47973.2019.8975478.
- [42] D. M. R. Korada, M. K. Mishra, and R. S. Yallamilli, “Dynamic Energy Management in DC Microgrid using Composite Energy Storage System,” in *2020 IEEE International Conference on Power Electronics, Smart Grid and Renewable Energy, PESGRE 2020*, 2020, no. 2, pp. 1–6, doi: 10.1109/PESGRE45664.2020.9070693.
- [43] O. Ellabban, H. Abu-Rub, and F. Blaabjerg, “Renewable energy resources: Current status, future prospects and their enabling technology,” *Renew. Sustain. Energy Rev.*, vol. 39, pp. 748–764, 2014.
- [44] N. L. Panwar, S. C. Kaushik, and S. Kothari, “Role of renewable energy sources in environmental protection: A review,” *Renew. Sustain. Energy Rev.*, vol. 15, no. 3, pp. 1513–1524, 2011.
- [45] V. Devabhaktuni, M. Alam, S. S. S. R. Depuru, R. C. Green, D. Nims, and C. Near, “Solar energy: Trends and enabling technologies,” *Renew. Sustain. Energy Rev.*, vol. 19,

- pp. 555–564, 2013, [Online]. Available: <http://dx.doi.org/10.1016/j.rser.2012.11.024>.
- [46] B. Parida, S. Iniyana, and R. Goic, “A review of solar photovoltaic technologies,” *Renew. Sustain. Energy Rev.*, vol. 15, no. 3, pp. 1625–1636, 2011, [Online]. Available: <http://dx.doi.org/10.1016/j.rser.2010.11.032>.
- [47] REN21, “Renewables 2020 Global Status Report,” Paris, 2020. [Online]. Available: <http://www.ren21.net/resources/publications/>.
- [48] REN21, “Renewables 2019 Global Status Report,” Paris, 2019.
- [49] J. Ramos Hernanz, J. J. Campayo Martín, I. Zamora Berver, J. Larrañaga Lesaka, E. Zulueta Guerrero, and E. Puelles Pérez, “Modelling of photovoltaic module,” *Int. Conf. Renew. Energies Power Qual. Granada, Spain*, vol. 1, no. 8, 2010, [Online]. Available: <http://icrepq.com/icrepq'10/619-Hernanz.pdf>.
- [50] M. G. Villalva, J. R. Gazoli, and E. R. Filho, “Comprehensive approach to modeling and simulation of photovoltaic arrays,” *IEEE Trans. Power Electron.*, vol. 24, no. 5, pp. 1198–1208, 2009, doi: 10.1109/TPEL.2009.2013862.
- [51] H. Samani, “Microgrid System Including PV Generation and Hybrid Backup System,” Master dissertation, Ryerson University, Toronto, Ontario, Canada, 2016.
- [52] P. I. Muoka, “Control of Power Electronic Interfaces for Photovoltaic Power Systems for Maximum Power Extraction,” PhD thesis, University of Tasmania, 2014.
- [53] L. El Chaar, L. A. Lamont, and N. El Zein, “Review of photovoltaic technologies,” *Renew. Sustain. Energy Rev.*, vol. 15, no. 5, pp. 2165–2175, 2011, doi: 10.1016/j.rser.2011.01.004.
- [54] F. Z. Amatoul, M. T. Lamchich, and A. Outzourhit, “Design Control of DC /AC Converter for a grid Connected PV Systems using Matlab/Simulink,” 2011.
- [55] H. Chen, T. N. Cong, W. Yang, C. Tan, Y. Li, and Y. Ding, “Progress in electrical energy storage system: A critical review,” *Prog. Nat. Sci.*, vol. 19, no. 3, pp. 291–312, 2009, [Online]. Available: <http://dx.doi.org/10.1016/j.pnsc.2008.07.014>.
- [56] M. C. Argyrou, P. Christodoulides, and S. A. Kalogirou, “Energy storage for electricity generation and related processes: Technologies appraisal and grid scale applications,” *Renew. Sustain. Energy Rev.*, vol. 94, pp. 804–821, 2018, doi: 10.1016/j.rser.2018.06.044.
- [57] IRENA, “REthinking Energy 2017: Accelerating the global energy transformation,” International Renewable Energy Agency, Abu Dhabi, 2017.
- [58] United States Department of Energy, “DOE Global Energy Storage Database,” *Office of Electricity Delivery & Energy Reliability*, 2017. <http://energystorageexchange.org/projects/> (accessed Nov. 01, 2017).
- [59] P. Medina, A. W. Bizuayehu, J. P. S. Catalao, E. M. G. Rodrigues, and J. Contreras, “Electrical Energy Storage Systems: Technologies’ State-of-the-Art, Techno-economic Benefits and Applications Analysis,” *47th Hawaii Int. Conf. Syst. Sci.*, pp. 2295–2304, 2014, doi: 10.1109/HICSS.2014.290.
- [60] ARTS Energy, “Glossary & Technicals Terms,” 2017. <http://www.arts-energy.com/glossary/> (accessed Nov. 01, 2017).
- [61] Energy Storage Association, “Glossary,” 2017. <http://energystorage.org/energy-storage/glossary> (accessed Nov. 01, 2017).
- [62] M. G. Molina, “Energy Storage and Power Electronics Technologies : A Strong Combination to Empower the Transformation to the Smart Grid,” *Proc. IEEE*, 2017.

- [63] K. D. Thompson, "Power Conditioning Systems for Renewables, Storage, and Microgrids," 2012. <https://www.nist.gov/programs-projects/power-conditioning-systems-renewables-storage-and-microgrids> (accessed Nov. 01, 2017).
- [64] J. M. Carrasco *et al.*, "Power-Electronic Systems for the Grid Integration of Renewable Energy Sources : A Survey," *IEEE Trans. Ind. Electron.*, vol. 53, no. 4, pp. 1002–1016, 2006.
- [65] I. Hadjipaschalis, A. Poullikkas, and V. Efthimiou, "Overview of current and future energy storage technologies for electric power applications," *Renew. Sustain. Energy Rev.*, vol. 13, no. 6–7, pp. 1513–1522, Aug. 2009, Accessed: Mar. 22, 2014. [Online]. Available: <http://linkinghub.elsevier.com/retrieve/pii/S1364032108001664>.
- [66] A. Poullikkas, "Optimization analysis for pumped energy storage systems in small isolated power systems," *J. Power Technol.*, vol. 93, no. 2, pp. 78–89, 2013.
- [67] M. Beaudin, H. Zareipour, A. Schellenberglabe, and W. Rosehart, "Energy storage for mitigating the variability of renewable electricity sources: An updated review," *Energy Sustain. Dev.*, vol. 14, no. 4, pp. 302–314, 2010, [Online]. Available: <http://dx.doi.org/10.1016/j.esd.2010.09.007>.
- [68] T. Kousksou, P. Bruel, A. Jamil, T. El Rhafiki, and Y. Zeraouli, "Energy storage: Applications and challenges," *Sol. Energy Mater. Sol. Cells*, vol. 120, pp. 59–80, 2014.
- [69] A. Morabito, J. Steimes, O. Bontems, G. Al Zohbi, and P. Hendrick, "Set-up of a pump as turbine use in micro-pumped hydro energy storage: a case of study in Froyennes Belgium," in *Journal of Physics: Conference Series*, 2017, vol. 813, no. 1, p. 012033, doi: 10.1088/1742-6596/755/1/011001.
- [70] G. D. e Silva and P. Hendrick, "Pumped hydro energy storage in buildings," *Appl. Energy*, vol. 179, pp. 1242–1250, 2016, doi: 10.1016/j.apenergy.2016.07.046.
- [71] C. K. Ekman and S. H. Jensen, "Prospects for large scale electricity storage in Denmark," *Energy Convers. Manag.*, vol. 51, pp. 1140–1147, 2010, [Online]. Available: <http://dx.doi.org/10.1016/j.enconman.2009.12.023>.
- [72] X. Luo, J. Wang, M. Dooner, J. Clarke, and C. Krupke, "Overview of current development in compressed air energy storage technology," *Energy Procedia*, vol. 62, pp. 603–611, 2014, doi: 10.1016/j.egypro.2014.12.423.
- [73] T. M. Masaud, K. L. K. Lee, and P. K. Sen, "An overview of energy storage technologies in electric power systems: What is the future?," in *North American Power Symposium NAPS 2010*, 2010, pp. 1–6, [Online]. Available: http://ieeexplore.ieee.org/xpl/freeabs_all.jsp?arnumber=5619595.
- [74] P. Angheliță, M. Chefneux, R. Balaban, and L. Trocan, "Energy storage systems for buildings equipped with photovoltaic cells," in *Electrical and Electronics Engineering (ISEEE), 2010 3rd International Symposium on IEEE*, 2010, pp. 332–335.
- [75] J. Baker, "New technology and possible advances in energy storage," *Energy Policy*, vol. 36, no. 12, pp. 4368–4373, 2008, doi: 10.1016/j.enpol.2008.09.040.
- [76] H. Ibrahim, A. Ilinca, and J. Perron, "Energy storage systems - Characteristics and comparisons," *Renew. Sustain. Energy Rev.*, vol. 12, no. 5, pp. 1221–1250, 2008.
- [77] K. Bradbury, "Energy Storage Technology Review," 2010.
- [78] L. Geissbühler *et al.*, "Pilot-scale demonstration of advanced adiabatic compressed air energy storage, Part 1: Plant description and tests with sensible thermal-energy storage," *J. Energy Storage*, vol. 17, pp. 129–139, 2018, doi: 10.1016/j.est.2018.02.004.
- [79] M. Yekini Suberu, M. Wazir Mustafa, and N. Bashir, "Energy storage systems for

- renewable energy power sector integration and mitigation of intermittency,” *Renew. Sustain. Energy Rev.*, vol. 35, pp. 499–514, 2014, doi: 10.1016/j.rser.2014.04.009.
- [80] D. O. Akinyele and R. K. Rayudu, “Review of energy storage technologies for sustainable power networks,” *Sustain. Energy Technol. Assessments*, vol. 8, pp. 74–91, 2014, doi: 10.1016/j.seta.2014.07.004.
- [81] X. Luo, J. Wang, M. Dooner, and J. Clarke, “Overview of current development in electrical energy storage technologies and the application potential in power system operation,” *Appl. Energy*, vol. 137, pp. 511–536, 2015, [Online]. Available: <http://dx.doi.org/10.1016/j.apenergy.2014.09.081>.
- [82] J. Cho, S. Jeong, and Y. Kim, “Commercial and research battery technologies for electrical energy storage applications,” *Prog. Energy Combust. Sci.*, vol. 48, pp. 84–101, 2015, [Online]. Available: <http://dx.doi.org/10.1016/j.pecs.2015.01.002>.
- [83] D. Akinyele, J. Belikov, and Y. Levron, “Battery Storage Technologies for Electrical Applications: Impact in Stand-Alone Photovoltaic Systems,” *Energies*, vol. 10, no. 11, p. 1760, 2017, doi: 10.3390/en10111760.
- [84] N. K. C. Nair and N. Garimella, “Battery energy storage systems: Assessment for small-scale renewable energy integration,” *Energy Build.*, vol. 42, no. 11, pp. 2124–2130, 2010, doi: 10.1016/j.enbuild.2010.07.002.
- [85] International Electrotechnical Commission (IEC), “Electrical Energy Storage: white paper,” Switzerland, 2011. [Online]. Available: <http://www.iec.ch/whitepaper/pdf/iecWP-energystorage-LR-en.pdf>.
- [86] A. B. Gallo, J. R. Simões-Moreira, H. K. M. Costa, M. M. Santos, and E. Moutinho dos Santos, “Energy storage in the energy transition context: A technology review,” *Renew. Sustain. Energy Rev.*, vol. 65, pp. 800–822, 2016, doi: 10.1016/j.rser.2016.07.028.
- [87] B. Dunn, H. Kamath, and J.-M. Tarascon, “Electrical Energy Storage for the Grid: A Battery of Choices,” *Science (80-.)*, vol. 334, pp. 928–935, 2011.
- [88] A. Poullikkas, “A comparative overview of large-scale battery systems for electricity storage,” *Renew. Sustain. Energy Rev.*, vol. 27, pp. 778–788, 2013, [Online]. Available: <http://dx.doi.org/10.1016/j.rser.2013.07.017>.
- [89] L. Lu, X. Han, J. Li, J. Hua, and M. Ouyang, “A review on the key issues for lithium-ion battery management in electric vehicles,” *J. Power Sources*, vol. 226, pp. 272–288, 2013, doi: 10.1016/j.jpowsour.2012.10.060.
- [90] B. Diouf and R. Pode, “Potential of lithium-ion batteries in renewable energy,” *Renew. Energy*, vol. 76, pp. 375–380, 2015, doi: 10.1016/j.renene.2014.11.058.
- [91] A. Khaligh and Z. Li, “Battery, ultracapacitor, fuel cell, and hybrid energy storage systems for electric, hybrid electric, fuel cell, and plug-in hybrid electric vehicles: State of the art,” *IEEE Trans. Veh. Technol.*, vol. 59, no. 6, pp. 2806–2814, 2010, doi: 10.1109/TVT.2010.2047877.
- [92] N. Nitta, F. Wu, J. T. Lee, and G. Yushin, “Li-ion battery materials: Present and future,” *Mater. Today*, vol. 18, no. 5, pp. 252–264, 2015, doi: 10.1016/j.mattod.2014.10.040.
- [93] X. Cai, L. Lai, Z. Shen, and J. Lin, “Graphene and graphene-based composites as Li-ion battery electrode materials and their application in full cells,” *J. Mater. Chem. A*, vol. 5, pp. 15423–15446, 2017, doi: 10.1039/C7TA04354F.
- [94] L. Jiao *et al.*, “An advanced lithium ion battery based on a high quality graphitic graphene anode and a Li [Ni 0.6 Co 0.2 Mn 0.2] O 2 cathode,” *Electrochim. Acta*, vol. 259, pp. 48–55, 2018, doi: 10.1016/j.electacta.2017.10.155.

- [95] W. Yuan, Y. Zhang, L. Cheng, H. Wu, L. Zheng, and D. Zhao, "The applications of carbon nanotubes and graphene in advanced rechargeable lithium batteries," *J. Mater. Chem. A*, vol. 4, no. 23, pp. 8932–8951, 2016, doi: 10.1039/C6TA01546H.
- [96] X. Li and L. Zhi, "Graphene hybridization for energy storage applications," *Chem. Soc. Rev.*, 2018, doi: 10.1039/C7CS00871F.
- [97] R. Mertens, "Is Tesla developing a graphene-enhanced Li-Ion battery?," 2014. <https://www.graphene-info.com/tesla-developing-graphene-enhanced-li-ion-battery> (accessed May 13, 2018).
- [98] R. Peleg, "Fisker unveils new EV with graphene-enhanced battery," 2016. <https://www.graphene-info.com/fisker-unveils-new-ev-graphene-enhanced-battery> (accessed May 13, 2018).
- [99] I. H. Son *et al.*, "Graphene balls for lithium rechargeable batteries with fast charging and high volumetric energy densities," *Nat. Commun.*, vol. 8, no. 1, pp. 1–10, 2017, doi: 10.1038/s41467-017-01823-7.
- [100] S. Koochi-Kamali, V. V. Tyagi, N. A. Rahim, N. L. Panwar, and H. Mokhlis, "Emergence of energy storage technologies as the solution for reliable operation of smart power systems: A review," *Renew. Sustain. Energy Rev.*, vol. 25, pp. 135–165, 2013, doi: 10.1016/j.rser.2013.03.056.
- [101] W. Wang, Q. Luo, B. Li, X. Wei, L. Li, and Z. Yang, "Recent progress in redox flow battery research and development," *Adv. Funct. Mater.*, vol. 23, no. 8, pp. 970–986, 2013, doi: 10.1002/adfm.201200694.
- [102] F. Díaz-González, A. Sumper, O. Gomis-Bellmunt, and R. Villafáfila-Robles, "A review of energy storage technologies for wind power applications," *Renew. Sustain. Energy Rev.*, vol. 16, no. 4, pp. 2154–2171, 2012, doi: 10.1016/j.rser.2012.01.029.
- [103] C. Choi *et al.*, "A review of vanadium electrolytes for vanadium redox flow batteries," *Renew. Sustain. Energy Rev.*, vol. 69, pp. 263–274, 2017, doi: 10.1016/j.rser.2016.11.188.
- [104] M. Uhrig, S. Koenig, M. R. Suriyah, and T. Leibfried, "Lithium-based vs. Vanadium Redox Flow Batteries - A Comparison for Home Storage Systems," *Energy Procedia*, vol. 99, pp. 35–43, 2016, doi: 10.1016/j.egypro.2016.10.095.
- [105] L. F. Arenas, A. Loh, D. P. Trudgeon, X. Li, C. Ponce de León, and F. C. Walsh, "The characteristics and performance of hybrid redox flow batteries with zinc negative electrodes for energy storage," *Renew. Sustain. Energy Rev.*, vol. 90, pp. 992–1016, 2018, doi: 10.1016/j.rser.2018.03.016.
- [106] M. S. Guney and Y. Tepe, "Classification and assessment of energy storage systems," *Renew. Sustain. Energy Rev.*, vol. 75, pp. 1187–1197, 2017, doi: 10.1016/j.rser.2016.11.102.
- [107] S. Pintaldi, C. Perfumo, S. Sethuvenkatraman, S. White, and G. Rosengarten, "A review of thermal energy storage technologies and control approaches for solar cooling," *Renew. Sustain. Energy Rev.*, vol. 41, pp. 975–995, 2015, [Online]. Available: <http://dx.doi.org/10.1016/j.rser.2014.08.062>.
- [108] International Energy Agency (IEA), "Technology Roadmap: Concentrating Solar Power," Paris, France, 2010. [Online]. Available: https://www.iea.org/publications/freepublications/publication/csp_roadmap.pdf.
- [109] C. Barile, "Solar thermal energy storage systems," 2010. <http://large.stanford.edu/courses/2010/ph240/barile2/> (accessed Nov. 01, 2017).

- [110] S. A. Kalogirou, *Solar energy engineering: processes and systems*, Second. United States of America: Academic Press, 2014.
- [111] G. Li and X. Zheng, “Thermal energy storage system integration forms for a sustainable future,” *Renew. Sustain. Energy Rev.*, vol. 62, pp. 736–757, 2016, doi: 10.1016/j.rser.2016.04.076.
- [112] U. Pelay, L. Luo, Y. Fan, D. Stitou, and M. Rood, “Thermal energy storage systems for concentrated solar power plants,” *Renew. Sustain. Energy Rev.*, vol. 79, pp. 82–100, 2017, doi: 10.1016/j.rser.2017.03.139.
- [113] S. Kuravi, J. Trahan, D. Y. Goswami, M. M. Rahman, and E. K. Stefanakos, “Thermal energy storage technologies and systems for concentrating solar power plants,” *Prog. Energy Combust. Sci.*, vol. 39, no. 4, pp. 285–319, 2013, doi: 10.1016/j.peccs.2013.02.001.
- [114] R. Amirante, E. Cassone, E. Distaso, and P. Tamburrano, “Overview on recent developments in energy storage: Mechanical, electrochemical and hydrogen technologies,” *Energy Convers. Manag.*, vol. 132, pp. 372–387, 2017, doi: 10.1016/j.enconman.2016.11.046.
- [115] T. U. Daim, X. Li, J. Kim, and S. Simms, “Evaluation of energy storage technologies for integration with renewable electricity: Quantifying expert opinions,” *Environ. Innov. Soc. Transitions*, vol. 3, pp. 29–49, 2012, doi: 10.1016/j.eist.2012.04.003.
- [116] S. M. Mousavi G, F. Faraji, A. Majazi, and K. Al-Haddad, “A comprehensive review of Flywheel Energy Storage System technology,” *Renew. Sustain. Energy Rev.*, vol. 67, pp. 477–490, 2017, doi: 10.1016/j.rser.2016.09.060.
- [117] T. M. I. Mahlia, T. J. Saktisahdan, A. Jannifar, M. H. Hasan, and H. S. C. Matseelar, “A review of available methods and development on energy storage; Technology update,” *Renew. Sustain. Energy Rev.*, vol. 33, pp. 532–545, 2014, [Online]. Available: <http://dx.doi.org/10.1016/j.rser.2014.01.068>.
- [118] A. González, E. Goikolea, J. A. Barrena, and R. Mysyk, “Review on supercapacitors: Technologies and materials,” *Renew. Sustain. Energy Rev.*, vol. 58, pp. 1189–1206, 2016, doi: 10.1016/j.rser.2015.12.249.
- [119] P. Zhao, J. Wang, and Y. Dai, “Capacity allocation of a hybrid energy storage system for power system peak shaving at high wind power penetration level,” *Renew. Energy*, vol. 75, pp. 541–549, 2015, [Online]. Available: <http://dx.doi.org/10.1016/j.renene.2014.10.040>.
- [120] G. Fuchs, B. Lunz, M. Leuthold, and D. U. Sauer, “Technology Overview on Electricity Storage,” *Inst. Power Electron. Electr. Drives (ISEA), RWTH Aachen Univ.*, 2012, [Online]. Available: http://www.sefep.eu/activities/projects-studies/120628_Technology_Overview_Electricity_Storage_SEFEP_ISEA.pdf.
- [121] J. K. Kaldellis, D. Zafirakis, and K. Kavadias, “Techno-economic comparison of energy storage systems for island autonomous electrical networks,” *Renew. Sustain. Energy Rev.*, vol. 13, no. 2, pp. 378–392, 2009, doi: 10.1016/j.rser.2007.11.002.
- [122] T. Aquino, M. Roling, C. Baker, and L. Rowland, “Battery energy storage technology assessment,” 2017. [Online]. Available: <https://www.prpa.org/wp-content/uploads/2017/10/HDR-Battery-Energy-Storage-Assessment.pdf>.
- [123] International Energy Agency (IEA), “Technology Roadmap: Energy Storage,” 2014.
- [124] B. Zakeri and S. Syri, “Electrical energy storage systems: A comparative life cycle cost analysis,” *Renew. Sustain. Energy Rev.*, vol. 42, pp. 569–596, 2015, doi: 10.1016/j.rser.2014.10.011.

- [125] A. Castillo and D. F. Gayme, “Grid-scale energy storage applications in renewable energy integration: A survey,” *Energy Convers. Manag.*, vol. 87, pp. 885–894, 2014, doi: 10.1016/j.enconman.2014.07.063.
- [126] T.-T. Nguyen, V. Martin, A. Malmquist, and C. A. S. Silva, “A review on technology maturity of small scale energy storage technologies,” *Renew. Energy Environ. Sustain.*, vol. 2, no. 36, 2017, doi: 10.1051/rees/2017039.
- [127] P. J. Hall and E. J. Bain, “Energy-storage technologies and electricity generation,” *Energy Policy*, vol. 36, no. 12, pp. 4352–4355, 2008, doi: 10.1016/j.enpol.2008.09.037.
- [128] S. Sabihuddin, A. E. Kiprakis, and M. Mueller, “A numerical and graphical review of energy storage technologies,” *Energies*, vol. 8, no. 1, pp. 172–216, 2015, doi: 10.3390/en8010172.
- [129] M. Aneke and M. Wang, “Energy storage technologies and real life applications – A state of the art review,” *Appl. Energy*, vol. 179, pp. 350–377, 2016, doi: 10.1016/j.apenergy.2016.06.097.
- [130] A. Slaughter, “Electricity Storage Technologies, Impacts, and Prospects,” *Deloitte Cent. Energy Solut.*, 2015.
- [131] G. N. Prodromidis and F. A. Coutelieris, “Simulations of economical and technical feasibility of battery and flywheel hybrid energy storage systems in autonomous projects,” *Renew. Energy*, vol. 39, no. 1, pp. 149–153, 2012, doi: 10.1016/j.renene.2011.07.041.
- [132] Royal Swedish Academy of Engineering Sciences, “Energy Storage: Electricity storage technologies,” Stockholm, 2016. [Online]. Available: www.iva.se.
- [133] C. Naish, I. McCubbin, O. Edberg, and M. Harfoot, “Outlook of energy storage technologies,” *Eur. Parliam. Comm. Ind. Res. Energy*, 2008.
- [134] X. Tan, Q. Li, and H. Wang, “Advances and trends of energy storage technology in Microgrid,” *Int. J. Electr. Power Energy Syst.*, vol. 44, no. 1, pp. 179–191, 2013, doi: 10.1016/j.ijepes.2012.07.015.
- [135] M. Bragard, N. Soltan, S. Thomas, and R. W. De Doncker, “The balance of renewable sources and user demands in grids: Power electronics for modular battery energy storage systems,” *IEEE Trans. Power Electron.*, vol. 25, no. 12, pp. 3049–3056, 2010.
- [136] S. Ould Amrouche, D. Rekioua, T. Rekioua, and S. Bacha, “Overview of energy storage in renewable energy systems,” *Int. J. Hydrogen Energy*, vol. 41, no. 45, pp. 20914–20927, 2016, doi: 10.1016/j.ijhydene.2016.06.243.
- [137] P. Li, “Energy storage is the core of renewable technologies,” *IEEE Nanotechnol. Mag.*, pp. 13–18, 2008, doi: 10.1109/MNANO.2009.932032.
- [138] J. Barton and D. Infield, “Energy Storage and its Use with Intermittent Renewable Energy,” *IEEE Trans. Energy Convers.*, vol. 19, no. 2, pp. 441–448, 2004.
- [139] F. Rahman, S. Rehman, and M. A. Abdul-Majeed, “Overview of energy storage systems for storing electricity from renewable energy sources in Saudi Arabia,” *Renew. Sustain. Energy Rev.*, vol. 16, no. 1, pp. 274–283, 2012, doi: 10.1016/j.rser.2011.07.153.
- [140] R. Benato, S. D. Sessa, G. Crugnola, M. Todeschini, and S. Zin, “Sodium nickel chloride cell model for stationary electrical energy storage,” 2015, doi: 10.1109/AEIT.2015.7415241.
- [141] J. L. Sudworth, “The sodium/nickel chloride (ZEBRA) battery,” *J. Power Sources*, vol. 100, no. 1–2, pp. 149–163, 2001.

- [142] M. Farhadi and O. Mohammed, "Energy Storage Technologies for High-Power Applications," *IEEE Trans. Ind. Appl.*, vol. 52, no. 3, pp. 1953–1962, 2016, doi: 10.1109/TIA.2015.2511096.
- [143] C. Zhang, Y. L. Wei, P. F. Cao, and M. C. Lin, "Energy storage system: Current studies on batteries and power condition system," *Renew. Sustain. Energy Rev.*, vol. 82, pp. 3091–3106, 2018, doi: 10.1016/j.rser.2017.10.030.
- [144] K. C. Divya and J. Østergaard, "Battery energy storage technology for power systems- An overview," *Electr. Power Syst. Res.*, vol. 79, no. 4, pp. 511–520, 2009, doi: 10.1016/j.epsr.2008.09.017.
- [145] D. Rastler, "Electricity Energy Storage Technology Options: A White Paper Primer on Applications, Costs, and Benefits," Electric Power Research Institute (EPRI), California, USA, 2010. [Online]. Available: <http://www.epri.com/abstracts/Pages/ProductAbstract.aspx?ProductId=000000000001020676>.
- [146] P. Alotto, M. Guarnieri, and F. Moro, "Redox flow batteries for the storage of renewable energy: A review," *Renew. Sustain. Energy Rev.*, vol. 29, pp. 325–335, 2014, doi: 10.1016/j.rser.2013.08.001.
- [147] T. Diaz de la Rubia, F. Klein, B. Shaffer, N. Kim, and G. Lovric, "Energy storage: Tracking the technologies that will transform the power sector," 2015.
- [148] S. M. Schoenung, "Characteristics and Technologies for Long-vs. Short-Term Energy Storage : A Study by the DOE Energy Storage Systems Program," *United States Dep. Energy*, 2001, doi: 10.2172/780306.
- [149] T. E. Hoff, R. Perez, and R. M. Margolis, "Maximizing the value of customer-sited PV systems using storage and controls," *Sol. Energy*, vol. 81, no. 7, pp. 940–945, 2007.
- [150] "Battery and Energy Technologies: Grid Scale Energy Storage Systems." http://www.mpoweruk.com/grid_storage.htm (accessed Nov. 01, 2017).
- [151] R. Carnegie, D. Gotham, D. Nderitu, and P. V. Preckel, "Utility Scale Energy Storage Systems: Benefits, Applications, and Technologies," *State Util. Forecast. Gr.*, 2013.
- [152] A. Nourai, "Large-Scale Electricity Storage Technologies for Energy Management," *Power Eng. Soc. Summer Meet. 2002 IEEE*, vol. 1, pp. 310–315, 2002, doi: 10.1109/PESS.2002.1043240.
- [153] E. Hossain, M. R. Tur, S. Padmanaban, S. Ay, and I. Khan, "Analysis and Mitigation of Power Quality Issues in Distributed Generation Systems Using Custom Power Devices," *IEEE Access*, vol. 6, pp. 16816–16833, 2018, doi: 10.1109/ACCESS.2018.2814981.
- [154] H.-R. Seo *et al.*, "Power quality control strategy for grid-connected renewable energy sources using PV array and supercapacitor," *Int. Conf. Electr. Mach. Syst.*, pp. 437–441, 2010.
- [155] Y. Ghiassi-Farrokhfal, S. Keshav, C. Rosenberg, and F. Ciucu, "Solar Power Shaping : An Analytical Approach," *IEEE Trans. Sustain. Energy*, vol. 6, no. 1, pp. 162–170, 2015.
- [156] T. Senjyu, M. Datta, A. Yona, and T. Funabashi, "PV Output Power Fluctuations Smoothing and Optimum Capacity of Energy Storage System for PV Power Generator," *Icrepq.Com*, pp. 3–7, 2008, [Online]. Available: http://www.icrepq.com/icrepq-08/213_senjyu.pdf.
- [157] O. M. Toledo, D. Oliveira Filho, and A. S. A. C. Diniz, "Distributed photovoltaic generation and energy storage systems: A review," *Renew. Sustain. Energy Rev.*, vol. 14,

no. 1, pp. 506–511, 2010.

- [158] A. Zahedi, “Maximizing solar PV energy penetration using energy storage technology,” *Renew. Sustain. Energy Rev.*, vol. 15, no. 1, pp. 866–870, 2011, doi: 10.1016/j.rser.2010.09.011.
- [159] A. K. Rohit and S. Rangnekar, “An overview of energy storage and its importance in Indian renewable energy sector: Part II – energy storage applications, benefits and market potential,” *J. Energy Storage*, vol. 13, pp. 447–456, 2017, doi: 10.1016/j.est.2017.07.012.
- [160] M. C. Argyrou, P. Christodoulides, C. C. Marouchos, S. A. Kalogirou, G. A. Florides, and L. Lazari, “Overview of energy storage technologies and a short-term storage application for wind turbines,” 2016.
- [161] A. Lahyani, P. Venet, A. Guermazi, and A. Troudi, “Battery / Supercapacitors Combination in uninterruptible power supply (UPS),” *IEEE Trans. Power Electron.*, vol. 28, no. 4, pp. 1509–1522, 2013.
- [162] G. Fitzgerald, J. Mandel, and J. Morris, *The economics of battery energy storage: How multi-use, customer-sited batteries deliver the most services and value to customers and the grid*. Basalt, Colorado, US: Rocky Mountain Institute, 2015.
- [163] T. Bocklisch, “Hybrid energy storage systems for renewable energy applications,” *Energy Procedia*, vol. 73, pp. 103–111, 2015, doi: 10.1016/j.egypro.2015.07.582.
- [164] V. Khare, S. Nema, and P. Baredar, “Solar-wind hybrid renewable energy system: A review,” *Renew. Sustain. Energy Rev.*, vol. 58, pp. 23–33, 2016, doi: 10.1016/j.rser.2015.12.223.
- [165] R. Hemmati and H. Saboori, “Emergence of hybrid energy storage systems in renewable energy and transport applications – A review,” *Renew. Sustain. Energy Rev.*, vol. 65, pp. 11–23, 2016, doi: 10.1016/j.rser.2016.06.029.
- [166] T. Bocklisch, “Hybrid energy storage approach for renewable energy applications,” *J. Energy Storage*, vol. 8, pp. 311–319, 2016, doi: 10.1016/j.est.2016.01.004.
- [167] S. Vazquez, S. M. Lukic, E. Galvan, L. G. Franquelo, and J. M. Carrasco, “Energy Storage Systems for Transport and Grid Applications,” *IEEE Trans. Ind. Electron.*, vol. 57, no. 12, pp. 3881–3895, 2010, doi: 10.1109/TIE.2010.2076414.
- [168] J. Wang *et al.*, “Overview of compressed air energy storage and technology development,” *Energies*, vol. 10, no. 7, 2017, doi: 10.3390/en10070991.
- [169] S. Lemofouet and A. Rufer, “Hybrid energy storage systems based on compressed air and supercapacitors with maximum efficiency point tracking,” *2005 Eur. Conf. Power Electron. Appl.*, 2005.
- [170] M. Martinez, M. G. Molina, F. Frack, and P. E. Mercado, “Dynamic Modeling, Simulation and Control of Hybrid Energy Storage System Based on Compressed Air and Supercapacitors,” *Lat. Am. Trans. IEEE*, vol. 11, no. 1, pp. 466–472, 2013, doi: 10.1109/TLA.2013.6502847.
- [171] P. Zhao, Y. Dai, and J. Wang, “Design and thermodynamic analysis of a hybrid energy storage system based on A-CAES (adiabatic compressed air energy storage) and FESS (flywheel energy storage system) for wind power application,” *Energy*, vol. 70, pp. 674–684, 2014, doi: 10.1016/j.energy.2014.04.055.
- [172] M. Sander and R. Gehring, “LIQHYSMES—A Novel Energy Storage Concept for Variable Renewable Energy Sources Using Hydrogen and SMES,” *IEEE Trans. Appl. Supercond.*, vol. 21, no. 3, pp. 1362–1366, 2011, doi: 10.1109/TASC.2010.2088359.

- [173] T. Hamajima *et al.*, “Application of SMES and fuel cell system combined with liquid hydrogen vehicle station to renewable energy control,” *IEEE Trans. Appl. Supercond.*, vol. 22, no. 3, 2012, doi: 10.1109/TASC.2011.2175687.
- [174] P. Thounthong, S. Raël, and B. Davat, “Control strategy of fuel cell/supercapacitors hybrid power sources for electric vehicle,” *J. Power Sources*, vol. 158, no. 1, pp. 806–814, 2006, doi: 10.1016/j.jpowsour.2005.09.014.
- [175] M. Uzunoglu and M. S. Alam, “Dynamic Modeling, Design, and Simulation of a Combined PEM Fuel Cell and Ultracapacitor System for Stand-Alone Residential Applications,” *IEEE Trans. Energy Convers.*, vol. 21, no. 3, pp. 767–775, 2006, doi: 10.1109/PSCE.2006.296164.
- [176] A. Payman, S. Pierfederici, F. Meibody-Tabar, and B. Davat, “An Adapted Control Strategy to Minimize DC-Bus Capacitors of a Parallel Fuel Cell/Ultracapacitor Hybrid System,” *IEEE Trans. Power Electron.*, vol. 26, no. 12, pp. 3843–3852, 2011, doi: 10.1109/TPEL.2009.2030683.
- [177] W. Greenwell and A. Vahidi, “Predictive Control of Voltage and Current in a Fuel Cell-Ultracapacitor Hybrid,” *IEEE Trans. Ind. Electron.*, vol. 57, no. 6, pp. 1954–1963, 2010, doi: 10.1109/TIE.2009.2031663.
- [178] A. Hajizadeh, M. A. Golkar, and A. Feliachi, “Voltage Control and Active Power Management of Hybrid Fuel-Cell/Energy-Storage Power Conversion System Under Unbalanced Voltage Sag Conditions,” *IEEE Trans. Energy Convers.*, vol. 25, no. 4, pp. 1195–1208, 2010, doi: 10.1109/TEC.2010.2062516.
- [179] A. Payman, S. Pierfederici, and F. Meibody-Tabar, “Energy management in a fuel cell/supercapacitor multisource/multiload electrical hybrid system,” *IEEE Trans. Power Electron.*, vol. 24, no. 12, pp. 2681–2691, 2009, doi: 10.1109/TPEL.2009.2028426.
- [180] E. L. V. Eriksson and E. M. Gray, “Optimization and integration of hybrid renewable energy hydrogen fuel cell energy systems – A critical review,” *Appl. Energy*, vol. 202, pp. 348–364, 2017, doi: 10.1016/j.apenergy.2017.03.132.
- [181] S. G. Tesfahunegn, O. Ulleberg, P. J. S. Vie, and T. M. Undeland, “Optimal shifting of Photovoltaic and load fluctuations from fuel cell and electrolyzer to lead acid battery in a Photovoltaic/hydrogen standalone power system for improved performance and life time,” *J. Power Sources*, vol. 196, no. 23, pp. 10401–10414, 2011, doi: 10.1016/j.jpowsour.2011.06.037.
- [182] N. Bigdeli, “Optimal management of hybrid PV/fuel cell/battery power system: A comparison of optimal hybrid approaches,” *Renew. Sustain. Energy Rev.*, vol. 42, pp. 377–393, 2015, doi: 10.1016/j.rser.2014.10.032.
- [183] P. Thounthong *et al.*, “DC Bus Stabilization of Li-Ion Battery Based Energy Storage for Hydrogen / Solar Power Plant for Autonomous Network Applications,” *IEEE Trans. Ind. Appl.*, vol. 51, no. 4, pp. 1–8, 2015, doi: 10.1109/TIA.2015.2388853.
- [184] M. Patterson, N. F. Macia, and A. M. Kannan, “Hybrid microgrid model based on solar photovoltaic battery fuel cell system for intermittent load applications,” *IEEE Trans. Energy Convers.*, vol. 30, no. 1, pp. 359–366, 2015, doi: 10.1109/TEC.2014.2352554.
- [185] S. J. Andreasen, L. Ashworth, I. N. Menjón Remón, and S. K. Kær, “Directly connected series coupled HTPEM fuel cell stacks to a Li-ion battery DC bus for a fuel cell electrical vehicle,” *Int. J. Hydrogen Energy*, vol. 33, no. 23, pp. 7137–7145, 2008, doi: 10.1016/j.ijhydene.2008.09.029.
- [186] X. Li *et al.*, “Online management of lithium-ion battery based on time-triggered controller area network for fuel-cell hybrid vehicle applications,” *J. Power Sources*, vol.

- 195, no. 10, pp. 3338–3343, 2010, doi: 10.1016/j.jpowsour.2009.11.099.
- [187] W. Gao, “Performance comparison of a fuel cell-battery hybrid powertrain and a fuel cell-ultracapacitor hybrid powertrain,” *IEEE Trans. Veh. Technol.*, vol. 54, no. 3, pp. 846–855, 2005, doi: 10.1109/TVT.2005.847229.
- [188] D. J. L. Brett *et al.*, “Concept and system design for a ZEBRA battery-intermediate temperature solid oxide fuel cell hybrid vehicle,” *J. Power Sources*, vol. 157, no. 2, pp. 782–798, 2006, doi: 10.1016/j.jpowsour.2005.12.054.
- [189] O. Briat, J. M. Vinassa, W. Lajnef, S. Azzopardi, and E. Woirgard, “Principle, design and experimental validation of a flywheel-battery hybrid source for heavy-duty electric vehicles,” *IET Electr. Power Appl.*, vol. 1, no. 5, pp. 665–674, 2007, doi: 10.1049/iet-epa.
- [190] H. Lee, B. Y. Shin, S. Han, S. Jung, B. Park, and G. Jang, “Compensation for the Power Fluctuation of the Large Scale Wind Farm Using Hybrid Energy Storage Applications,” in *IEEE Transactions on Applied Superconductivity*, 2012, vol. 22, no. 3, p. 5701904, doi: 10.1109/TASC.2011.2180881.
- [191] A. Windhorn, “A Hybrid Static/Rotary UPS System,” *IEEE Trans. Ind. Appl.*, vol. 28, no. 3, 1992.
- [192] B. G. Beaman and G. M. Rao, “Hybrid battery and flywheel energy storage system for LEO spacecraft,” in *The thirteenth Annual Battery Conference on Applications and Advances*, 1998, pp. 113–116, doi: 10.1109/BCAA.1998.653851.
- [193] J. W. Shim, Y. Cho, S. J. Kim, S. W. Min, and K. Hur, “Synergistic control of SMES and battery energy storage for enabling dispatchability of renewable energy sources,” *IEEE Trans. Appl. Supercond.*, vol. 23, no. 3, 2013, doi: 10.1109/TASC.2013.2241385.
- [194] S. Wang *et al.*, “Design and advanced control strategies of a hybrid energy storage system for the grid integration of wind power generations,” *IET Renew. Power Gener.*, vol. 9, no. 2, pp. 89–98, 2015, doi: 10.1049/iet-rpg.2013.0340.
- [195] A. Cansiz, C. Faydaci, M. T. Qureshi, O. Usta, and D. T. Mcguiness, “Integration of a SMES – Battery-Based Hybrid Energy Storage System into Microgrids,” *J. Supercond. Nov. Magn.*, pp. 1–9, 2017.
- [196] T. Ise, M. Kita, and A. Taguchi, “A Hybrid Energy Storage With a SMES and Secondary Battery,” *IEEE Trans. Appl. Supercond.*, vol. 15, no. 2, pp. 1915–1918, 2005, doi: 10.1109/TASC.2005.849333.
- [197] A. Kuperman and I. Aharon, “Battery-ultracapacitor hybrids for pulsed current loads: A review,” *Renew. Sustain. Energy Rev.*, vol. 15, no. 2, pp. 981–992, 2011, doi: 10.1016/j.rser.2010.11.010.
- [198] H. Kanchev, D. Lu, F. Colas, V. Lazarov, and B. Francois, “Energy management and operational planning of a microgrid with a PV based active generator for smart grid applications,” *IEEE Trans. Ind. Electron.*, vol. 58, no. 10, pp. 4583–4592, 2011.
- [199] F. Liu, J. Liu, and L. Zhou, “A novel control strategy for hybrid energy storage system to relieve battery stress,” *2nd Int. Symp. Power Electron. Distrib. Gener. Syst.*, pp. 929–934, 2010, [Online]. Available: <http://ieeexplore.ieee.org/lpdocs/epic03/wrapper.htm?arnumber=5545824>.
- [200] G. Zhang, X. Tang, and Z. Qi, “Research on battery supercapacitor hybrid storage and its application in MicroGrid,” *Asia-Pacific Power Energy Eng. Conf. APPEEC*, pp. 5–8, 2010.
- [201] F. S. Garcia, A. A. Ferreira, and J. A. Pomilio, “Control Strategy for Battery-

- Ultracapacitor Hybrid Energy Storage System,” in *Twenty-Fourth Annual IEEE Applied Power Electronics Conference and Exposition, 2009 (APEC 2009)*, 2009, pp. 826–832, doi: 10.1109/APEC.2009.4802757.
- [202] J. Cao and A. Emadi, “A New Battery/UltraCapacitor Hybrid Energy Storage System for Electric, Hybrid, and Plug-In Hybrid Electric Vehicles,” *IEEE Trans. Power Electron.*, vol. 27, no. 1, pp. 122–132, 2012, doi: 10.1109/TPEL.2011.2151206.
- [203] Z. Song, H. Hofmann, J. Li, J. Hou, X. Han, and M. Ouyang, “Energy management strategies comparison for electric vehicles with hybrid energy storage system,” *Appl. Energy*, vol. 134, pp. 321–331, 2014, doi: 10.1016/j.apenergy.2014.08.035.
- [204] Y. Zhang, Z. Jiang, and X. Yu, “Control Strategies for Battery/Supercapacitor Hybrid Energy Storage Systems,” 2008, doi: 10.1109/ENERGY.2008.4781031.
- [205] G. Wang, M. Ciobotaru, and V. G. Agelidis, “Power smoothing of large solar PV plant using hybrid energy storage,” *IEEE Trans. Sustain. Energy*, vol. 5, no. 3, pp. 834–842, 2014, doi: 10.1109/TSTE.2014.2305433.
- [206] S. Sumathi, L. A. Kumar, and P. Surekha, “Application of MATLAB/SIMULINK in Solar PV Systems,” in *Solar PV and Wind Energy Conversion Systems: An Introduction to Theory, Modeling with MATLAB/SIMULINK, and the Role of Soft Computing Techniques*, Springer, 2015.
- [207] R. Zamora and A. K. Srivastava, “Controls for microgrids with storage: Review, challenges, and research needs,” *Renew. Sustain. Energy Rev.*, vol. 14, no. 7, pp. 2009–2018, 2010, [Online]. Available: <http://dx.doi.org/10.1016/j.rser.2010.03.019>.
- [208] X. Fang, S. Misra, G. Xue, and D. Yang, “Smart Grid — The New and Improved Power Grid: A Survey,” *IEEE Commun. Surv. Tutorials*, vol. 14, no. 4, pp. 944–980, 2012, [Online]. Available: <http://ieeexplore.ieee.org/lpdocs/epic03/wrapper.htm?arnumber=6099519>.
- [209] I. Koutsopoulos and L. Tassiulas, “Challenges in demand load control for the smart grid,” *Network, IEEE*, vol. 25, no. 5, pp. 16–21, 2011, [Online]. Available: <http://ieeexplore.ieee.org/lpdocs/epic03/wrapper.htm?arnumber=6033031>.
- [210] G. K. Singh, “Solar power generation by PV (photovoltaic) technology: A review,” *Energy*, vol. 53, pp. 1–13, 2013, doi: 10.1016/j.energy.2013.02.057.
- [211] M. C. Argyrou, P. Christodoulides, C. C. Marouchos, and S. A. Kalogirou, “Hybrid battery-supercapacitor mathematical modeling modeling for PV application using Matlab/Simulink,” in *2018 53rd International Universities Power Engineering Conference (UPEC)*, 2018, pp. 1–6, doi: 10.1109/UPEC.2018.8541933.
- [212] Y. Kim, V. Raghunathan, and A. Raghunathan, “Design and Management of Battery-Supercapacitor Hybrid Electrical Energy Storage Systems for Regulation Services,” *IEEE Trans. Multi-Scale Comput. Syst.*, vol. 3, no. 1, pp. 12–24, 2017, doi: 10.1109/TMSCS.2016.2627543.
- [213] V. Vega-Garita, L. Ramirez-Elizondo, G. R. C. Mouli, and P. Bauer, “Review of residential PV-storage architectures,” *2016 IEEE Int. Energy Conf. ENERGYCON 2016*, 2016, doi: 10.1109/ENERGYCON.2016.7514039.
- [214] H. C. Hesse, M. Schimpe, D. Kucevic, and A. Jossen, *Lithium-ion battery storage for the grid - A review of stationary battery storage system design tailored for applications in modern power grids*, vol. 10, no. 12. 2017.
- [215] A. Parwal *et al.*, “Energy management for a grid-connected wave energy park through a hybrid energy storage system,” *Appl. Energy*, vol. 231, pp. 399–411, 2018, doi: 10.1016/j.apenergy.2018.09.146.

- [216] T. S. Babu, R. V. Krishnakumar, V. K. Ramachandaramurthy, S. B. Sani, S. Chemud, and R. M. Lajim, “A Comprehensive Review of Hybrid Energy Storage Systems: Converter Topologies, Control Strategies and Future Prospects,” *IEEE Access*, vol. 8, pp. 148702–148721, 2020, doi: 10.1109/ACCESS.2020.3015919.
- [217] W. Jing, C. H. Lai, W. S. H. Wong, and M. L. D. Wong, “A comprehensive study of battery-supercapacitor hybrid energy storage system for standalone PV power system in rural electrification,” *Appl. Energy*, vol. 224, pp. 340–356, 2018, doi: 10.1016/j.apenergy.2018.04.106.
- [218] G. Celsa and G. M. Tina, “Matlab/Simulink model of photovoltaic modules/strings under uneven distribution of irradiance and temperature,” 2015, doi: 10.1109/IREC.2015.7110944.
- [219] B. P. Singh, M. Singh, and S. K. Roy, “Mathematical modeling of electronic devices and circuits,” *AIP Conf. Proc.*, vol. 1324, no. 65, pp. 65–69, 2010, doi: 10.1063/1.3526268.
- [220] W. Xiao, *Photovoltaic Power System: Modeling, Design, and Control*. John Wiley & Sons, 2017.
- [221] B. Fekkak, M. Mena, and B. Boussahoua, “Control of transformerless grid-connected PV system using average models of power electronics converters with MATLAB/Simulink,” *Sol. Energy*, vol. 173, pp. 804–813, 2018, doi: 10.1016/j.solener.2018.08.012.
- [222] Q. Wang *et al.*, “Dynamic modeling and small signal stability analysis of distributed photovoltaic grid-connected system with large scale of panel level DC optimizers,” *Appl. Energy*, vol. 259, p. 114132, 2020, doi: 10.1016/j.apenergy.2019.114132.
- [223] S. Jiao, R. Wu, and W. Xiao, “Fast Simulation Technique for Photovoltaic Power Systems using Simulink,” 2019, doi: 10.1109/IFEEC47410.2019.9014990.
- [224] R. W. Erickson and D. Maksimovic, *Fundamentals of power electronics*, Second ed. Springer Science & Business Media, 2007.
- [225] W. Xiao, *Power Electronics Step-by-Step: Design, Modeling, Simulation, and Control*. McGraw Hill Professional, 2021.
- [226] N. M. A. A. Shannan, N. Z. Yahaya, and B. Singh, “Single-Diode Model and Two-Diode Model of PV Modules : A Comparison,” *Proc. - 2013 IEEE Int. Conf. Control Syst. Comput. Eng. ICCSCE 2013*, pp. 210–214, 2013, doi: 10.1109/ICCSCE.2013.6719960.
- [227] A. Salem, Farhan, “Modeling and Simulation issues on PhotoVoltaic systems, for Mechatronics design of solar electric applications,” *IPASJ Ineternational J. Mechanical Eng.*, vol. 2, no. 8, pp. 24–47, 2014, [Online]. Available: <http://ipasj.org/IJME/Volume2Issue8/IJME-2014-08-22-8.pdf>.
- [228] F. Adamo, F. Attivissimo, A. Di Nisio, A. M. L. Lanzolla, and M. Spadavecchia, “Parameters Estimation for a Model of Photovoltaic Panels,” 2009, [Online]. Available: http://www.imeko2009.it.pt/Papers/FP_622.pdf.
- [229] H. B. Vika, “Modelling of Photovoltaic Modules with Battery Energy Storage in Simulink / Matlab,” Master dissertation, Norwegian Univ. of Science and Technology (NTNU), 2014.
- [230] H. Bellia, R. Youcef, and M. Fatima, “A detailed modeling of photovoltaic module using MATLAB,” *NRIAG J. Astron. Geophys.*, vol. 3, no. 1, pp. 53–61, 2014, doi: 10.1016/j.nrjag.2014.04.001.
- [231] T. Salmi, M. Bouzguenda, A. Gastli, and A. Masmoudi, “MATLAB / Simulink Based

- Modelling of Solar Photovoltaic Cell,” *Int. J. Renew. Energy Res.*, vol. 2, no. 2, 2012, doi: 10.1234/IJRER.V2I2.157.
- [232] H. J. El-Khozondar, R. J. El-Khozondar, and K. Matter, “Parameters Influence on MPP Value of the Photo Voltaic Cell,” *Energy Procedia*, vol. 74, pp. 1142–1149, 2015, doi: 10.1016/j.egypro.2015.07.756.
- [233] J. F. Sultani, “Modelling, Design and Implementation of D-Q Control in Single-Phase Grid-Connected Inverters for Photovoltaic Systems Used in Domestic Dwellings,” PhD dissertation, De Montfort University, Leicester, UK, 2013.
- [234] Luxor, “Photovoltaic module Eco Line 60/230-250W, LX-250P.” <https://www.luxor-solar.com/en/solar-modules/eco-line/eco-line-classic.html>.
- [235] M. G. Villalva, T. G. De Siqueira, and E. Ruppert, “Voltage regulation of photovoltaic arrays: Small-signal analysis and control design,” *IET Power Electron.*, vol. 3, no. 6, pp. 869–880, 2010, doi: 10.1049/iet-pel.2008.0344.
- [236] B. Subudhi and R. Pradhan, “A Comparative Study on Maximum Power Point Tracking Techniques for Photovoltaic Power Systems,” *IEEE Trans. Sustain. Energy*, vol. 4, no. 1, pp. 89–98, 2013, doi: 10.1109/TSTE.2012.2202294.
- [237] H. Rezk and A. M. Eltamaly, “A comprehensive comparison of different MPPT techniques for photovoltaic systems,” *Sol. Energy*, vol. 112, pp. 1–11, 2015, doi: 10.1016/j.solener.2014.11.010.
- [238] T. Eswam and P. L. Chapman, “Comparison of Photovoltaic Array Maximum Power Point Tracking Techniques,” *IEEE Trans. Energy Convers.*, vol. 22, no. 2, pp. 439–449, 2007, doi: 10.1109/TEC.2006.874230.
- [239] L. Qin and X. Lu, “Matlab/Simulink-Based Research on Maximum Power Point Tracking of Photovoltaic Generation,” *Phys. Procedia*, vol. 24, pp. 10–18, 2012, doi: 10.1016/j.phpro.2012.02.003.
- [240] S. Umashankar, K. P. Aparna, R. Priya, and S. Suryanarayanan, “Modeling and Simulation of a PV System using DC-DC Converter,” *Int. J. Latest Res. Eng. Technol.*, vol. 1, no. 2, pp. 9–16, 2015, [Online]. Available: [http://www.ijlret.com/Papers/Vol-1-issue-2/2-A037 \(Final Version\).pdf](http://www.ijlret.com/Papers/Vol-1-issue-2/2-A037 (Final Version).pdf).
- [241] M. C. Argyrou, P. Christodoulides, C. C. Marouchos, and S. A. Kalogirou, “A grid-connected photovoltaic system: mathematical modeling using MATLAB/Simulink,” 2017, doi: 10.1109/UPEC.2017.8232009.
- [242] F. Liu, S. Duan, F. Liu, B. Liu, and Y. Kang, “A Variable Step Size INC MPPT Method for PV Systems,” *IEEE Trans. Ind. Electron.*, vol. 55, no. 7, pp. 2622–2628, 2008, doi: 10.1109/ICMCS.2014.6911212.
- [243] Y. Soufi, M. Bechouat, S. Kahla, and K. Bouallegue, “Maximum power point tracking using fuzzy logic control for photovoltaic system,” 2014.
- [244] J. K. Shiao, Y. C. Wei, and B. C. Chen, “A study on the fuzzy-logic-based solar power MPPT algorithms using different fuzzy input variables,” *Algorithms*, vol. 8, no. 2, pp. 100–127, 2015, doi: 10.3390/a8020100.
- [245] A. M. Z. Alabedin, E. F. El-Saadany, and M. M. A. Salama, “Maximum power point tracking for Photovoltaic systems using fuzzy logic and artificial neural networks,” 2011, doi: 10.1109/PES.2011.6039690.
- [246] S. Narendiran, S. K. Sahoo, R. Das, and A. K. Sahoo, “Fuzzy Logic Controller based Maximum Power Point Tracking for PV System,” 2016.
- [247] S. Karthika, K. Velayutham, P. Rathika, and D. Devaraj, “Fuzzy Logic Based Maximum

- Power Point Tracking Designed for 10kW Solar Photovoltaic System with Different Membership Functions,” *Int. J. Electr. Comput. Energ. Electron. Commun. Eng.*, vol. 8, no. 6, pp. 1013–1018, 2014.
- [248] A. M. Othman, M. M. M. El-arini, A. Ghitas, and A. Fathy, “Realworld maximum power point tracking simulation of PV system based on Fuzzy Logic control,” *NRIAG J. Astron. Geophys.*, vol. 1, no. 2, pp. 186–194, 2012, doi: 10.1016/j.nrjag.2012.12.016.
- [249] University of Colorado, “ECEN2060 MATLAB/Simulink materials,” 2012. <http://ecee.colorado.edu/~ecen2060/matlab.html> (accessed May 01, 2017).
- [250] Z. Sabiri, N. Machkour, M. B. Camara, and B. Dakyo, “DC / DC converters for Photovoltaic Applications- Modeling and Simulations,” in *International Renewable and Sustainable Energy Conference (IRSEC)*, 2014, pp. 209–213.
- [251] L. S. C. Kumar and K. Padma, “Matlab/Simulink Based Modelling and Simulation of Residential Grid Connected Solar Photovoltaic System,” *Int. J. Eng. Res. Technol.*, vol. 3, no. 3, 2014, doi: 10.1016/0168-7336(86)80016-X.
- [252] E. Hosseini, “Modeling and Simulation of Choppers Switching Via Matlab/Simulink,” *Sci. Bull. Petru Maior Univ. Targu Mures*, vol. 12, no. 1, 2015.
- [253] M. Assaf, D. Seshsachalam, D. Chandra, and R. K. Tripathi, “Dc-dc converters via matlab/simulink,” *Proc WSEAS Conf. Autom. Control. Model. Simul. (ACMOS'05)*, Prague, Czech Repub., pp. 464–471, 2005.
- [254] J. Li and M. S. Mazzola, “Accurate battery pack modeling for automotive applications,” *J. Power Sources*, vol. 237, pp. 215–228, 2013, doi: 10.1016/j.jpowsour.2013.03.009.
- [255] D. Rekioua, *Hybrid Renewable Energy Systems*. Springer, Cham, 2020.
- [256] S. Williamson, S. Rimmalapudi, and A. Emadi, “Electrical modeling of renewable energy sources and energy storage devices,” *Journal of Power Electronics*, vol. 4, no. 2, pp. 117–126, 2004, [Online]. Available: <http://www.dbpia.co.kr/Journal/ArticleDetail/393868>.
- [257] M. Chen and G. A. Rincon-Mora, “Accurate Electrical Battery Model Capable of Predicting Runtime and I – V Performance,” *IEEE Trans. Energy Convers.*, vol. 21, no. 2, pp. 504–511, 2006, doi: 10.1109/TEC.2006.874229.
- [258] H. Beltran, M. Swierczynski, N. Aparicio, E. Belenguer, R. Teodorescu, and P. Rodriguez, “Lithium ion batteries ageing analysis when used in a PV power plant,” *2012 IEEE Int. Symp. Ind. Electron.*, pp. 1604–1609, 2012, doi: 10.1109/ISIE.2012.6237330.
- [259] Y. Tian, D. Li, J. Tian, and B. Xia, “State of charge estimation of lithium-ion batteries using an optimal adaptive gain nonlinear observer,” *Electrochim. Acta*, vol. 225, pp. 225–234, 2017, doi: 10.1016/j.electacta.2016.12.119.
- [260] O. Erdinc, B. Vural, and M. Uzunoglu, “A dynamic lithium-ion battery model considering the effects of temperature and capacity fading,” in *2009 International Conference on Clean Electrical Power, ICCEP 2009*, 2009, pp. 383–386, doi: 10.1109/ICCEP.2009.5212025.
- [261] C. Sinkaram, K. Rajakumar, and V. Asirvadam, “Modeling battery management system using the lithium-ion battery,” in *2012 IEEE International Conference on Control System, Computing and Engineering (ICCSCE)*, 2012, pp. 50–55, doi: 10.1109/ICCSCE.2012.6487114.
- [262] L. W. Yao, J. A. Aziz, P. Y. Kong, and N. R. N. Idris, “Modeling of lithium-ion battery using MATLAB/Simulink,” in *IECON 2013 - 39th Annual Conference of the IEEE Industrial Electronics Society*, 2013, pp. 1729–1734, doi:

10.1109/IECON.2013.6699393.

- [263] LG Chem, “Home Battery: RESU 10.” <https://www.lgessbattery.com/eu/home-battery/product-info.lg> (accessed May 27, 2020).
- [264] Tesla, “Powerwall: The Tesla Home Battery.” <https://www.tesla.com/powerwall> (accessed May 01, 2019).
- [265] F. Belhachemi, S. Rael, and B. Davat, “A physical based model of power electric double-layer supercapacitors,” in *Conference Record of the 2000 IEEE Industry Applications Conference*, 2000, vol. 5, pp. 3069–3076, doi: 10.1109/IAS.2000.882604.
- [266] L. Zubieta and R. Bonert, “Characterization of double-layer capacitors for power electronics applications,” *IEEE Trans. Ind. Appl.*, vol. 36, no. 1, pp. 199–205, 2000, doi: 10.1109/28.821816.
- [267] Y. Parvini, J. B. Siegel, A. G. Stefanopoulou, and A. Vahidi, “Supercapacitor Electrical and Thermal Modeling, Identification, and Validation for a Wide Range of Temperature and Power Applications,” *IEEE Trans. Ind. Electron.*, vol. 63, no. 3, pp. 1574–1585, 2016, doi: 10.1109/TIE.2015.2494868.
- [268] M. Ceraolo, G. Lutzemberger, and D. Poli, “State-Of-Charge Evaluation Of Supercapacitors,” *J. Energy Storage*, vol. 11, pp. 211–218, 2017, doi: 10.1016/j.est.2017.03.001.
- [269] S. Lee and J. Kim, “Power capability analysis of lithium battery and supercapacitor by pulse duration,” *Electronics*, vol. 8, no. 12, p. 1395, 2019, doi: 10.3390/electronics8121395.
- [270] N. Mendis, K. M. Muttaqi, and S. Perera, “Management of battery-supercapacitor hybrid energy storage and synchronous condenser for isolated operation of PMSG based variable-speed wind turbine generating systems,” *IEEE Trans. Smart Grid*, vol. 5, no. 2, pp. 944–953, 2014, doi: 10.1109/TSG.2013.2287874.
- [271] P. Ariyaratna, K. M. Muttaqi, and D. Sutanto, “A novel control strategy to mitigate slow and fast fluctuations of the voltage profile at common coupling Point of rooftop solar PV unit with an integrated hybrid energy storage system,” *J. Energy Storage*, vol. 20, no. July, pp. 409–417, 2018, doi: 10.1016/j.est.2018.10.016.
- [272] B. V. P. Chong, L. Zhang, and A. Dehghani, “Modelling & control of a bidirectional converter for a stand-alone photovoltaic power plant,” 2007, doi: 10.1109/EPE.2007.4417357.
- [273] B. Y. Li, C. Xu, C. Li, and Z. Guan, “Working principle analysis and control algorithm for bidirectional DC/DC converter,” *J. Power Technol.*, vol. 97, no. 4, pp. 327–335, 2017.
- [274] K. H. Chao, M. C. Tseng, C. H. Huang, Y. G. Liu, and L. C. Huang, “Design and Implementation of a Bidirectional DC-DC Converter for Stand-Alone Photovoltaic Systems,” *Int. J. Comput. Consum. Control*, vol. 2, no. 3, pp. 44–55, 2013, doi: 10.4111/kju.2013.54.12.830.
- [275] K. S. Divya and T. N. Ajit, “Small Signal Modelling and Controller Design of Boost Converter using MATLAB,” *Int. Res. J. Power Energy Eng.*, vol. 3, no. 2, pp. 112–117, 2017.
- [276] B. Choi, *Pulsewidth Modulated DC-to-DC Power Conversion: Circuits, Dynamics, and Control Designs*. John Wiley & Sons, 2013.
- [277] A. A. Elbaset and M. S. Hassan, “Small-Signal MATLAB/Simulink Model of DC–DC Buck Converter,” in *Design and Power Quality Improvement of Photovoltaic Power*

- System*, Springer International Publishing, 2017, pp. 97–114.
- [278] R. W. Erickson, “DC-DC power converters,” *Wiley Encycl. Electr. Electron. Eng.*, 2001.
- [279] E. Ugur and B. Vural, “Comparison of different small signal modeling methods for bidirectional DC-DC converter,” in *3rd International Conference on Renewable Energy Research and Applications, ICRERA 2014*, 2014, pp. 913–915, doi: 10.1109/ICRERA.2014.7016518.
- [280] M. C. Joshi and S. Samanta, “Modeling and Control of Bidirectional DC-DC Converter Fed PMDC Motor for Electric Vehicles,” 2013.
- [281] P. Pany, R. Singh, and R. Tripathi, “Bidirectional DC-DC converter fed drive for electric vehicle system,” *Int. J. Eng. Sci. Technol.*, vol. 3, no. 3, pp. 101–110, 2011, doi: 10.4314/ijest.v3i3.68426.
- [282] J. Zhang, J. S. Lai, and W. Yu, “Bidirectional DC-DC converter modeling and unified controller with digital implementation,” in *IEEE Applied Power Electronics Conference and Exposition - APEC*, 2008, pp. 1747–1753, doi: 10.1109/APEC.2008.4522963.
- [283] Z. Rasin and M. F. Rahman, “Control of bidirectional DC-DC converter for battery storage system in grid-connected quasi-Z-source PV inverter,” in *2015 IEEE Conference on Energy Conversion, CENCON 2015*, 2015, pp. 205–210, doi: 10.1109/CENCON.2015.7409540.
- [284] Texas Instruments, “TI Designs: TIDA-00951 2-kW, 48- to 400-V, >93% Efficiency, Isolated Bidirectional DC-DC Converter Reference Design for UPS.” Texas Instruments Incorporated, 2017, [Online]. Available: https://www.ti.com/lit/ug/tidud04/tidud04.pdf?ts=1596102406648&ref_url=https%253A%252F%252F.
- [285] TDK-Lambda Corporation, “Bidirectional DC-DC Converters: Supporting smart grids,” *Tech J.*, vol. 20, pp. 1–6, 2014, [Online]. Available: https://product.tdk.com/en/techlibrary/archives/vol20_eza/TKD_TJ023_DC-DC_E.pdf.
- [286] TDK Corporation, “Introduction to the examples of use: Yutaka Electronics Industry Company Limited, ‘MPSs (multi-power systems) using the EZA2500 bidirectional DC-DC converter.’” https://product.tdk.com/info/en/products/power/switching-power/bidirect-converter/technote/app_eza.html (accessed Jul. 30, 2020).
- [287] S. Samerchur, S. Premrudeepreechacharn, Y. Kumsuwun, and K. Higuchi, “Power control of single-phase voltage source inverter for grid-connected photovoltaic systems,” in *2011 IEEE/PES Power Systems Conference and Exposition, PSCE 2011*, 2011, pp. 1–6, doi: 10.1109/PSCE.2011.5772504.
- [288] S. H. Ko, S. R. Lee, H. Dehbonei, and C. V. Nayar, “Application of voltage- and current-controlled voltage source inverters for distributed generation systems,” *IEEE Trans. Energy Convers.*, vol. 21, no. 3, pp. 782–792, 2006, doi: 10.1109/TEC.2006.877371.
- [289] C. Ma and C. Hsieh, “Investigation on Hybrid Energy Storage Systems and Their Application in Green Energy Systems,” *Electronics*, vol. 9, no. 11, p. 1907, 2020, doi: 10.3390/electronics9111907.
- [290] P. T. Krein, R. S. Balog, and M. Mirjafari, “Minimum energy and capacitance requirements for single-phase inverters and rectifiers using a ripple port,” *IEEE Trans. Power Electron.*, vol. 27, no. 11, pp. 4690–4698, 2012, doi: 10.1109/TPEL.2012.2186640.
- [291] M. H. Rashid, *Power electronics handbook*, Fourth ed. Butterworth-Heinemann, 2017.
- [292] A. H. M. Nordin, A. M. Omar, and H. Zainuddin, “Modeling and Simulation of Grid

- Inverter in Grid- Connected Photovoltaic System,” *Int. J. Renew. Energy Res.*, vol. 4, no. 4, pp. 949–957, 2014.
- [293] A. Panda, M. K. Pathak, and S. P. Srivastava, “A single phase photovoltaic inverter control for grid connected system,” *Sadhana*, vol. 41, no. 1, pp. 15–30, 2016, doi: 10.1007/s12046-015-0459-2.
- [294] S. S. Raghuwanshi and K. Gupta, “Modeling of a single-phase grid-connected photovoltaic system using MATLAB/Simulink,” 2015, doi: 10.1109/IC4.2015.7375633.
- [295] S. M. A. Faisal, “Model of Grid Connected Photovoltaic System Using MATLAB / SIMULINK,” *Int. J. Comput. Appl.*, vol. 31, no. 6, 2011.
- [296] S. Vavilapalli, U. Subramaniam, S. Padmanaban, and F. Blaabjerg, “Design and Controller-In-Loop Simulations of a Low Cost Two-Stage PV-Simulator,” *Energies*, vol. 11, no. 10, p. 2774, 2018, doi: 10.3390/en11102774.
- [297] N. R. Tummuru, M. K. Mishra, and S. Srinivas, “Dynamic Energy Management of Renewable Grid Integrated Hybrid Energy Storage System,” *IEEE Trans. Ind. Electron.*, vol. 62, no. 12, pp. 7728–7737, 2015, doi: 10.1109/TIE.2015.2455063.
- [298] R. W. Erickson and D. Maksimovic, *Fundamentals of Power Electronics*, Third ed. Springer Nature Switzerland AG, 2020.
- [299] S. I. Serna-Garces, D. Gonzalez Montoya, and C. A. Ramos-Paja, “Control of a charger/discharger DC/DC converter with improved disturbance rejection for bus regulation,” *Energies*, vol. 11, no. 3, p. 594, 2018, doi: 10.3390/en11030594.
- [300] A. Etxeberria, I. Vechiu, H. Camblong, and J. M. Vinassa, “Comparison of sliding mode and PI control of a hybrid energy storage system in a microgrid application,” *Energy Procedia*, vol. 12, pp. 966–974, 2011, doi: 10.1016/j.egypro.2011.10.127.
- [301] S. I. Serna-Garcés, D. G. Montoya, and C. A. Ramos-Paja, “Sliding-mode control of a charger/discharger DC/DC converter for DC-bus regulation in renewable power systems,” *Energies*, vol. 9, no. 4, p. 245, 2016, doi: 10.3390/en9040245.
- [302] S. Punna and U. B. Manthathi, “Optimum design and analysis of a dynamic energy management scheme for HESS in renewable power generation applications,” *SN Appl. Sci.*, vol. 2, no. 3, pp. 1–13, 2020, doi: 10.1007/s42452-020-2313-3.
- [303] S. Kotra, M. K. Mishra, and N. P. Chaithanya, “Design and small signal analysis of DC microgrid with hybrid energy storage system,” in *Asia-Pacific Power and Energy Engineering Conference, APPEEC*, 2017, pp. 1–6, doi: 10.1109/APPEEC.2017.8308995.
- [304] N. E. Zakzouk, A. K. Abdelsalam, A. A. Helal, and B. W. Williams, “PV Single-Phase Grid-Connected Converter: DC-Link Voltage Sensorless Prospective,” *IEEE J. Emerg. Sel. Top. Power Electron.*, vol. 5, no. 1, pp. 526–546, 2017, doi: 10.1109/JESTPE.2016.2637000.
- [305] N. A. Ninad and L. A. C. Lopes, “Operation of single-phase grid-connected inverters with large DC bus voltage ripple,” in *2007 IEEE Canada Electrical Power Conference, EPC 2007*, 2007, pp. 172–176, doi: 10.1109/EPC.2007.4520325.
- [306] Y. M. Chen, C. H. Chang, and H. C. Wu, “DC-link capacitor selections for the single-phase grid-connected PV system,” in *Proceedings of the International Conference on Power Electronics and Drive Systems (PEDS)*, 2009, pp. 72–77, doi: 10.1109/PEDS.2009.5385801.
- [307] P. K. Sahu, P. Shaw, and S. Maity, “Modeling and control of grid-connected DC/AC converters for single-phase micro-inverter application,” 2016, doi:

10.1109/INDICON.2015.7443537.

- [308] B. Yang, W. Li, Y. Zhao, and X. He, “Design and analysis of a grid-connected photovoltaic power system,” *IEEE Trans. Power Electron.*, vol. 25, no. 4, pp. 992–1000, 2010, doi: 10.1109/TPEL.2009.2036432.
- [309] M. A. Guerrero-Martinez, M. I. Milanes-Montero, F. Barrero-Gonzalez, V. M. Miñambres-Marcos, E. Romero-Cadaval, and E. Gonzalez-Romera, “A smart power electronic multiconverter for the residential sector,” *Sensors (Switzerland)*, vol. 17, no. 6, 2017, doi: 10.3390/s17061217.
- [310] V. M. Miñambres-Marcos, M. Á. Guerrero-Martínez, F. Barrero-González, and M. I. Milanés-Montero, “A grid connected photovoltaic inverter with battery-supercapacitor hybrid energy storage,” *Sensors*, vol. 17, no. 8, p. 1856, 2017, doi: 10.3390/s17081856.
- [311] Z. Cabrane, M. Ouassaid, M. Maaroufi, S. Marhraoui, and N. El Hichami, “Two proposed control algorithm of the management of supercapacitors-batteries combination in photovoltaic energy storage,” in *Proceedings of 2018 6th International Renewable and Sustainable Energy Conference, IRSEC 2018*, 2018, pp. 1–6, doi: 10.1109/IRSEC.2018.8702842.
- [312] U. Manandhar *et al.*, “Energy management and control for grid connected hybrid energy storage system under different operating modes,” *IEEE Trans. Smart Grid*, vol. 10, no. 2, pp. 1626–1636, 2019, doi: 10.1109/TSG.2017.2773643.
- [313] N. Šajn, “Electricity ‘Prosumers,’” 2016. [http://www.europarl.europa.eu/thinktank/en/document.html?reference=EPRS_BRI\(2016\)593518](http://www.europarl.europa.eu/thinktank/en/document.html?reference=EPRS_BRI(2016)593518) (accessed Jun. 01, 2017).
- [314] M. C. Argyrou, P. Christodoulides, and S. A. Kalogirou, “Modeling of a photovoltaic system with different MPPT techniques using MATLAB / Simulink,” 2018, doi: 10.1109/ENERGYCON.2018.8398734.
- [315] M. C. Argyrou, C. C. Marouchos, S. A. Kalogirou, and P. Christodoulides, “Modeling a residential grid-connected PV system with battery- supercapacitor storage: Control design and stability analysis,” *Energy Reports*, 2021 (submitted).
- [316] M. C. Argyrou, C. Spanias, C. C. Marouchos, S. A. Kalogirou, and P. Christodoulides, “Energy management and modeling of a grid-connected BIPV system with battery energy storage,” in *2019 54th International Universities Power Engineering Conference (UPEC)*, 2019, pp. 1–6, doi: 10.1109/UPEC.2019.8893495.
- [317] M. C. Argyrou, C. C. Marouchos, S. A. Kalogirou, and P. Christodoulides, “A novel power management algorithm for a residential grid-connected PV system with battery-supercapacitor storage for increased self-consumption and self-sufficiency,” *Energy Convers. Manag.*, 2021 (submitted).